SMART MATERIAL WING MORPHING FOR UNMANNED AERIAL VEHICLES

by

Alexander M. Pankonien

A dissertation submitted in partial fulfillment
of the requirements for the degree of
Doctor of Philosophy
(Aerospace Engineering)
in the University of Michigan
2015

Doctoral Committee:

Professor Daniel J. Inman, Co-Chair
Assistant Professor Karthik Duraisamy, Co-Chair
Professor Diann E. Brei
Professor Carlos E. Cesnik

Dedication

This dissertation is dedicated
in its entirety
to Ambi
without whom
I might have taken
a different, less bold journey.

Flying is learning how to throw yourself at the ground and miss.
– Douglas Adams

Your biggest failure is the thing you dreamed of contributing,
but didn't find the guts to do.
–Seth Godin

Acknowledgements

I would like to thank everyone who contributed to the research that made this dissertation possible. Without their help, I know I could not have even written this much. After all, I wrote the acknowledgements last!

First, I would like to thank my advisor, Dr. Daniel J. Inman. Principal Instigator would be an appropriate term to describe him. His positivity, willingness to tackle the status quo, and vision gave much needed lift to the research every step of the way. Through moving to a new school, together, seeking funding during sequestration, pushing me to publish when I wasn't sure what was even worth publishing, and asking me about my life when all I could think about was research, he played the role of mentor as well as advisor. He has joked that it's bad enough that his name had to go in the list of authors, but I often feel like simply putting his name on the papers is not credit enough. Anyone who has had the privilege to know him would agree.

I would also like to thank my committee for their contributions and insight throughout the research process. I also met Dr. Karthik Duraisamy before he started at the University of Michigan. From our first conversation, I appreciated his energy, ideas, and willingness to collaborate. Although this dissertation did not take the exact path that we had expected, it would still not be possible without his insight into computational fluid dynamics and mitigating errors in the experiments. Dr. Carlos Cesnik graciously shared his equipment and laboratory, which directly led to the results in every single chapter. Additionally, his persistent admonitions, while as my teacher and then later as committee member, to improve the impact, scope and quality of the research have pushed me to test the limits of not just the technical components during my investigations, but also myself. Dr. Diann Brei wore many hats in another department. Despite that, my conversations with her, her technical staff, and graduate students greatly shaped the way that I looked at the concepts from an actuation perspective.

Thanks to my friends, for inspiring this work and then making me actually do something about it. I grew the most as a researcher from the experiences of working alongside some of the best, brightest, and most forgiving labmates around. So, thank you specifically to: Jared Hobeck, Cassio Thome de Faria, Ji-Duck Choi, Amin Karami, Ya Wang, Katie Reichl, and Brittany Essink.

Additional thanks are required to the technical support staff for the Aerospace Engineering department. Building the lab from the first day was made significantly easier with their help. The expert craftsmanship of Terry Larrow, the guidance through electrical diagrams provided by Aaron Borgman, and the knowledge and patience of Chris Chartier while operating the wind tunnels all contributed directly to the results in the following chapters. Their advice, assistance, and insight were greatly appreciated.

I am deeply thankful to my family for their support. Travelling from Texas to Michigan was neither the first nor the last of many crazy ideas that they have backed. I thank them for instilling the values and drive in me that allowed me to write this dissertation. Regular phone calls were especially helpful, but never quite the same as seeing them in person.

Although the dedication speaks the best way that I can imagine, I would again like to thank my wife, Ambi, for her support throughout this process. I believe God gave her to me to keep me accountable for the inspiration and thoughts with which He blessed me. I stole this line, but having such a great wife to remind me that there's more to life than engineering and science while still giving me time to do work is *the best.*

Finally, thanks to you, the reader, who makes this work relevant (or not). Try to see past the shortcomings in the following chapters, perceive the crux of the concepts, and if possible, be inspired. Read the "future work" sections, try new things, and make the future worth living in.

Table of Contents

List of Figures

List of Tables

List of Appendices

List of Selected Acronyms and Symbols

Common acronyms

MFC Macro-Fiber Composite

SMA Shape Memory Alloy

SMTE Spanwise Morphing Trailing Edge

SSMA Synergistic Smart Morphing Aileron

UAV Unmanned Aerial Vehicle

Geometric Parameters

AR Wing aspect ratio

b Wing span

$\bar{b}$ Effective span ratio

c Airfoil chord

δ_{tip} Tip deflection

E Chordwise normalized flap extent

η Effective flap angle

Flow Parameters

α Angle of attack

Re Reynolds number

V_∞ Freestream flow speed

q Dynamic pressure

Force Parameters

C_p Pressure coefficient

C_D Drag coefficient

C_l Rolling moment coefficient

C_L Lift coefficient

C_m Pitching moment coefficient

Force Derivative Parameters

$\Delta C_{"X"}$ Change in "X"th nondimensional force

C_{L_α} Lift-curve slope

C_{D_η} Drag control derivative

C_{l_η} Roll control derivative

C_{L_η} Lift control derivative

C_{m_η} Pitch control derivative

Time-Scale Characterization Parameters

Δ Peak-to-peak tip deflection amplitude

T Forcing period

τ_r Relative time constant

τ_∞ First-order time constant

τ_0 Baseline, first-order time constant

Abstract

Morphing, or geometric adaptation to off-design conditions, has been considered in aircraft design since the Wright Brothers' first powered flight. Decades later, smooth, bio-mimetic shape variation for control over aerodynamic forces still remains elusive.

Unmanned Aerial Vehicles are prime targets for morphing implementation as they must adapt to large changes in flight conditions associated with locally varying wind or large changes in mass associated with payload delivery. The Spanwise Morphing Trailing Edge (SMTE) concept is developed to locally vary the trailing edge camber of a wing or control surface, functioning as a modular replacement for conventional ailerons without altering the wing's spar box. The SMTE design was realized utilizing alternating active sections of Macro Fiber Composites (MFCs) driving internal elastomeric compliant mechanisms and passive sections of anisotropic, elastomeric skin with tailorable stiffness, produced by additive manufacturing. Experimental investigations of the modular design via a new scaling methodology for reduced-span test articles revealed that increased use of more MFCs within the active section did not increase aerodynamic performance due to asymmetric voltage constraints. The comparative mass and aerodynamic gains for the SMTE concept are evaluated for a representative finite wing as compared with a conventional, articulated flap wing. Informed by a simplistic system model and measured control derivatives, experimental investigations identified a reduction in the adaptive drag penalty up to 20% at off-design conditions.

To investigate the potential for augmented aeroelastic performance and actuation range, a hybrid multiple-smart material morphing concept, the Synergistic Smart Morphing Aileron (SSMA), is introduced. The SSMA leverages the properties of two different smart material actuators to achieve performance exceeding that of the constituent materials. Utilizing the relatively higher work density and phase transformation of Shape-Memory Alloys combined with the larger bandwidth and conformal bending of MFCs, the resultant design is demonstrated

to achieve the desired goals while providing additional control authority at stall and for unsteady conditions through synergistic use of reflex actuation. These advances highlight and motivate new morphing structures for the growing field of UAVs in which adaptation involves advanced compliance tailoring of complex geometry with synergistic actuation of embedded, smart materials.

Chapter 1
Introduction and Literature Review

1.1. Motivation and scope of dissertation

Aircraft are highly complex systems involving competing performance requirements from many disciplines that can vary even within the same flight. Adaptive actuation via shape-changing, i.e. “morphing”, has been investigated since mankind first dreamed of flight to maximize performance under these diverse and changing constraints. The complexity of the field and the need for effective utilization of new materials and technologies have kept the state of the art evolving, now over a century after the first powered flight.

Recently, interest in morphing aircraft has focused on unmanned aerial vehicles (UAVs) or unmanned aerial systems (UASs). By removing the pilot from the aircraft, long-standing constraints (e.g. cockpit, life support, pilot endurance and loss acceptability), are also eliminated from the tightly coupled design process, enabling new capabilities and increased performance. This paradigm shift has resulted in a rapid growth in the number of military UAVs over the past several decades. This growth is not specific to the military alone as demand for commercial UAVs grows. The Federal Aviation Administration (FAA) is currently expecting over 10,000 commercial UAVs in the National Airspace System by 2020 and $94 billion in related spending over the next ten years [1]. As of June 10, 2014, the first commercial UAV was permitted by the FAA to fly over land to survey pipelines [2]. As integration of UAVs enables shared new technology, the breadth of applications and demand on performance will also be expected to grow

Whereas the adaptation of new technologies in manned aircraft has been restricted due to a number of technical and certification requirements, these requirements for unmanned aircraft are much less stringent, largely because they are still being developed in both practice and

principle [3,4]. Exploiting this avenue for accelerated adoption of advanced technologies, smart materials can be implemented and tested for use in adaptive actuation via morphing in UAVs. Acting as transducers by converting energy at the atomistic level, smart materials combine both structure and actuator to enable new configurations. Their effective implementation can potentially reduce mass, size and complexity of integrated actuation systems and structures while still increasing performance. Accordingly, the objective of this dissertation is to explore the advantages of new morphing trailing edge configurations via smart materials for the improved performance of UAVs via adaptive control by identifying and comparing relevant metrics with conventional technology

1.2. Background of morphing

Since the Wright brothers first utilized wing-warping via cables connecting the wing and vertical tail in the Wright Flyer, aircraft have utilized shape deformation to adapt to changes in their surroundings while flying. The ability of birds and other flying animals to modify the shape and size of their wings has inspired a variety of morphing aircraft concepts, seeking to exploit similar gains in aerodynamic efficiency. This increased efficiency then increases the aircraft's effectiveness over a variety of flight conditions.

The desired aerodynamic result is then an aircraft that can undergo a large geometry changes to perform efficiently over a variety of flight conditions, necessitating a structural design that is compliant where necessary for shape-change. Still, the structure of the aircraft must support the aerodynamic loads throughout the morphing process and at all flight conditions, necessitating a stiffer structural design and actuators capable of overcoming the aerodynamic loads. Additionally, the weight of the aircraft negatively impacts its performance, penalizing heavy, complex solutions for the actuators and structure. Thus the coupled design of a morphing concept must consider all of these topics concurrently [5], resulting in many different solutions, varying for different flight regimes [6].

The definition of morphing is still widely open to interpretation. Derived from the Greek word "morphos" meaning "shape", morphing in the context of aircraft has commonly been defined as large shape change or more generally as "efficient multipoint adaptability" [7,8]. The latter definition inherently implies novel mechanisms or materials or a reduction in energy use to differentiate morphing from conventional designs. An even broader definition of "morphing

aircraft" also includes other conventional adaptive mechanisms such as slotted flaps, retractable landing gear, variable pitch propellers, and variable sweep [9]. In the following section, a framework is discussed to contextualize the current study of morphing wings in this otherwise broad field.

1.2.1. Framework for morphing

As the primary lifting surface for the aircraft the wing presents a significant opportunity for incremental gains in aerodynamic efficiency to dramatically improve performance for the entire aircraft. Recent work by De Breuker, has sought to bring the variety of morphing wing concepts under a generalized analysis and design framework [10]. The premise of the framework is that a wing is based upon an extruded airfoil shape. While the framework focuses on the primary lifting surface of the aircraft, the wing, it can be generalized to any airfoil-shaped surface extending into the flow, such as horizontal tail, vertical tail, canards, or even an entire blended wing-body aircraft. Through this framework morphing wings and control surfaces can be split into two categories: global and local morphing by how they alter the basic airfoil unit. Global morphing is defined as changing the overall wing planform configuration by altering sweep, twist or extension, representing rigid body deformations of the airfoil profile without stretching. Local morphing stretches the local airfoil shape by altering the local camber or thickness, including the trailing edge. Both local and global morphing can be used to affect the flow and control the aircraft. This study focuses specifically on local morphing by modifying the trailing edge camber of a representative airfoil.

1.2.2. History of morphing trailing edge wings

The first designs of variable geometry aircraft occurred in the 1930s. In an attempt to improve cruise performance in aircraft by reducing induced drag, global morphing designs such as telescoping or folding wings allowed for changes in aircraft performance to be made before flight. Also during this time, aircraft construction materials transitioned largely from cloth and wood to rigid metal to increase structural stiffness for faster aircraft. Thus, the local morphing concepts pioneered by the Wright brothers were largely eliminated from aircraft as increased flow speeds demanded localized compliance in the form of hinges and pivots that could be blocked by the simplistic actuators of the time. Still, global morphing designs progressed to in-flight adaptation that included sweep, dihedral and folding [11].

The first modern instance of distributed local morphing in modern aircraft was the Mission Adaptive Wing (MAW), developed in the 1980s as a testbed for a multirole F-111 tactical aircraft requiring supersonic cruise speed and high maneuverability [12]. The aircraft attempted to eliminate the discontinuities due to discrete flaps and hinges by creating a smooth upper surface from composite materials that bent due to actuation. Continuous local morphing was achieved with hydraulic actuators that varied leading and trailing edge camber in flight. The leading edge actuation was a single-span surface, but the trailing edge utilized three spanwise-separated panels capable of independent actuation. Additionally, the aircraft could sweep its wings to achieve global morphing for reduced drag at high cruising speeds. Although it used conventional actuators with a relatively limited number of discrete spanwise sections, the concept demonstrated that spanwise variation of local morphing can reduce loading on the wing, improve ride quality, cruise performance and maneuverability [13].

Starting in the early 1990s, the NASA Aircraft Morphing Program attempted to enable "self-adaptive flight" by integrating novel smart technologies including embedded actuation, sensing, and control logic to improve aircraft efficiency [14]. The program covered a very wide scope, attempting to combine multiple disciplines to perform system studies for identifying component technologies with the highest benefit in a real aircraft. One target capability identified by the program was active flow separation control for a 15 percent decrease in high lift system weight [15]. The result was a focus on "smart materials" to address the multidisciplinary aspect of the program and enable program objectives of active aerodynamic and aeroelastic control [8,16]. Section 1.2.4 will further discuss the implementation of smart materials and their applications in morphing aircraft.

In a similar fashion, the DARPA/AFRL/NASA Smart Wing program sought to develop and demonstrate the use of "smart" technologies, including smart materials to improve aerodynamic performance, for a transonic military aircraft. Divided into two phases, operating from 1995 until 2001, the program tested spanwise-varying hinge-less "smart" trailing and leading edges compared to conventional control surfaces for Mach numbers of 0.3 and 0.8, corresponding to a representative take-off and cruise condition [17]. The design focused on local morphing for of the airfoil while leaving the spar box of the aircraft unaffected. The smooth morphing design sought to improve pitching and rolling moment while improving overall

pressure distribution over a range of angles of attack. In Phase 1 of the program, the control surfaces, composed of a flexible honeycomb covered with silicone skin, were driven with smart material actuators, namely shape memory alloys torque tubes, on a 16% scale wing for a representative transonic aircraft. The need for internal positional sensors was noted as only external sensors tracked position. The deformation of the wings under actuation and aerodynamic loads were measured using two methods: first, by tracking reflective disks placed on the surface of the wing with cameras as part as a video model deformation (VMD) analysis, and second by projection Moirè interferometry (PMI) using an infrared laser. The interformetery produced higher positional resolution analysis, but with less displacement accuracy. The results noted low actuation bandwidth of the shape memory alloys and recommended a potential hybrid design to reach rate actuation requirements.

In Phase 2 of the Smart Wing program, the design application was refined as a highly swept-wing UAV, shown in Figure 1.1 to enable a larger scale model (30%) to be tested that allowed for thicker wings to better fit an actuation system [18]. The SMA torque tubes in the trailing edge were replaced with 10 spanwise segments of eccentuators driven by ultrasonic motors, an example of which shown in Figure 1.2. . The new actuation systems improved tip deflection rates to greater than 75 degrees per second with maximum actuation of +/- 20 degrees [19]. Linear voltage differential transformers provided positional feedback for closed-loop control of the trailing edge deflections. The PMI and VMD tracking systems from Phase 1 were also used to track wing deflections.

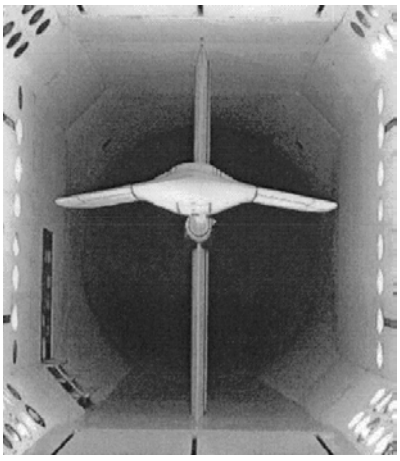

Figure 1.1 Phase 2 Smart Wing Test Article [19]

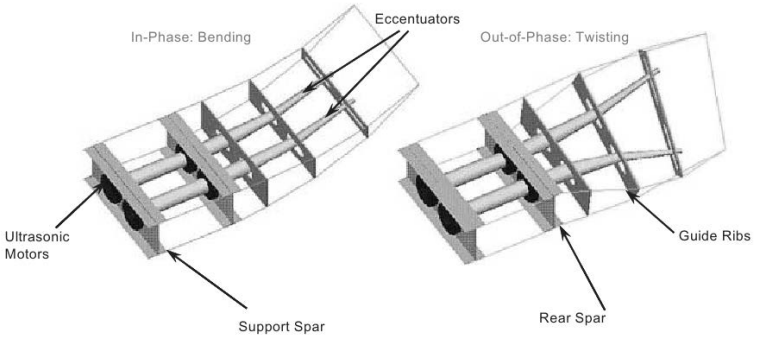

Figure 1.2 Eccentuator actuation diagram [17]

Several spanwise variations of the trailing edge actuators were investigated to determine the effect on pitch and roll control of the aircraft including combinations of uniform actuation, linear, and sinusoidal spanwise variation for roll control, shown in Figure 1.3. The cosine-like "bathtub" configuration was investigated as a possible low-observability control configuration. Both the linear and bathtub variations of configurations were found to exhibit sufficient roll control of the vehicle at the representative take-off and cruise conditions. The revised smart wing showed an improvement of approximately 17% in roll control [17]. It was reported that the other shapes achieved similar results with respect to pitching moment. The concept showed that distributed control surface actuation could offer additional control fidelity for maneuver and cruise. Additional research utilizing aeroelastic effects on wing flexibility was recommended to realize the full potential of the eccentuator controls surfaces [20].

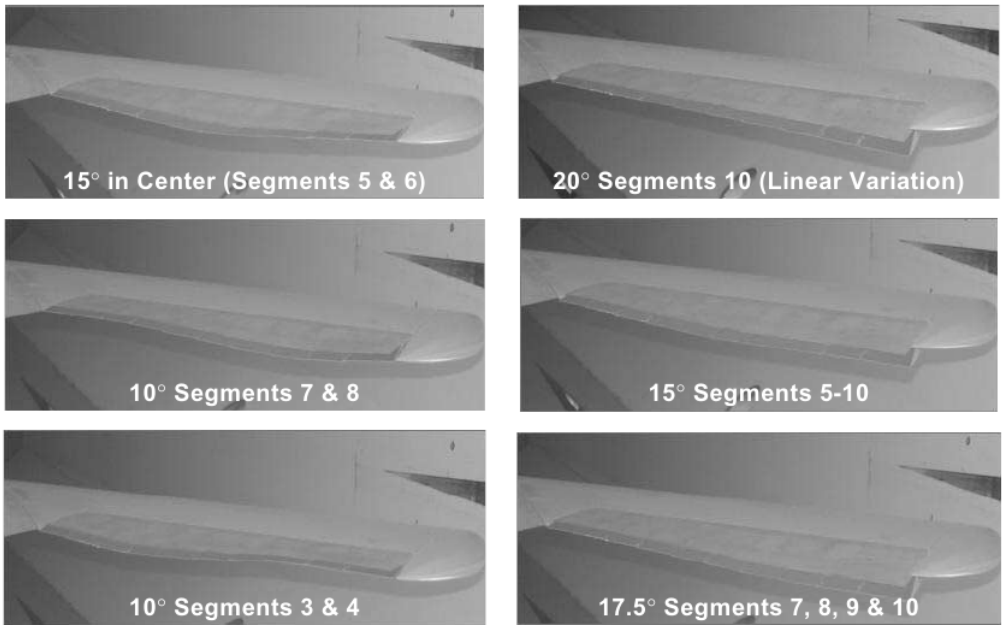

Figure 1.3 Representative actuations
from Phase 2 Smart Wing [17]

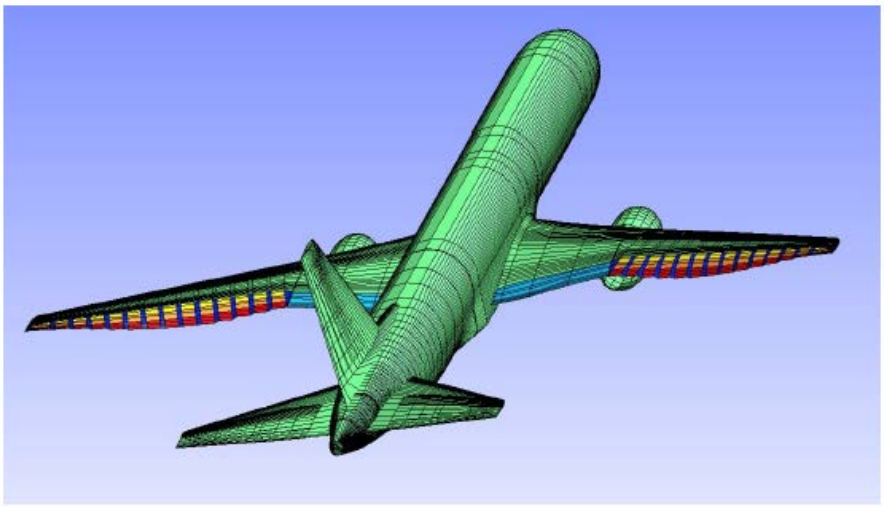

Figure 1.4 Modelled Variable Camber Continuous Trailing Edge Flap system on a generic transport aircraft [21]

The DARPA Morphing Adaptive Structures Program followed as a more general program to investigate enabling technologies for morphing wings in military applications from 2002 to 2007 [7]. Specifically, the program sought to enable a multi-role aircraft that could provide persistent reconnaissance followed by a rapid attack and maneuverability segment. For this mission, the program identified objectives that morphing wings should provide including: the ability to persist for long periods of time, an ability to change roles on demand and a time-critical ability to respond quickly. The program funded several proof-of-concept aircraft including: the Z-wing morphing UAV from Lockheed Martin that globally morphed by folding its wings in flight, the Raytheon Missile Systems adaptive missile, and the Next Gen Batwing with variable sweep and stretchable skin [22,23].

Beginning in 2012, Boeing and NASA began jointly conducting a study of a Variable Camber Continuous Trailing Edge Flap (VCCTEF) system, shown in Figure 1.4 [24]. This project has sought to produce a mission-adaptive lift and drag performance for a generic transport-class aircraft. The trailing edge of the wing was segmented into twelve spanwise and three chordwise segments for distributed local morphing [25]. To achieve the necessary power, rate and load actuation requirements, the design planned to use a combination of shape memory alloys, and electromechanical actuators, as depicted in Figure 1.5. Initially simulations with a vortex lattice aerodynamics code computed that the VCCTEF concept could result potential

reduction of 2.6% in drag during cruise during 80% fuel load, and up to 9.8% for a lightly loaded aircraft [26].

Further analysis of the design, including aeroelastic flutter analysis, flight dynamic stability analysis, control system design, and aeroelastic wing shaping subject to actuation constraints have been modeled for reduced-stiffness version of a Boeing 757 wing [21,27–29]. It was shown that the trailing edge could be effective under small deflections at suppressing vibrations in the wing, but was also subject to a reduced flutter speed due to the reduced wing stiffness. It was also proposed to bridge the gaps between the segments of the trailing edge flaps with an elastomeric material using a continuous mold-line link (CML) technology [30]. Previously, CML technology has been focused on noise reduction for high-lift hinged flaps [31]. From the variable camber continuous trailing edge studies, the proposed actuation configuration for cruise, shown in Figure 1.6, closely resembles that of the “bathtub” configuration previously investigated for roll maneuver in the Smart Wing program.

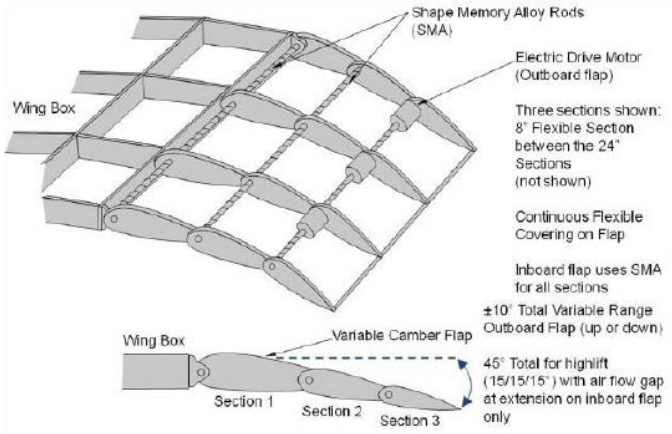

Figure 1.5 VCCTEF Actuator Layout [27]

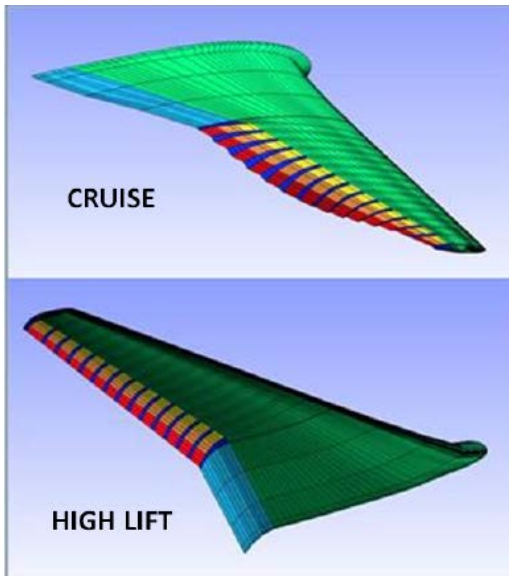

Figure 1.6 VCCTEF Proposed Configurations [21]

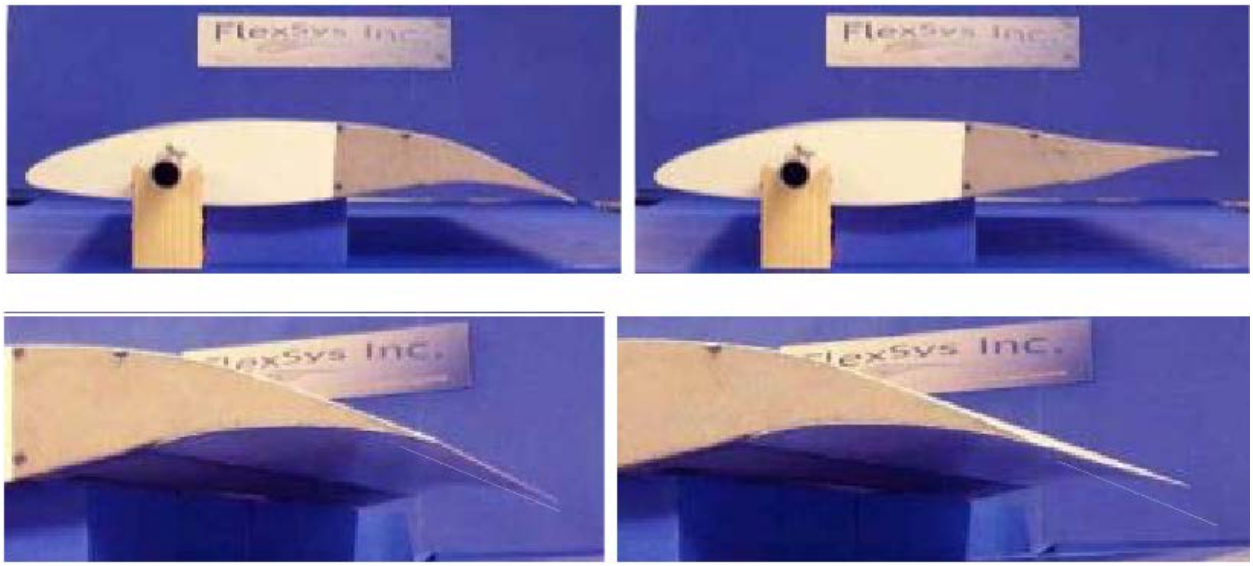

Figure 1.7 Mission Adaptive Compliant Wing Concept [32]

Another approach to trailing edge morphing has also been developed by FlexSys Inc. of Ann Arbor, Michigan as the Mission Adaptive Compliant Wing (MACW) concept [32]. The MACW utilized internal compliant mechanisms, designed to optimize the shape under actuation of an adaptive morphing trailing edge while meeting stress, stability, dynamic behavior and stiffness constraints. Concluding that smart materials suffer from inadequate displacement, insufficient bandwidth, excessive power consumption, and excessive complexity and/or weight the morphing airfoil utilized conventional electromechanical actuators. An early version of the concept with representative actuations was shown in Figure 1.7.

Working in collaboration with the Air Force Research Laboratory, the design was originally implemented into a natural laminar flow airfoil consistent with a “SensorCraft” application [33]. Focusing specifically on trans-sonic cruise, the adaptive trailing edge was predicted to provide a 40% increase in control authority per degree deflection and up to 25% lower drag. The concept was implemented in a representative section with a 50 inch span and 30 inch chord with elliptical endplates and flight tested at full-scale dynamic pressure, Mach 0.4 to 0.55 at 40k feet, on the Scaled Composites White Knight aircraft, shown in Figure 1.8 [34]. It was reported that for a max-G pull-up maneuver that the MACW required 33% less actuation force and 17% lower peak power than a conventional flap while still actuating up to 30 degrees per second. The compliant flap’s cruise lift to drag ratio was improved by 3.3% over a

conventional airfoil. Examining aerodynamic improvements alone, it was expected that the MACW technology could increase the endurance of a SensorCraft by 15%.

The aerodynamic benefits of the FlexSys adaptive morphing trailing edge concept for a transonic twin-aisle passenger aircraft have also been investigated [35]. Using high fidelity three-dimensional Reynolds-Averaged Navier-Stokes simulations, morphing configurations for the NASA Common Research Model wing were optimized with a nonlinear gradient based solver to minimize overall drag. It was found that by simulating both a fully-morphing wing and a morphing trailing edge that it was sufficient to only morph the trailing edge shape for drag reduction at on-design conditions. All trailing edge deflections were found to be within 2 degrees, corresponding to the relatively small changes in actuation required for cruise. A 1% overall drag reduction at on-design conditions and 5% drag reduction at off-design conditions was predicted by the multi-point optimization. Focusing solely on cruise rather than climb and descent, the morphing wing saw only a 1% cruise fuel burn reduction. Considerations for future work noted that a multidisciplinary study including aerodynamics, structures and controls is needed to thoroughly realize the benefit of the concept. Indeed, when analyzing the gust-response (an off-design condition) of optimized configurations, it was found that the optimized morphing configurations would not satisfy failure criteria for spar buckling, skin stress, or skin buckling [36,37].

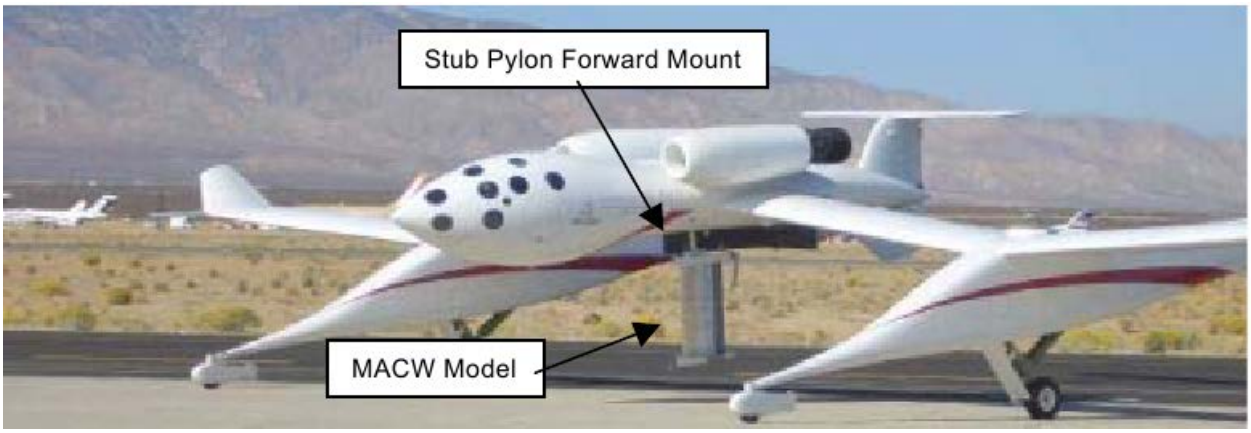

Figure 1.8 Flight Testing of Mission Adaptive Compliant Wing [32]

1.2.3. Morphing trailing edges in wind turbines

Seeking similar gains in efficiency as morphing aircraft, morphing surfaces have also been developed for rotating blade systems such as wind turbines to tailor both steady and unsteady aerodynamic forces. Wind turbine blades require high aerodynamic efficiency while taking into account factors such as gust alleviation and stall. The rotational velocities for the tip of the blades can reach aerodynamic speeds comparable to that of aircraft. Additionally, the scale of their design often requires simplistic construction and basic weight considerations. Due to the similarities between the applications, several wind turbine morphing concepts have resulted in simulations and experiments that also provided insight for morphing aircraft applications. The following section highlights selected pertinent examples. For a detailed overview of both global and local morphing in wind turbine applications, existing review papers are available [38,39].

The “smart” wind turbine rotor blade concept utilized multiple control surfaces to alleviate aerodynamic loads on a wind turbine blade [40]. Implemented into a scaled non-rotating rotor blade, two trailing edge flaps were utilized to minimize the root bending moment. Utilizing piezoelectric Thunder TH6-R actuators to bend a foam trailing edge, the flaps were effectively used with closed-loop control to reduce periodic and turbulence based disturbances by 90% and 55%, respectively.

Morphing trailing edge geometries for implementation in blade-like applications have also been developed with conventional electromechanical motors. Daynes also used a flexible honeycomb core covered with silicone skin to create an adaptive trailing edge flap, shown in Figure 1.10, for a representative section of a 90 meter diameter wind turbine [41]. Four flap segments of 250 mm span were implemented into a representative 1 meter span blade with a 1.3 meter chord. The four flap segments were able to actuate up to 10 degrees in either direction at up to 9 degrees per second. For experimental testing end plates were placed on the representative section to approximate two dimensional conditions, seen in Figure 1.11.

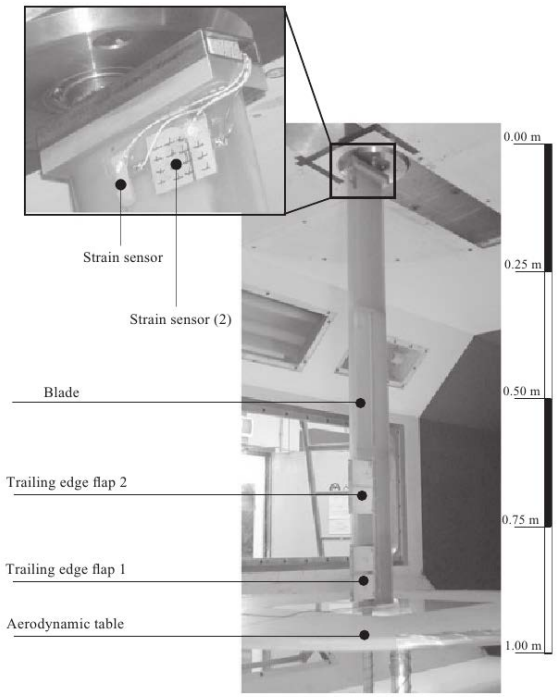

Figure 1.9 Smart Blade Trailing Edge Flaps being use for root load alleviation [40]

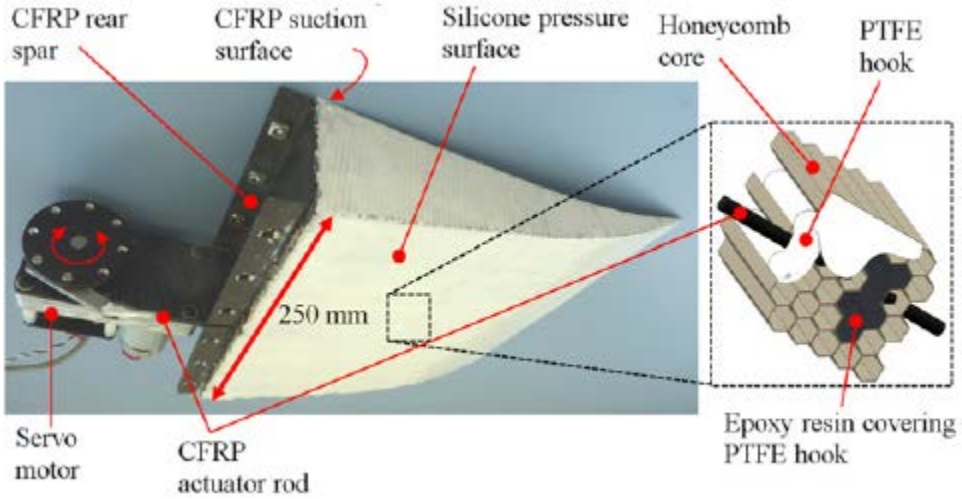

Figure 1.10 Adaptive Trailing Edge driven by servo motor [41]

Effect of uniform flap actuation flap at 40 m/s on lift drag, and pitching moment coefficients were evaluated in a wind tunnel. Chordwise pressure taps were also used to record the morphed airfoil pressure profile. Non-uniform segmented actuation configurations were

identified including a “twist” and “braking” mode. The braking mode was experimentally shown to produce very little pitching moment or lift but to add significantly to drag, potentially a useful configuration for controlling a wind turbine’s rotational speed.

The two-dimensional aeroelastic performance was also modelled utilizing a fluid structure interaction simulation coupling a nonlinear finite element analysis ABAQUS and a panel code, XFOIL. The fluid structure interaction simulations matched very well with the experimental results and allowed for extrapolation of force and strain requirements up to 70 m/s. The simulation also allowed for design investigations on the effect of varying stiffness of the adaptive trailing edge’s core and the bending stiffness of the skin. It was noted that effective loads on the actuator decreased as the core stiffness and skin stiffness decreased. However, the location of minimal actuator force and variability in lift coefficient occurred when bending stiffness of the skin was increased, but the effective modulus of the core was at a minimum. Thus new adaptive trailing edge design was theorized where the skin was stiff to out-of plane loading but the core of the morphing concept was empty.

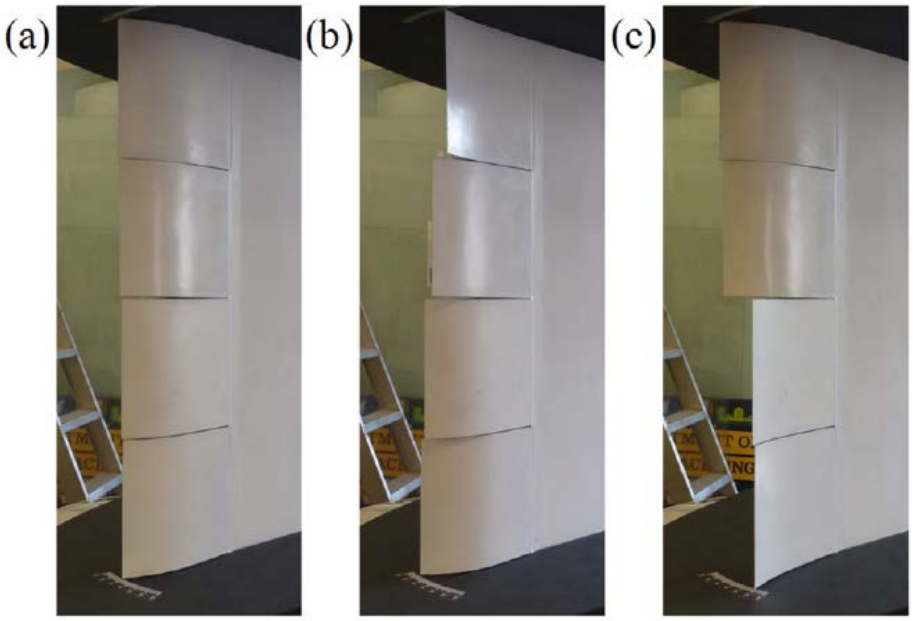

Figure 1.11 Adaptive trailing edge with 3 geometries (left to right) uniform, twist and braking [41]

1.2.4. Smart materials for morphing

As mentioned in Section 1.2.2, the use of smart materials in morphing came naturally from the development of enabling technologies to improve aircraft efficiency. Smart materials, which act as transducers, combine both the structure and actuator into a single element as an adaptive structure. Intuitively, this has led to their implementation in morphing aircraft in an effort to reduce the mechanical complexity of morphing concepts and potentially weight. Smart materials can also form solid state actuators, which have no discrete moving parts, increasing the overall system reliability by reducing the amount of components subjected to failure. The enabling materials identified by the NASA Aircraft Morphing program for potential use in adaptive structures included shape memory alloys, piezoelectric fiber composites, and magnetostrictive materials [15]. In addition, shape memory polymers have also been implemented as skin in morphing wings [42].

Since the completion of the NASA Aircraft Morphing program, UAVs have taken a much larger role in the exploration of morphing technologies resulting in many smart actuation concepts. Although very few of these concepts have been tested in a wind tunnel much less flown on aircraft, they capture radical ideas for morphing often utilizing smart materials in ways that would have been difficult to implement in a manned aircraft. Reviews of the many recent morphing ideas for UAVs already exist in literature [6],[43]. Focusing on local morphing, i.e. changing the airfoil profile, the following section will provide a brief overview of the role these smart materials play in UAV morphing applications.

Shape memory alloys (SMAs) are thermally driven, producing strains up to approximately 8% with relatively high blocking stresses [44]. SMAs, for example, the common nickel-titanium alloy (NITINOL), undergo actuation by a solid-state phase change between a high-strain, low-temperature phase (martensite) and a low-strain, high-temperature phase (austenite) [45]. They exhibit high specific work, i.e. are relatively light for the amount of work they can produce, but are relatively limited in bandwidth by their heat diffusion when used as bulk materials. Additionally, they must be strained from an initial shape to a deformed shape which they can later recover upon actuation. Thin SMA materials are often used for their high surface area to volume ratio, which reduces the time required for heat diffusion throughout the material, especially in the cooling process. Additionally, thin structures allow for Joule heating

via electrical currents while reducing implementation complexity. Several representative actuation concepts utilizing thin SMA materials include: an elastic substrate embedded with SMA wires [46], SMA ribbons, SMA thin films [47], elastic structures with a single SMA wire [48], elastic hinges driven by a pair of SMA wires[49], and hinges rotated by a pair of antagonistically-actuated SMA wires [50,51].

Shape memory polymers (SMPs) are also thermally driven, producing very large strains, up to 1100% [52]. Compared to shape memory alloys, their blocking stresses are several orders of magnitude lower and they are often cheap, light and easy to process [53]. Due to their high stroke and low blocking stress, SMPs have largely seen interest in morphing in use as an adaptive skin for a morphing wing, but their use as actuators has been limited by their relatively low stiffness [54].

Magnetostrictive materials exhibit strain with applied magnetic field. Advantageously, the actuation exhibits very little hysteresis, although the effect can be highly nonlinear. Because the effect is driven by magnetic fields, the actuators can reach high frequencies (kHz) at limited stroke, approximately 0.2%. They are often seen as a replacement to traditional electromechanical motors. Although the use of magnetostrictive materials is somewhat limited in morphing applications, TERFENOL-D, a proprietary alloy, is the most commonly implemented material. Implemented in concept called a “Linear-Wave Motor”, these materials have successfully morphed trusses in the wing box of an adaptive-wing concept actuated an adaptive trailing edge on a track for a Gulfstream sized aircraft [55]. Additionally, magnetostrictive pumps have been proposed to drive geometry changes within a wing, including but not limited to global changes such as a telescoping spar in a UAV [56].

Piezoelectric ceramics are driven by electric fields, and have a very high bandwidth and actuation force comparatively improving their performance. The permanent dipoles within piezoelectric materials at the crystal or molecular scale can be slightly expanded or contracted by applying an electric field. However, the monolithic piezoceramics such as Lead Zirconate Titanate (PZT) are brittle and have limited maximum actuation strains, about 0.2%. To facilitate the implementation of piezoelectric materials in flexible applications the Active-Fiber Composites (AFC) and then the Macro-Fiber Composites (MFC), shown in Figure 1.12, were developed [57,58]. These composites use high voltages applied across interdigitated electrodes to

create strong electric fields to actuate long, thin piezoceramic fibers, which are embedded in an epoxy matrix, creating a flexible piezoelectric actuator with relatively high strains. Among other applications, MFCs can be used to induce bending when bonded to a thin substrate, which has seen recent use in wing warping for Micro Air Vehicles [59,60]. Still, challenges remain in compensating for hysteresis and creep in actuator design, which can be either approximately addressed through inverse hysteresis models or precisely addressed via closed loop control with an added sensor [61,62].

Leveraging experience with MFCs, Bilgen created an all-morphing control surface aircraft, shown in Figure 1.13 [63]. The trailing edge control surfaces of the aircraft were constructed using flat MFC bimorphs with steel substrate, actuating in bending. The sharp, flat nature of the trailing edge was the result of balancing the need for a compliant airfoil that can maximize actuation with the need to sustain the aerodynamic loads. Through aerodynamic simulations, it was determined that despite small tip deflections the airfoils would perform comparably to conventional profiles with a discrete trailing edge. Wind tunnel tests were performed on the final aircraft, showing good performance when morphing all control surfaces uniformly. During flight tests, the aircraft seemed sluggish rather than aerobatic, and was prone to overcompensation, most likely due neglecting hysteresis and control lag in the controller design. It is this design and these issues that motivate several of the concepts detailed in this dissertation.

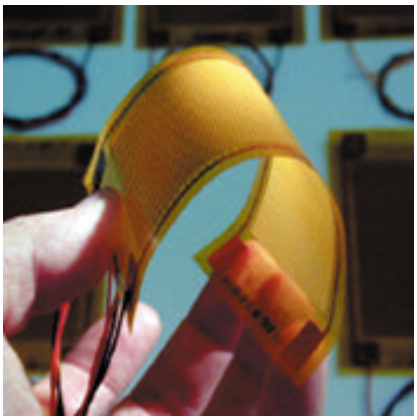

Figure 1.12 Macro-Fiber Composite [64]

Figure 1.13 Virginia Tech All-Morphing Demonstrator [63]

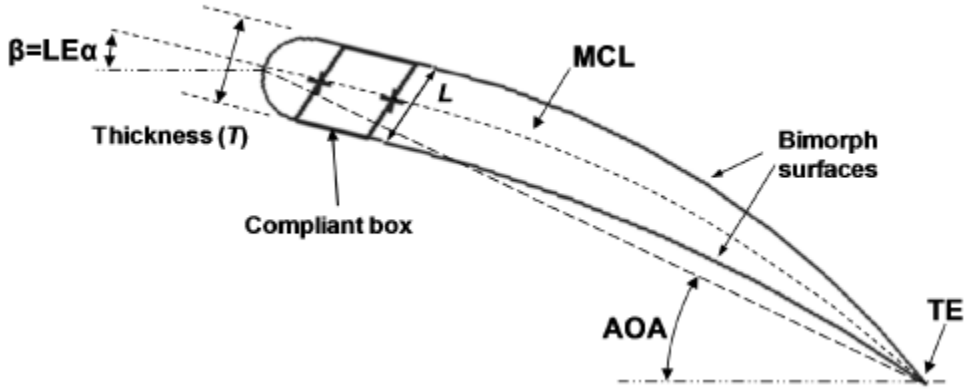

Figure 1.14 MFC – Actuated Morphing Trailing Edge with Compliant Box [65]

Another morphing airfoil device developed by Bilgen, utilized an internal compliant mechanism, namely a compliant box, to alter the effective root boundary condition of the morphing trailing edge control surface [65]. By increasing chordwise compliance, the novel design, shown in Figure 1.14, improved the maximum range of trailing edge actuation. This novel "cascading bimorph" concept was tested as an alternative flow control method as compared to a change in rigid angle of attack at 15 m/s for a rounded leading edge [66]. The actuation results showed a 72% higher lift curve slope of the variable-camber morphing wing when compared to the rigid rotation of a symmetric NACA 0009 airfoil. The increased thickness of this morphing trailing edge as compared to the simple bimorph trailing edge motivates the current interest for refinement and implementation of the design into more conventional airfoils and complex aeroelastic manipulation.

1.2.5. Multiple smart materials for morphing

As detailed in the Section 1.2.4 many different applications have been developed that use a single smart material to replace the role of a conventional actuator for local morphing. By focusing on the implementation of a single smart material, the design complexity is reduced; however, the actuation limitations of the design are governed largely by the limitations of the specific smart material. For example, as seen in Figure 1.15, neither SMA nor PZT exhibits comparatively superior actuation stress, actuation strain, frequency response and specific work. Piezoelectric materials exhibit a larger actuation bandwidth (up to 750 kHz depending on electric field strength and dynamic effects), but shape memory alloys exhibit larger blocking stress and actuation strains. Consequently, actuation designs using piezoelectric materials typically show

small displacements but quick response and conversely, designs using shape memory materials show larger displacements or forces but a slower response.

With this knowledge, ideally, a design would combine these smart materials in a complementary or “synergistic” manner to create a hybrid actuation design that could realize performance beyond that of the individual materials. The added complexity of designing a structure with multiple smart actuators has limited the number of multi-material designs in literature much less local morphing of an airfoil. Still, the combined advantage of using multiple actuators has motivated designs that successfully utilize the mismatch in smart material properties to their advantage. For example, shape memory materials can be used as both fiber and matrix in a material, so that all elements of the composite can actuate to a greater extent on the same timescale [67]. Alternatively, a piezoelectric matrix was used to induce stress transformations within shape memory alloy inclusions in a piezo-SMA composite, increasing the “actuation” speed of the slower SMA [68]. A flapping wing robot used shape memory polymers to tune the stiffness of a flexure hinge for positioning a flapping wing actuated by a piezoelectric bimorph [69]. The shape memory polymer was treated as a static method of tunable stiffness rather than as another dynamic actuator and focused on flapping flight. Examining only morphing airfoil concepts, Chinaud used piezostacks combined with SMA wires to actuate rigid flaps with small deflections in order to control vortices with frequencies from 1 Hz to 1 kHz over a plate [70].

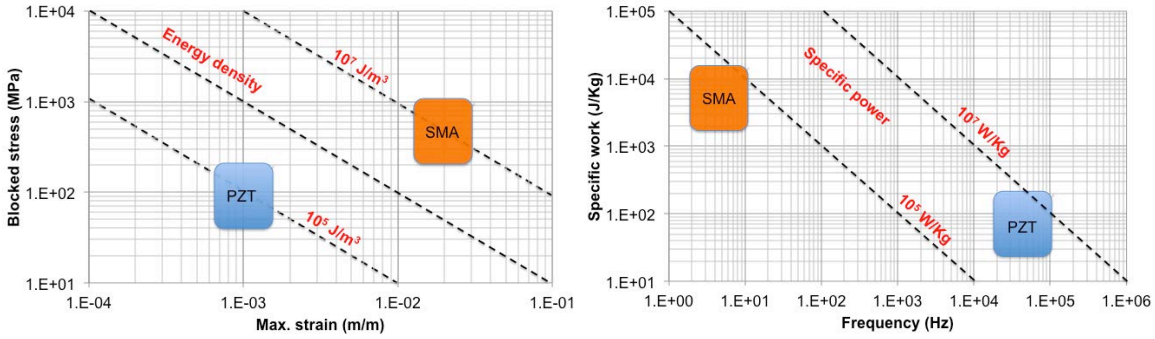

Figure 1.15 Smart Material Actuator Comparison (Adapted from- NASA/JPL/EAP website) [71]

To achieve a reduction in implementation complexity, a hybrid morphing mechanism can also be realized by combining smart materials and conventional actuation concepts. The previously-described Smart Wing concept utilized an SMA actuated leading edge to adapt to high lift flight conditions over long timescales while the eccentuators of the trailing edge attempted to affect aerodynamic loads over a shorter timescale for maneuvering [17]. Similarly, the Variable Camber Continuous Trailing Edge Flap also utilizes a combination of conventional electromechanical motors and Shape Memory alloys to affect aerodynamic loads over a maneuvering timescale while realizing the weight and power benefits of the SMAs torque tubes [29].

1.2.6. Bio-inspiration for morphing

As detailed in the prior sections on the history of morphing trailing edge designs, a significant effort of recent research on morphing wings has focused on improving cruise performance for transonic aircraft. At these speeds, very small reductions in drag at cruise can result in large monetary savings in fuel, such as saving 64,000 gallons a year per aircraft for a 3.3% improvement in the lift to drag ratio [34]. As mentioned, recent studies have shown relatively little impact on performance of morphing on at the on-design condition, i.e. cruise, compared to conventional actuators [35]. This is largely because conventional wing are generally optimized before construction for high efficiency at cruise conditions. Rather than designing performance around a single flight condition, morphing aircraft should adapt to changing flight conditions and mission requirements. An ideal mission for the application of morphing would involve sudden requirement changes. Even for large passenger transport aircraft, morphing could be highly advantageous and relevant to aircraft operating near load limit constraints for common events such as wind gusts [37].

These adaptations become even more relevant for smaller aircraft flying at slower speeds where variations in local flight conditions can influence performance to a greater degree. Examining gliding and soaring animals in nature, the flight regimes most related to fixed-wing UAVs, both global and local morphing mechanisms are utilized and are highly significant in adapting to changing flight conditions. In fact, current knowledge about how birds and bats locally morph their wings during flight and the purpose behind these deviations is incredibly limited, even more so than in insects with flapping flight [72]. It has been observed that while

gliding, birds utilize relatively small movements of their feathers and exhibit variable spanwise camber. Under positive loading conditions, the thin trailing edge of the wing gives rise to reflex for unknown reasons. Quantitative analysis of the effects of these changes is especially difficult to obtain as the complete system of the wing is only active in live specimens during flight. The current study seeks to improve knowledge about the possible aerodynamic and aeroelastic advantages of these variations as applied to low-speed UAVs.

1.3. Technical approach and impact

This dissertation demonstrates that both variable spanwise camber and chordwise reflex camber are highly useful for unmanned aerial vehicle control through means of smart material actuation concepts. By successfully leveraging new production technology for the precise location of compliant mechanisms via multi-material additive manufacturing, a modular compliant trailing edge actuated by MFCs is developed and produced. Similarly, an additively-manufactured elastomeric honeycomb skin is designed to precisely tailor aerodynamic loads while still allowing for large-geometry deformation from active components.

This modular trailing edge is implemented in a two-dimensional demonstrator to perform a design study on how the number of MFC actuators affects aerodynamic control forces. The results show that for the evaluated configurations, adding more smart material actuators does not necessarily improve the actuation range when the actuators have asymmetric constraints. Scaling the span of the demonstrator reveals a novel scaling methodology for reduced-span aeroelastic testing.

The representative modular section is then repeated and implemented into a finite wing for variable spanwise actuation of trailing edge camber. The results show that spanwise variation of a smooth morphing trailing edge exhibits superior control derivative performance as compared to conventional control surfaces. A novel characterization methodology informed by a simplistic system model is used to leverage the improved control derivatives to measure a reduction in adaptation drag at off-design conditions.

To further augment the range and capabilities of the morphing concept, a hybrid multiple smart material morphing trailing edge concept is developed and characterized. This concept, consisting of SMAs and MFCs, has the ability to approximate an actuator that has both larger tip

displacement and aeroelastic authority, but actuates over the timescale of the faster concept. The complexity of characterizing the potential benefits of this concept is identified without a control system both with and without aerodynamic loads, identifying expected bandwidth for improvement of the combined concept over its constitutive materials. A high fidelity fluid-structure interaction simulation is developed and showed that in addition to increasing aerodynamic control authority within the linear flight regime, reflex actuation can augment flow control under high loading conditions near stall, compensating for the more compliant actuator. Prescribed-motion simulations also show unsteady aerodynamic advantage to actuating through reflex camber. Realistic sensors and simplistic controllers are developed to allow for closed-loop position control of the combined system. The projected advantages of reflex actuation through this hybrid concept are modeled via uncoupled simulations and implemented for a demonstrator, free of aerodynamic loading.

These results have far-reaching applications for the design of control surfaces of UAVs that continue to seek improved performance under changing flight conditions. Adoption of these smart material technologies could improve performance for light actuators near stall or in off design conditions such as payload delivery or gust conditions. In addition, the methods for analysis and effects noted for these artificial actuators could be used to gain better insight for local morphing flight mechanisms used in gliding birds in nature.

1.4. Dissertation outline

This chapter has defined the scope for the dissertation, morphing trailing edges of wing-like surfaces using smart materials to improve the control performance of UAVs and introduced the background literature.

Chapter 2 introduces the three-dimensional Smooth Morphing Trailing Edge (SMTE) concept to investigate the potential advantages for bio-mimetic smooth “feathering” of the trailing edge camber of a wing. The development of the characteristic section is described, detailing the manufacturing process of both the active and inactive sections. An elastomeric honeycomb constructed through additive manufacturing is developed to create anisotropy necessary for compliant morphing skin. A simple characterization method and relevant metrics for the effect of the inactive elastomeric skin on multiple actuators are developed and discussed.

Chapter 3 describes a design study on the number of MFC patches in the flexure box. Their impact on mass, power, and aerodynamic control is also investigated. During this investigation an embedded sensor and closed-loop control of the smart material trailing edge is demonstrated. The sensor and controller are utilized in a low aspect ratio wind tunnel tests to evaluate the capabilities of the actuators. Increasing the span of the test article for a rigid airfoil allow for extrapolation of uniform actuation to a theoretically infinite wing. These results are then confirmed by a single test with several modular sections actuating uniformly.

Chapter 4 describes the experimental testing of the SMTE concept on a finite wing. Performance of a morphing wing utilizing feathering is compared to a conventional wing is compared through of mass and resultant control derivatives.

Chapter 5 further explores the capabilities of the SMTE concept by utilizing a refined measurement of the control derivatives in a simplistic system model to predict the optimal configurations for achieving a design lift distribution from an off-design flight condition. The resultant drag penalty, defined as the "adaptive drag" penalty, is used to show the drag improvement of the SMTE in adapting to off-design conditions.

Chapter 6 details the design and development of the hybrid multiple-material morphing aileron concept, otherwise known as the Synergistic Smart Morphing Aileron (SSMA). A spectral characterization method is described that allows for identification of bandwidth where actuation of a fast, large displacement actuation is possible. Theoretical aerodynamic simulations of the SSMA are performed to identify performance capabilities and provide extrapolation beyond that of the experimental results. Coupling a Navier-Stokes simulation with a corotational beam finite element simulation, a high-fidelity two dimensional aeroelastic analysis of a flexible airfoil is achieved. First, purely aerodynamic simulations on a rigid structure are performed to identify the effects of both actuators from the Synergistic Smart Morphing Aileron. Then, aeroelastic simulations of both actuators are performed, identifying actuation constraints. Finally, prescribed-motion dynamic simulations are performed confirming dynamic actuation benefits.

Chapter 7 provides a summary of the work, conclusions and contributions of the current work.

Chapter 2

Spanwise Morphing Trailing Edge Concept

As mentioned in the introduction, very little literature exists about the effective losses incurred by smooth variation of camber along the trailing edge of a wing, specifically for the UAVs in a transitional flow environment. The discrete nature of flaps or ailerons on a wing cause drag-inducing vortices in the aileron gaps and contribute to the drag of the aircraft limiting the performance and range [34,73]. A schematic of losses typical for a finite wing with an aileron is shown in in Figure 2.1. Just as the tip vortex is formed from air flowing from higher to lower pressure, the same effect happens at gaps between the flap and the wing, causing additional "spanwise" losses in lift. The sharp discontinuity in chordwise camber can also spoil the flow causing large amounts of separation and drag. These chordwise and spanwise losses due to flap use are undesirable, but several limitations hinder the analysis and adaptation of smooth trailing edge designs.

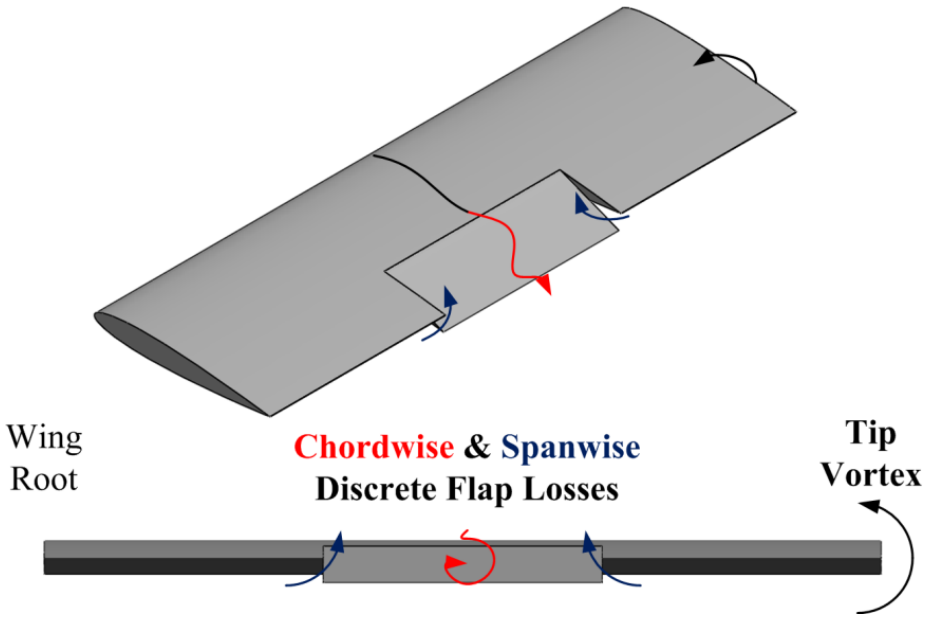

Figure 2.1 Illustration of chordwise and spanwise losses due to discrete flap actuation

These limitations or constraints for a morphing concept can be summarized by the basic challenge of achieving the aerodynamically desirable shapes without significantly increasing complexity and thus mass of the morphing concept. To achieve this objective, the stiffness of the structure and the strength of any actuation mechanism must be well-matched to the expected aerodynamic loads and actuation authority. Subsequently, the structural solution to morphing at different magnitudes of loading will utilize different materials and actuation concepts to maximize design efficiency. The optimal solution and fidelity of the disciplines investigated is highly dependent upon the expected role of the aircraft, and can result in various solutions for differing aircraft roles requiring differing mixtures of flight conditions (flow speed, angle of attack, etc.). The robustness of the required analysis to cover the multitude of possibilities often prohibits a detailed analysis. Thus, for an assessment of a morphing design, a low-fidelity analysis is typically developed which can lead to significant overstatement of a morphing by improperly addressing even a single constraint, such as the effect of viscous aerodynamic forces generated by a shape. Even when appropriately modelling all necessary disciplines, the method, *e.g.* sequential vs. concurrent, of simultaneously optimizing the individual disciplines can arrive at different results [5].

Hence, this work takes a largely experimental approach towards researching the necessary structures and identifying the relevant constraints associated with a morphing trailing edge concept that eliminates the losses due to discrete flaps, improving aerodynamic performance. The goal is not to supplant multi-disciplinary optimization, but rather to create a design that can realize these potential aerodynamic improvements while also identifying relevant constraints with realistic structures and materials for this complex, multi-disciplinary problem.

Accordingly, this chapter will detail the motivation, initial design and testing of the Spanwise Morphing Trailing Edge (SMTE) concept, a smooth, spanwise-varying, camber-morphing trailing edge for the wing of a small UAV. During the research and early testing of the morphing concept, appropriate aerodynamic and structural constraints are identified with simplistic tests for a representative section.

This chapter specifically contributes to morphing research in the following ways. It extends previous two-dimensional simulations and experiments by Bilgen *et al.* and Sanders *et al.* to a three-dimensional concept that preserves the smooth morphing surface in the spanwise as

well as the chordwise directions. Novel actuation mechanisms utilizing smart materials and novel passive sections utilizing 3D-printed elastomeric honeycombs are developed to meet the requirements of such an application. Higher fidelity simulations are used to predict the expected improvement of the adapted actuation mechanism with increased accuracy as compared to the results from Sanders. Finally, new techniques for characterizing the impact of actuation skin and aerodynamic loads on these unique smart material active sections are developed. This chapter also represents the first effort to eliminate the aerodynamic losses from Figure 2.1 by creating a smooth, continuous skin for a UAV, which results in a design for a test bed concept and the experimental testing of a representative section. The results from this chapter then motivate the studies of the following chapters.

2.1. Motivation for conformal morphing for UAVs

Eliminating the gaps between the flap and the wing could be simply addressed by forming a transitional spanning section with a technology similar to the continuous mold-line link, but for a smaller-scale aircraft [31]. Yet, this technology alone would not address the chordwise losses associated with a discrete flap. The following section introduces the concept of "conformal morphing" which represents a second aspect of the proposed morphing concept.

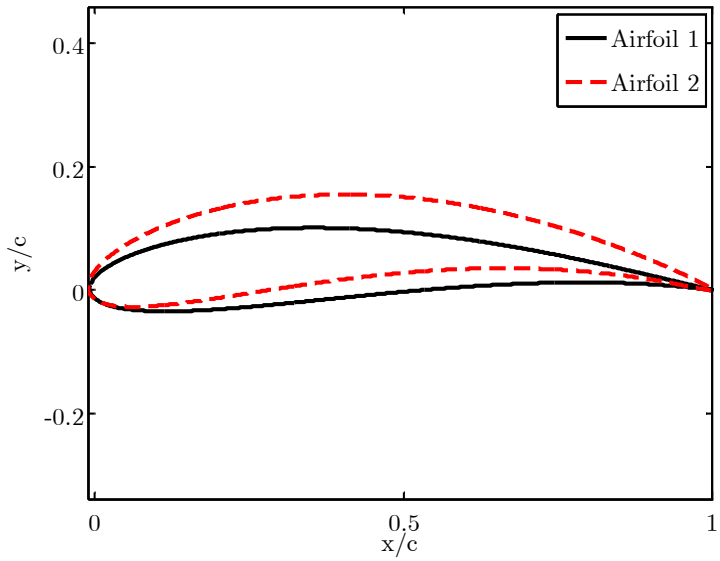

Figure 2.2. Examples of airfoils produced from disks by Joukowski's conformal mapping

The word “conformal” is derived from Latin *conformālis* meaning “form together”[74]. The term was originally used with respect to projections in the late 1700s as “conformal mapping” to describe the process in cartography of projecting the Earth, a sphere, onto a map, a plane. The term therefore came to refer to the transformation of a shape by which the local angles of the original shape are preserved during this deformation. The field of conformal mapping expanded beyond cartography with the help of many famous researchers such as D’Alembert, Jacobi, Euler, Lagrange, Cauchy, Riemann, and Hilbert to the field of complex analysis. Conformal mapping was first used in aerodynamic analysis by Zhukovskii (also Joukowski) to map circular cylinders in the complex plane into airfoil-shaped objects in the real plane, allowing for closed-form solutions of the potential flow fields around airfoils [75]. The airfoil shapes achieved by this mapping technique are smooth, i.e. continuously differentiable, except for a sharp trailing edge, as seen in Figure 1.1 [76]. It is this conformal mapping technique that allowed for the earliest aerodynamic simulations of pressure distributions and resultant aerodynamic forces for airfoils.

This terminology was first used by Sanders *et al.* 2003 to describe smooth control surface variations as “conformal”, specifically contrasting smoothly varying control surfaces to conventional articulated designs [77]. Additionally, these control surfaces were intended for implementation in an aircraft as part of morphing design [20]. Derived from this work, shape-changing , i.e. “morphing”, with smooth , i.e. “conformal”, control surfaces has been abbreviated as “conformal morphing” to describe smoothly varying airfoil geometry from one shape to another.

Intuitively, smooth shapes reduce drag by eliminating features that would spoil smooth, attached flow over the airfoil and reducing adverse pressure gradients. The two-dimensional, analytical, potential-flow solutions presented by Sanders *et al.* investigated the benefits of conformal control surfaces as opposed to conventional surfaces from thin airfoil theory. These results were calculated utilizing the analytical, conformal mapping techniques and summarized the expected influence of control-surface on aerodynamic forces by examining the chordwise-normalized location of the beginning of the control surface. The results showed that as the chordwise extent of the airfoil devoted to the control surface increased, the conformal control surface increased in effectiveness compared to conventional airfoil. Another interesting result

from the analysis was that the conformal control surface improved performance over the conventional control surface for all possible chordwise sizing.

The cause of this aerodynamic benefit was investigated by testing the effect of higher-order conformal surfaces on the airfoil pressure distribution. The "order" of conformal control surface was described by the highest degree in the polynomial used to describe the curvature of the control surface. For example, assume a thin airfoil with a unit chord. The mean camber line of this airfoil for a 1st order or "articulated" control surface, i.e. y_1, could be described as

$$y_1(x) = \begin{cases} 0 & \text{for } x < x_{hinge} \\ \delta_{tip}\left(\dfrac{x - x_{hinge}}{c - x_{hinge}}\right) & \text{for } x \geq x_{hinge} \end{cases} \tag{2.1}$$

where x is the chordwise position, x_{hinge} represented the fixed chordwise position of the control surface's hinge, δ_{tip} the magnitude of the trailing edge deflection. In a similar manner, the mean camber line of an airfoil with an n^{th}-order control surface could then be defined as:

$$y_N(x) = \begin{cases} 0 & \text{for } x < x_{hinge} \\ \delta_{tip}\left(\dfrac{x - x_{hinge}}{c - x_{hinge}}\right)^N & \text{for } x \geq x_{hinge} \end{cases} \tag{2.1}$$

where n can represent any real number greater than 1. This formulation allows for equivalent tip deflections to be compared between various "orders" of control surfaces. For clarity, these camber lines were plotted for first to fourth order control surfaces with a representative hingeline at 75% cord with matched tip deflections of 10% chord in Figure 2.3. The discontinuity is completed eliminated by the second order control surface and the magnitude of actuation is moved increasing toward the trailing edge with increasing order of the control surface.

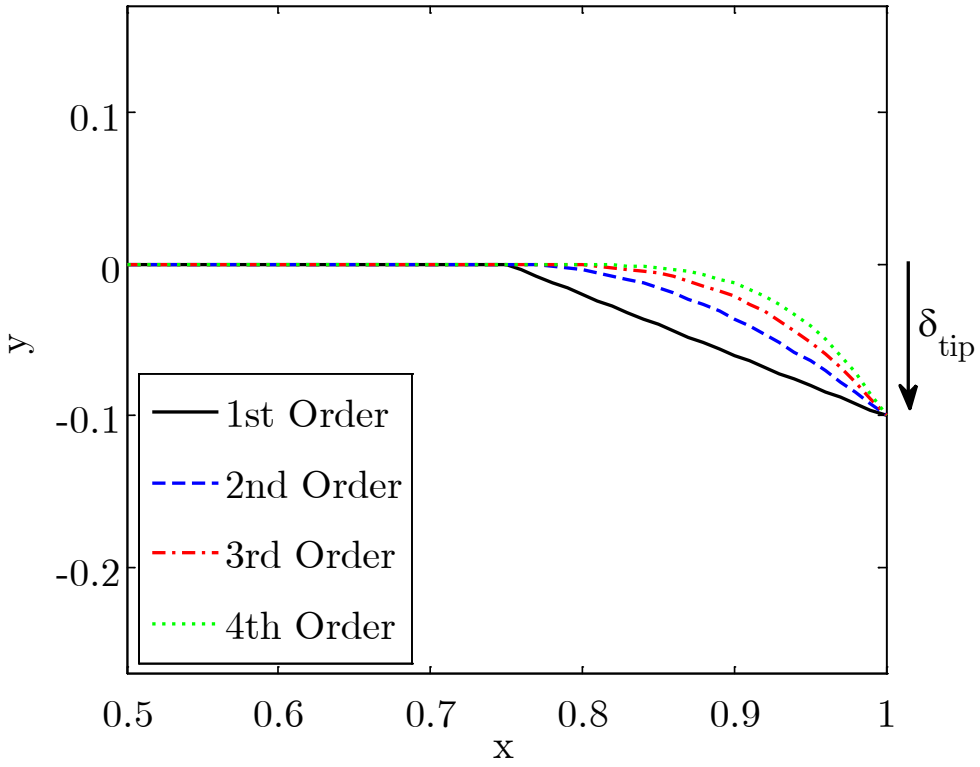

Figure 2.3. Various orders of conformal control surfaces, adapted from [77]

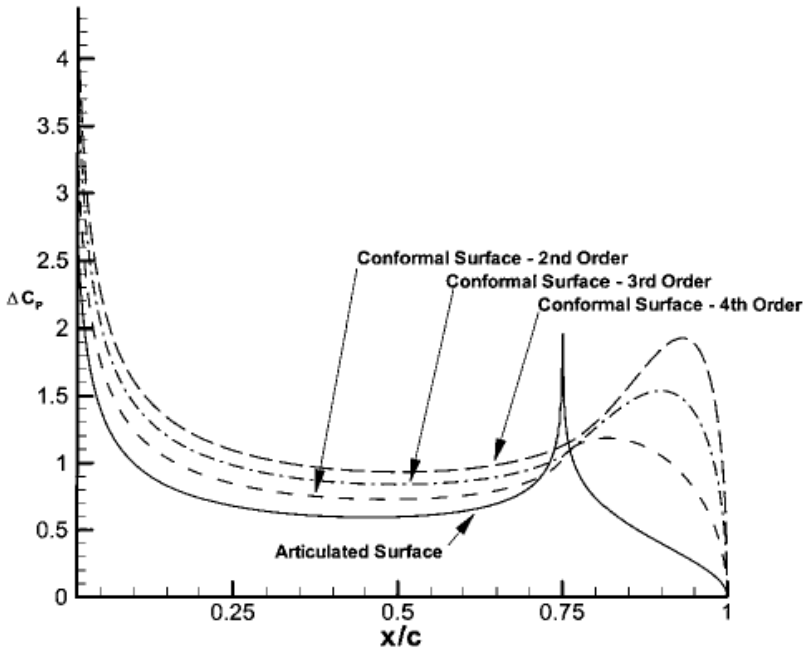

Figure 2.4 Pressure distributions
comparing articulated (N=1) and conformal (N>1) surfaces [77]

Sanders *et al.* investigated how these higher-order control surfaces affected the change in pressure coefficient (ΔC_p) for this representative case with the hingeline at 75% chord, the results of which are reproduced with permission in Figure 2.4 for clarity. Forward of the hingeline, the pressure distribution was noted to be higher for the conformal control surface, signifying increased ability to create lift. For the articulated surface, a sharp pressure spike was caused by the abrupt change in pressure of the flow about the discontinuity in the surface. Also, the conformal morphing surfaces resulted in smooth, large pressure differences after the "hingeline" location, showing increased flow control due to the smooth variation. These results were confirmed for wind tunnel tests of a typical fighter wing showing roll rate increases of 25-30% when using a conformal control surface.

It is important to note that these results applied to potential flow solutions where viscous effects were ignored. The large spike in the pressure distribution of the articulated surface results in a sharp adverse pressure gradient. This gradient is aerodynamically undesirable because it result in large aerodynamic losses due to flow separation and transition for airfoil profiles Reynold's numbers in the 10^5 to 10^6 range. Meso-UAVs, such as Low-Altitude Short Endurance (LASE), Low-Altitude Long Endurance (LALE), or Medium-Altitude Long Endurance (MALE) predominately fly within this Reynold's number range [78,79]. For UAVs of this scale, typical examples of which are shown in Figure 2.5, these aerodynamic losses can be substantial with respect to the total power availability, warranting improvements in control performance [60]. All images are reproduced via fair use from Open Access journals under the Creative Commons Attribution License.

Thus conformal morphing has the potential to suppress these aerodynamic losses by delaying the transition from laminar to turbulent flow over the airfoil, reducing skin friction drag, reducing the possibility of a laminar separation bubble, and lowering profile drag [73]. It is these benefits that have motivated prior work to extend conformal morphing to this scale of UAVs and motivates the current design to also utilize these smoothly varying shapes [59,60,80].

a)

b)

Figure 2.5 Representative a) Low-altitude [79] and b) Medium-altitude UAVs [79,81]

2.2. Spanwise morphing trailing edge concept

Building on the previous work of the all-morphing conformal control surface aircraft from Bilgen, the Spanwise Morphing Trailing Edge (SMTE) concept, a smooth spanwise-varying camber trailing edge surface, is proposed [80,82]. A picture comparing the SMTE concept with a conventional aileron on a wing is provided Figure 2.6. The purpose of this concept is to investigate the potential aerodynamic advantages of eliminating surface discontinuities for a spanwise-variable camber morphing concept for a representative UAV typical of the scale found in Figure 2.5.

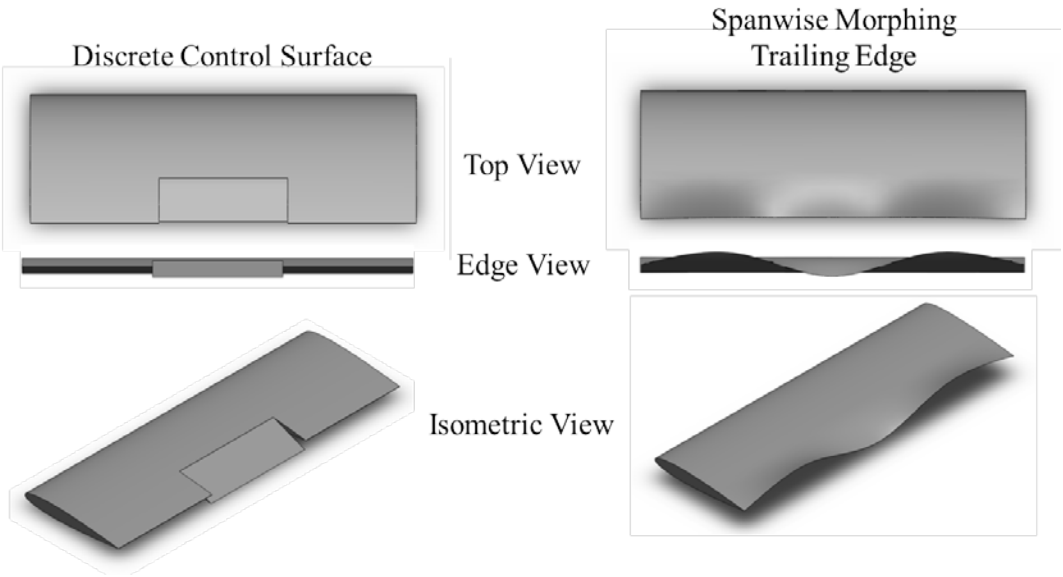

Figure 2.6 Comparison of Discrete Aileron Wing and
Spanwise Morphing Trailing Edge Concept

The aerodynamic advantage of such a configuration has been proposed and tested previously for discrete ailerons (articulated surfaces) and 2-D morphing ailerons (conformal surfaces) [38]. For example, for long-timescale aerodynamic conditions, the ailerons can be actuated to reduce drag while operating within the constraints for the root bending moment of the wing . Thus, these ailerons can maximize the range or endurance of the aircraft by allowing it to remain in a low drag bucket for various flight conditions. Additionally, the ailerons can redistribute spanwise loading for high-g turns [83]. The challenge of SMTE concept is then to eliminate the gaps and discontinuities in the wing surface associated with conventional control surface design, while still permitting relatively independent spanwise variation in actuation control.

As stated before, it was not sufficient to merely design a complex mechanical morphing concept that is capable of achieving the desired shapes. Such a structure would not be practically implemented in a UAV application due to the added weight and/or maintenance complexity. Rather, the requirements of the design were driven from the perspective of requiring minimal modification of an assumedly predesigned wing, tail or horizontal stabilizer. In this manner a

UAV could be designed with conventional control surface, which could then be replaced with conformal morphing control surfaces.

Then, the requirements for the morphing design were as follows. The concept could not alter the spar box of the wing and would be required to achieve realistic airfoil shapes from typical wing designs. To qualify the wing parameters further, it was decided that the rear spar should be located no more than 50% aft of the total chord and the wing should be designed utilizing traditional 4-digit NACA airfoils, representing a typical UAV lifting surface such as a horizontal stabilizer, tail wing or canard. Additionally, driven by the desired aerodynamic advantages, the structure should achieve smooth spanwise-varying camber. Finally, it was desirable to maintain or improve the weight and power consumption as compared to a traditional, articulated control surface.

To meet these requirements, a modular design is proposed that alternates between active and passive sections over the span of the wing, as shown in Figure 2.7 [82] . An active section was defined as a two-dimensional morphing concept where uniform conformal morphing could be achieved. Similarly, a passive section would not contain an actuation material, but would rather be elastically deformed by the active section. The purpose of the passive section would be to span the gap between active sections.

The modular design has several benefits over a wing with finer compliance distribution by reducing design and implementation complexity through the use of a common unit. By utilizing only a single two-dimensional morphing concept for the active section, off-the-shelf morphing designs could be used, removing the need to completely design a new actuation method. Additionally, the spanwise repetition would allow the active sections to be built in batches, further reducing design complexity. Finally, utilizing novel actuation methods comes with increased risk of failure. Modular design allows for individual active sections to be easily replaced in the event of failure, a vital consideration for the adaptation of new technologies.

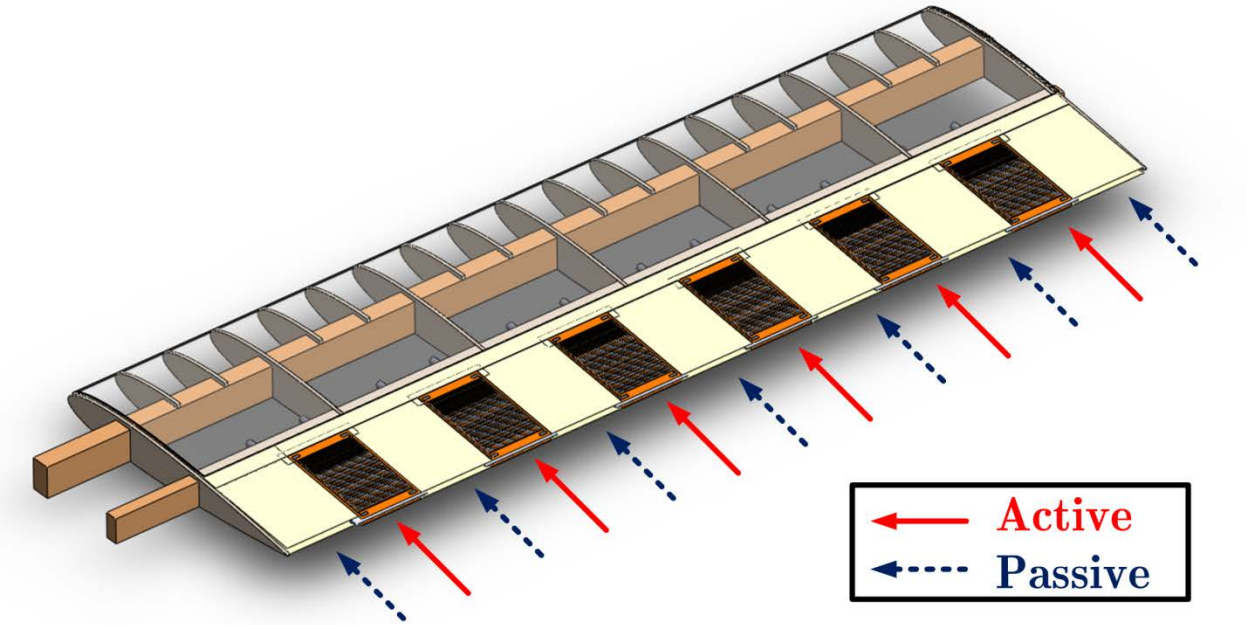

Figure 2.7 SMTE modular test bed

2.3. Test bed design

The wing chosen for the implementation of this modular design was sized for a typical meso-scale UAV, the details of which are summarized in Table 2.1. Per the prior discussion in Section 2.1, the chordwise spacing of the beginning of the trailing edge was chosen to be approximately 60% chord to emphasize potential performance differences with a conventional aileron. The airfoil was chosen to be a symmetric airfoil to separate any asymmetry due to the actuation concept from the lift-offset of the airfoil at zero angle of attack. A 12% chord thickness airfoil was chosen as that typical of a wing or lifting surface for this scale of UAV.

Table 2.1 Parameters for selected half-span wing

Parameter	Value
Chord, c	30.4 cm
Rear spar location	18 cm
Aspect Ratio	3
Airfoil Designation	NACA 0012

The sizing and spanwise spacing of the modular active sections was another important design point that has no guiding principles within standard wing design. By placing the active sections closer together, the spanwise fraction of the wing that is "active" would be increased, but the capability for relatively "smooth" variation in spanwise actuation would be reduced as larger discontinuities would be generated from antagonistically actuating sections. Accordingly, such a design would introduce large strains in the passive sections, constraining the configurations achievable by the design. Opposingly, by placing the active sections further apart, the total actuation energy relative to the size of the wing would decrease as would the ability of the control surfaces to act against aerodynamic loads. For the purposes of this initial investigation, the spanwise distribution of active sections was chosen to be evenly spaced at approximately 50% of the total span fraction. The investigation of the impact of this "active span-fraction" is placed outside the scope of the current work.

Another consideration for the test bed design was the spanwise width of the individual active sections. As shown in Figure 2.8, for a finite span wing, uniformly decreasing the width of the active sections increases the number of active sections, N. As $N \rightarrow \infty$, the potential to recreate arbitrary smooth shapes increases. However, increasing the amount of active material elements also increases the complexity of implementation, and weight. The number of active sections was thus driven by the minimum number required to achieve several prescribed geometries.

Since the goal of the SMTE concept was to investigate the aerodynamic advantage of smooth variation over several atypical spanwise-varying configurations, the geometries were informed by typical UAV configurations. Examining UAVs representative of this scale, a tail or wing typically has only one or two control surfaces for additional take-off and maneuver loads [79]. For an initial estimate of number of active sections required for this test bed UAV wing, six active sections were chosen to provide a reasonable range of options for spanwise variation compared to the current number of control surfaces typically available on a comparable aircraft. This number of active sections allowed for several complex spanwise-varying configurations such as quadratic and sinusoidal trailing edge displacements, shown in Figure 2.8 to be approximated. Also, it allowed for MFCs of available size to be utilized in the current wing.

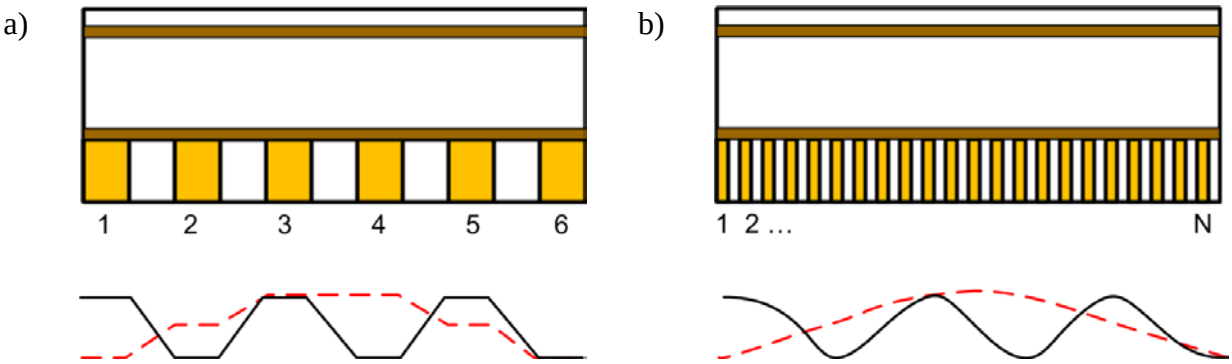

Figure 2.8 SMTE implementation for a) six active sections and b) N active sections with approximate effect on recreating quadratic (dotted) and sinusoidal (solid) variations in trailing edge displacement

2.4. Active section development

With a chosen wing planform and desired morphing geometry, a two-dimensional modular active section design was needed. First, a literature review was performed seeking an adequate two-dimensional morphing design to serve as the actuation mechanism, section, structure and skin for the active section. The active section was required to achieve smooth camber variation for the finite thickness of the airfoil. Although servo-driven compliant mechanisms, such as the Smart Wing Eccentuators, and the FlexSys compliant trailing edge exist in literature, they were predominately used for higher aerodynamic loads than the scale of aircraft of interest [17,34]. Additionally the small parts, linkages and hinges in these designs were deemed to be prone to manufacturing and positioning error. Finally, the details of these designs were largely restricted by the nature of the projects, precluding detailed analysis.

As stated in the Chapter 1, previous work by Bilgen *et al.* and Ohanian *et al.* and others have shown that Macro-Fiber Composites (MFCs) can be effectively integrated into airfoils to achieve a bending trailing edge for small UAVs [60,84]. Also beneficially, MFCs have a higher bandwidth than servos [85]. The expected reduction in complexity and mass associated with these active bending patches motivated their selection over conventional servo actuation designs. This work is far from the first to select a smart material as a

Although the patches can be simply glued to an existing structure or form a thin airfoil, it was desired to maintain a typical airfoil profile with typical thickness. Accordingly, the cascading bimorph airfoil concept, detailed in the introduction, was chosen as the base two-dimensional morphing concept to meet the active section requirements of finite thickness and

constant camber morphing [65]. The design utilizes a complaint mechanism, namely a compliant box, to enhance the range of bending for a morphing trailing edge. The cascading bimorph was designed to be implemented with constant actuation over the span of the airfoil. Although further iterations of this design have resulted in variable spanwise actuation, the skin was inextensible and spanwise variations were relatively small [86]. To achieve the large spanwise variations in actuation, a modular version of the concept was required to be adapted. The development of the particular design utilized in this work is detailed in the following section.

2.4.1. Modular compliant box development

The modular design, shown in Figure 2.9, allowed for the cascading bimorph concept to be connected to the rear spar of the wing at any spanwise station while conforming to the width requirements from the test bed design. The modular trailing edge was mounted to the rear spar with two bolts that could be removed and allow the morphing trailing edge to be maintained or replaced from the test bed as required.

The compliant, hinged box and trailing edge stub were produced with rapid prototyped parts made from ABS plastic via the Dimension Elite Fused Deposition Modeling machine at the University of Michigan 3D Lab. The hinges were created by force-fitting steel pins on the outside of the hinge while using clearance fits on the inside of the hinge.

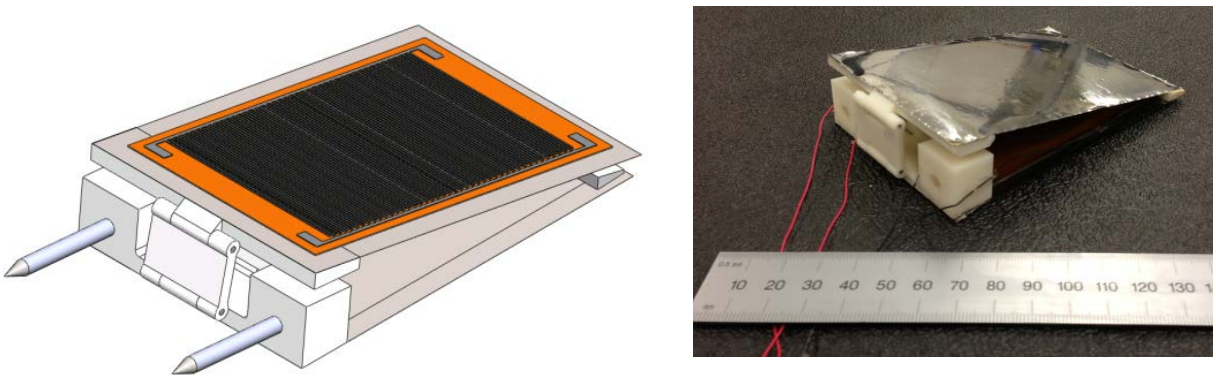

Figure 2.9 a) Modular Compliant Box design and b) construction

Each side of the active bending trailing edge utilized M8557-P1 MFC from Smart Material Corporation to 25.4 μm thick stainless steel shim from McMaster-Carr using 3M Scotch-Weld DP-460 epoxy in a vacuum bag under 0.6 ATM of pressure for 24 hours. The number of MFCs utilized during the construction process could be varied. For simplicity of construction and to create a smooth aerodynamic surface, the initial concept was built in the "unimorph" configuration consisting of only two MFCs, mounted to the inside of the morphing aileron as seen in Figure 2.10 . The impact on the amount of smart material on the performance of the morphing aileron is the subject of investigation in Chapter 3.

The result is the smooth, metallic outer surface shown in Figure 2.9b. In the process of producing several of the boxes for further experimental testing, it was noted that control of friction in the joints during the fabrication process was difficult to control and maintain between the various compliant boxes. Also, it was noted during initial dynamic tests that the hinge exhibited very low structural stiffness or damping to externally applied tip loads. To improve the reproducibility of the design, alternative methods for introducing compliance to the attachment points of the MFCs were explored, resulting in the use of elastomeric flexures to replace the discrete hinges, also reflected in Figure 2.10. Further discussion about these elastomeric flexures follows.

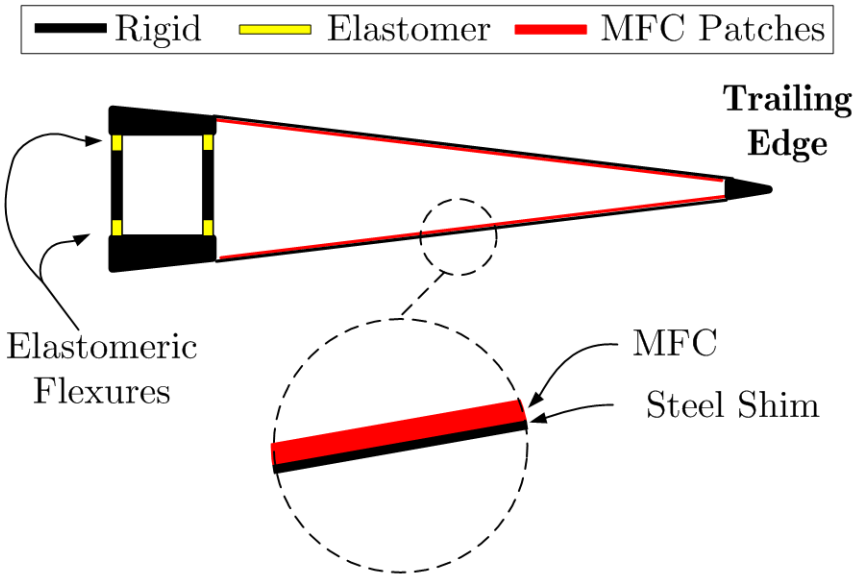

Figure 2.10 Diagram of Flexure Box aileron in "unimorph" configuration

2.4.2. Flexure box development and testing

Recent work has shown that compliant structures can replace conventional mechanisms while allowing for smooth geometry change, improved reproducibility in design, and no backlash or wear, all of which are well-suited for morphing aircraft [38,87,88]. Thus, the proposed Flexure Box design replaced the hinges of the hinged, compliant box design with flexure sections, shown in Figure 2.11. The use of these compliant mechanisms also has the added advantage of allowing for variation of the internal structure to maximize the displacement of the active section while reducing the impact due to aerodynamic loads.

The Flexure Box is created by additive manufacturing to allow for precise control of geometrical arrangement and structural stiffness without frictive positioning errors or losses. Utilizing the Objet Connex 500 3D Printer, the flexure box design was printed as a combination of elastomeric material and rigid plastic. The functionality of this machine differs from a typical 3D printer in that local compliance can be tailored by varying the material properties. Similar to previous work, these multi-material printers can be used to create end-use compliant structures [87]. The resultant design eliminated the friction in the hinge joints, and presented the capability of parametrically altering the compliance while also improving the reproducibility of the Flexure Box.

a)

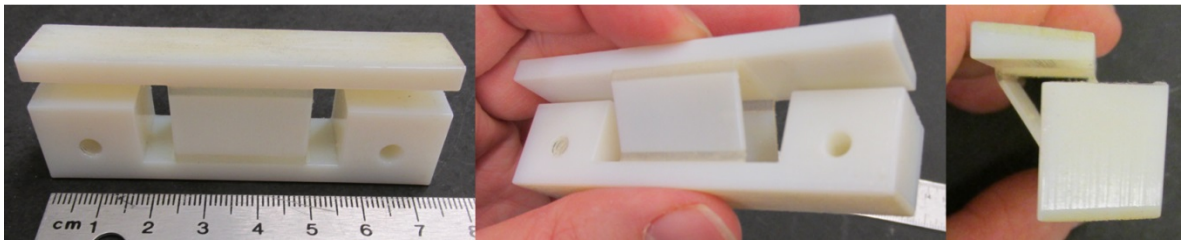

b)

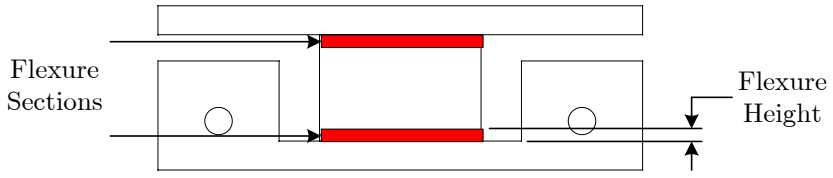

Figure 2.11 a) Flexure Box construction and b) stiffness parameterization

A simple test was performed to evaluate the effect of using a flexure mechanism rather than a hinged mechanism on the ability of the aileron to actuate. The flexure box was substituted for the hinged box in the cascading bimorph design and the resultant trailing edge deflection with the intent of measuring the effect on trailing edge displacement. The resultant active section was referred to as the “Flexure Box aileron” to simplify the name. To assess the impact of varying sizes and stiffnesses of flexure mechanisms, the geometry of the compliant elastomeric material was varied.

The compliance of the Flexure Box could then be modeled as two beams linking a rigid top and bottom structure. The width of each beam was determined by the allowable width of teach spanwise section. Then, to alter the compliance the thickness and the length of each compliant section on the beam could be varied. For the purpose of this test wall thickness, out of the plane in Figure 2.11, of 1 mm was chosen for each side of the flexure box. This value was decided as the minimum thickness allowable by tests on the adhesion of the interface between the elastomeric and rigid material. Smaller thicknesses resulted in a surprising reduction in the ability of the interface to withstand bending loads. A discussion of the cause of this mechanism can be found in Appendix A.

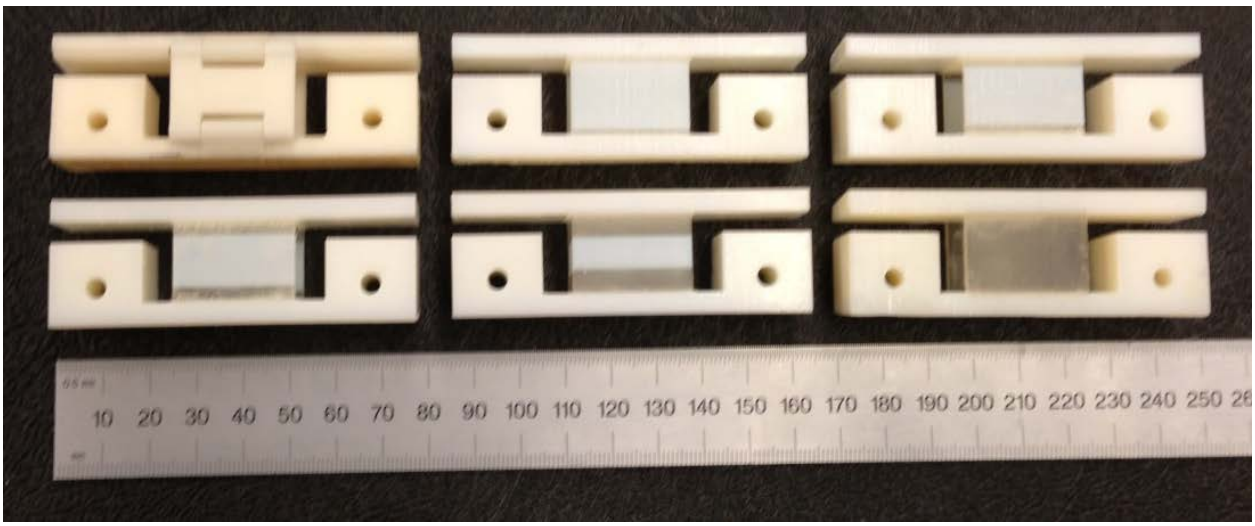

Figure 2.12 Flexure Boxes with Varying Compliant Lengths
(top) Hinged, 1mm Flexure, 2mm Flexure
(bottom) 3 mm Flexure, 5 mm Flexure, 8.5 mm Full Flexure

Then, a single parameter, the flexure height was then used to characterize the compliance of the flexure box structure, as depicted in Figure 2.11. Flexure heights beginning with 1mm and increasing to a full flexure hinge (8.5 mm hinge height) were evaluated. As a baseline, the hinged model from the cascading bimorph design was also compared to evaluate the performance. All tested compliant boxes can be found in Figure 2.12.

The MFCs within the flexure box design were controlled using a TREK 2220 High Voltage Amplifier as well as the solid-state electrical voltage divider circuit developed by Bilgen *et al.* 2013 [80]. This solid-state circuit distributes voltages between antagonistic MFCs in a 3:1 voltage ratio so that only the allowable voltage range of 1.5kV to -0.5kV is achievable with a single bipolar high-voltage amplifier (HVA) with +/- 2kV range. Thus, the HVA was cycled between -2kV and +2kV to actuate the upper and lower surface of the cascading bimorph antagonistically. A Keyence LKG-402 laser displacement sensor was used to track the displacement of the aileron at approximately 0.5 cm from the trailing edge, i.e. tip, of the morphing aileron. The positions of the trailing edge were taken as time-averaged data over 5 seconds, with a 5 second wait time in between each data point to eliminate the effect of creep on the results. Each data set was repeated for a total of 3 cycles in sequence to show the repeatability. The results are shown in Figure 2.13. For clarity of orientation negative values are defined as the tip actuating downward.

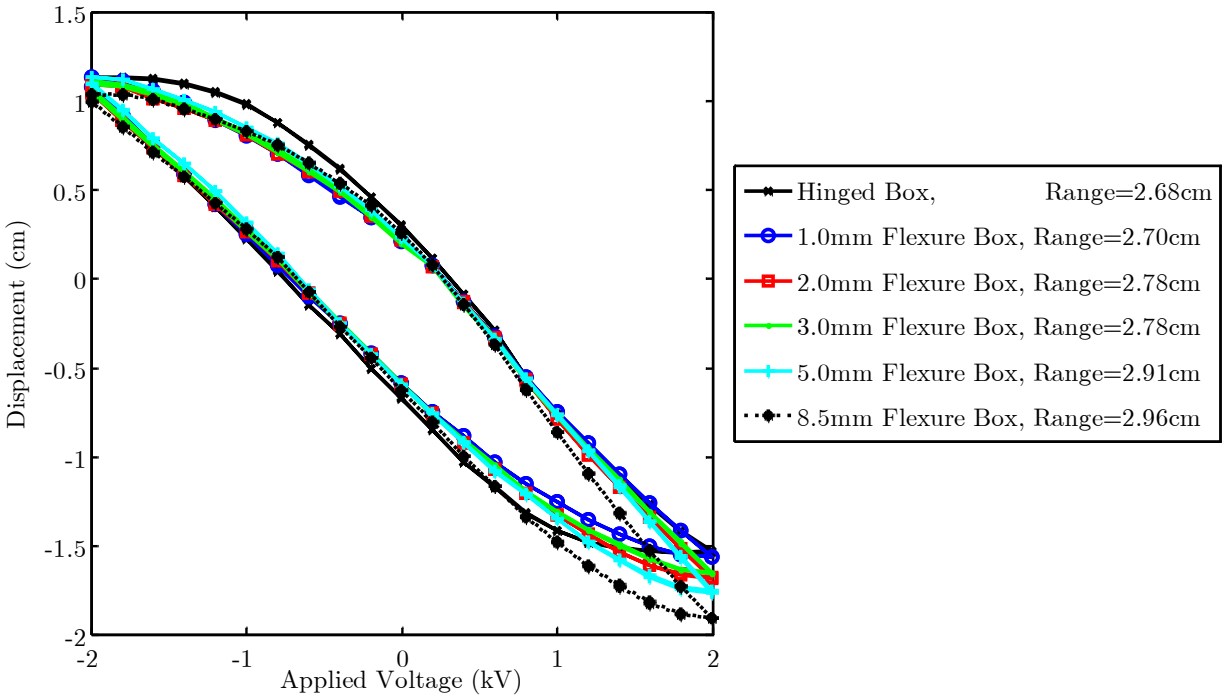

Figure 2.13 Effect of Flexure Hinge Size on Actuation Range

The results show that as the flexure height and thus the compliance of the flexure box is increased, the total range of the actuation concept also increases. The full flexure box improved actuation range by 10.7% over the hinged baseline case, mostly in the downward direction. This result is described by the compliance of the flexure hinge providing an additional degree of freedom to the trailing edge. Whereas the hinged box can only shear chordwise, the two flexing supports of the flexure box can also buckle varying amounts, resulting in an angular change between the top and bottom of the flexure mechanism, denoted as θ in Figure 2.14.

Figure 2.14 Flexure Box Buckling (foreground) and Hinged Box (background**)**

This additional compliance has the potential disadvantage of allowing this compliant box to deform under aerodynamic loads, an effect which is not captured in this test and is the subject of investigation in later chapters. Still, an initial characterization of the concept under aerodynamic loads is detailed in Section 2.6. To provide an initial estimate of the best-case scenario where the performance is not degraded by aeroelastic effects, a purely aerodynamic simulation of the shape of the Flexure Box aileron from experimentally measured shapes was performed.

2.4.3. Modeled aerodynamic performance of the flexure box concept

The structural concept of a morphing control surface was developed in the previous section, but the question remained as to whether the resultant shapes could still recover the improvement in aerodynamic force control from Section 2.1. The results from Sanders *et al.* modeled the airfoil as simply a flat plate with varying orders of curvature at the trailing edge [77]. With the actual morphing structure created, a higher fidelity analysis of the performance could be performed.

A two-dimensional aerodynamic simulation of the Flexure box morphing airfoil was performed to investigate the viability of this particular morphing active section concept design to improve aerodynamic performance over a typical discrete aileron [89]. This refined assessment of the concept was performed by matching an “equivalent” flap to the morphing concept and comparing the effects on pressure distribution and aerodynamic forces, similar to the analysis from Sanders *et al.* in Section 2.1. The morphed shape used for the analysis was constructed

from digital image correlation of experimentally tracked points on the airfoil from actuation tests. This shape was then added to the leading edge airfoil shape from the test bed design in Section 2.3 to beginning at the location of the rear spar. To reduce the effect of position measurement errors on the simulation the data was smoothed in the surface arc length domain "s" normalized by the chord then converted to the spatial domain, as seen in Figure 2.15.

a)

b)

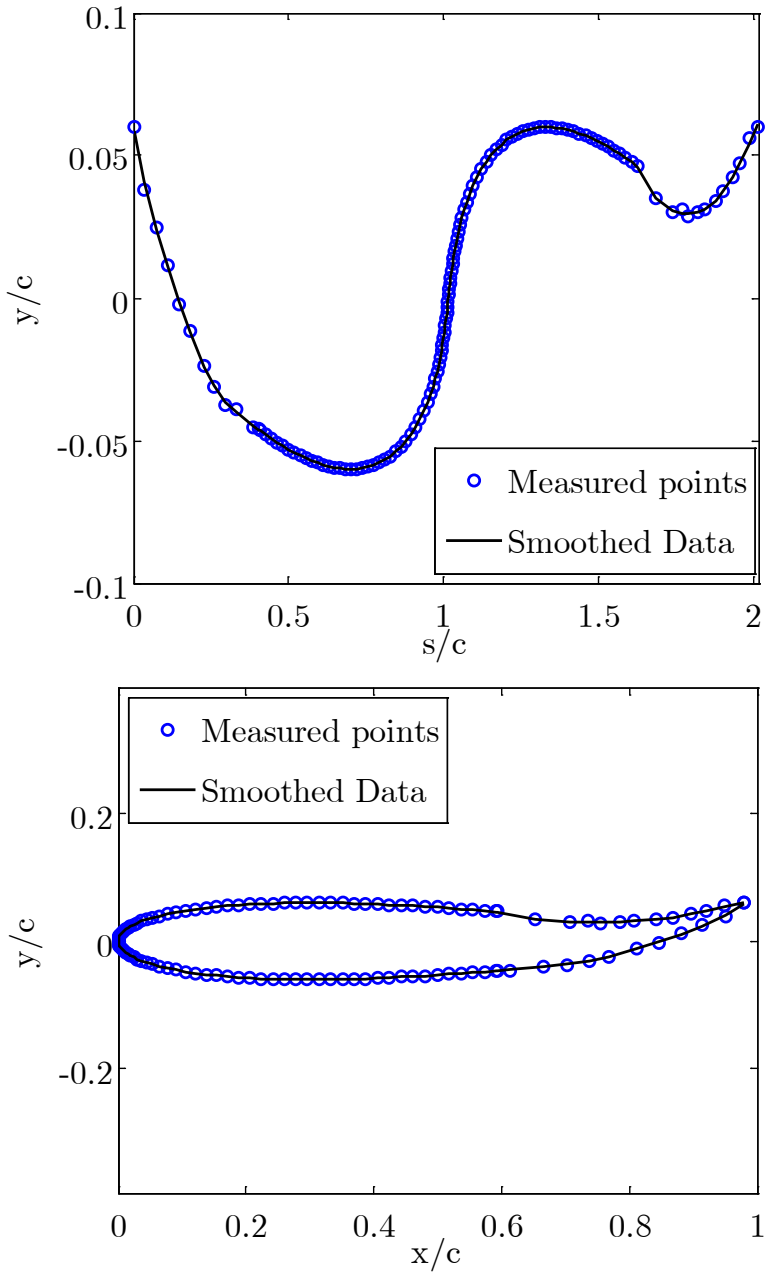

Figure 2.15 a) Arc-length and resultant b) spatial smoothing of morphing displacements

The equivalent flap was matched to the morphing data in a manner similar to that from Section 2.1 by placing the hingeline of the articulated flap at the beginning of the morphing surface. The trailing edge deflection of the flap was then matched to that of the experimentally measured morphed shape, as shown in Figure 2.16a. The trailing edge deflection of both control surfaces is 6.08% of the chord.

A Reynolds-Averaged Navier-Stokes simulation utilizing a Spalart-Alarmas turbulence model was performed on these matched, actuated shapes for a representative flow condition [89]. The simulation utilized a structured mesh at 0 degrees angle of attack for a Reynolds number of approximately 3.14 $x10^5$, which would correspond to approximately 15 m/s flow speed for the scale of test bed under investigation.

The results of this initial investigation are summarized in Figure 2.16b and represent the first time that [89] is compared to higher-fidelity aerodynamic analysis, and specifically for a finite-thickness morphing airfoil concept. The results verify the improvement predicted by Sanders *et al.* albeit at a slightly reduced level. An advantage of the higher resolution simulation is the ability to capture drag in addition to lift and moment on the airfoil. As a result, the lift to drag ratio of this particular conformal morphing concept can be directly compared to its articulated equivalent airfoil.

The simulated pressure distributions in Figure 2.16b generally follow the previous analytical results from Section 2.1. The simulate results from this section represent a more accurate assessment of the capabilities of the morphing surface, because they also allow for calculation of the pressure on the upper and lower surfaces and drag on the airfoil, due to the incorporation of viscous effects. The large spike in pressure coefficient previously predicted for the equivalent “articulated” flap is somewhat mitigated by these viscous effects. The jagged pressure distributions are partly numerical due to sharpness of the joint at the discrete flap. However, even though the magnitude of this spike is not singular, it is still significantly greater than the more gradual curve predicted for the conformal morphing concept. The curved, morphing surface shows a large increase in pressure differential between the upper and lower surface aft of the hingeline, also representative of the prior thin-airfoil results.

a)

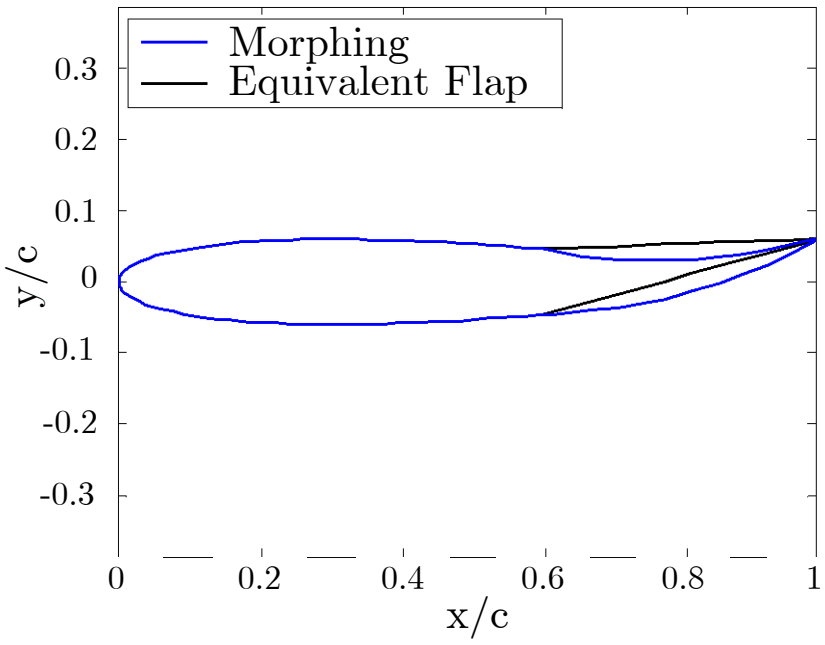

b)

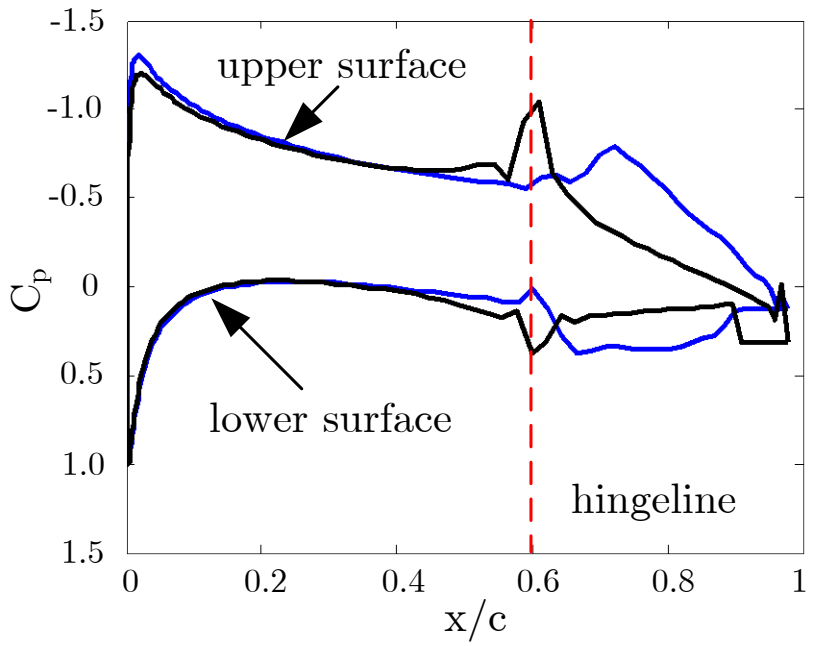

Figure 2.16 a) Matched morphing and flap trailing edge deflection and b) pressure distributions for Re=1.34 x 10^5

Table 2.2 Initial comparison of aerodynamic forces

	C_L	C_D	C_M	Lift/Drag
Equivalent Flap	-0.684	0.0226	0.0732	-30.3
Morphing	-0.793	0.0166	0.131	-47.9
Calculated Improvement	16%	27%	79%	58%
Predicted Improvement [77]	40%	N/A	91%	N/A

These increases in pressure difference, and more gradual pressure gradients result in improved control over aerodynamic forces, shown in Table 2.2. The morphing airfoil slightly improved lift performance, approximately 16%, while decreasing drag by 26% and increasing pitching moment by nearly 80%, resulting in an overall gain of L/D of nearly 60%. These results are compared with the extrapolated values from Sanders *et al.* [77]. Clearly, the lift and pitching moment improvements are not as significant as the inviscid results predicted, but the viscous analysis also predicted a notable drag improvement. The resultant Lift/Drag ratio, which is typically an identifier of achievable range for a UAV, was improved by 58%. Thus it was determined that the flexure box morphing concept, at least in two dimensional flow, would produce a notable improvement in control authority over a conventional discrete aileron. It then remained to determine whether these benefits could be expected when the concept was integrated into the SMTE test bed, at other flight conditions, and under aerodynamic loading. These topics will be addressed in later chapters.

2.5. Passive section development

The skin of the SMTE test bed posed a unique challenge due to the competing requirements of the structural and aerodynamic constraints. The skin needed to be designed such that the impact on the range of the active section was minimized, but still be stiff enough to carry the aerodynamic loads without significant deformation. Previous work has proposed anisotropic materials that can be used to tailor the compliance of the skin according to the needs of the specific morphing application [54]. These skins permit camber deformation with low in-plane axial stiffness while resisting aerodynamic loads with high out-of-plane bending stiffness. The constraints typically important for consideration in these designs are local skin “bubbling” and “buckling” [90,91].

Many different methods have been used to create anisotropic skins including, but not limited to: bistable plates, composite skins, corrugated skins, compliant structures and cellular honeycombs [38,92–94]. Of these concepts, cellular honeycombs have received significant attention, in part, due to the ability of the effective material properties to be parametrically described by the properties of honeycomb unit cell, which can take many different shapes [95–97]. However, the analytic equations describing the effective properties assume infinitesimal strains and isotropic material properties and are known to deviate due to geometric and material nonlinearities in the loading of the unit cell.

2.5.1. Elastomeric honeycombs via additive manufacturing

For the current test bed, cellular hexagonal honeycomb cores were chosen due to existing descriptions of the trends of the cell design parameters on effective material properties [95]. Further leveraging the abilities of the Objet Connex 500 3D Printer to create complex, compliant structures, a compliant honeycomb was developed. The goal of the honeycomb was to permit rapid parametric design of a complex anisotropic skin that supresses the out of plane-bubbling due to aerodynamic loads while still allowing for adequate active section range. The optimal design of the honeycomb's structure was not the focus of this current work, but rather an initial design showing the capabilities of the concept was chosen.

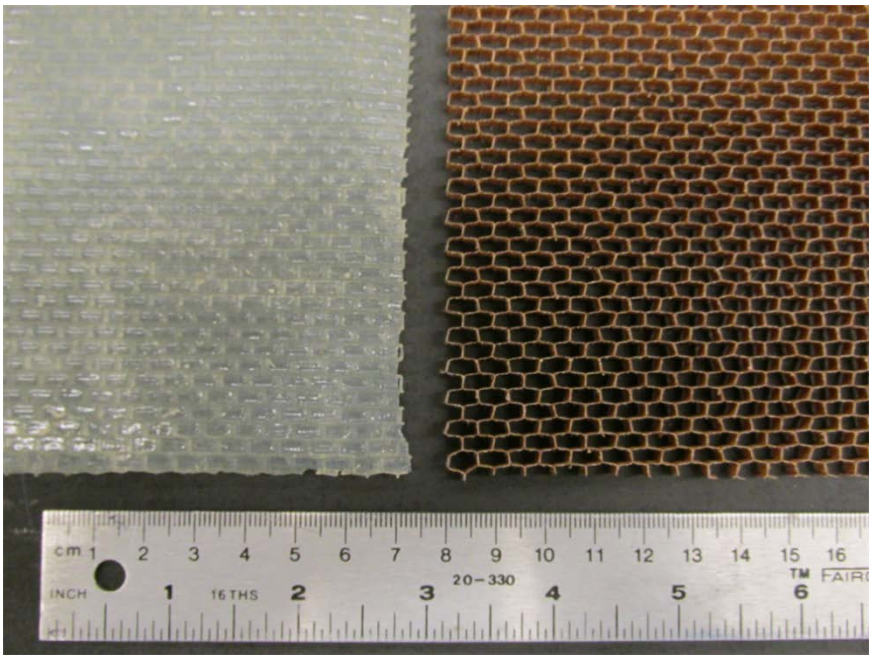

Figure 2.17 Printed honeycomb sizing (left) compared to aramid fiber honeycomb (right)

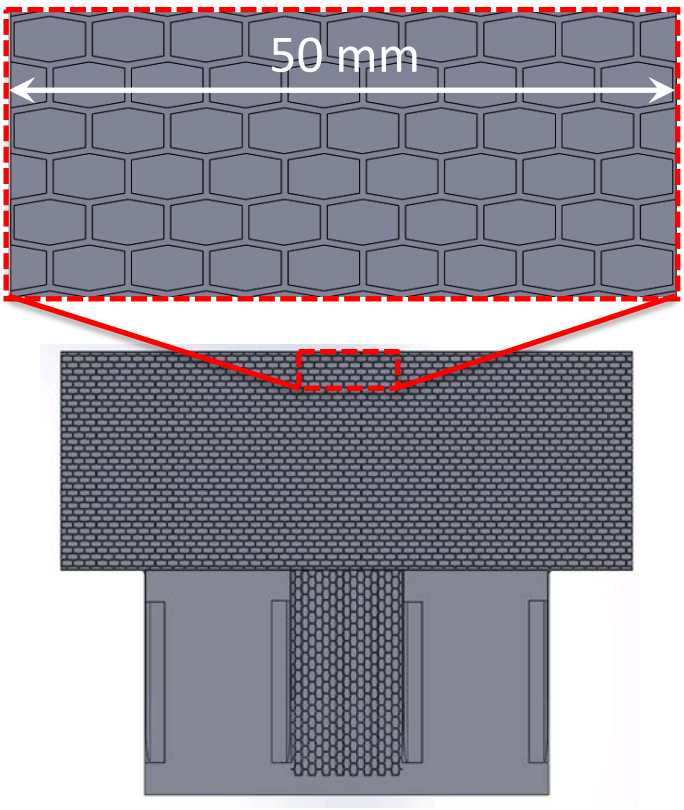

Figure 2.18 Honeycomb alignment in the skin

The honeycomb cell size for the demonstration skin was designed by mimicking the sizing of Plascore aramid fiber honeycombs made with Nomex paper and phenolic resin [98]. Using the trends of the effects of geometric parameters on in-plane material properties and flexural bending stiffness established by Olympio *et al.*, the honeycombs' compliant directions were aligned in the expected directions of greatest expected in-plane strain, which is spanwise between the active sections and chordwise in front of the active sections , as shown in Figure 2.18 [95]. The honeycomb and skin were printed from TangoPlus, the most compliant elastomer available with this manufacturing method, equivalent to approximately 10A durometer hardness.

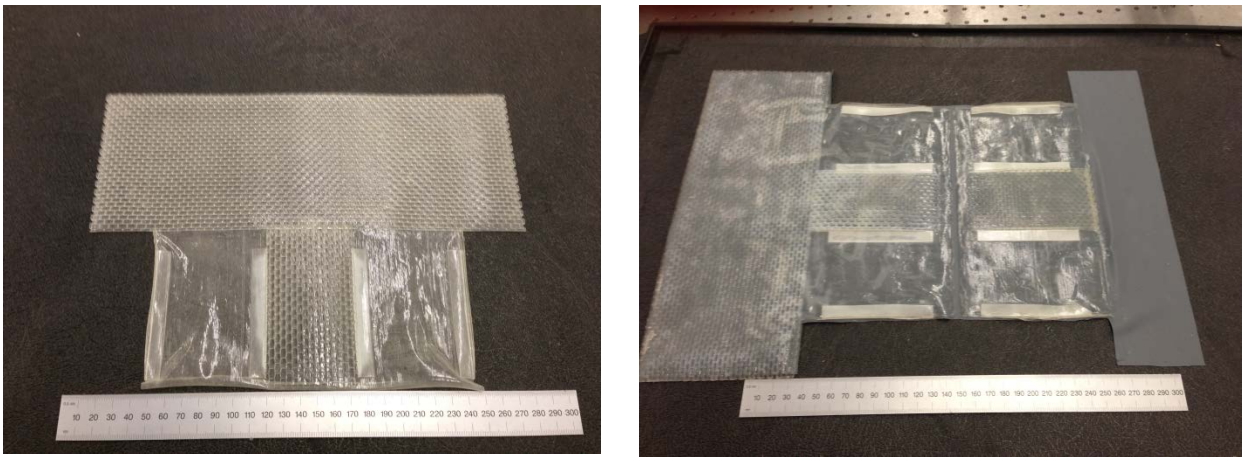

Figure 2.19 3D-printed elastomeric honeycomb-skin and final skin bonded to silicone

When predicting the effective properties of a honeycomb skin, it is typically assumed that the skin is significantly more compliant than the honeycomb. Although geometrically possible, actuating honeycombs with thin printed skins of TangoPlus resulted in tearing of the thin skin. The nature of these skins resulted in few-layer thicknesses that were prone to tearing due to same reasons discussed in Appendix A. However, by bonding these skins using silicone sealant to a thin, compliant silicone sheet, a resilient, compliant skin with the potential for localized stiffness control was created, shown in Figure 2.19.

2.6. Initial characterization of representative section

A representative section of the test bed was created to evaluate the effects of various skin configurations on the active sections' ranges with aerodynamic considerations. As noted by the prior two-dimensional results, the expected aerodynamic advantage of the morphing concept over articulated ailerons is on the order of 20% to 60% for relevant force metrics when tip deflections are matched. If the skin influences the deflection of the Flexure Box aileron on a similar scale, then it will represent a significant factor in the evaluation of the performance of the morphing test bed.

The representative section utilized the same chordwise scale and active section spacing of the test bed from Section 2.3, but its span was reduced to encompass only two active sections and a single passive section located between the two active sections, as seen in Figure 2.20a. The total chord, per the test bed design, was 305 cm and the total span of the section was 210 cm, generating a finite wing with an aspect ratio of approximately 0.7. The airfoil forward of the

rear spar was not the focus of this investigation, and was created using a carbon fiber-layup over a foam core. The rear wooden spar was included for mounting the active sections and a steel shaft with coupling was embedded into the foam with epoxy to create a front mounted spar.

To aerodynamically mimic an infinite-span wing, it was desired for the representative section to span the entire wind tunnel, but the spanwise sizing of the section was governed by the test bed spacing and left approximately a 90 cm gap between the end of the section and the wall of the wind tunnel. Accordingly, end plates were attached spanwise at both root and tip to minimize spanwise aerodynamic losses to the finite span of the airfoil, also pictured in Figure 2.20a.

2.6.1. Characterization without aerodynamic loads

With the representative section construction complete, initial tests on the representative section were performed without aerodynamic loads to evaluate the effect on the ability of the active sections to actuate. The effect of the skin on the active sections was assessed by stepping the bottom active section through its complete range while cycling the top active section through a full hysteresis loop, a processed describe in greater detail in the following section. The voltages applied to the Flexure Box ailerons were controlled from a PC through National Instruments DAQ interfaced with an AVID Dual Channel MFC Bimorph High-Voltage Driver, which allowed for simultaneous, independent control of both morphing ailerons [99]. The displacement ranges of the two active sections were measured at their respective spanwise centers at 298 mm chord using two Keyence LKG-402 laser displacement sensors, shown in Figure 2.20b.

a)

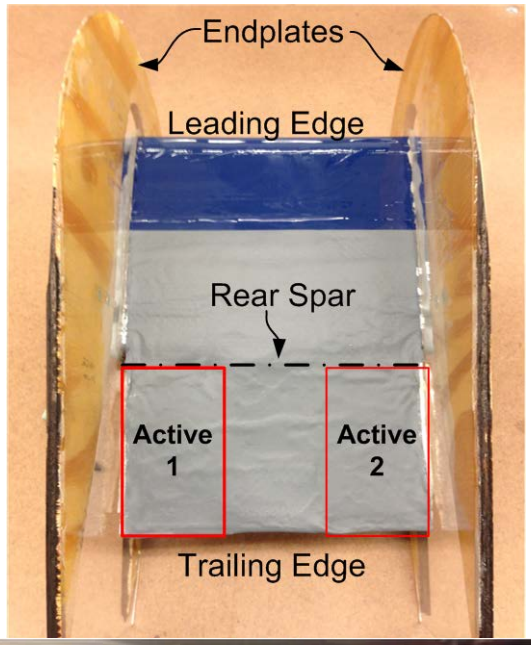

b)

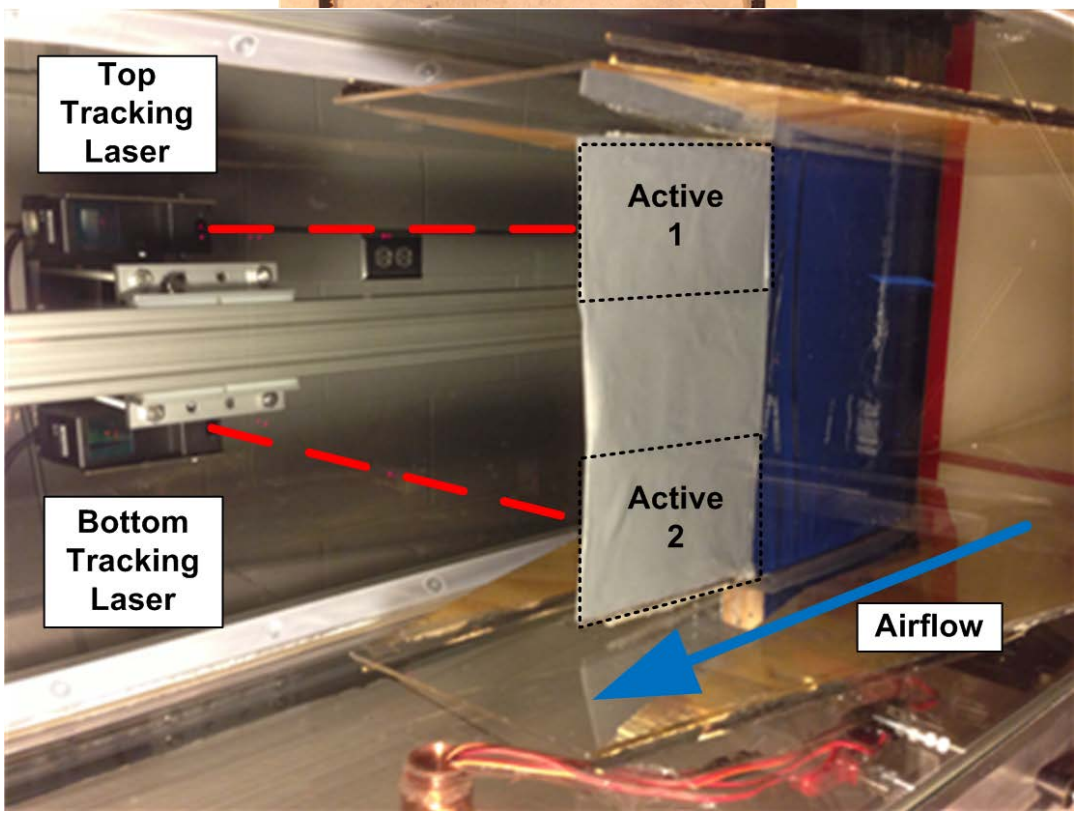

Figure 2.20 a) Representative test section diagram and
b) displacement tracking in wind tunnel

For the assessment of possible skin configurations, five different configurations were tested with various boundary conditions on the skin, summarized in Table 2.3 and Figure 2.21. The “BC0” boundary condition represents the free trailing edge of the morphing concept as well as the lack of attachment to the end plates. This boundary condition is thus “free” for all configurations by nature of the experimental setup. The “BC1” boundary condition represents whether the two active sections are attached, which is true for all configurations except the unconstrained case. The “BC2” boundary condition represents the presence of attached skin at the rear spar. Finally, the “BC3” boundary condition represents whether the skin is allowed to contract in the spanwise direction. This third boundary condition is significant because honeycombs are known to exhibit increased stiffness when constrained from contracting due to Poisson’s effects. This condition is relevant because a high aspect ratio wing would result in an essentially attached boundary condition due to the repeating nature of the honeycomb.

The various skin configurations are related to the above boundary conditions as follows. The “No Skin” configuration represents the active sections without the skin attached at any boundary condition. Clearly, the lack of skin would not suffice as an aerodynamic surface, but is referenced only as a baseline to measure the effects of the skins. An isotropic, “pre-stressed silicone” skin was also tested to evaluate the additional stiffness provided by the honeycomb skin. The honeycomb skin was tested in several configurations. The “Spanning Honeycomb Skin with Wiper” configuration used a wiper at boundary condition “BC1” rather than a pre-stressed skin. Here a wiper is defined as a sliding surface that maintains C0 surface continuity, where the resultant surface is continuous but not strictly differentiable at the point of contact. This wiper configuration is preferred structurally as it eliminates a large portion of the required skin, but the impact of this wiper on aerodynamic performance is not quantified here but is investigated further in Chapter 3. The “Full Honeycomb Skin with Fixed Sides” and “Full Honeycomb with Free Sides” investigate the effect of the spanwise boundary conditions on the honeycomb. In the “Prestressed Silicone” configuration and both “Full Honeycomb Skin” configurations, the morphing skin was secured at 90 cm along the chord with approximately 10% of prestrain in the skin to prevent buckling during actuation.

Table 2.3 Description of Skin Boundary Conditions

Configuration	BC0	BC1	BC2	BC3
No Skin	Free	Free	Free	N/A
Prestressed Silicone	Free	Attached	Attached	Attached
Spanning Honeycomb with Wiper	Free	Attached	Free	N/A
Full Honeycomb Free Sides	Free	Attached	Attached	Free
Full Honeycomb Fixed Sides	Free	Attached	Attached	Attached

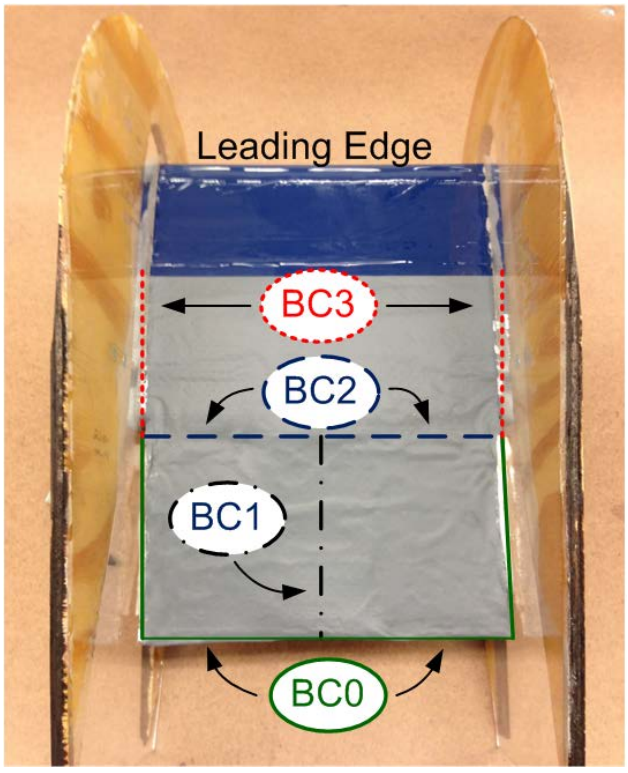

Figure 2.21 Boundary conditions for various skin configurations

The effect of these various skin boundary conditions on the range of the active section's ranges are characterized in Figure 2.22. In this figure, the *x* axis represents the achievable displacement ranges of the second active section (the bottom active section in Figure 2.20b) and the *y* axis represents the range of the first active section (the top active section in Figure 2.20b). The shaded boxes in the figure bound the various achievable displacements, or the "actuator space" of the two active sections for each skin configuration. These boxes are significant because they can help identify the effects of the various skin configurations on the active sections to determine which would be most suitable for implementation in the full-scale test bed.

2.6.1.1. Measurement procedure

The data were created by commanding a constant voltage to the second active section while cycling the first active section over its entire voltage range, creating a data set for the achievable range of one active section while the other has no change in input. The magnitude of the dataset is defined as the "local range", which can be found by taking the difference between the maximum and minimum of the displacement of the first active section for a constant voltage of the second active second. This process only maintains the position of the second active section if the first active section has no influence over it. Such a situation occurs if the active sections are sufficiently stiff relative to the loads communicated through the skin or if no skin exists. The lack of the first active section affecting the second is represented by the data sets appearing as vertical lines on the plot. Once a single cycle of the first active section is complete, the voltage of the second active section is incremented slightly, moving the second active section. This process is repeated over the entire range of allowable voltages for the second active section. Utilizing this method, a collection of data points for possible actuations for the active sections for each skin configuration is constructed.

Due to the nature of the hysteresis loop of the MFC active sections, as seen previously in Figure 2.13, the actuation spaces of the various skin configurations is not convex. Determining the total area of the allowable configurations from a finite number of points then required alpha shapes to analyze non-convex planar shapes. A generalization of the convex hull concept, alpha shapes are useful for cluster analysis of points that form non-convex shapes, such as these linked hysteretic active sections, by allowing for the construction of a closed space from a cluster of points [100]. The construction of these alpha shapes allows for the efficient analysis of effects of

the skin on the total range of the active sections. Because the hysteresis curve has concave sides, a negative-alpha shape was used with a characteristic radius on the same order of magnitude as the local range of each active section, i.e. 1 cm. The actuation spaces are then described by the alpha shapes are shown shaded in Figure 2.22. Also, they provide useful metrics for characterizing the actuations without bias from concentration of points within the actuation domain, several of these metrics are detailed in Table 2.4 . The use of alpha shapes could be additionally useful for describing actuator spaces in real-time during experiments, and could be generalized to higher-order spaces associated with more active sections, i.e ailerons.

Table 2.4 Characterization of Skin Tests

Configuration	**Actuation Space**	**Actuation Space Center [2^{nd} , 1^{st}]**	**Total Range [2^{nd} , 1^{st}]**	**Mean Local Range**	**Mean Local Shear**
Baseline value	8.88 cm^2	0.26 cm, -0.26 cm	2.98 cm, 2.98 cm	2.98 cm	2.98 cm
No Skin	100 %	-0.26 cm, -0.26 cm	100%, 100%	100%	0%
Prestressed Silicone	21.8 %	-1.85 cm, -1.94 cm	62.8%, 50.9%	50.2%	27.4 %
Spanning Honeycomb with Wiper	31.9 %	-0.21 cm, -0.21 cm	80.6% , 79.7 %	51.4%	60.7%
Full Honeycomb Free Sides	7.78 %	-0.61 cm, -0.47 cm	40.3% , 29.7 %	31.4%	28.4%
Full Honeycomb Fixed Sides	6.75 %	-0.54 cm ,-0.38 cm	28.2% , 36.8 %	21.0%	34.4%

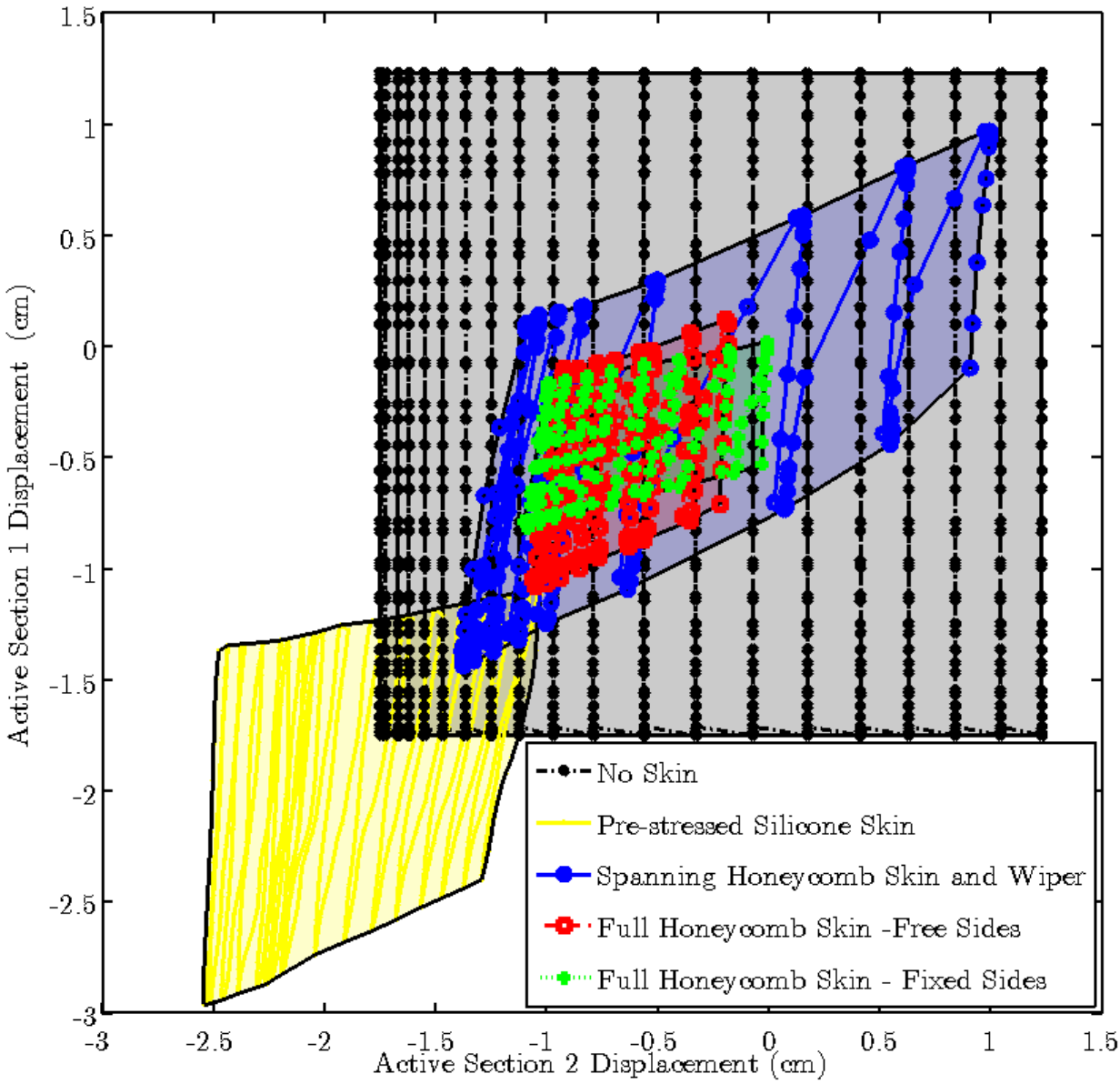

Figure 2.22 Active section ranges for various skin configurations

2.6.1.2. Results

The results relate a complex picture of the effect of the skin on the active sections' ranges and a description of the various metrics from Table 2.4 follows. For purposes of comparison all metrics except for the center of the range have been normalized by the unconstrained configuration's values. The actuator space is defined as the area of the alpha shape constructed by the testing points of the previous configuration. The center of the actuation space is then the centroid of this space. The total ranges are determined by measuring the total projection of the

actuation space onto the respective axes (i.e. the *y* axis for the first active section, and the *x* axis for the second active section). These metrics are useful for determining how the different skin configurations restrict and shift the maximum achievable ranges of the morphing active sections.

The local range, as described previously, was defined in the context of the range of the first active section as the applied voltage of the second active section was held constant. The mean local range was then defined by the mean of the projections of each local range onto the *y* axis. The mean shear was then the mean of the projections of each local range onto the *x* axis, normalized by the *y* axis projection. These metrics are useful for quantitatively assessing the extent to which actuating the first active section affects the positioning of the second active section.

Using these metrics to analyze the various skin configurations, the "no skin" configuration retains all of the range of the active sections, without any shear as no skin connects the two active sections. The pre-stressed silicone skin restricts the total actuation space to only 21% of its unconstrained range. Additionally, the offset on the range due to prestressing the skin results in roughly a 60% offset in range, which shows a major disadvantage in positioning using a prestressed isotropic skin. Compared to the isotropic pre-stressed silicone skin, the spanning honeycomb with wiper allows for the active sections to maintain a significant porition of the unconstrained range while still maintaining the same mean local range without the positioning offset.

Comparing the full honeycomb configurations to the prestressed silicone and wiper configurations shows that this area needs the most improvement to fully realize conformal morphing capabilities. While the spanning honeycomb configuration allows for almost 80% of the original total range, the fully honeycomb configurations are restricted to around 35% of the original range. These configurations also showed less offset due to initial prestress than the silicone configuration.

All configurations showed "shear" in their local ranges as the bottom active section changed position. The meaning of shear is the relative positioning error of one active section when the other's active section was specified. Anotherway to think of this concept is the penalty in positioning if closed-loop controllers are not used. Shear was as high as 60% for the spanning

honeycomb configuration, and at least 30% for all other configurations. This result confirms that spanwise morphing restrictions are important in adapting a morphing concept from 2D to 3D and must be considered as the performance of this concept to be properly assessed [88]. Additionally, a positioning sensor with closed-loop control will be necessary for achieving the desired configurations of the test bed concept.

2.6.2. Characterization with aerodynamic loads

The characteristic section was tested at zero degrees angle of attack at various flow speeds ranging from 0 m/s to 20 m/s to identify the relevance of aerodynamic constraints on the representative section. The silicone skin, although pre-stressed, exhibited skin bubbling, as indicated in Figure 2.23, at flow speeds as low as 10 m/s. However, this effect that was not observed by the spanning honeycomb skin at flow speeds up to 20 m/s. Since the wiper configuration was shown to produce actuation ranges nearly double that of the full honeycomb configurations while doubling the achievable flow speeds before bubbling, it was chosen for further investigation of actuation under aerodynamic loading.

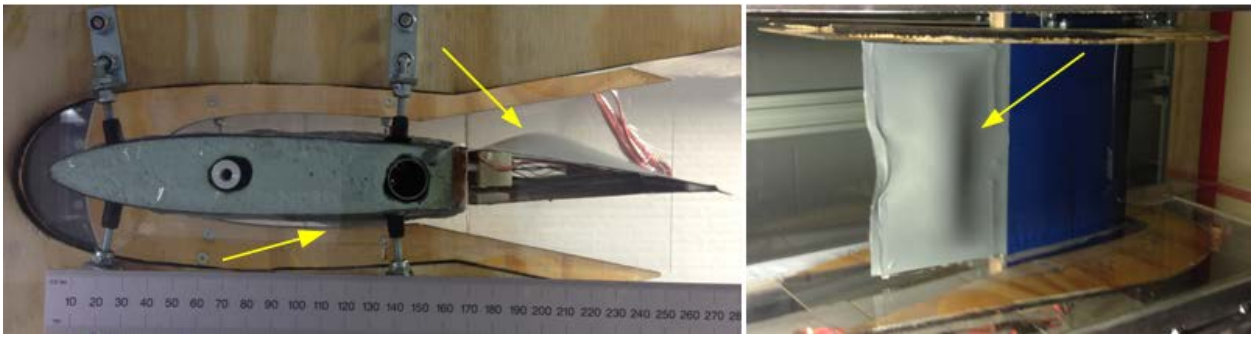

Figure 2.23 Bubbling due to aerodynamic loads for the pre-stressed silicone skin configuration

The following test was used to start to answer how the concept scales as flight speed and aerodynamic loads increase. Using the “Spanning Honeycomb with Wiper” configuration from

the previous section, an initial characterization of the aerodynamic loads on the active sections was performed to determine the flight regimes at which the concept would be feasible. Both active sections were actuated together uniformly from -2kV to 2kV to observe the impact of aerodynamic loads on the range. As seen in Figure 2.24, even for a low angle of attack flight condition, the range of the active sections is reduced to less than half of the unloaded range. Previous work by Bilgen et *al*. reported no significant aeroelastic effects for the cascading bimorph concept without skin for flow speeds of 15 m/s and fan-driven flow speeds as high as 45 m/s [66]. The current results show that as the SMTE concept is developed for higher flow speeds and larger aircraft, the unimorph configuration will not be as capable of resisting aerodynamic forces. Still, there remains a trade-off between design weight, complexity and performance for the active sections, further explored in Chapter 3.

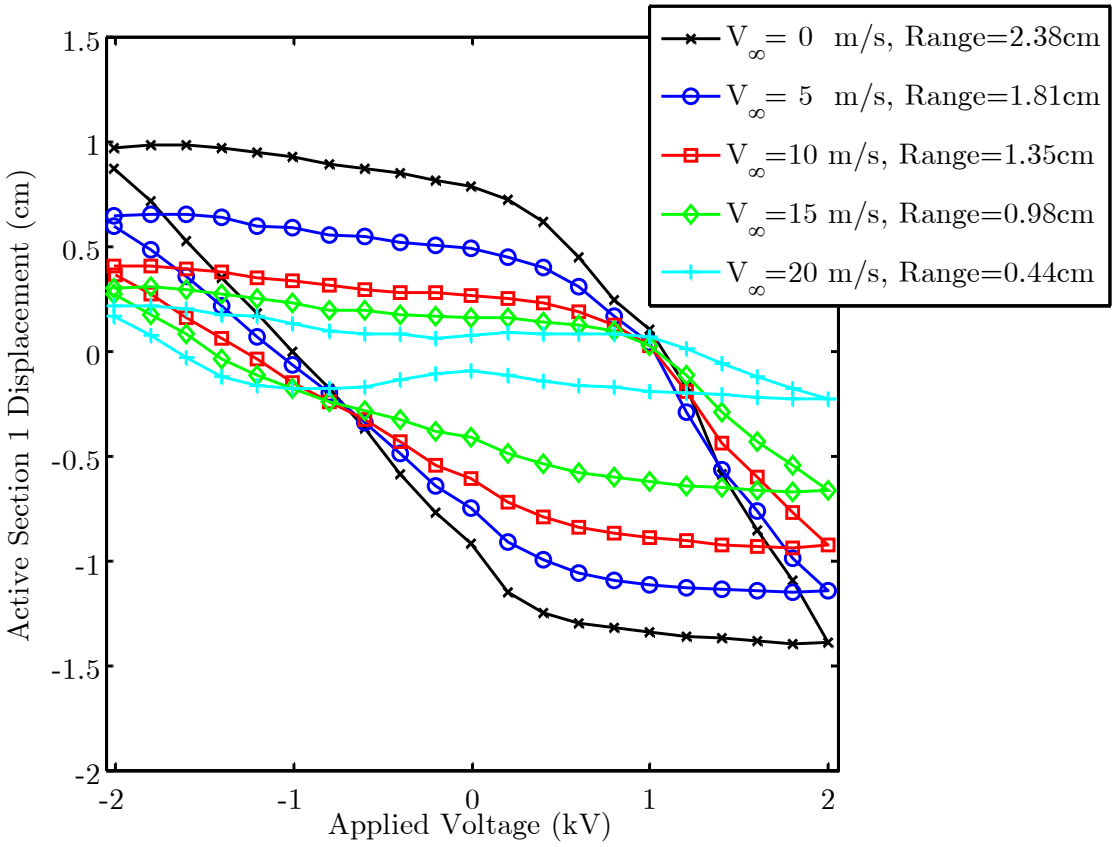

Figure 2.24 Aerodynamic Loading Effect on Section Range with Uniform Actuation

2.7. Conclusions

This chapter detailed the motivation, development and initial characterization of the Spanwise Morphing Trailing Edge (SMTE) concept. The purpose of this concept was to investigate the potential aerodynamic advantages of eliminating surface discontinuities for a spanwise-variable camber morphing concept for a representative UAV wing, specifically targeting Low-Altitude and Medium-Altitude Long Endurance (LALE and MALE) aircraft.

A modular concept consisting of alternating active and passive sections was developed for implementation in a test bed wing typical of this scale of aircraft. The internal structure of the modular active section concept was developed using MFCs compliant mechasisms printed using a multi-material 3D printer that allowed for elastomeric as well as rigid material to be precisely constructed together. The development of the flexure box concept showed improved performance in actuation range due to added freedom in the active section. The expected aerodynamic performance of this active section in two-dimensional flow was modeled and compared to previously-published thin-airfoil results, motivating the further investigation provided in the following chapters. An integrated elastomeric honeycomb skin with tailored stiffness was also built using the same multi-material 3D printer. Using a representative section of the test bed, the impact of several different boundary conditions for the honeycomb skin on actuation capabilities were tested and compared with a pre-stressed isotropic silicone skin. Alpha shapes were used to describe the non-convex actuation space from the experimental results and compare the effects of the skin on actuation range. The wiper configuration of the honeycomb skin was able to maintain the same range as the pre-stressed isotropic skin while doubling the effective control velocity by suppressing bubbling.

The impact of the work in this chapter was focused primarily on developing the relevant actuation mechanism and structural configuration to investigate the SMTE concept. Novel use of 3D-printed elastomeric materials were used to create hingeless morphing active sections and anisotropic honeycomb-reinforced skin. The hingeless active sections were used to reduce friction and relevant positioning errors. The honeycomb skin was used to suppress bubbling due to aerodynamic loading without restricting actuation range. In the process, novel use of alpha shapes to characterize the actuation space for a representative section was performed. Also a dramatic reduction in control effectiveness due to aerodynamic loading was characterized. This

represents the first stages and motivation for characterizing aeroelastic performance of this morphing active section. These results and methods, specifically the parametric construction of anisotropic elastomeric skins and their characterization in a morphing airfoil design should be relevant for other morphing concepts.

Chapter 3
Scaled Aspect Ratio Testing of the Flexure Box Morphing Aileron

The previous chapter showed several interesting results about the Flexure Box aileron, the modular solid-state actuation mechanism that functioned as the active section in the Spanwise Morphing Trailing Edge (SMTE) concept. The initial characterization tests of the active section under aerodynamic loads were limited in order to reduce experimental complexity. Specifically, the active section was integrated into a representative section of the SMTE test bed and only the out-of plane displacements of the trailing edge at were measured for a single angle of attack at varying flow speeds. The test identified that flow speeds of at least 20 m/s could degrade the actuation of the Flexure Box aileron as integrated in the SMTE test bed by up to 80% as compared to no aerodynamic loads. This test began to answer the question regarding the scalability of the design for higher flow speeds and loading conditions. Still, questions remained about the performance of the active section in isolation: how does the Flexure Box aileron perform at various angles of attack, what portion of the performance in the active section is lost to aeroelastic effects, and how are these issues related to the mass, stiffness, and power consumption of the concept. Thus, a more thorough analysis was needed to identify the scalability of the actuator, isolated from the design choices of the skin.

This chapter sought to address these issues by investigating a single topic: the scalability of the Flexure Box morphing airfoil concept. Here scalability was taken to mean the ability to affect aerodynamic control forces at increased flow velocities. The chapter addressed this topic by quantifying the comparative performance of two morphing concepts that vary only in the amount of smart material used. By increasining the amount of active material, the stiffness, mass, and total material contributing to actuation increased, but it was desired to determine if

performance increased, and under what conditions.The analysis of these two concepts then provided valuable design information for the active section about the trade-offs between mass, power consumption, complexity, and performance by means of trailing edge displacement and aerodynamic loads.

The organization and contributions of this chapter were then arranged in the following manner. First, an experimental investigation for a reduced span test article quantified the performance of the MFC-driven morphing concept, the Flexure Box aileron, where the MFC is varied between two and four. The intuitive assumption was that increasing the amount of smart material that acted as an actuation mechanism would also increase performance. Contrary to this intutition, for some lower flow speeds, reduced use of smart material was shown to improve performance, namely the ability to affect lift. To reach this conclusion, a novel experimental setup was devised that allowed comparision of aerodynamic forces for a reduced-span test article. This setup allowed for two morphing concepts to be experimentally compared without producing large-scale test articles that would use more smart materials. This test thus reduced the complexity and cost of the test articles that used for the comparative analysis. A method for extrapolating the change in lift and tip displacements from this test utilizing a rigid non-morphing concept to an infinite-span wing was created. The results of this extrapolation were then experimentally confirmed with a larger-span test article. The results allowed for a realistic predictioin of the performance of the two concepts for an infinite-span wing and could be utilized to quickly compare flexible morphing concepts under aerodynamic loading.

3.1. Comparative morphing airfoil test

This section detailed a design study on the number of MFC patches, i.e. two or four, in the Flexure Box concept to investigate their impact on mass, power, and aerodynamic control. The two and four MFC configurations, detailed further in the following section as “unimorph” and bimorph respectively, were common configurations for utilizing an MFC in bending. To aid in the comparison of these two configurations an embedded sensor and closed-loop control of the smart material trailing edge was demonstrated. The sensor and controller were utilized in reduced-span, i.e. low aspect ratio, wind tunnel tests to evaluate the capabilities of the actuators.

3.1.1. Description of study

Previous studies on other morphing concepts that used MFCs to morph a small UAV wing have investigated aerodynamic forces, power consumption, weight, and the ability of a morphing concept to hold its shape under aerodynamic loading as compared to conventional servo-driven ailerons [85]. In a similar manner the current work sought to experimentally evaluate the design impact of additional MFCs in the Flexure Box aileron, using the metrics stated here.

Specifically, the study focuses on the impact of choosing the "unimorph" vs the "bimorph" configuration for the Flexure Box aileron. As mentioned in Section 2.4, the basic unit of bending actuation is a single MFC patch bonded to the thin steel substrate, which is referred to as a unimorph. A bimorph in this context is then defined as two MFC patches bonded to either side of the thin steel substrate. The two configurations under investigation were defined by the basic active unit of their constructions. More explicitly, the unimorph configuration of the Flexure Box concept was constructed utilizing two unimorphs for a total of 2 MFCs and the bimorph configuration was constructed utilizing two bimorphs for a total of 4 MFCs. Figure 2.10 detailed the exact location and construction of both versions of the Flexure Box.

To understand the reasoning for selecting these specific configurations, the operation of the actuation mechanism was described. An MFC patch was actuated via high voltage applied via interdigitated electrodes which induced an electric field within the patch. The electric field was transduced into stress by the embedded fibers via the direct piezoelectric effect. The resultant stress could place the fibers in tension or compression depending on the sign of the voltage. If unbonded to any substrate, the MFC patch would not bend, but merely elongate or contract as the fibers worked against the inherent stiffness of the inactive components of the patch. Such a structure would not make an ideal conformal morphing surface. When bonded to a thin, stiff substrate, the mismatch in elastic modulus with the MFC under actuation resulted in bending. Similarly, if the MFC patch was bonded to another MFC patch and both were opposingly actuated, the resultant structure would bend. These bending actuation configurations have commonly been described as unimorphs and bimorphs, respectively. The only modification to the bimorph configuration was the steel shim included between the two MFCs for ease of construction and continuity with the other components of the morphing aileron. Because the

shim was very thin and located near the expected neutral axis of the bending configuration, it was assumed that this design choice had little impact on the resulting actuation.

The choice of the thin stainless steel substrate was motivated by previous results by Bilgen [101]. Cantilevered beam analysis was used to show a thin substrate of approximately 10% thickness relative to the MFC would maximize the quasi-static tip displacement. The intuitive explanation for this result was balance of locating the MFC far from the neutral axis of the beam while minimizing the quantity of inactive material strained. The balance between those two features in an asymmetric beam resulted in an optimal distribution. The bimorph case was not considered in that analysis, but Euler beam theory could intuitively be used to verify that the tip displacement of the bimorph would be maximized when the substrate thickness was minimized [102].

An important caveat of MFC voltage actuation was that asymmetric voltage application was necessary to operate the opposing MFC patches. The advised limits from Smart Material Corporation for the negative and positive applied voltages to an MFC were -500V and +1500V, respectively [64]. The restriction on the negative voltage range restricted the brittle piezoelectric ceramic fibers from compressively fracturing during actuation. The entire voltage range, up to these limits, has commonly been used throughout literature to maximize the strain and displacement of MFCs used as actuation mechanisms [62]. Thus opposing MFCs often used asymmetric voltages when actuated together. Because the MFCs were installed on the inside of the aileron in the unimorph configuration, those two MFCs were opposing actuators with asymmetric voltage requirements. In a similar manner, each bimorph was actuated as opposing MFCs in an antagonistic manner. A common method for addressing this asymmetric requirement was to create a high voltage circuit that proportionally applied the voltage in a three-to-one ratio between the opposing actuators. That same methodology was utilized in this study. Regardless of the voltage application ratio between opposing MFCs, the asymmetric limits of the actuation voltage should be noted as inherent to the piezoelectric material used.

The Flexure Box aileron was sized according to the widest available MFC from Smart Material Corporation, the M8557-P1. For simplicity, the same scale MFC and flexure box were also used in this comparison. This sizing consideration also permitted direct characterization of the two-dimensional characteristics of the active sections in the SMTE, and reuse of components

during future tests. A diagram of the design of both configurations is shown in Figure 3.1and as assembled in Figure 3.2. The study examined the mass of these concepts, their actuation ranges, average power consumption and ability to influence aerodynamic loads in a wind tunnel. The work also detailed the development and implementation of an embedded sensor to control the actuations of the aileron under aerodynamic loads.

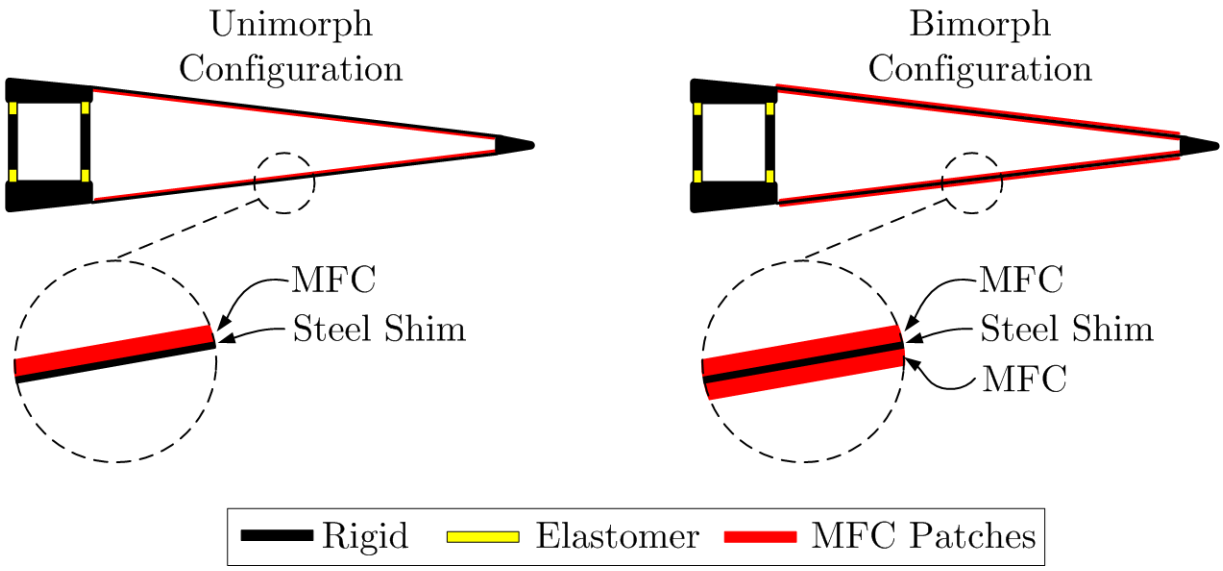

Figure 3.1 Diagram of Flexure Box ailerons as “unimorph” and “bimorph” configurations

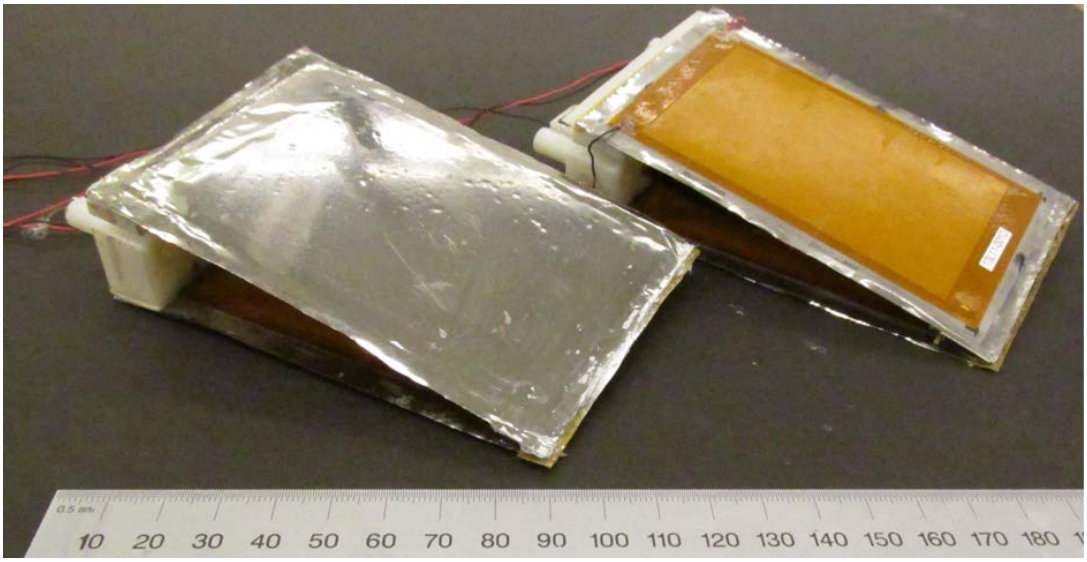

Figure 3.2 Assembled (left) unimorph and (right) bimorph configurations

3.1.2. Control surface design and characterization

The following section detailed the development, construction and characterization of the two flexure box aileron configurations: “unimorph” and “bimorph” for performance comparison under aerodynamic loads.

3.1.2.1. Active section design

In accordance with the SMTE test bed scale from Section 2.3, the Flexure Box ailerons were constructed for a NACA 0012 airfoil with 304.8 mm chord and a rear spar located at 180mm. A diagram of the overall airfoil is shown in Figure 3.3. The flexure box is mounted 1.27 cm aft of the rear spar so to prevent interference as the flexure box which shifted its upper rigid section slightly chordwise during actuation due to the elastomeric flexures. Also in the diagram are the sensors which will be detailed in Section 3.1.2.2. Per the scale of the SMTE active section, the span of each active section was 7.62 cm.

Following previously established construction methodology, the inactive components were constructed using the Objet Connex 500 3D Printer at the University of Michigan Medical Innovation Center Design and Prototype Lab. The multimaterial 3D printer allowed for both rigid plastic and compliant elastomer to be printed in the same part. This manufacturing process was used to improve the reproducibility while precisely tailoring the compliance and dimensions of the flexure box under actuation [82]. The elastomeric hinges also eliminated friction and improve wear over conventional hinges and add the possibility of stiffness tailoring.

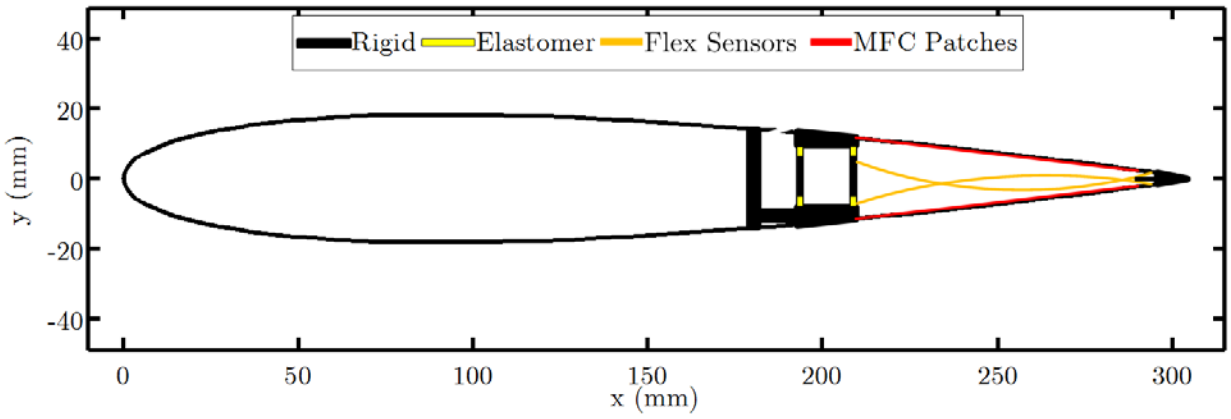

Figure 3.3 Diagram of airfoil cross section with embedded sensors

The sizing of the structural components of the Flexure Box aileron was driven by the results of the initial aerodynamic loading test from the previous chapter. This test revealed significant buckling in the full length elastomeric flexure and previously unreported reduction in actuation range due to aerodynamic loading. To isolate the effect of just the MFCs on the design, it was desired to eliminate the potential for buckling while still maintaining improvement over the previous hinged design. Aided by simultaneous investigation by aeroelastic simulations that will be further covered in Section 6.3.2, the elastomeric flexure was chosen to be approximately 2 mm tall which provided sufficient compliance under actuation while while reducing the likelihood of buckling [103]. The material selected for the hinge was TangoPlus, a rubber-like material with Shore 27A hardness [104]. The spanwise width was prescribed per the width of the active section of the SMTE concept as 25.4 mm.

Views of the design for the flexure box are shown in Figure 3.4 with a reference scale of 5 cm. The updated design contained several improvements over the previous concept including: reduced mass, a notch in the upper surface for simplistic incorporation of the wiper mechanism, and centralized mounting. The design also included spacers as stand-offs from the rear spar of the wing as well as mounts for integrated sensors, detailed in the following section.

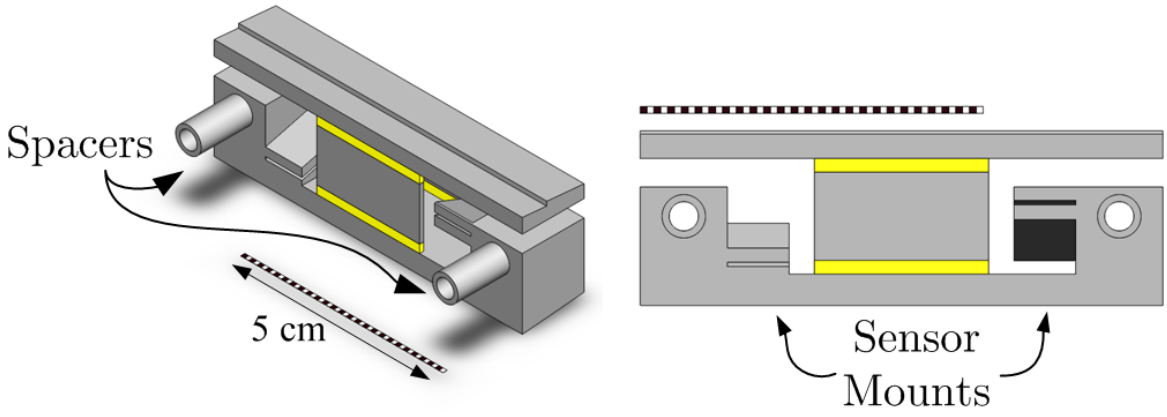

Figure 3.4 Isometric and frontal view of the compliant mechanism in the flexure box

To complete the construction of each configuration, the active components (either unimorph or bimorph depending on the configuration) were bonded to the top and bottom of the compliant mechanism to form the front of the Flexure Box aileron. Thin, flexible wires controlling the MFCs ran internally from the trailing edge to the front of the aileron. In the "bimorph" configuration additional flexible wires ran from the electrodes on the outer surface of the MFCs, visible in Figure 3.2, and were bonded to the flexure box with slack so as not to impact actuation. The trailing edge of the aileron was formed by bonding the active components to an additively manufactured trailing edge.

3.1.2.2. Sensor selection and design

In the previous chapter, the Flexure Box aileron's performance was modeled or measured without embedded sensing or closed-loop control of actuator's state. The MFCs used to actuate the flexure box experience nonlinear effects including creep and hysteresis in large-scale actuation. Hysteresis, specifically, in the MFC actuators used has been shown to interfere with the controllability of flight test models due to the inability to assess the state of the morphing aileron, leading to catastrophic failures [80]. Integration of this active section into complex morphing techniques such as the SMTE concepts required precise positional control of the actuators.

Previous work has shown that hysteresis and creep for these actuators could be addressed through models or precisely addressed via closed loop control with an added sensor [61,62]. Significant efforts have been made in the past to compensate for hysteresis via feed-forward control as well as in an open-loop manner by training an inverse hysteresis operator to effectively predict the positional state of the MFCs for a known input voltage [85]. These methods required conditions on the actuator under training to be similar to the expected loading and still require a complex system model. Due to the previous results for the aileron showing aerodynamic loading to significantly affect the actuation range of the active section, it was determined that closed-loop control would be necessary under aerodynamic loads.

Aerodynamic modelling of the Flexure Box aileron, covered in Chapter 5, showed that the Flexure Box aileron tip deflection could be an adequate indicator of structural state of the Flexure Box aileron, even under aerodynamic loads. Accordingly, it was desired that the sensor measure the tip displacement of the Flexure Box. Still, the sensor requirements were stringent.

The sensor needed to adequately asses the state of the Flexure Box aileron under a wide range of aerodynamic loads without restricting actuation. Additionally, the sensor would need to provide accurate positional information regardless of the orientation of the test article (i.e. angle of attack for two dimensions). The high voltage applied to the MFCs also needed to be effectively isolated from the sensor. For systems-level consideration and reduction of complexity, the sizing, mass and power requirements also needed to be small relative to the previous sensor-free design.

An external sensor was considered for the ailerons as the previously-mentioned laser displacement sensors can provide highly accurate displacements in real time. The use of the laser displacement sensor posed several practical implementation problems. Most significantly, the laser would need to track the orientation of the test article as it was moved through angles of attack, necessitating a complex tracking system that could interfere with measurements from the load cell. Additionally, the presence of the laser displacement sensors or any other external sensor near the wing could interfere with the aerodynamics and would represent an impractical solution for a realistic implementation of the design in a UAV due to weight and complexity. An external sensor, by means of a motion capture system, was eventually used to independently measure positional data for the SMTE test bed, but it was not available at this point in the research.

An embedded positional sensor was determined as an efficient method to provide real-time positional data about the active section without complex system models or external sensors. The embedded sensor had the additional benefit that it could be used during flight. The modular design of the Flexure Box aileron permitted the design of a single sensor that could then be repeated for both the unimorph and bimorph configurations.

Initial studies into possible candidates for the embedded sensor including miniature Linear Variable Differential Transformers (LVDT) per the Smart Wing test and variable resistors [17]. The displacement range, mass constraints, and spatial constraints of the interior of the Flexure Box were considered along with secondary motivations such as cost and reliability. It was determined that the LVDT sensors would provide the most accurate measurement over the range, but posed significant integration challenges with respect to sizing, mass, and cost. The primary concern in using an LVDT was the size integration. The range of the sensor needed to be at least 3 cm to adequately capture the range of the aileron. To accommodate the sliding core of

the LVDT, interference with the rear spar mounting location and the flexure mechanism. For example, the appropriately scaled DC-EC 1000 LVDT from Measurement Specialties had a main body length of nearly 20 cm, nearly 60% longer than the entire Flexure Box aileron. The Smart Wing program accommodated the size requirements of the LVDTs by mounting them forward of the aft spar [105]. Since it was desired to create a modular morphing aileron per the design criteria, components external to the aileron were undesirable. Per this sizing consideration, it was concluded that LVDTs would only represent a viable measurement option for non-modular designs, currently outside the scope of this work. Accordingly an alternative, integrated sensor option was desired that eliminate the long stroke core which violated the sizing constraints of the modular design.

The sizing constraint for the aileron was met by seeking a sensor that measured the bending of the aileron by a method other than linear stroke. The Spectra Symbol Flex Sensor was thus chosen as a method for embedded sensing of the trailing edge position, shown unflexed, normal to the plane of bending in Figure 3.5. The flex sensors were highly-flexible, low mass, uni-directional variable resistors that changed resistance under bending. By covering the flex sensors in Kapton electrical tape, they were effectively insulated from the high voltage used to actuate the MFCs. The sensors were implemented into a half Wheatstone bridge powered by a 5 Volt supply, converted to +15V to -15V potential across the resistors by a muRata NKA0515SC DC-DC converter. The output was tuned via potentiometer and the difference in the nodes of the bridge was amplified via a INA128P instrumentation amplifier. The bridge, dc-dc converter, and instrumentation amplifer were mounted on a solderable breadboard that was stored internal to the airfoil. The average power consumption of the total sensor was approximately 0.3 Watts, but could be tuned according to the applied voltage and instrumentation amplifier. The two flex sensors per aileron weighed only approximately 1 gram.

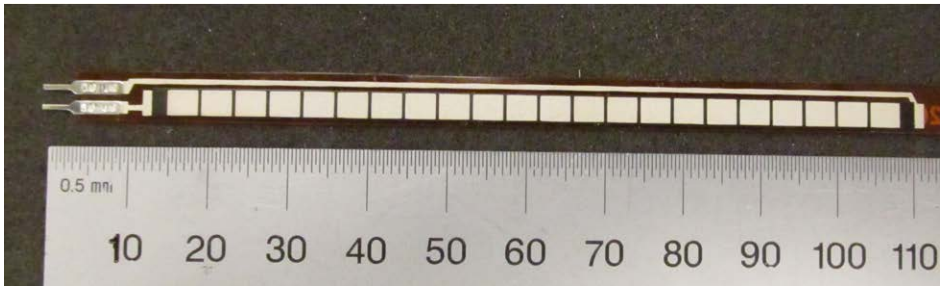

Figure 3.5 Flex sensor used for positional control of Flexure Box aileron

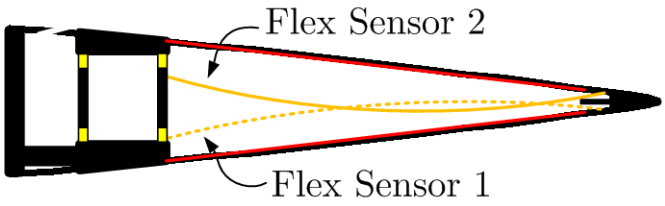

Figure 3.6 Flex sensor used for positional control of Flexure Box aileron

The two sensors were mounted in a prestrained configuration shown in Figure 3.6 to maintain a constant state of uni-directional bending. Through slots at preset angles, shown in the flexure box diagram in Figure 3.4, the sensors were installed in a constantly-flexed antagonistic fashion, as presented in the airfoil cross section in Figure 3.6 to maintain functionality at all actuation states. The tips of the flex sensors slid slightly along a small plastic piece designed to protrude internally from the trailing edge, which followed the tip deflection of the aileron. This mounting configuration allowed for the individual sensors to be removed or replaced as needed. By doing so, no measurable effect on the actuation range of the sensor was noted. The result was an integrated, tunable, high gain, analog, embedded sensor that could be calibrated to measure the tip deflection of the aileron without impacting the operation of the flexure box aileron, meeting the aforementioned requirements.

3.1.2.3. Characterization of control surface stiffness

After the Flexure box aileron was constructed with installed flex sensors, it was desired to measure the comparative stiffness of the unimorph and bimorph concepts. From aerodynamic simulations, presented in Section 6.3.1, tip displacement had identified as a suitable identifier of aerodynamic control effectiveness. Then to provide an initial characterization of the unimorph and bimorph configurations' susceptibility to aerodynamic loading, the response of the two configurations to a vertical line load was tested.

A diagram of the characterization setup was presented in Figure 3.7. The Flexure Box aileron was fixed at its mounting location to a representative spar. A 1 mm thick nylon line was temporarily adhered to the trailing edge through which calibrated masses were applied as a tip load. A Keyence LKG-402 laser displacement sensor tracked the displacement of the flexure box at a known location near the tip (120 mm aft chordwise of the rear spar). A camera was used to

track displacement for image correlation of the laser displacement sensor to the tip displacement, δ_{tip}, of the aileron. For the characterization of the effect of the flex sensors on the overall stiffness of the morphing concept, the test was performed with and without the sensors. No appreciable difference in the stiffness was detected between the two results

The correlation between tip line load and tip displacement is shown in Figure 3.8. Although largely linear when loaded upward, nonlinear effects occur in downward loading due to large movement of the flexure box. The linear stiffness approximation about zero tip displacements were calculated from the experimental data and the approximate unit two-dimensional stiffness of the two concepts were 6.48 N/cm and 9.78 N/cm for the unimorph and bimorph, respectively. The compliance of the elastomeric flexure box made the overall stiffness of the systems more comparable than if rigid boundary conditions had been used and the stiffness of the bimorph concept to tip loading is only 50.8% more than that of the unimorph.

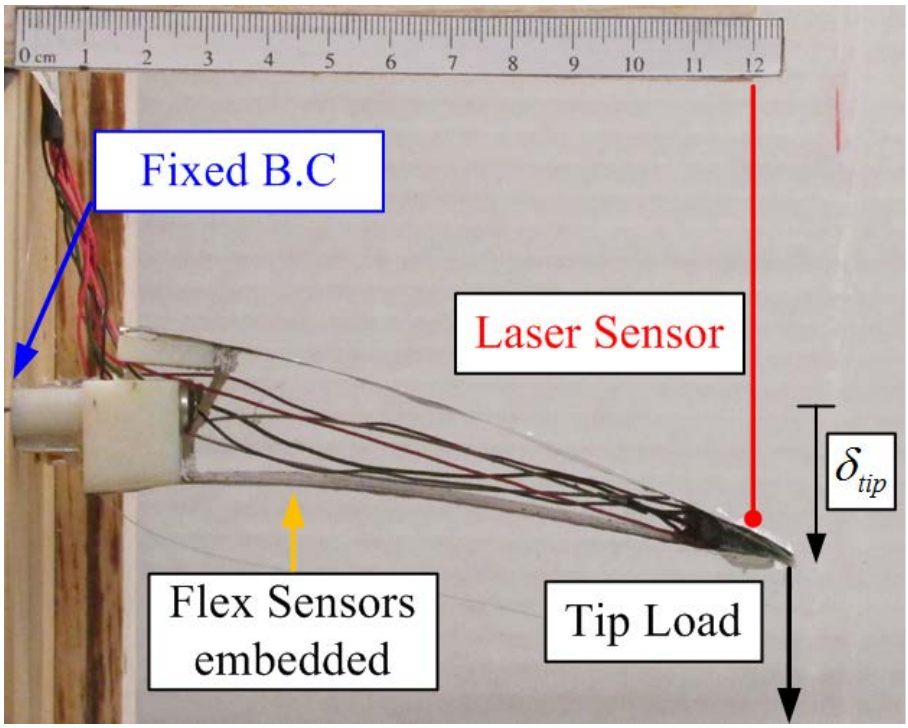

Figure 3.7 Flexure Box characterization diagram

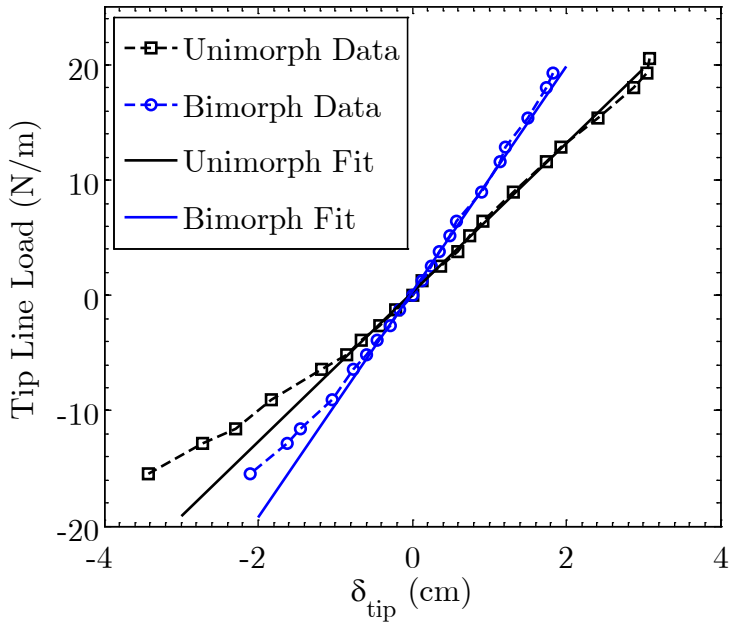

Figure 3.8 Actuator stiffness comparison

3.1.2.4. Calibration of sensors

Although the flex sensors met the sizing, mass and power constraints of the modular design, they were not absolute position sensors, like the LVDTs. To calibrate the sensors through the actuation range, the experimental setup from the stiffness characterization was used, albeit actuated by the MFCs rather than a tip line load. This method automated the calibration as it did not require calibrated masses and it also ensured that no leakage current due to the high voltage MFCs was present.

The previous tip loading tests were used to create a relationship between tip displacement and the laser displacement sensor. This relationship allowed the laser to measure the actual nonlinear tip displacement without repeated image calibration. The laser displacement sensor was then used to calibrate the embedded sensor by tracking the relationship between tip displacement and sensor output over several actuation cycles.

As mentioned in Section 3.1.1, the applied voltage range was asymmetric, ranging from -0.5 kV to 1.5 kV. A high voltage driver board was used to apply the appropriate voltages in a 3:-1 ratio. For example, in the unimorph configuration, when one unimorph was actuated to bend upward with 1.2 kV, the other unimorph was actuated to bend upward with -0.4 kV. A normalized actuation voltage range was then used to represent the normalized actuation range so that -1 results in full downward tip deflection and +1 results in full upward tip deflection.

A representative calibration cycle for the unimorph configuration, presented in Figure 3.9, illustrated the results for normalized actuation voltage, displacement measured by the laser (δ_{laser}) and the sensor output in volts. The calibration curves were formed by discretizing the actuation voltage actuation domain into 21 levels, actuating to each level for 2 complete cycles and averaging the output from both sensors for four seconds at each level. Although both the laser and flex sensors show that tracking actuation voltage results in significant hysteresis, the correlation between the two sensors show that the sensor reduces the effect of hysteresis on tip displacement so that the tip position can be defined with an accuracy of approximately 5% of the total range. The fit presented in the image was a third order polynomial, but an R-squared value of 0.98 was also possible with a simple linear fit. Thus, the calibration, if restricted close to the expected range could utilize the higher order polynomial fit. If the deflections outside this domain were measured, the linear fit is recommended with slightly decreased accuracy.

With a calibrated embedded sensor that could effectively measure the tip displacement, a simple closed-loop PID controller was implemented to compensate for hysteresis and creep during the wind tunnel test. Rather than discretizing the voltage domain, which is prone to hysteresis and creep, the controller allowed for the experiment to discretize the tip displacement domain which was assumed to provide a more accurate assessment of the structural deformation due to aerodynamic loads. An example of the sensor tracking a series of set positions while compensating for hysteresis and creep is detailed in Figure 3.10. In this plot δ_{sensor} signified the position as measured by the sensor and the set point was a series of prescribed positions by an external measurement device, namely a National Instruments DAQ. The various lengths of the set positions reflect the various settling times for the PID control to reach the necessary convergence criteria. A one second pause is taken between each prescribed position to identify any influences due to creep.

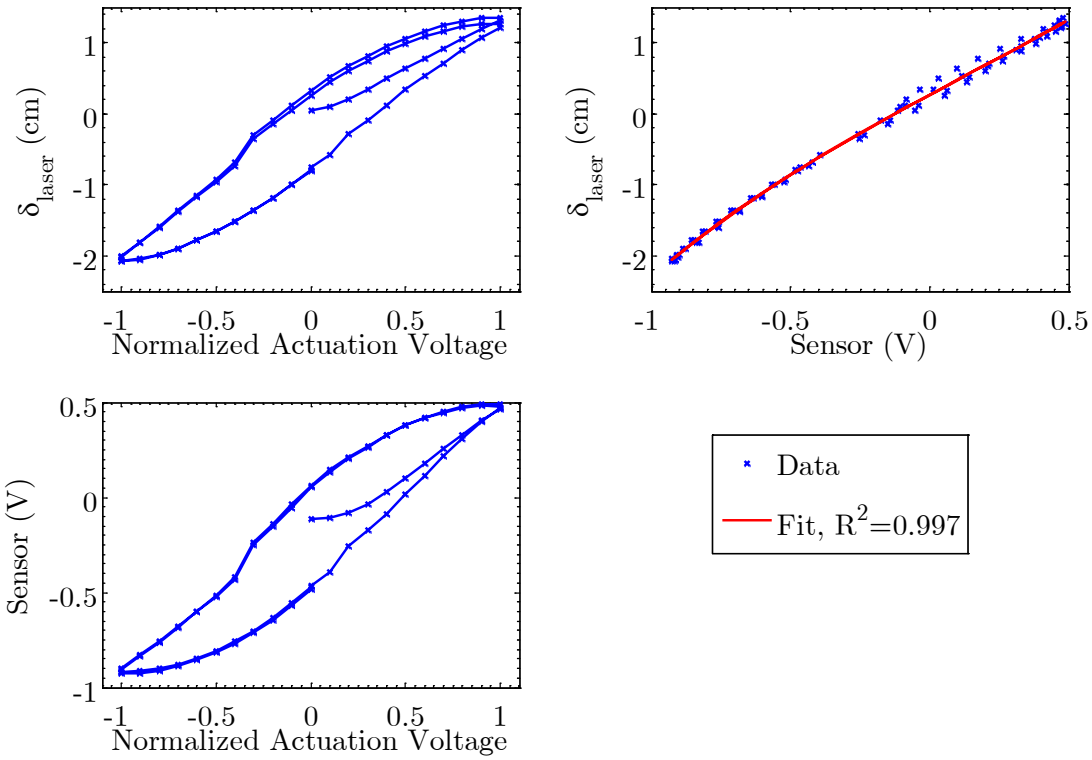

Figure 3.9 Calibration of Sensor vs Laser for Unimorph

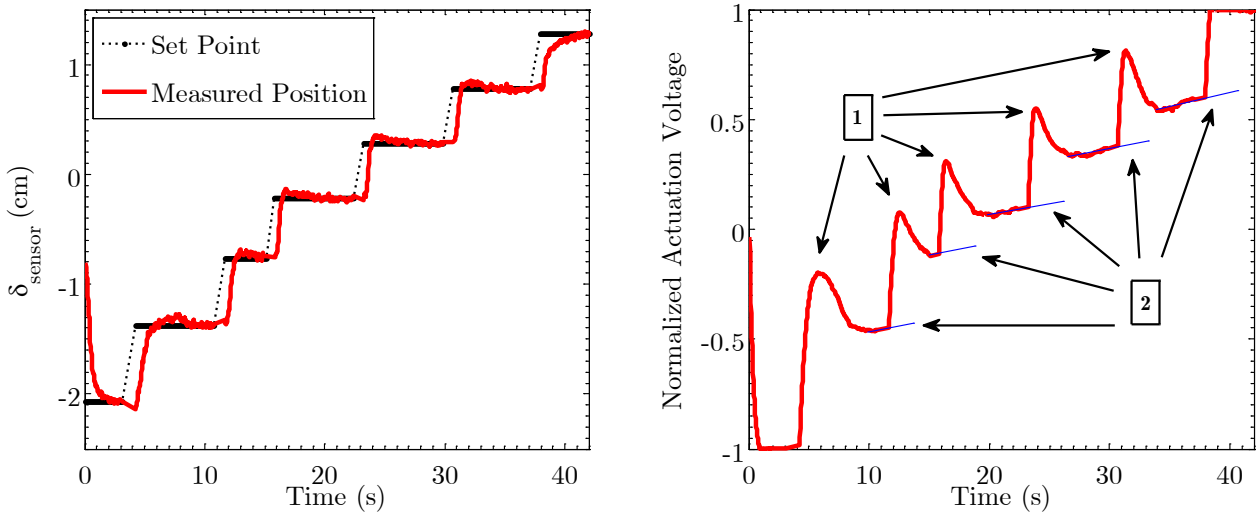

Figure 3.10 PID control with flex sensors

To the authors' best knowledge, this result was the first documented closed-loop control of an MFC-driven morphing aileron using an embedded sensor. Notably, the gains for the PID controller in this example were not tuned for optimal control, but rather for illustrative purposes of meaningful effects to consider.

As was seen by the normalized actuation voltage, the effects due to hysteresis and creep was appreciable. The overshoot in applied actuation voltages, seen marked by box 1 in Figure 3.10 represented the controller effectively adjusting for hysteresis while trying to maintain the active section's position. Over a long timescale, i.e. several seconds, the actuation voltage actually crept slightly as the controller attempted to compensate for creep in the MFCs, as marked by non-horizontal slopes of the long-timescale actuation in box 2.

From these results, it could clearly be seen that even for a two-dimensional MFC morphing concept, specifying actuation state via applied voltage alone would not be sufficient for control. Both hysteresis and creep could lead to positioning errors that would incorrectly specify the state of the actuator. The flex sensors, utilized as part of a closed-loop control system, were shown to effectively compensate for both of these nonlinearities for experimental purposes.

3.1.3. Setup description

With the two active section configurations comparatively characterized and a closed-loop sensor developed, the method for characterizing the aerodynamic performance of the two concepts was developed.

3.1.3.1. Test article

Fundamentally, the two actuation concepts affect only the trailing edge, with their actuation authorities highly dependent on the flow over of the leading edge. To highlight actuation asymmetry while providing comparison with other well documented airfoils, a symmetric NACA 0012 airfoil was chosen for the leading edge. Because the weight and construction of the leading edge is outside the scope of the existing study, the leading edge was constructed using ABS plastic via fused deposition modeling on a Stratsys Dimension Elite 3D printer. Although selecting a suitable skin for morphing applications has posed significant

challenges for implementation in the past [54], a sliding interface (wiper), was chosen as the least restrictive option that would simplify the comparison analysis of the two configurations.

As previously mentioned, a highly reduced aspect ratio was desired to reduce both the complexity of the test articles and the quantity of smart material used for the experimental test. Initially, an aspect ratio of 0.25 was chosen utilizing only one modular morphing trailing edge. To better approximate two-dimensional flow for this aspect ratio, end plates were attached to the test article to limit spanwise airflow around the edges of the airfoil. Each end plate was constructed from a 2.5 mm thick sheet of acrylic plastic cut into an ellipse with 45.7 cm major axis oriented chordwise and a 30.5 cm minor axis, sharpened about its leading edge. An elliptical end plate was chosen over a circular endplate to allow the test article to fit into a 1 foot by 1 foot wind tunnel located in the research laboratory. Although the final test was to be performed in a larger wind tunnel, the smaller wind tunnel allowed for other pilot tests to be conducted without reconstructing the setup. The effect of the reduced aspect ratio and end plates on aerodynamic forces was explored further in the following sections.

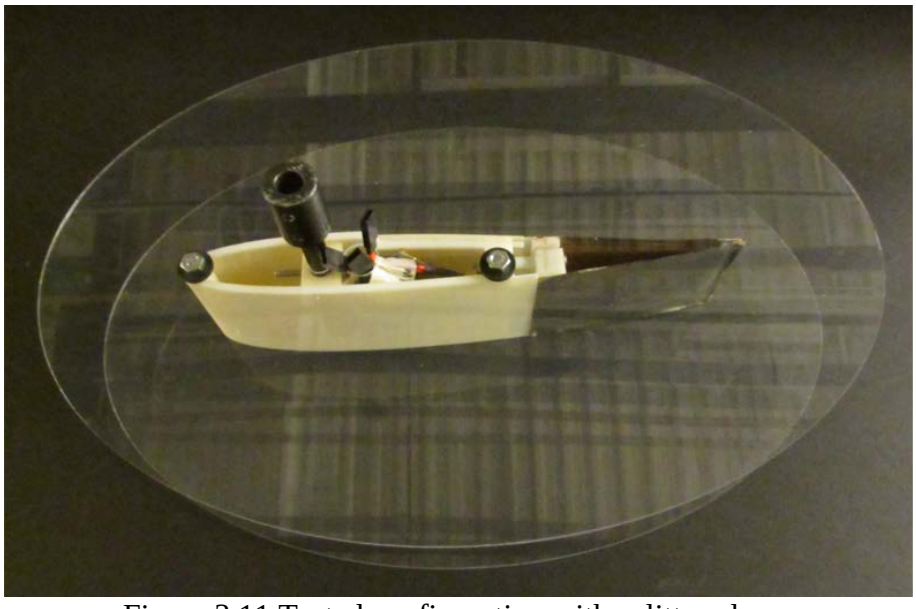

Figure 3.11 Tested configuration with splitter places

3.1.3.2. Test description

The open-loop 2'x2' (60 cm x 60 cm) wind tunnel at the University of Michigan was used to measure the effect of aerodynamic loads on the different configurations. A diagram of the experimental setup is given in Figure 3.12. Three load cells were calibrated to measure the aerodynamic forces on the airfoil. Two load cells were equally spaced in the *x* direction to measure lift in the *z* direction and pitching moment differentially about the *y* axis. A third load cell measured drag in the *x* direction. The airfoil was mounted at its quarter-chord by a stainless steel rod, clamped to a rotary stage. The rotary stage was connected to a stepper motor, providing discrete control over angle of attack accurate to $1/80^{th}$ of a degree via a worm gear drive, was mounted on the force balance table attached to the load cells. A pitot tube was located approximately 2.5 cm from the upper wind tunnel wall approximately 0.5 meters upstream of the airfoil to provide accurate freestream velocity data without influencing flow over the airfoil.

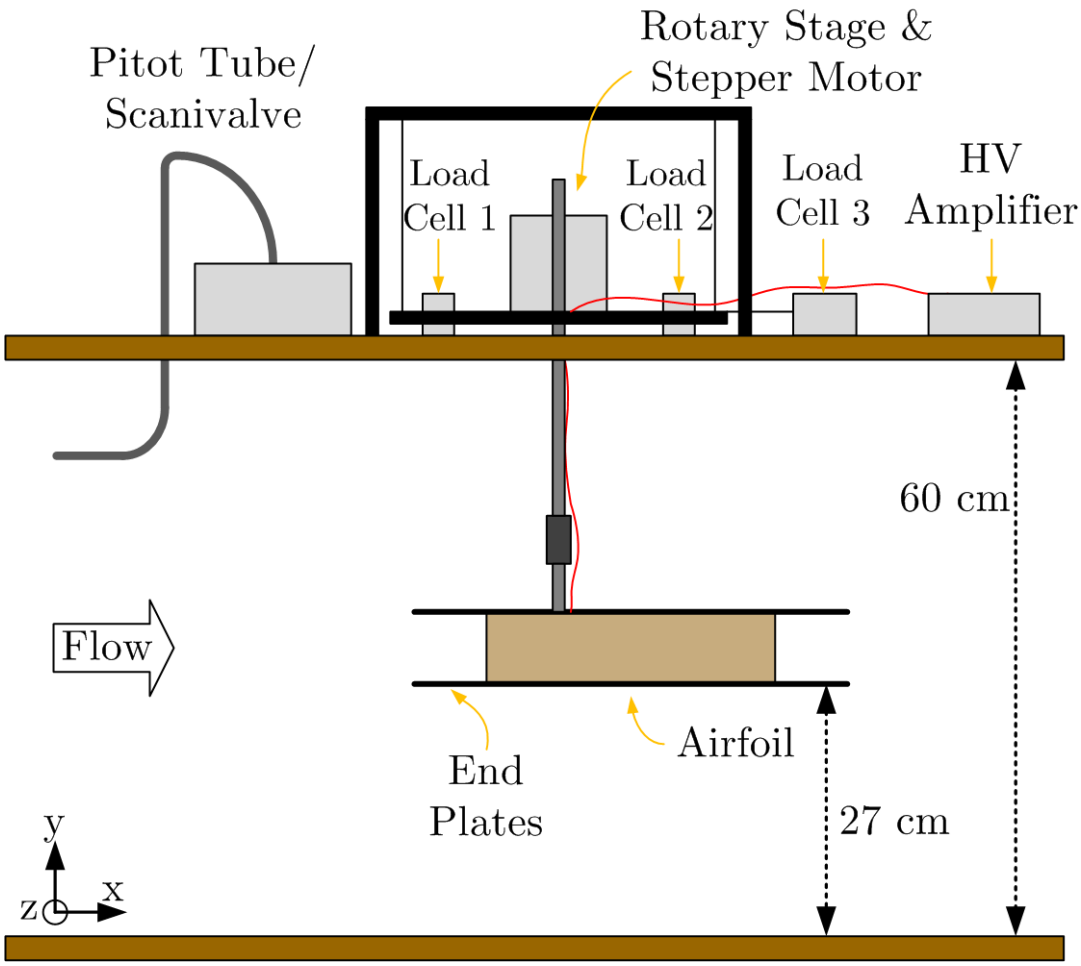

Figure 3.12 Wind tunnel setup for comparative aerodynamic testing

The MFCs of the flexure box aileron were actuated using a high voltage AVID Dual Channel MFC Driver Board. Originally designed to actuate MFCs for small UAVs, the high voltage driver board uses voltages typical of 2-3 Lithium Polymer batteries corresponding to a voltage supply anywhere from 8-12 Volts. For simplicity of power measurement, a 10V supply was used. A custom current monitoring circuit derived from a ratiometric hall-effect linear current sensor the Allegro ACS712, produced an analog output with a ratio of 1 Volts per 0.1 amp consumed by the driver board. Thus an analog output signal could directly relay the power output of the High Voltage driver board with 0.05 Watt accuracy.

The performance of both configurations was investigated over a range of angles of attack and flow speeds to identify the effect of the splitter plate configuration on aerodynamic forces. The flow speeds chosen were 5,10,15, and 20 meters per second representing Reynolds numbers of $1.05x10^5$, $2.11x10^5$, $3.16x10^5$, and $4.22x10^5$ respectively with angles of attack varying from -20 degrees to +20 degrees. For the comparative test of the configurations the displacement domain was discretized into 7 steps and the closed-loop control ensured the actuator remained at each step while the average power and aerodynamic forces were measured. The range of the tip deflections was also recorded utilizing the embedded sensor.

3.1.4. Results

3.1.4.1. Tip deflections

The results from the tip displacements under aerodynamic loads provide an intuitive starting point for the comparative investigation of the two configurations. The range of achievable tip displacements at each flow speed and angle of attack was measured with the embedded flex sensor detailed in Section 3.1.2.2. Shown below in Figures 7a and 7b, the unimorph configuration is seen to exhibit superior tip deflections over the bimorph at 5 and 10 m/s. Although the bimorph has a greater amount of smart material, the MFC patches are actuated asymmetrically due to voltage limitations in compression and add disproportionate stiffness relative to actuation authority in the overall design. As a result, the unimorph achieves a tip deflection range of 4.79 cm at 0 degrees angle of attack and 5 m/s, as opposed to the 4.24 cm tip deflection of the bimorph at the same conditions, nearly 13% more. Both the unimorph and

bimorph experience a reduction in tip deflection with increased flow speed until their ranges have reduced by 53% and 49% at 0 degrees angle of attack and 20 m/s. By 20 m/s the bimorph performs roughly equivalent to the unimorph due to aerodynamic loading.

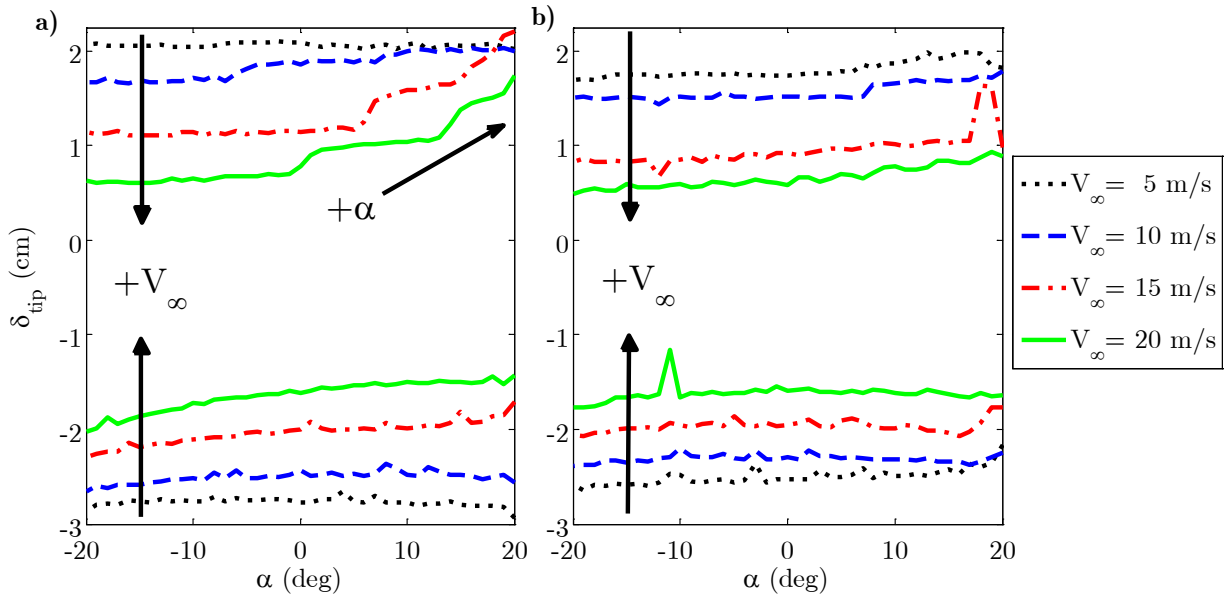

Figure 3.13 Actuation Range for
a) Unimorph and b) Bimorph Configurations

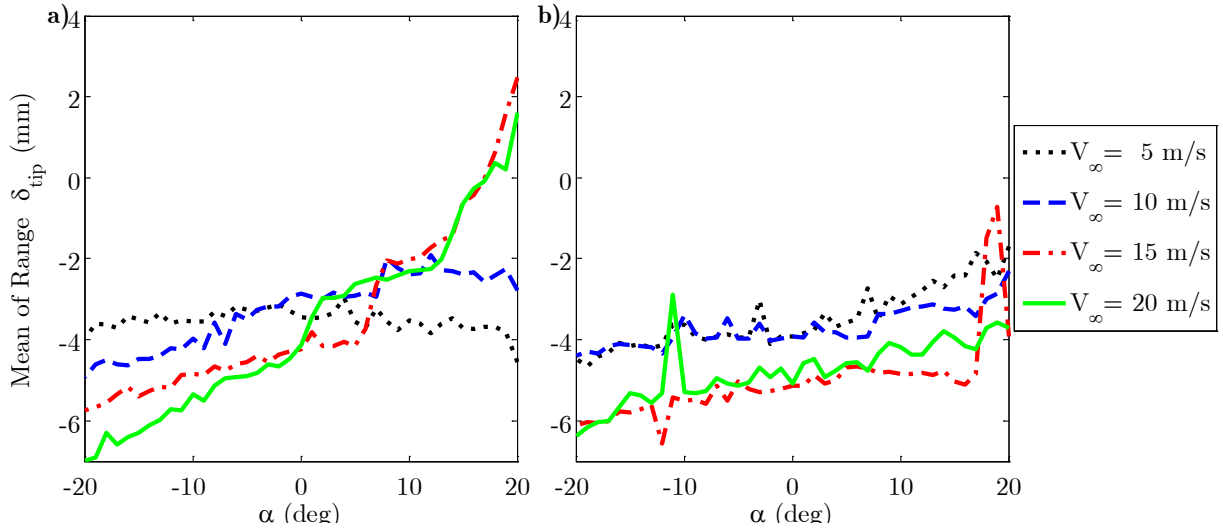

Figure 3.14 Slew in Actuation Range for
a) Unimorph and b) Bimorph Configurations

An interesting result of the tip deflection comparisons is the slew of the mean range for the unimorph configuration due to aerodynamic loads, shown in Figure 3.14. Increasing with flow speed, the slew in displacement range appears to occur for tip-up actuation for positive angles of attack and tip-down actuation for negative angles of attack. The cause of the range slew is due to aerodynamic loads bending the morphing aileron. The tip deflection for high angles of attack (18-20 degrees) for a high flow speed condition (15 m/s) of the unimorph actually causes the actuation to exceed the bounds of a low flow speed case (5m/s).The bimorph configuration also experiences this effect but to a significantly lesser degree. The bounds of the tip displacement range for the unimorph change only 8% at 10 m/s as angle of attack is varied, but that deviation grows to 42% at 15 m/s and 63% at 20 m/s. By 20 m/s the unimorph experienced a nearly 0.85 cm shift in its mean range between -20 degrees and +20 degrees, as opposed to only 0.26 cm shift in the case of the bimorph. Comparatively, the tip displacement of the range of the bimorph changes 9% at 10 m/s, 9% at 15 m/s and 22% at 20 m/s. The cause of this decreased slew is this increased stiffness of the bimorph relative to the unimorph. An example of the differences in deflections due to aerodynamic loading is shown in Figure 3.17. For the purposes of controllability, failure to consider changes in aerodynamic loading due to angle of attack would result in positioning errors greater than 10% for flow speeds greater than 10 m/s for the unimorph and 20 m/s for the bimorph.

a)

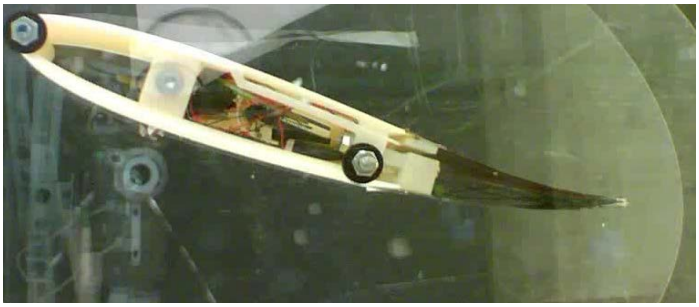

b)

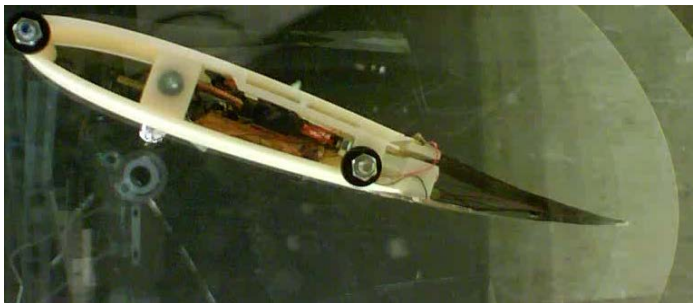

Figure 3.15 Tip deflection at V=20 m/s , alfa = 20 deg, max Actuation for a) Unimorph and b) Bimorph

3.1.4.2. Aerodynamic forces

The nondimensional forces for the various actuations were also measured at each flight condition. Examining the difference between these maximum and minimum values reveals the authority of the respective actuators in each flight condition. Examining the difference between these maximum and minimum values of each of the forces reveals the authority of the respective actuators in each flight condition. Figure 8 shows the difference between the maximum and minimum values at each configuration. For both configurations, the range of achievable influence on nondimensional forces decreases at every angle of attack with increasing flow speed due to aeroelastic loading restricting actuation. The maximum influence over lift and pitching moment for every flow speed occurs at zero angle of attack where flow separation is minimal, and the forces normal to the aileron are relatively low. However, the influence of drag is greater at increased angle of attack as the ailerons can influence flow separation. Both actuators show asymmetric authority with decreased authority when stall occurs, almost at 20 degrees angle of attack.

Comparatively, the forces show that the less stiff unimorph exhibits superior flow control for speeds up to 15 m/s. At 20 m/s the influences on nondimensional forces are approximately equal. However, for the maximum speeds under study the forces were largely comparable between the two actuators.

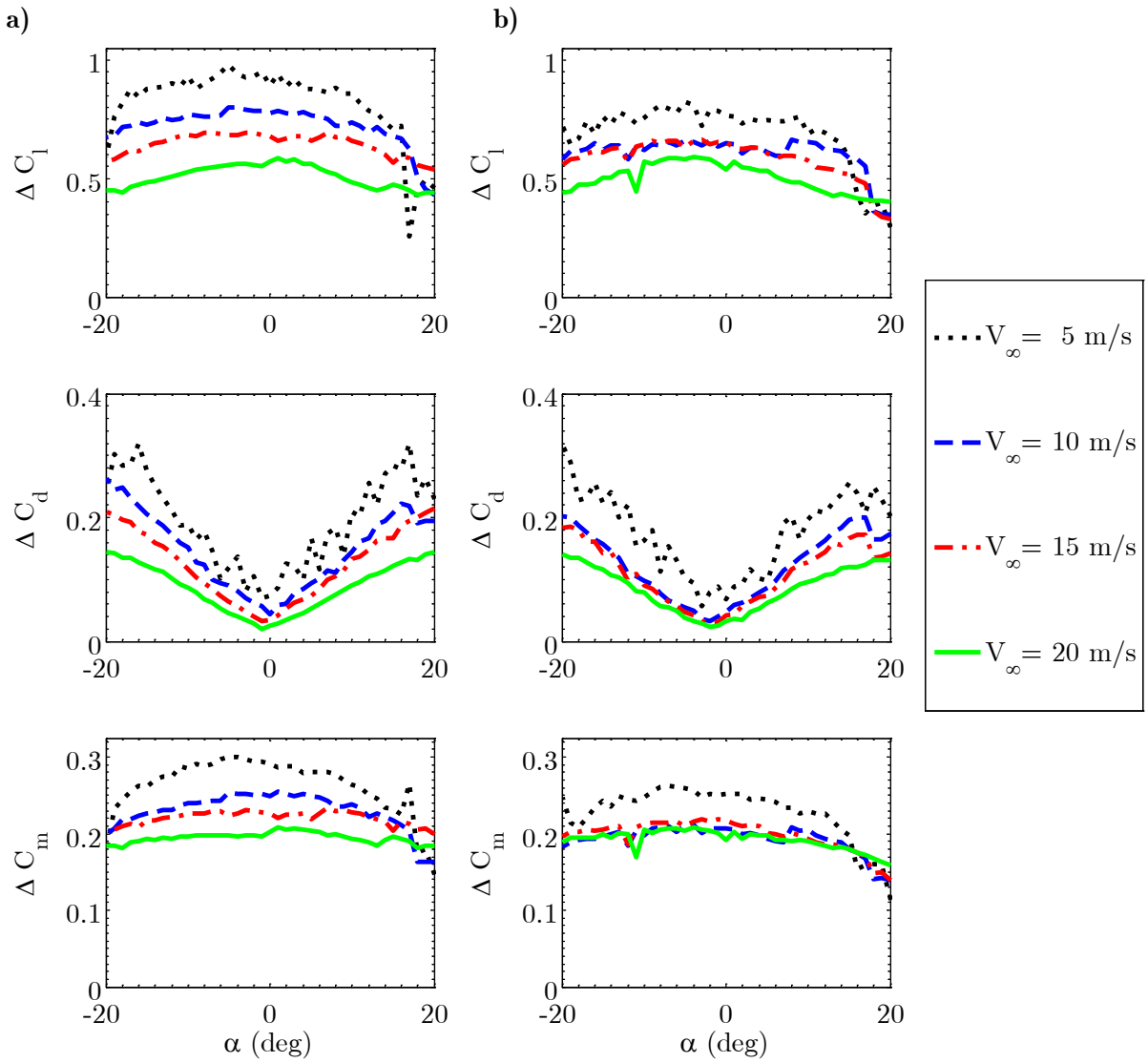

Figure 3.16 Aerodynamic control forces for a) Unimorph and b) Bimorph

3.1.4.3. Mass

The mass of the various components for both flexure box aileron concepts was tabulated for comparison with other existing concepts in Table 3.1. For ultra-light applications, the mass of the high voltage amplifier and a weight of a leading edge of similar span were included for relevance. Clearly, the MFCs' mass dominated the weight of the overall aileron: 46%, and 61% of the total mass for the unimorph and bimorph configurations respectively. The flexure box also represented a significant fraction of the total mass of the bimorph configuration, however, the material used in construction was chosen for ease of manufacturing, not to minimize mass.

Further refinements in the design of the flexure box are possible and lighter construction materials could further reduce its contribution to actuator mass.

The materials in the MFCs, specifically the piezoceramics, were inherently required for this actuation concept. Accordingly, it would be very difficult to further reduce the weight of the MFCs and they would represent a sizeable consideration in the actuator choice for lighter wing designs. For ultra-light applications, the mass of the high voltage amplifier and a weight of a leading edge of similar span are included for relevance. It can be seen that the added weight of amplifier and rigid leading edge can also prove significant and require consideration[85]. Although, it should be noted that the surface of the MFC serves as the outer skin of the airfoil, which could reduce the mass penalty relative to conventional designs with heavy or thick skins A recommendation for further mass reduction of the flexure box on this scale would come from foam-like structures or 3D printed parts with low-fill cores, simulation a bone-like porous structure.

Table 3.1 Summary of Component Mass

Aileron		**Leading Edge**		**Circuitry**	
Component	**Mass (g)**	**Component**	**Mass (g)**	**Component**	**Mass (g)**
Flexure Box	20	Carbon Fiber /Foam/ and Balsa Spa	58	HV Amplifier	34
Trailing Edge Stub	2	Total:	58	Total:	34
2 Flex Sensors	1				
2 Unimorphs	20 / -				
2 Bimorphs	- / 36				
Total	**43 / 59 (Uni / Bimorph)**				

3.1.4.4. Power

The power consumed by the MFCs is small due to their largely capacitive nature, but the high voltage DC-DC converters needed to drive the MFCs consume measureable power. With the custom current monitoring circuit described in Section 3.1.3.2, the average power required to hold the position for each actuation level was recorded. The resultant average power required for actuation at each flow speed is plotted against the resultant tip deflection in Figure 3.17 creating a range of expected power levels at each flow speed. The lines were composed by taking the mean of the power consumption for all angles of attack at each commanded position.

The results reconfirm the result from before that the range is compressed by the flow for both configurations. As the flow speed increases, the mechanical work done on the structure by the flow also increases, requiring more energy from the MFCs to actuate to the same tip deflection. When the maximum achievable power level is reached, the MFC saturates at its maximum voltage and the achievable range is limited was generated to describe expected power consumption related to flow speed and tip displacement. The range forms a U-like shape due to the increased power draw of the high voltage DC-DC converters when higher output voltage is needed to actuate the MFC to the desired position. Again, because the driving circuit largely dictates the power consumption, the approximate levels of power consumption were roughly equivalent.

The high voltage driver board is capable of quasi-statically driving multiple MFCs with the same voltage split at once with a single command due to the largely capacitive nature of MFCs. However, scope of the current work does not include actuating multiple ailerons at different levels or the dynamic actuation rate of the circuit. For real applications with dynamic constraints or distributed actuation requirements, these issues would further affect power considerations.

If the power consumed by the MFCs alone had been measured, rather than the power consumed by the high voltage amplifier, the result would most likely have been different. Because the bimorph utilized twice as many MFCs, the power draw would have been approximately twice as much as the unimorph concept. However, from the systems-level perspective taken in this analysis, this difference on the material level was negligible due to the largely capacitive nature of the MFCs and the static nature of the testing.

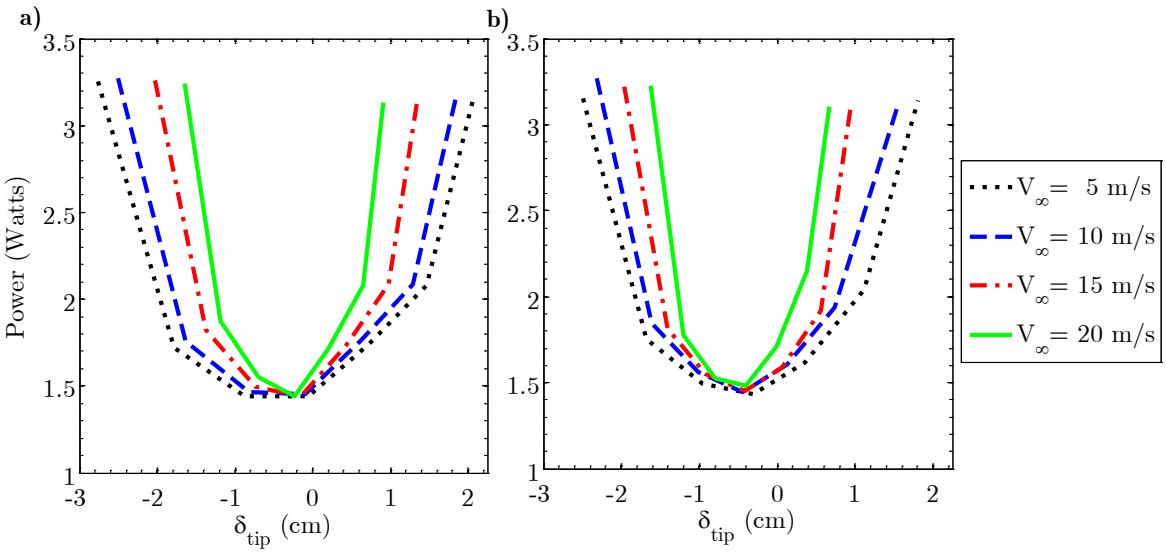

Figure 3.17 Mean system power consumption per position for a) Unimorph and b) Bimorph

3.1.5. Comparative test summary

The benefits and costs of the number of Macro-Fiber Composite (MFC) patches in the flexure box aileron concept were investigated experimentally for static actuation under aerodynamic loads. Bimorph and unimorph configurations consisting of 2 and 4 MFCs, respectively, were constructed for NACA 0012 airfoils with 304.8 mm chord by 3D-printing the compliant components. An embedded flexible sensor was designed and calibrated to measure the tip displacement of the configurations under aerodynamic loads. The actuation authority for both configurations was measured in the 60 cm by 60 cm wind tunnel at the University of Michigan for flow speeds ranging from 5 to 20 meters per second and -20 to +20 degrees angle of attack. The results showed the unimorph exhibiting superior ability to influence flow up to 15 m/s, with equivalent power consumption and lower overall mass. At 20 meters per second, the bimorph exhibited superior ability to control aerodynamic forces.

The static stiffness of each constructed configuration was characterized by tip loading the aileron with known forces. The added MFCs from the unimorph to bimorph concept increased the overall mass by 37% but also increased the overall stiffness of the actuator to tip loads by 50%. At the lowest flow speed, the tip displacement of the unimorph configuration was also slightly larger 4.79 cm as opposed to 4.24 cm, a 13% difference. As measured by the embedded sensor, both the unimorph and bimorph configuration saw roughly proportional reductions in tip

range corresponding to an approximately 50% reduction at 20 meters per second. The bimorph experienced much less slew in its actuation range than the unimorph, which experienced a 63% change in its actuation bounds at 20 meters per second solely due to variation in angle of attack. The result confirms the ability of the tip displacement sensor as an insightful indicator for examining fine comparisons of actuation capabilities across flow speeds. Also, the results showed the need for compensation for aerodynamic forces in the unimorph concept for speeds above 10 meters per second.

Although the current test configuration posed challenges for effectively comparing non-dimensional aerodynamic forces over an order of magnitude range difference in loading, the results showed several meaningful trends. Actuator effectiveness for lift and pitching moment was maximized for both configurations and all flow speeds at zero degrees angle of attack, corresponding to low separation and normal aerodynamic forces. The configurations ability to influence drag increased with absolute angle of attack as the actuators represented ability to influence flow separation. The bimorph exhibited flow control equal to the unimorph at 15 meters per second, as shown by its ability to influence lift, drag and pitching moment and superior flow control at 20 meters per second.

The mass added to the flexure box aileron by doubling the number of MFCs from the unimorph to bimorph concept increased the total mass by 16 grams, or 37%. Considering that additional refinements could be made to the flexure box to lower its mass through alternative construction materials and design refinement, this difference could grow much larger for highly mass-constrained applications. A high voltage driver circuit designed for small UAVs actuated the ailerons. Due to the largely capacitive nature of the MFCs, and the increasing power consumption of dc-dc converter with output voltage, the peak and minimum power consumed by the two concepts was equal and followed similar U-shaped trends when plotting mean power consumption against tip position.

3.2. Aspect ratio scaling

It was desired to connect the results from the previous comparative test at a reduced aspect ratio with two-dimensional simulations and experiments. By connecting the comparative test to two-dimensional results, the impact of the results would be broadened by allowing comparison with other technologies and aeroelastic simulations. The previous results were then scaled by a new methodology which was detailed in the following section.

3.2.1. Motivation for scaling methodology

Early comparison of the experimental results from the previous section to other experimental results and simulations showed two results that motivated the need for a scaling methodology to properly interpret the previous experiment as a two-dimensional result.

First, the nondimensional forces for the reduced-span airfoil utilized in Section 3.1 did not match the expected two-dimensional results from other experiments. Although it was difficult to directly compare the results as every morphing configuration was different, the performance of the rigid airfoil compared to other configurations could be assessed. Accordingly, the morphing trailing edges were replaced with a rigid trailing edge and the nondimensional forces were compared with nondimensional forces from Sheldahl *et al.* [106] . As shown in Figure 3.18, when compared with other experimental results at a relevant Reynold's number, the drag from the lift curve slope, i.e. $dC_l/d\alpha$, for all of the flow speeds were remarkably consistent, and much lower than the results expected for two-dimensional flow. Although the peak lift coefficients were similar, the stall angles were much higher. The difference in drag results was much clearer. The elliptical end plates were increasing the baseline drag, C_{d0}, significantly above the expected two-dimensional result. Also, the drag rise associated with stall was delayed to the point of being un-noticeable in the results.

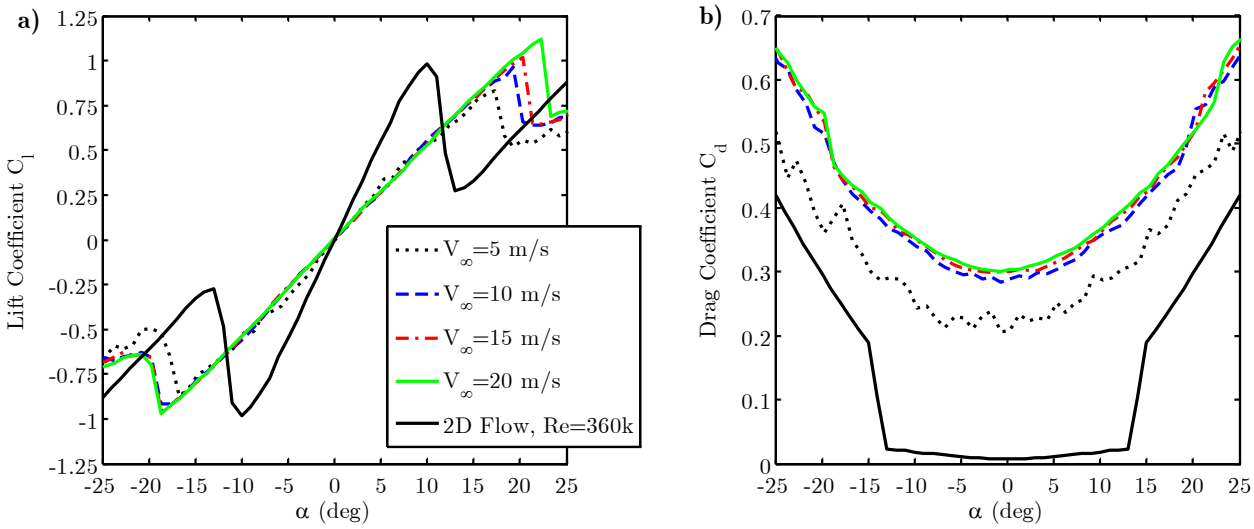

Figure 3.18 Nondimensional a) lift and b) drag forces on test article with rigid trailing edge

Second, comparing the change in aerodynamic control forces with simulations also motivated the need for a scaling methodology. If the span of the test article affected the lift curve slope, then it would also stand to reason that it could affect the ability of the morphing aileron to control the aerodynamic forces. The morphing aileron configuration was modeled using the Reynolds-Averaged Navier Stokes simulation, previously mentioned in Section 2.4.3 and detailed in Section 6.3. This two-dimensional simulation took into account Reynolds-number effects as well as the morphing airfoil shape, as measured from experimental tests, described in Section 2.4.3. The morphing airfoil provided only the shape simulated and no aeroelastic effects were considered.

The result from the rigid, aerodynamics-only simulation did not take into account any aeroelastic effects on the trailing edge, but provided an upper-bound for the performance of the morphing concept, i.e. without aeroelastic effects. As seen in Figure 3.19, the experimentally measured ability of the morphing ailerons at the reduced aspect ratio to affect lift was significantly less than the simulated values. Even for the lowest flow speed, the change in lift was off by nearly a factor of two. The upward trend in the simulation is due to the result of increasing Reynold's number. The downward trends due to the experiments are due to the aeroelastic effects on the morphing trailing edges.

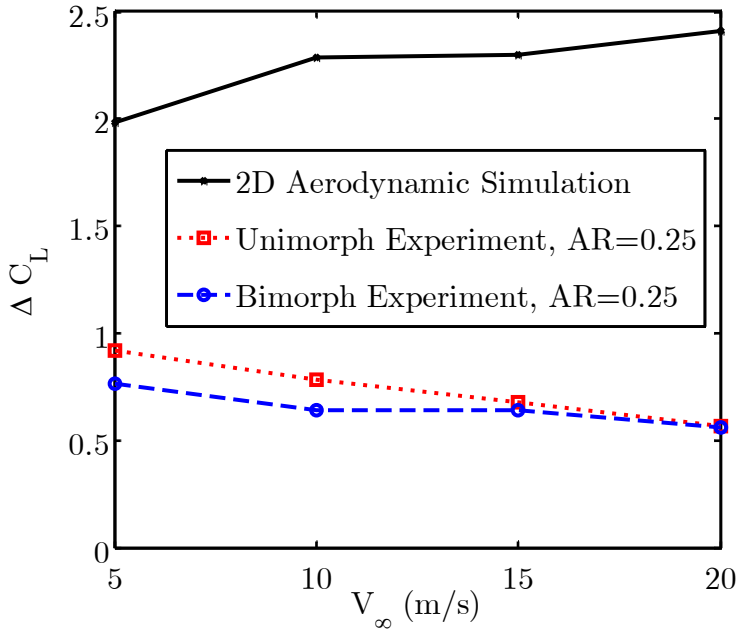

Figure 3.19 Aerodynamic simulation compared with experimental results

It stood to reason that if the test configuration could reduce the ability of the change in angle of attack to affect lift, then it could also reduce the ability of the morphing ailerons to affect lift in the same manner. This though motivated the scaling methodology in the following sections

3.2.2. Aspect ratio scaling

The first task in establishing a scaling methodology was to determine how the reduced endplates had impacted the aerodynamic forces on the reduced aspect airfoil. The novel nature of the morphing trailing edges precluded precise comparison with existing results in literature. Additionally, the aeroelastic effects on the morphing trailing edge, as see in Figure 3.19, prevented a simple comparison with purely aerodynamic simulations. To isolate the aerodynamic effects on the experimental setup from an analysis of the effect of the aspect ratio on aerodynamic forces with a rigid trailing edge was performed.

By increasing the aspect ratio of the test article, it was sought to diminish the relative effect of the end plates allowing for a closer approximation two-dimensional flow. Leveraging the modular design, additional leading and trailing edges were fabricated, shown in Figure 3.20a, creating a scalable aspect ratio airfoil with a removable trailing edge as shown in Figure 3.20b. The basic unit of the airfoil was then the same modular leading edge section with a span of 7.6 cm from Section 3.1.2.1. Due to the size of the endplates, the 2' x 2' (60 cm by 60 cm) wind tunnel at the University of Michigan seven discrete configurations were possible, ranging from an aspect ratio of 0.25 to 1.75, shown in Figure 3.21a and Figure 3.21b, respectively.

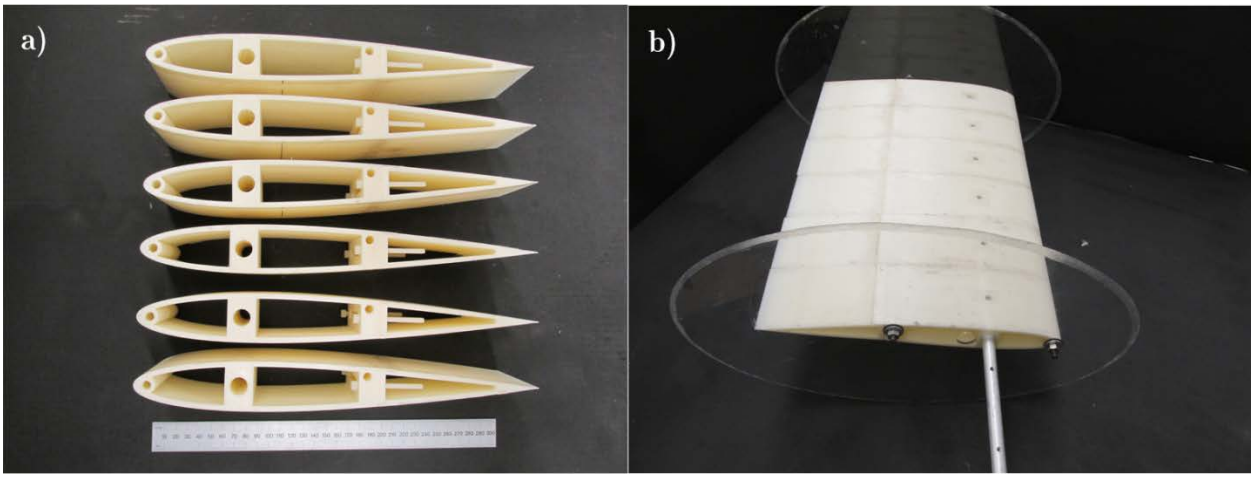

Figure 3.20 a) Modular sections used for b) scalable aspect ratio wing with end plates

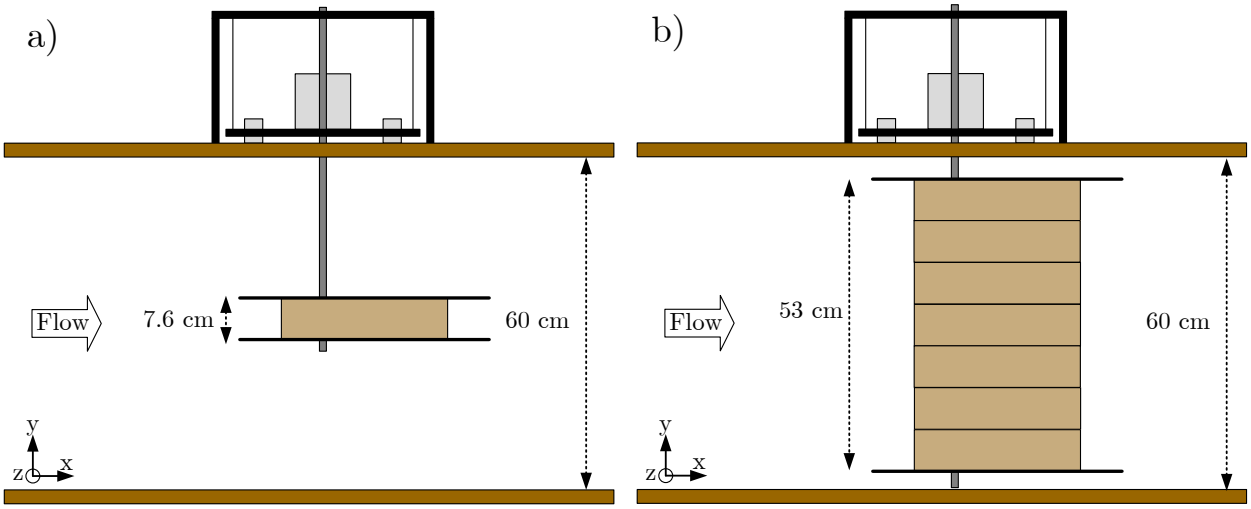

Figure 3.21 Experimental setup for aspect ratio test at a) AR=0.25 and b) AR=1.75

3.2.3. Results of aspect ratio scaling

In a manner similar to the previous test, the forces were measured on the airfoil for the same range of flow speeds and angles of attack. The results from the largest aspect ratio test were presented in Figure 3.22 compared with the experimental results from [106].

Comparing these results with those from Figure 3.18, i.e. the smallest aspect ratio, the results are clear. For the smallest aspect ratio, the endplates reduced the sensitivity of lift with respect to angle of attack, while increasing the profile drag and delaying flow separation. Notably, for attacheed flow, the lift and drag forces remained largely comparable for all flow speeds. Only for the lowest flow speed (5 m/s) was the calibration offset due to noise significant, but the overall trend for forces remained consistent. Thus, even at this flow case, changes in nondimensional forces were determined to be valid even if force offsets were not. Further analyzing the effect on lift in Figure 3.23, it can be seen that the sensitivity of the change in lift coefficient with respect to angle of attack is reduced by almost 50% compared to the larger aspect ratio. Again, the profile drag trend remained constant for all flow speeds, exhibiting a roughly quadratic trend towards two-dimensional theory.

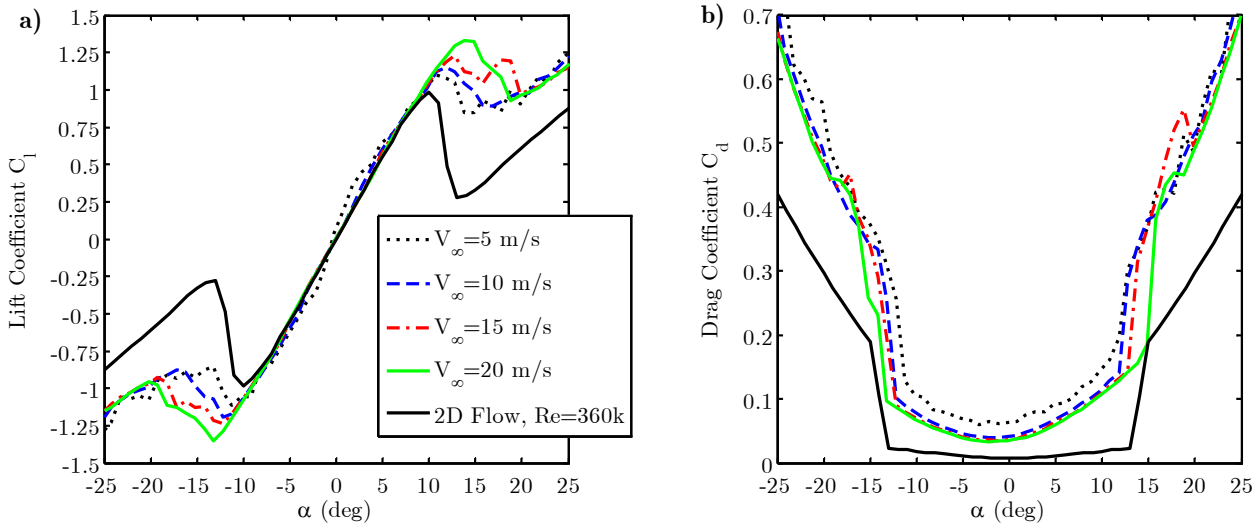

Figure 3.22 Aerodynamic a) lift and b) drag data for rigid trailing edge with AR=1.75

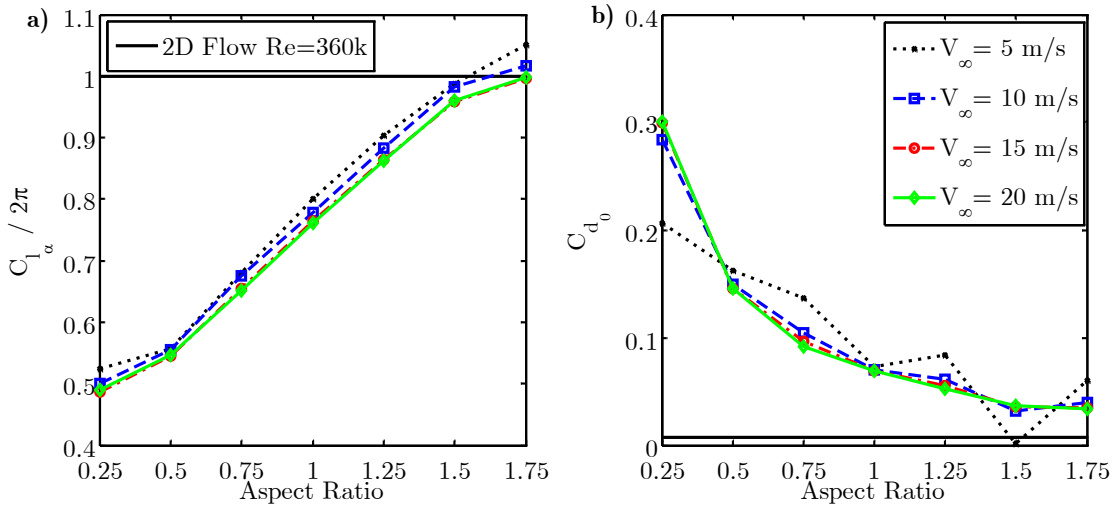

Figure 3.23 a) Lift curve slope and b) baseline drag coefficient plotted against aspect ratio

An intuitive explanation for the reduction in lift sensitivity is that the end plates' boundary layers cause an effective reduction of the test article span exposed to freestream flow. Thus, to approximate the appropriate span exposed to the flow an effective correction parameter was introduced. The effective span fraction, $\bar{b}$, was then defined by dividing the mean lift by the quantity predicted by thin airfoil theory, as

$$\bar{b} = \frac{b_{effective}}{b_{physical}} = \frac{C_{l_\alpha}(AR)}{C_{l_\alpha}(2D)} = \frac{C_{l_\alpha}}{2\pi} \tag{3.1}$$

which is the ratio of the effective span of the wing to the physical or geometric span of the wing. The values for the effective span fraction were found by taking the mean of the lift curve slopes at all flow speeds, resulting in the values from Table 3.2. The effective span fraction approached the infinite span result as the aspect ratio is increased. The rigid airfoil test with an aspect ratio of AR=1.5 resulted in less than a 5% deviation from two-dimensional results. Thus, the ability of various span test articles to replicate infinite-span test results was quantified.

Table 3.2 Relationship between aspect ratio and effective span

AR	0.25	0.5	0.75	1.0	1.25	1.5	1.75	∞
$\bar{b}$	0.50	0.55	0.67	0.77	0.88	0.97	1.0	1.0

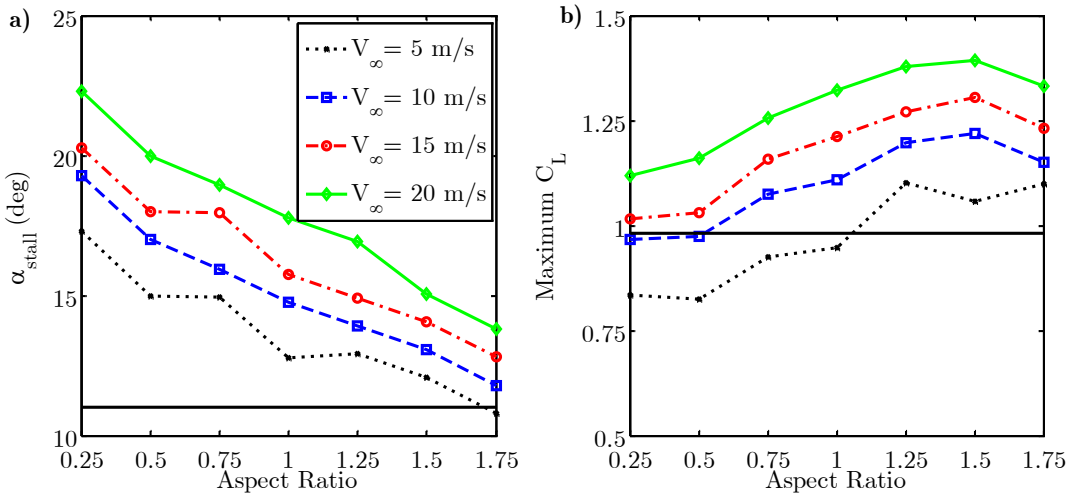

Figure 3.24 Effect of aspect ratio on a) stall angle and b) maximum lift

From the data in the tests, it was then possible to identify the stall angle and maximum lift coefficient from the maximum value of the lift curve slope. As shown in Figure 3.24, the trend in the stall angle is clear at all flow speeds. Even by the largest tested aspect ratio, the stall angle was still over predicted by approximately 3 degrees. Another interesting revelation was the maximum lift coefficient, which increased by approximately 25% for all flow speeds and aspect ratios. These parameters did not share the same agreement as the lift curve slope because they were dependent on the Reynolds number of the test conditions. From this data, it was concluded that even near stall the experiment reached reasonable two-dimensional performance by an aspect ratio of 1.5. However, the effective span fraction would not be a useful parameter for scaling aerodynamic forces near stall.

3.3. Increased aspect ratio morphing test

To identify whether the scaling method, i.e. the effective span fraction, could provide useful prediction of forces in two-dimensional flow from the lower aspect ratio test, a morphing airfoil with an increased aspect ratio relative to the previous test was constructed and tested. The details of the experiment and extrapolation of the force results are presented in this section.

3.3.1. Test description

Drawing from the conclusions of the previous section, a morphing airfoil was constructed with an increased aspect ratio (AR=1.5), utilizing 6 modular sections, to achieve infinite-span results within 5% error. The unimorph configuration was chosen as the comparative test showed that it could achieve better control over aerodynamic forces. Constructed using the same modular leading edges as in the aspect ratio test, the morphing trailing edges were bonded together at the tip to create uniform spanwise actuation. Because the lack of gaps between the modular ailerons, this method did not allow for independent closed loop control between the various ailerons and only two morphing actuations were investigated, actuating the tip completely down and up. A cross-section of the larger aspect ratio under construction is shown in Figure 3.25. Note that in this image, the wiper was not yet installed and clearly showed the chordwise location of the Flexure Box aileron.

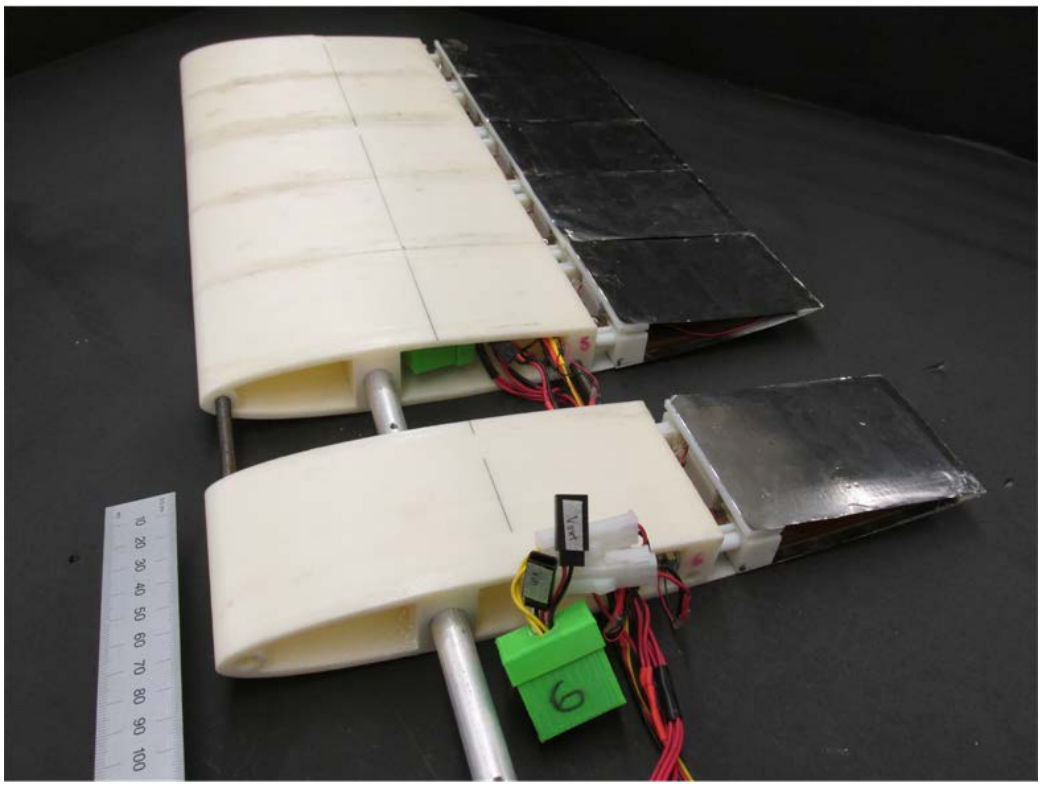

Figure 3.25 Construction of larger aspect ratio morphing airfoil

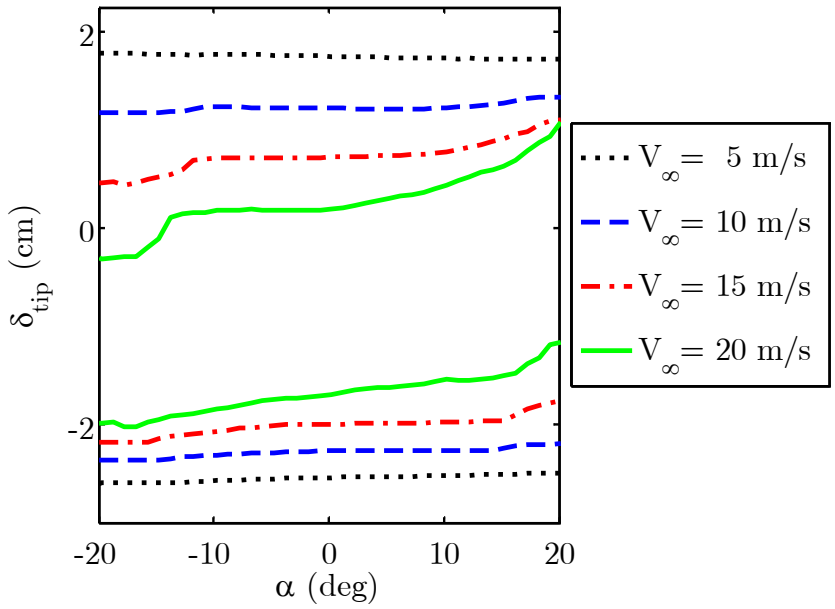

Figure 3.26 Range of tip deflections for larger Unimorph AR=1.5

3.3.2. Results from increased aspect ratio morphing test

In this experiment, the overall tip deflections due to actuation were lower due to the increased effect of aerodynamic loads on the morphing airfoil. Seen in Figure 3.26 the same slewing effect due to angle of attack is apparent at higher speeds. Above 15 degrees, where the flow separates, the aileron's ability to actuate against the flow is significantly reduced.

A simple metric for comparing the effectiveness of the morphing aileron at different aspect ratios was identified by examining the effect on tip deflection and lift, near zero degrees angle of attack. As seen from the previous sections, the morphing airfoil exhibits its greatest ability to affect lift at this angle of attack. To reduce error due to load-cell noise a mean of the values were taken from +5 degrees to -5 degrees. The resultant effectiveness of the morphing configurations on tip displacement and lift at different loading conditions (i.e. flow speeds) and aspect ratios is summarized in Figure 3.27.

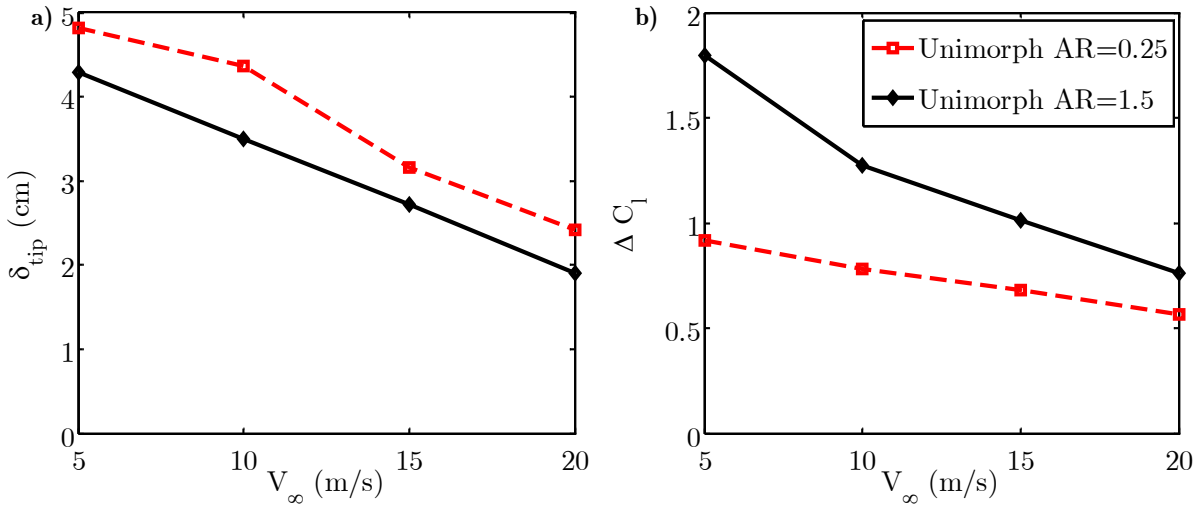

Figure 3.27 Comparison for both aspect ratios at zero degrees angle of attack of actuation effect on a) tip deflection and b) lift

Compared with the reduced aspect ratio results from Section 3.1, the increased aspect ratio morphing aileron resulted in additional reduction of tip deflections of approximately 10% at 5 m/s up to almost 20% at 20 m/s. Over those same conditions, the unimorph exhibited an improvement in ability to affect lift from 95% down to only 34%. This result is explained as the increased span test resulted in higher aerodynamic loading on the morphing aileron while also improving the configurations ability to affect lift, consistent with the overall trends of the aspect ratio scaling tests.

3.3.3. Scaling methodology

A scaling methodology was needed to reconcile the difference in ability to alter lift between the two aspect ratios. The effective span ratio was shown for rigid trailing edges to provide a scaling method of the lift effectiveness versus flow speed over a range of aspect ratios. This factor approximates the reduction in lift effectives by scaling the span of the airfoil that contributes to lift generation. It was assumed that the change in lift generation due to actuation could be scaled by the same ratio as the change in lift due to changes in angle of attack, which can be expressed as

$$\frac{\Delta C_l(AR_2)}{\Delta C_l(AR_1)} = \frac{\bar{b}_2}{\bar{b}_1} \tag{3.2}$$

Then, the ability of the aileron to affect lift can be extrapolated to an infinite span (i.e. 2D results) by letting $\bar{b}_2 = 1$, reducing the former equation to

$$\Delta C_l(2D) = \Delta C_l(AR_1) \,/\, \bar{b}_1 \tag{3.3}$$

A second factor is needed to account for the increased loading on the compliant airfoil. This factor was needed because even though the amount of the airfoil exposed to the freestream was reduced, the stiffness of the structure was not. Thus, for a compliant airfoil, a small aspect ratio will overpredict the stiffness due to aerodynamic loading. Because the morphing aileron concept is stiff spanwise, it is assumed to experience the same fractional reduction in aerodynamic forces as the rigid airfoil from the tests in Section 3.2, due to the end plates. Thus the applied loads to the morphing airfoil were scaled by the relationship

$$\frac{F_{applied}(AR_1)}{F_{applied}(AR_2)} = \frac{\bar{b}_1}{\bar{b}_2} \tag{3.4}$$

When plotting change in lift against flow speed, the flow speeds represent an effective loading condition on the aileron. Because aerodynamic loads are proportional to dynamic pressure and the square of freestream velocity, the flow speed is then scaled by the square root of the effective span. Then, the flow velocity as a metric of aerodynamic loading can be extrapolated to an infinite span (i.e. 2D results) by letting $\bar{b}_2 = 1$, as before and recovering the result

$$V_\infty(2D) = \sqrt{\bar{b}_1} V_\infty(AR_1) \tag{3.5}$$

3.3.4. Scaled results

Utilizing the scaling methods described in the previous section, the results from the various configurations tested are summarized in Figure 3.28. In this plot, the scaled lift effectiveness for the various experiments is compared against aerodynamic loading as expressed by scaled freestream flowspeed. Scaling by the effective span ratio for both lift effectiveness and loading allows for both the unimorph and bimorph configurations from the previous test to be compared to each other as well as provide extrapolation to an infinite span test by $\bar{b} \to 1$. Linear

fit lines for the extrapolated results are used to predict the approximate loading scenario at which the bimorph would show increased stiffness over the unimorph for a two-dimensional experiment. Using this method the unimorph results from the increased aspect ratio test (AR=1.5) are scaled only by approximately 3%, providing approximate infinite-span confirmation for the extrapolation capabilities of the reduced aspect ratio results. The results from both aspect ratios of the unimorph configuration show agreement with each other to approximately 10% error.

The scaled results predict that the unimorph configuration will only surpass the bimorph configuration in lift effectiveness until approximately 15 m/s, where the bimorph configuration will exhibit improved authority. This result differs in the estimated speed from the comparative test at AR=0.25 which over predicted the stiffness of both concepts while under predicting their ability to change lift. Still, the general trends for the comparative test hold, albeit at reduced lift effectiveness.

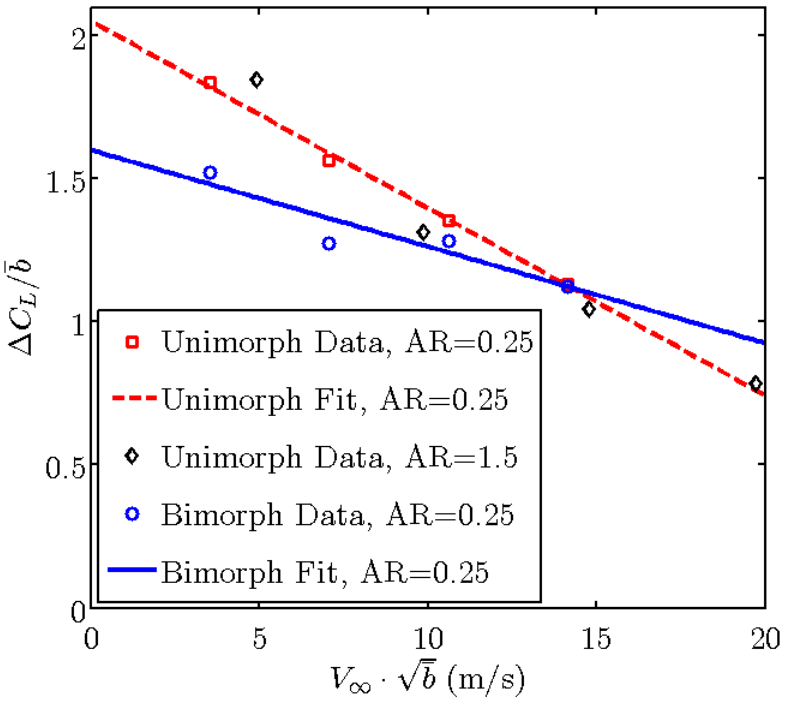

Figure 3.28 Lift effectiveness
for all tested configurations with effective span correction

3.4. Discussion

3.4.1. Unimorph vs bimorph comparison

Independent of this research, Prazenic *et al.* were simultaneously investigating a similar study of a unimorph and bimorph actuator for a MFC actuator for integration on a fixed wing UAV [107]. The results of both this study and the other study were published at the same conference, in the same session [107,108]. The following section addresses compares their research in light of the results from this chapter.

The structures utilized in the comparative study by Prazenic *et al.* were a true unimorph and bimorph, meaning they were simply the cantilevered beam with a fixed boundary condition. Despite this reduction in complexity compared to the "unimorph" and "bimorph" configurations from this chapter, their results also found that the bimorph deflection levels were smaller than the unimorph. Additionally, both of their experimental configurations showed significantly lower deflection results compared to the theoretical linear beam analysis by Wang *et al.* [102]. Clarifying their results, reproduced in Figure 3.29, the authors stated:

> In fact, in direct contradiction to the theoretical model, the bimorph deflection levels were actually lower than those observed from the unimorph actuator. The most likely explanation for this result is that the bimorph fabrication process necessarily created two layers of epoxy, which added significantly to the stiffness of the structure, reducing the deflection.

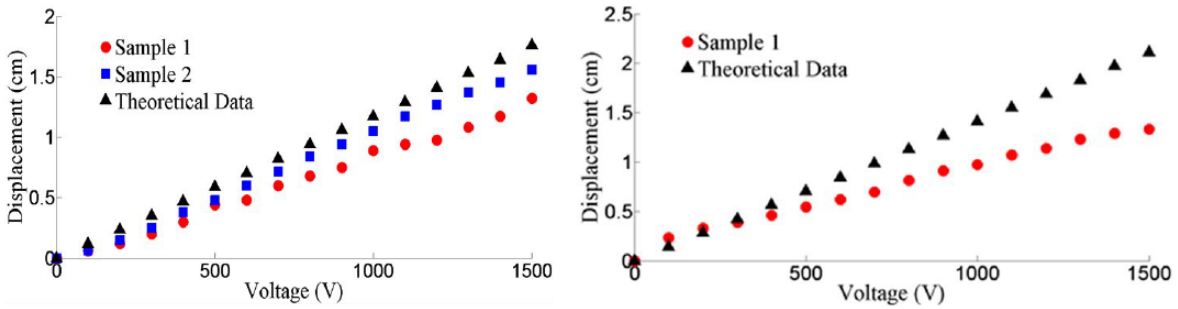

(a) Unimorph Actuator **(b) Bimorph Actuator**

Figure 3.29 Comparison of Theoretical and Experimental Unimorph and Bimorph Deflections from [107]

Working against this explanation, the thickness of the MFC in their test was 0.3 mm while the thickness of the substrate was 0.4 mm. As noted by Bilgen *et al.*, a typical level of epoxy for bonding an MFC to a substrate was approximately 0.02 mm or almost an order of magnitude less than either the substrate or the MFC utilized in this experiment [101]. Also, their sample 2 was created with only a few small droplets of epoxy, creating a non-homogeneous beam which was inconsistent with the theoretical modelling.

Other explanations that were not considered to explain this discrepancy between their experimental and theoretical results included the nonlinearity of the piezoelectric coupling coefficient and the asymmetric voltage limits applied to the MFCs. As presented in several plots throughout this thesis, the hysteresis and nonlinearity of deflection versus applied voltage for MFCs in this voltage range was significant. Also, the voltage range applied to both configurations by Prazenic *et al.* was 0 to 1500 volts, this represented an unrealistic scenario, as -1500 V used for the one side of the bimorph actuator would have irreversibly damaged the actuator and the high voltage amplifier used in the experiment was specifically designed to adhere to the commonly-utilized lower limit of -500 V [109]. This asymmetry limit on the voltage range of the bimorph was not accounted for in the theoretical results of Prazenic *et al.*, which utilized the equations by Wang *et al*. for equal application of voltage and linear piezoelectric coupling coefficients.

3.4.1.1. Asymmetric field correction

To compensate for the asymmetry of the voltage limits in any use of the bimorph, the following new results are derived. The unimorph and bimorph configurations from this chapter were complicated to analytically model. Accordingly, the simple cantilevered unimorph and bimorphs from [107] were chosen as the focus of the investigation of the impact of the asymmetric voltage limits. It was sought to prove that these assymmetric voltage limits could account for the measured result from [107] that the unimorph results in larger tip deflects than the bimorph. Then, by proxy, the same result, shown previously in this chapter, for the more complicated “unimorph” and “bimorph” configurations could be verified and understood.

The cantilevered bimorph from Wang *et al.* was utilized by Prazenic *et al.*as their theoretical analysis. The following paragraphs then address the asymmetric field correction to the cantivlevered bimorph model. The theoretical tip deflection δ, for the bimorph, uncorrected

for asymmetric voltage was found using the equation, where the electric field $E_3^{uniform}$ was proportional to the applied voltage

$$\delta\left(E_3^{uniform}\right) = \frac{6s_{11}^S\left(t_s + t_{MFC}\right)t_{MFC}L^2}{2s_{11}^S\left(3t_s^2t_{MFC} + 6t_st_{MFC}^2 + 4t_{MFC}^3\right) + s_{11}^{MFC}t_S^3} d_{33}E_3^{uniform} \tag{3.6}$$

which is of the form:

$$\delta\left(E_3^{uniform}\right) = Kd_{33}E_3^{uniform} \tag{3.7}$$

where the deflection is related to the a stiffness parameter, *K*, the piezoelectric coupling coefficient, d_{33}, and the single electric field applied to both piezoelectric elements, E_3. If instead, the voltage and thus, electric field was different between the two piezoelectric patches, then the above form would need to be re-derived from the balance of moments within the unloaded beam with two different applied electrical fields. Rather than $E_{uniform}$, the electric fields for the upper and lower piezoelectric elements were E_{lower} and E_{upper}. The balance of moments within the beam was then substituted into the equation by Wang *et al.*, shown by,

$$\begin{aligned} M= & \int_{-\left(t_{MFC}+\frac{t_s}{2}\right)}^{-\frac{t_s}{2}} \left(\frac{1}{s_{11}^{MFC}}\kappa y - \frac{1}{s_{11}^{MFC}}d_{33}E_3^{lower}\right) wydy \\ & \int_{-\frac{t_s}{2}}^{\frac{t_s}{2}} \left(\frac{1}{s_{11}^{s}}\kappa y\right) wydy \\ & \int_{\frac{t_s}{2}}^{\frac{t_s}{2}+t_{MFC}} \left(\frac{1}{s_{11}^{MFC}}\kappa y + \frac{1}{s_{11}^{MFC}}d_{33}E_3^{upper}\right) wydy \end{aligned} \tag{3.8}$$

where the first second and third terms represent the moment contribution of the lower piezoelectric element, the substrate, and the upper piezoelectric elements, respectively. By integrating through the thickness, and setting the applied moment equal to zero, the equation for the curvature of the beam, κ, as a function of the electric fields were then found. Integrating the curvature twice over the length of the beam, the tip deflection as a function of both electric fields was then found as:

$$\delta = \frac{3s_{11}^{S}\left(t_s + t_{MFC}\right)t_{MFC}L^2}{2s_{11}^{S}\left(3t_s^2 t_{MFC} + 6t_s t_{MFC}^2 + 4t_{MFC}^3\right) + s_{11}^{MFC}t_S^3} d_{33}\left(E_3^{lower} + E_3^{upper}\right)$$

$$\delta\left(E_3^{lower}, E_3^{upper}\right) = Kd_{33}\frac{\left(E_3^{lower} + E_3^{upper}\right)}{2} \tag{3.9}$$

which was simply the mean of the two fields acting together. Then, correcting the previous theoretical result for the bimorph, the electric fields were proportional to the applied voltages, namely a 3:1 ratio. By making the substitutions that:

$$\begin{aligned} E_3^{lower} &= 1\ /\ 3 \cdot E_3^{uniform} \\ E_3^{upper} &= E_3^{uniform} \end{aligned} \tag{3.10}$$

to account for the reduced electric field in the bottom element into Equation (3.9), the mean was found to be 2/3 of the result from Equation (3.7). Table 3.3 corrected for this result, which shows that the asymmetric voltage application alone could account for the discrepancy between the experimental results and the theoretical result.

Table 3.3 Tip Deflections and Ratios

	Unimorph Deflection (cm)	**Bimorph Deflection (cm)**	**Unimorph to Bimorph Ratio**
Modular Aileron Experiment from Section 3.1	4.86	4.27	1.14
Experimental Results from [107]	1.32/1.56	1.33	1/1.17
Theoretical Results from [107]	1.78	2.12	0.83
Theoretical Results from [107] **corrected for voltage limits**	1.78	1.41	1.26

Once the theoretical results from [107] were corrected for the assymmetric voltage limits in the bimorph configuration, the theoretical result matched the experimental results from this work as well as the experimental work from [107]. Then, the conclusion followed that a properly designed unimorph, i.e. thin and stiff substrate, will outperform the bimorph in deflections on the test stand, without aerodynamic loads.

If a symmetric voltage limit had been used rather than the asymmetric voltage limit associated with the maximum range, the deflection resulted would have been expected to resemble the theoretical results by [107]. In this scenario the added smart material of the bimorph would result in a proportional increase in both stiffness and actuation as compared to the unimorph. Then, the larger volume fraction of the active material in the bimorph should slightly augment its overall range, providing it with superior actuation authority and stiffness as compared to the unimorph. Although symmetric voltage constraints are not currently possible with existing technology if the limits of the MFCs are to be reached, reducing the applied voltage below the limits to achieve symmetric voltage has several advantages including: reduced complexity of the high voltage electronics and increased lifecycle of the piezoelectric components. The disadvantage of decreased applied voltage would be decreased actuation authority, and thus control over aerodynamic forces.

3.4.2. Aeroelastic estimation

The scaled experimental results from Sections 3.3 were combined with the aerodynamic simulations mentioned in Section 3.2.1 to estimate the modelling accuracy of these concepts. Examining the data compared to the simulation in Figure 3.30, the simulation is shown to uniformly overestimate the performance of all configurations of the Flexure Box Aileron at every flow speed. The modeled results agree best at the lowest modeled flow speed, 5 m/s, where aeroelastic effects are the least. As the flow speed is increased to 20 m/s, the measured change in lift decreases by 50% while the modeled performance increases.

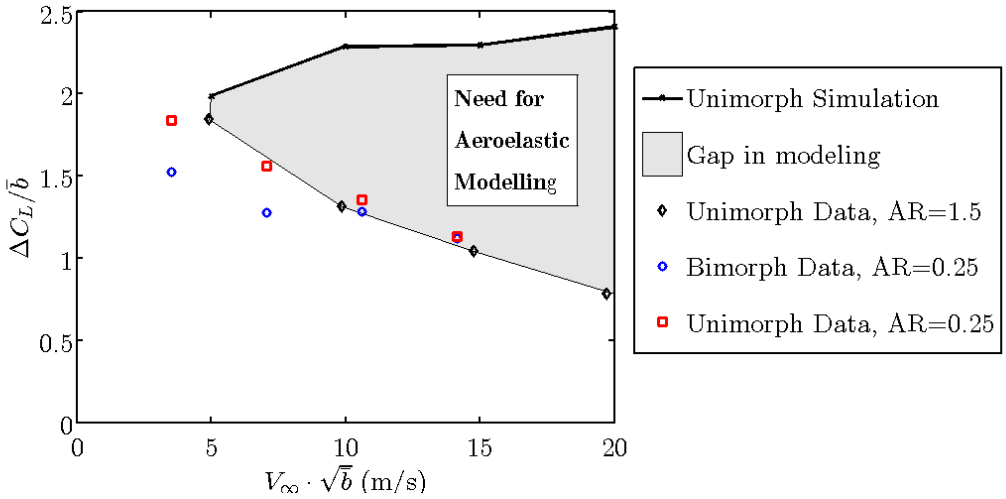

Figure 3.30 Lift effectiveness
for all tested configurations with effective span correction

The discrepancy between the experiments and simulation can be explained by the fidelity of the simulation. The simulation used in this figure modeled only aerodynamic performance of a specified geometric shape. No structural model or aeroelastic effects were included in the simulation. This large discrepancy between the simulated and experimental results then motivates the necessity of an aero-structural model to predict the performance of the Flexure Box aileron. This conclusion motivated the analysis performed in Chapter 6.

3.5. Conclusions

This chapter presented a method for experimentally comparing compliant morphing trailing edge concepts at a reduced aspect ratio with end plates, reducing complexity compared to finite wing or large span tests, while scaling the aerodynamic lift effectiveness due to aspect ratio. The motivation for this investigation was to better understand the scalability of the Flexure Box aileron concept under aerodynamic loading relevant to the scale of UAV discussed in Chapter 2. The study focused specifically on how the number of Macro-Fiber Composite (MFC) patches utilized in the morphing concept affected performance and the scalability of that performance.

To measure this scalability, bimorph and unimorph configurations consisting of 2 and 4 MFCs, respectively, were constructed for NACA 0012 airfoils with 304.8 mm chord by additive manufacturing of the compliant components. An embedded flexible sensor was designed and

calibrated to measure the tip displacement of the configurations under aerodynamic loads. The actuation authority for both configurations was measured in the 60 cm by 60 cm wind tunnel at the University of Michigan for flow speeds ranging from 5 to 20 meters per second and -20 to +20 degrees angle of attack for a reduced aspect ratio section (AR=0.25) with end plates.

Expectedly, the bimorph configuration showed an increase in stiffness of 50% under a tip line load as compared to the unimorph configuration. Contrary to intuition, the unimorph showed larger overall actuation range than the bimorph, due to its reduced stiffness and the asymmetric voltage requirements for MFCs. Measured by the embedded sensor, both the unimorph and bimorph configuration saw roughly proportional reductions in actuation range with increasing flow speed, corresponding to an approximately 50% reduction at 20 meters per second. The bimorph experienced much less slew in its actuation range than the unimorph, which experienced a 63% change in its actuation bounds at 20 meters per second solely due to variation in angle of attack.

Aerodynamic force comparison between the two concepts largely confirmed the results from the tip deflections. The results also showed the need for compensation for aerodynamic forces in the unimorph configuration for speeds above 10 meters per second. Both configurations were measured to consume approximately the same amount of power from a system-level perspective as the power was driven by the high voltage DC converters rather than the number of MFCs, which are largely capacitive. Compared to the unimorph configuration, the bimorph configuration proved a stiffer actuator that used the same power, increased mass by 37%, and showed reduced ability to change lift until approximately 20 m/s. Thus, the decreased aspect ratio section allowed for a simple comparison of the two configurations via mass, power consumption, and lift effectiveness.

The impact on aerodynamic forces due to the decreased aspect ratio was investigated by increasing the span of the airfoil with a rigid trailing edge, showing a reduction in lift sensitivity due to angle of attack of nearly 50%. An effective span ratio was developed to quantify the effect of the end plates and reduced aspect ratio on the lift. A larger aspect ratio unimorph concept was tested to confirm the extrapolated results using the effective span ratio. The extrapolated results confirmed that the unimorph exhibited superior ability to influence lift up to 15 m/s, reduced

from 20 m/s for the comparative test. The unimorph configuration was thus shown to provide superior control over lift for reduced mass and equivalent power consumption.

The results from this research were compared to other experimental and theoretical results from a simple unimorph and bimorph beam in actuation. This comparison confirmed that the asymmetric voltage limits applied to the bimorph were most likely the root cause for the unexpected advantage of the unimorph configuration. It was also confirmed by comparison of the aerodynamic results to theoretical modelling that aeroelastic modeling was needed to predict scalability of performance at higher flow speeds.

Chapter 4
Characterization of the Spanwise Morphing Trailing Edge Testbed

Previous chapters have introduced the design for the Spanwise Morphing Trailing Edge (SMTE) testbed as a finite wing for small UAVs and characterized the design considerations regarding both its active and inactive sections. The following chapter details the development and initial characterization of the SMTE concept, to inform a model for more precise investigation of expected benefits.

The first section, Section 4.1, describes the construction and characterization of the SMTE testbed as well as an equivalent articulated flap wing, for comparison with existing state-of-the-art technology. The characterization focuses largely on the measurement of control derivatives via non-intrusive displacement tracking with matched forces.

In the second section, Section 4.2, these control derivatives are compared with two-dimensional results to provide a reference for the measured values. Both the two-dimensional results from Chapter 3 and thin-airfoil theory are used to provide context for the relative magnitudes of the measured control derivatives.

The final section, Section 4.3, addresses the response of the SMTE at higher flow speeds. As stated previously, the novelty of the concept was centered on the smaller scale of aircraft for the SMTE test-bed as compared to previous variable camber trailing edge concepts, namely Low-Altitude and Medium-Altitude Long Endurance (LALE and MALE) UAVs. Because of the generality of the sizing for these aircraft, it was desired to determine how the concept would perform as flow speed, and dynamic pressure increased. Reflecting earlier results from the representative section in Chapter 2, the pre-strained silicone skin forward of the rear spar is

found to adversely limit the maximum speed of the testbed. Informed from previous tests, a sliding wiper design is implemented, increasing the SMTE's tip deflection range. This wiper design decreased the overall mass of the system and reduced impact on the airfoil forward of the rear spar while increasing the maximum allowable speed of the concept.

4.1. Initial control derivative characterization of SMTE

This section details the development and initial performance evaluation of a Spanwise Morphing Trailing Edge (SMTE) testbed for implementation in a low speed (M<0.1), high performance UAV and was derived from the previously published work[110]. The SMTE concept eliminated the gaps and sharp discontinuities in the wing surface associated with conventional control surface design, seen previously in Figure 2.1, while still permitting relatively independent spanwise variation in actuation control. It was expected that eliminating these discontinuities would provide improved control authority at varying flight conditions compared to conventional control surfaces with reduced aerodynamic losses. The following chapter represented the first force and deformation analysis of a morphing wing with a smooth surface allowing independent spanwise actuation for this scale of aircraft. The performance of the morphing concept was compared via experimental testing against discrete flap actuation for a representative half-span, finite wing in a wind tunnel.

4.1.1. Construction of morphing wing and equivalent articulated wing

4.1.1.1. Motivation for construction of finite wing

Although the previous test of the representative section in Chapter 2 allowed for a preliminary assessment of the authority of the actuators under aerodynamic loads, the resultant control configurations were limited by the number of actuators within the test section, namely two, and the limited size of the wind tunnel which prevented accurate testing of three-dimensional flow. Modelling the three-dimensional flow about the compliant section with sufficient fidelity to distinguish performance differences as compared to conventional flaps was deemed to be prohibitive in complexity due to the number of disciplines involved including complex geometries, smart materials, soft materials, and viscous flow. Accordingly, an experimental test for differential spanwise actuation was determined to allow for an initial assessment of performance capabilities. A finite wing was chosen to investigate the ability of the SMTE concept to adapt to spanwise changes in flow and separation at different flight conditions.

Differing spanwise flow scenarios corresponding to different flight conditions could then be created by varying the angle of attack of the wing.

4.1.1.2. Parameters of finite wing

The SMTE testbed, in accordance with the designs from Chapter 2, was constructed for a half-span finite wing with NACA 0012 airfoil and a chord of 0.305 m with 6 active sections. Including a 0.14 m cowling at the root to cover the mounting structure, the wing had semi-span of 0.91 m, resulting in an aspect ratio of 6. Prior investigation of the flexure box morphing aileron showed that the lighter "unimorph" version, utilizing only two MFCs (previously defined as Macro-Fiber Composites), was suitable for characterization of the maximum control benefits of the concept up to approximately 15m/s [108]. Accordingly only two MFCs were utilized in each active modular section. Each active section then consisted of an M-8557-P1 MFC from Smart Material Corporation, which is approximately 6.4 cm in active width. Each active section was spaced 12.8 cm apart spanwise, creating an effective 50% distribution of active and passive material over the span of the trailing edge of the wing.

The skin was constructed with an elastomeric honeycomb, which was adhered to a 0.25 mm thick silicone sheet with a two-part silicone mixture via a film-casting procedure with a Teflon-covered micrometer film applicator (Gardco AP-99501003/T). The stretchable trailing edge of the morphing skin was created by bonding two sides together for the last 0.6 cm of the chord using the same two-part silicone mixture, resulting in a 0.5 cm thick trailing edge. The skin was then adhered to the actuators via thin two-sided silicone to cyanoacrylate adhesive tape and was then pre-strained by approximately 10% to the leading edge where it was secured by high-strength adhesive. The construction of the morphing wing is shown in Figure 4.1a with inner honeycombs exposed during the construction process. To form a positive pressure surface under the silicone, balsa sheeting covered with Monokote provided a smooth, hard surface. This double-surface anticipated difficulties with the pre-strained silicone skin at higher flow speeds, utilizing previous experimental test knowledge for the SMTE representative section in Chapter 2. If the pre-strained silicone forward of the rear spar proved problematic at the test speeds, it could then be trimmed to form a wiper configuration, as discussed later in Section 4.3.2. However, for this initial investigation, it was desired to test a completely smooth outer skin, ideally minimizing the impact of viscous effects on the wing.

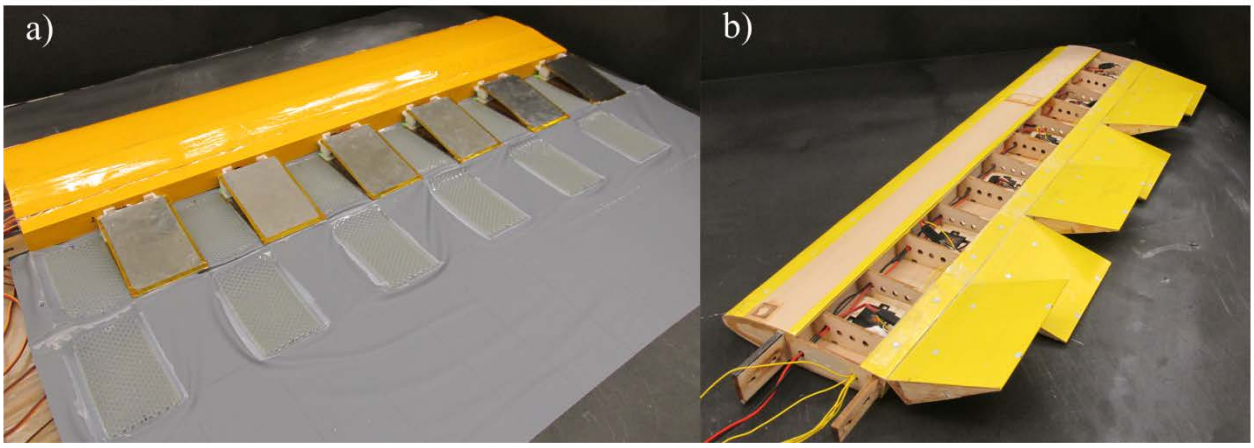

Figure 4.1 a) Construction of SMTE Wing with inactive honeycombs and active MFC sections
b) Servo distribution and hingeline in comparative discrete flap wing

Due to the relative complexity of the test article, a conventional wing composed of discrete flaps was also constructed to provide a comparative baseline against which the performance of the morphing wing could be identified. The flaps were sized to have a chordwise hingeline location equivalent to the beginning of the morphing sections. For consistency of comparison, both wings utilized mostly identical construction methodology forward of the rear spar. The wing box was constructed via carbon-fiber capped spars with integrated ribs and balsa wood sheeting for a pressure surface and, shown in Figure 4.1b.

Several efforts were made to minimize the impact of the hinge and servo-arm linkage on the flow and thus provide a fair assessment of the morphing wing with best practices in construction methodology for discrete control surfaces. The flaps were hinged with no gap along the top surface consistent with methodology used to minimize gap losses in conventional wings. The control arm was embedded within the airfoil profile surface so as not to cause additional drag. The maximum flap deflection angles of the servos were sized at approximately +/- 25^{o}, consistent with a typical application for UAVs. Although this tip displacement range exceeded that of the capabilities of the morphing wing, for initial assessment and practical comparison the range was not limited. Additional sections will address the impact of this on the range of the applicable ailerons. The active span of the articulated flap wing was divided into 6 flaps of

approximately 14 cm in span with no passive spanning sections. This allowed for a comparison of the morphing concept with discrete flaps of varying size.

4.1.1.3. Relevant metrics

Although currently subject to debate within the field, increased mass of a morphing concept relative to conventional designs has been generally viewed as a penalty that detracts from the desirability of the morphing concept. For example, morphing structures with increased mass could appreciably increase the rolling moment of inertia, thereby decreasing the maneuverability of the concept [111]. Accordingly, the mass should be minimized via high fidelity finite element should be minimized by high fidelity finite element analysis subject to constraints from FAR certification, in the manner of Molinari [112]. To document the additional mass of the SMTE concept as compared to the articulated wing, a component summary was compiled in Table 4.1.

Examining the mass, as constructed, the SMTE wing was approximately 38% heavier than the flapped wing, but as noted in Chapter 3, the additively-manufactured plastic components in the active sections of the wing account for 46% of the mass of the active sections, *i.e*. 15% of the mass of the total wing. As previously noted, the construction of the SMTE was not optimized to minimize mass. Had the structure and materials of the internal compliant mechanism for the active section been optimized by established best practices as the construction of the articulated wing was, the SMTE wing would weigh much less. For example, if the redundant wiring in the SMTE demonstrator and imagined a 50% reduction in the mass of the flexure box consistent with a choice of lighter material, the resultant wing would only be 20% heavier. This theoretical reduction would be consistent with replacing the plastic ABS (1.07 g/cm^3) within the morphing aileron with balsa wood (0.16 g/cm^3), regardless of physical dimension optimization. In this scenario, the mass of the morphing ailerons would be approximately equal to that of the servos, including flaps and linkages. The additional 20% increase in mass would be due solely to the skin and honeycombs. Currently, the construction methodology utilizing additive manufacturing severely restricted the materials available for use in the skin. However, if the wings were mass-manufactured, molding technology could potentially eliminate this discrepancy as well by increasing the range of materials available.

Table 4.1 Summary of Wing Component Mass

Component	Current SMTE (measured)	Flapped Wing (measured)	Balsa SMTE (theoretical)
Front section	686 g	686 g	686 g
Wiring	70 g	30 g	30 g
Servos	-	110 g	-
Flaps and Linkages	-	188 g	-
Morphing Ailerons	454 g	-	307 g
Skin	142 g	-	142 g
Honeycombs	72 g	-	72 g
Total Wing Mass	**1424 g**	**1028 g**	**1250 g**
High Voltage Amplifiers	102 g	-	102 g
Total Mass	**1524 g**	**1028 g**	**1352g**

Finally, the high voltage amplifiers were also considered in the total mass of the concept. Each of the amplifiers, previously utilized in Chapter 3 for uniform actuation, were designed for independent and simultaneous control of two MFC-driven control surfaces [85,99] . Accordingly for the SMTE testbed, only three amplifier circuits were needed. As previously discussed, state of the high-voltage amplifier rather than the position of the MFC drove the power consumption because the MFCs operated in a capacitive manner. Similarly, the mass of the high voltage amplifier boards did not represent the minimum achievable mass, but rather the minimum achievable mass that was readily available. Custom circuitry design of a board to minimize the overall mass could further reduce the figure if a single high voltage amplifier were optimized for the current configuration. Finally, the high voltage amplifiers could be stored anywhere in the aircraft because the loss in actuation due to long high voltage lines would be minimal. Accordingly, the electronics would not represent an appreciable consideration for comparison between the two wings.

Regardless of these modifications, it was desired to evaluate whether the SMTE wing could provide a metric of increased rolling moment on the order of 20% to be competitive with the conventional flap technology.

4.1.2. Initial investigation of spanwise-varying configurations

Both the SMTE and articulated wings described in Section 4.1.1 were tested for authority over aerodynamic control forces at varying flight conditions in the 1.5 m x 2.1 m wind tunnel at the University of Michigan, seen in Figure 4.2a. The goal was to measure any improvement in

control performance of the SMTE morphing concept over discrete flaps for differing spanwise flow conditions.

4.1.2.1. Setup description

A single flow speed of 10 m/s, monitored by a hot-film anemometer in the test section, was chosen with consideration to the aeroelastic results from the previous chapter to limit the degradation of the morphing control surfaces. Considerations for control degradation due to aerodynamic loads were the subject of Section 4.3. The aerodynamic forces on the wings were measured about quarter-chord at the root of the wing utilizing a calibrated 6-axis force balance, mounted below the wind tunnel, which continuously streamed analog voltage data to a National Instruments compact DAQ (cDAQ) utilizing the NI 92105 and NI 9264 analog input and output modules. The wings were mounted vertically in the wind tunnel, directly to the force balance, eliminating the need for a yoke or other mounting device that could interfere with the aerodynamic forces or restrict the actuation of the compliant wing.

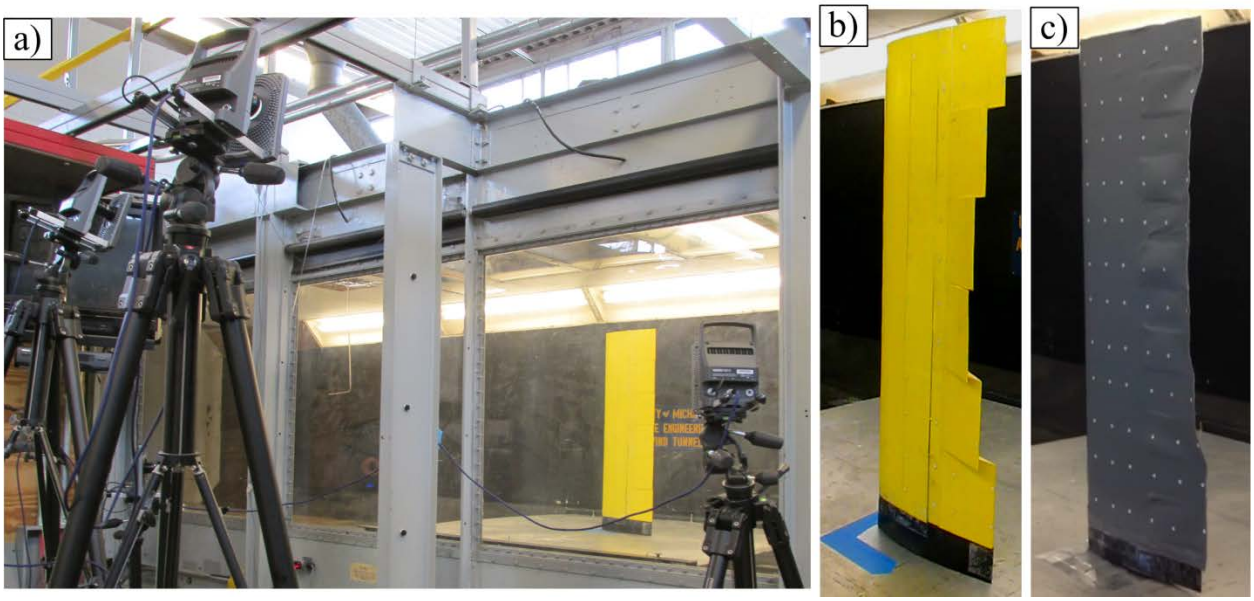

Figure 4.2 a) Vertically mounted finite wing in wind tunnel with tracking cameras
b) articulated flap and c) SMTE wings with quadratic variation (*S2*)

A ground plate approximately 30 cm from the floor of the wind tunnel was used to completely remove the wing from the boundary layer at the walls of the wind tunnel. A shroud shielded the force balance from the flow between the ground plate and floor of the wind tunnel. The gap between the finite wing and the splitter plate was necessary prevent the wing from rubbing against the ground plate, but the gap was minimized to ensure that it minimally impacted force results by allowing air to flow from the high pressure surface below the wind tunnel to the upper surface. The resultant gap between the wing root and the ground plate at the root of the wing was less than 0.6 cm, per general sizing recommendations by Barlow [113].

To estimate the quality of the experimental setup, the lift curve slopes of both wings were compared to finite wing theory. The relationship between the lift curve of an infinite-span wing was related to that of a finite wing by Equation (4.1), providing an estimate of the accuracy of the results [73]:

$$\frac{C_{L_\alpha}}{C_{L_{\alpha,2D}}} = \frac{1}{1 + \frac{C_{L_{\alpha,2D}}}{\pi e AR}} \qquad \approx 0.75 \tag{4.1}$$

where $C_{L,\alpha,2D}$ represented the two-dimensional lift-curve slope, $C_{L,\alpha}$ represented the lift-curve slope of the finite wing aspect ratio, *AR* represented the aspect ratio of the wing, and *e* was the Oswald efficiency factor. For an initial estimate that assumed maximum aerodynamic efficiency, *i.e.* where *e=1*, and given the lift curve slope of the NACA 0012 airfoil to be approximately 2π (rad^{-1}), the variation in lift due to angle of attack was expected to be limited to 75% of the two-dimensional value, due to downwash caused by the tip vortex.

Examining the unactuated wings, at several angles of attack ranging from -5^o to $+5^o$ and applying a linear fit, the slope of the lift curve was found to be approximately 70% of the two-dimensional value, representing less than 10% relative error as expected by finite wing theory, regardless of the spanwise efficiency of actuation. Thus the test setup was determined to provide sufficient accuracy for initial assessment of aerodynamic forces on a finite wing.

The positions of the flaps for the articulated flap wing were controlled internally by the digital servos to achieve the desired configurations. A pre-programmed Arduino Mega 2560 prescribed the necessary inputs to the servos according to configurations commanded by the cDAQ. For the SMTE wing, the Arduino control program was altered to utilize a time-averaged version of the PID positional control program, developed in prior work, to control the trailing edge position via calibrated embedded sensors [108]. Thus, similar to the control program within the servo, each morphing actuator within the SMTE concept continuously sought to reach each commanded position regardless of aerodynamic forces or the effects of the other actuators as conveyed by forces through the skin.

Novel to the experimental setup, positional data for the wings was measured non-intrusively via circular reflective markers, seen in both Figure 4.2b and Figure 4.2c, which were tracked via VICON Tracker utilizing a motion-capture system. The system consisted of four cameras positioned outside the wind tunnel, three of which were shown in Figure 4.2a, to independently track the three-dimensional positions of the reflective markers. This measurement system allowed for independent, non-intrusive measurement of the prescribed actuations to the control system. Once a prescribed configuration was achieved, the time-average positional data of the wing and resultant aerodynamic forces were recorded.

4.1.2.2. Test description

Two angles of attack, 5^o and 10^o, were chosen to represent flight conditions with attached flow and near-stall, respectively. To identify the capabilities of the two concepts to affect aerodynamic loads, several different spanwise variations in actuation were tested at each flight condition. Eight uni-directional and three spanwise-varying actuation configurations, shown in Figure 4.3 and Figure 4.4, respectively, were chosen to study the ability of the two wings to control aerodynamic forces at the different flight conditions. These figures showed the tip displacement of the configurations, and the equivalent flap angle, discussed further in Section 4.1.2.4. Note that, keeping with common sign conventions, positive δ_{tip} was downward, signifying a positive change in lift.

Eight uni-directional actuation configurations were chosen to study the effect of increasing the relative span of the control surface on the effectiveness of the actuated section. Thus, the actuations studied used an increasing number of actuators at their maximum possible

actuation. For simplicity of reduction in test parameters, only the maximum allowable actuations were tested for each wing. The unactuated configuration, *U0*, served as a baseline for comparison of aerodynamic forces between the two concepts, representing a clean, unactuated wing. Positive actuation was the focus of investigation, representing an increase in lift beyond the baseline caused by the positive angle-of-attack of the testing conditions. Thus configurations *U1+* through *U6+* were tested to symbolize an increasing-span flap or morphing surface beginning from the tip. Configuration *U6-* was chosen as a mirror-case for *U6+* to investigate alleviation of aerodynamic loads.

Examining the difference in magnitudes between the SMTE and articulated flap wing in Figure 4.3, the conventional servo-driven articulated flaps allowed for significantly larger tip-deflections, specifically greater than six times the total range of the SMTE. However, the relatively smooth variation of camber and spanwise actuation were expected to provide improved relative actuation over the discrete flaps. The variations in position between the configurations at the different angles of attack were a result of positioning errors in the control system as the actuators attempt to compensate for aerodynamic loading.

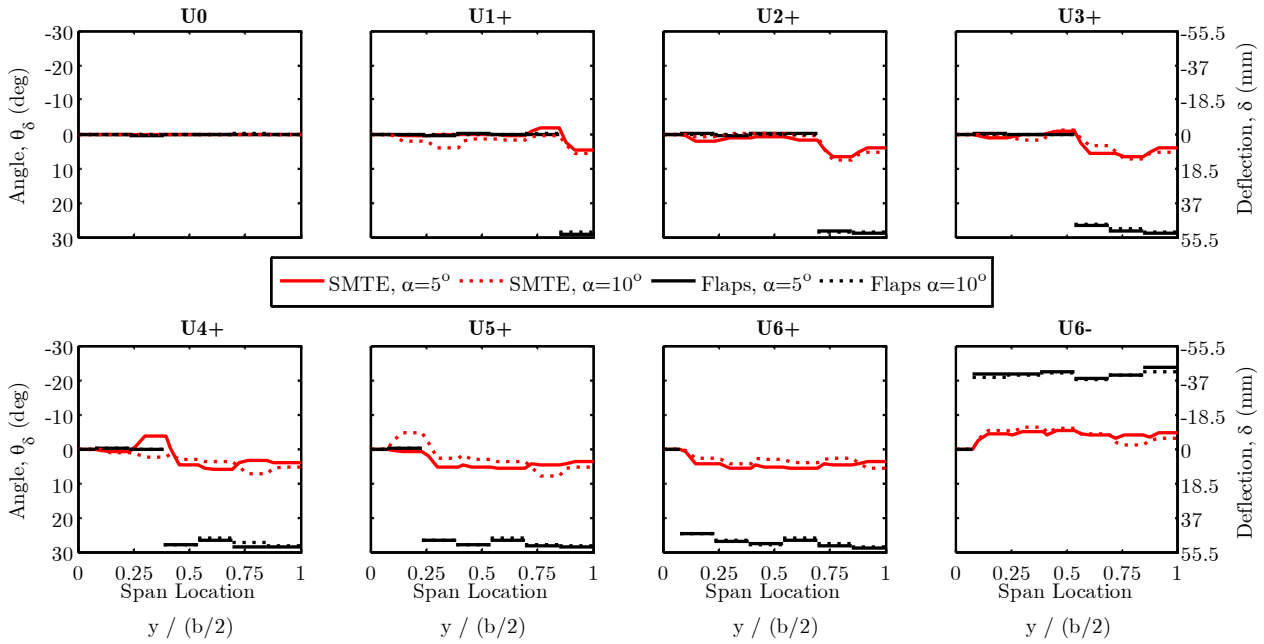

Figure 4.3 Uni-directional actuation configurations for SMTE and Articulated flap wings

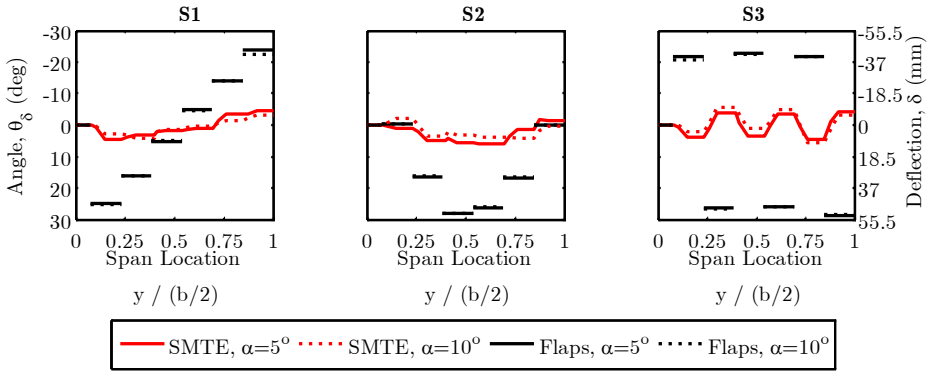

Figure 4.4 Spanwise-varying actuation configurations for SMTE and Articulated flap wings

The three spanwise actuation configurations chosen were a linear, quadratic, and sinusoidal (or braking) spanwise variation, shown in Figure 4.3. These configurations were symmetric about the spanwise-distribution of actuators and did not "adapt" to the downwash caused by the tip vortex, but rather were prescribed actuations. Configurations S1 and S3 were expected to generate no net change in lift or roll moment but large changes in drag due to their symmetry about U0. Configuration S2 was expected to generate lift, but with reduced losses in the flapped wing due to the gradual spanwise actuation.

4.1.2.3. Force measurements

The variation of forces created by the control surfaces at the tested flight conditions were summarized in Figure 4.5. These forces provided a general understanding of the comparative trends between the two wings. Changes in lift and rolling moment were shown as potentially desirable signed forces for aircraft control, while drag is the associated penalty for actuation. Pitching moment was also included for reference with respect to two-dimensional results, but could be viewed as a penalty or desired quantity dependent on the particular aircraft design. A cursory analysis of the comparative magnitudes and trends seen in the forces follows.

Beginning with the flapped wing, it was seen that increasing spanwise flaps (*U0* → *U6+*) resulted in an increase in lift at both flight conditions. For the stalling flight condition, $\alpha=10^{o}$, configurations *U4+* to *U6+* showed no increase in lift or pitching moment even as more flaps are actuated. At this flight condition configuration *U6 +* represented a slight decrease in roll moment, even as lift increased, showing the effects of tip stall. Additionally, the drag rise associated with actuating all flaps at this condition was significantly higher.

Comparatively, the SMTE wing was just as effective at increasing lift with increased span-actuation for attached flow at 5^o while decreased drag penalty. The ability of the SMTE wing to affect roll was also not as large as the flapped wing, as the relatively larger displacements near the wingtip largely dominated its ability to create rolling moment. Interestingly, examining the pitching moment showed was governed by the separation associated with the actuation method rather than the flight condition, and correlated most closely with drag.

Examining the spanwise-varying configurations for both wings, the linear (*S1*) and sinusoidal (*S3*) configurations were seen to effectively produce drag with very low lift, pitching or rolling moment, corresponding to a "braking mode". This result was expected as these configurations are relatively symmetric about the unactuated configuration. The quadratic (*S2*) configuration showed an increased in lift and drag relative to the baseline configuration, but it was difficult to determine the relative effectiveness of these configurations compared to uni-directional actuation.

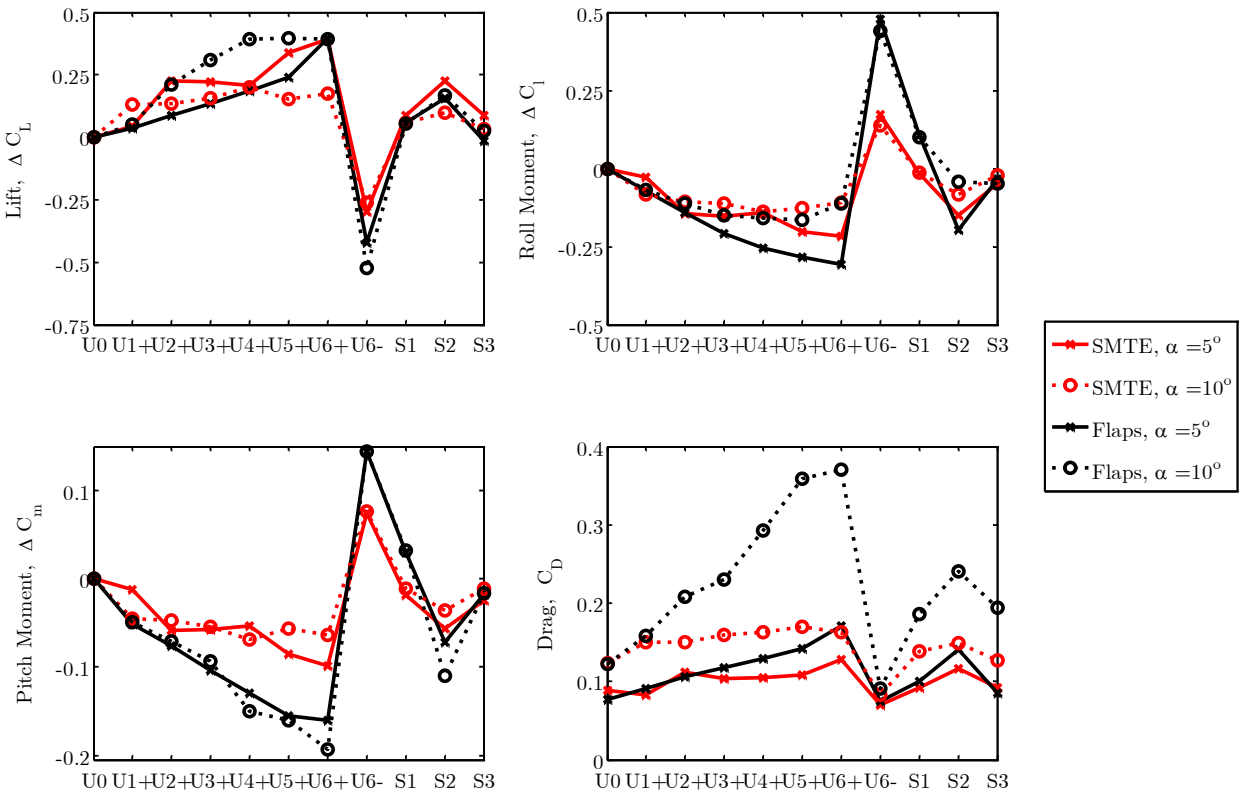

Figure 4.5 Change in non-dimensional forces for SMTE and Articulated flap wings

In summary, the SMTE wing did not generate roll or pitching moments magnitudes equal to the articulated flap wing. Still, the comparable lift and lower drag for the attached flow condition drew interest to the efficiency of the SMTE. However, the ranges of the two control concepts were not matched and the viscous effects due to flow separation were not quantified. To better gauge the comparative efficiency of these different wings and configurations, additional metrics were required and were the subject of investigation in the following sections

4.1.2.4. Experimentally measured secant control derivatives

As seen in the previous section, analyzing the change in aerodynamic forces between different wings and configurations beyond basic trends was difficult due to many different factors including: the interplay of spanwise actuation with the tip vortex, the inboard flap vortex, accounting for differences in range, and positioning errors for the individual actuators. To better compare the effectiveness of the two wings over the different actuation configurations, a performance metric was needed that accounted for these factors. This metric needed to include information about the magnitude of both chordwise and spanwise actuation as well as the resultant change in forces. As a common feature of both wing designs, the magnitude of the tip displacement for each configuration was used to summarize control authority.

Actuation authority was examined by normalizing the nondimensional forces with the equivalent flap angle derived from the tip displacement. The lift control derivative was derived from the measured experimental values as

$$C_{L_\eta} = \frac{\partial C_L}{\partial \eta} \approx \frac{\Delta C_L}{\Delta \eta} \tag{4.2}$$

where C_L was the lift coefficient, and η was the equivalent angle of a similarly-sized flap to reach the same tip deflection. In equation form, the equivalent flap angle η, was defined by the relationship:

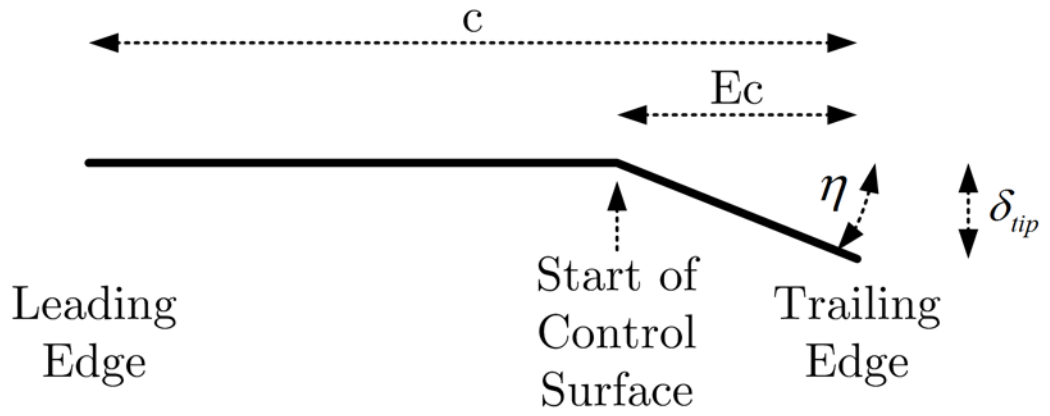

Figure 4.6 Thin airfoil representation of flapped airfoil

$$\eta = \tan^{-1}\left(\frac{\delta_{tip}}{E \cdot c}\right) \tag{4.3}$$

where δ_{tip} was the tip deflection of the control surface, c was the chord, and E was the fractional chordwise location of the equivalent hingeline measured from the trailing edge of the airfoil, as presented for an idealized thin airfoil, as pictured in Figure 3.9.

The equivalent flap angle could be less intuitive than simply normalizing the tip deflections by the chord, such as:

$$C_{L_\delta} \approx \frac{\Delta C_L}{\delta_{tip} \,/\, c} \tag{4.4}$$

where δ_{tip} was the deflection of the tip and c was the chord of the airfoil. However, the two metrics were related by a linearization of Equation (4.3) by a Taylor series expansion as:

$$\eta = \tan^{-1}\left(\frac{\delta_{tip}}{E \cdot c}\right) \approx \frac{\delta_{tip}}{E \cdot c} - \frac{1}{3}\left(\frac{\delta_{tip}}{E \cdot c}\right)^3 + \ldots \tag{4.5}$$

where the higher order terms of the expansion were omitted. A bound on the error for the angle when approximating the equivalent flap angle of the control surface as a linear function of the trailing edge deflection was then bounded by the second term in the expansion in Equation (4.5). For the parameters chosen for the SMTE testbed, per Table 2.1 and the data from Chapter 3 From Figure 3.26, a first order approximation for the SMTE control derivatives, as first published by Pankonien [110] utilizing Equation (4.4) resulted in less than 5% difference as

opposed to Equation (4.2) . Then, for simplicity, the equivalent flap angle of the SMTE and the tip deflection could be thought of interchangeably. For the articulated flap, several points on the flap surface were used to calculate the actual flap angle, eliminating angle measurement error for larger deflections. Still, the tip deflection was included as a linearized estimate of performance.

4.1.2.5. Control derivatives for uniform actuation

For uni-directional actuation, the control derivatives for both wings were approximated by dividing the change in nondimensional forces from the unactuated configuration (*i.e.* ΔC_L, ΔC_l, ΔC_m, ΔC_D) by the spanwise integral of the equivalent flap angle, normalized by chord. An example calculation for the lift control derivative was:

$$C_{L_\eta} = \frac{\partial C_L}{\partial \eta} \quad \approx \quad \frac{\Delta C_L}{mean(\eta)} = \quad \frac{\Delta C_L}{\int_{\bar{y}=0}^{\bar{y}=1} (\eta)\, d\bar{y}} \tag{4.6}$$

where η was the equivalent flap angle defined by Equation (4.3) from the inverse tangent of the tip deflection data.

This metric thus included force and displacement data, taking into account the span of the deformed section, chordwise control surface sizing and the magnitude of actuation. Since the tip displacements were measured directly from recorded data, these derivatives also accounted for positioning errors from the actuators. For simplicity of examination, the magnitude of the various control derivatives for lift, rolling moment, pitching moment and drag were summarized for the uni-directional configurations in Figure 4.7.

These results represented the first time that these control derivatives were externally and non-intrusively measured to investigate the control surface sizing for a compliant morphing wing. Although the “Smart Wing” concept nonintrusively measured flap positions via reflective discs and video model deformation as well as Moire interferometry, the results were not reported for any variation in active span size or other configurations [19]. Additionally, by that phase of the research, all smart materials had been eliminated from the concept.

As shown in the following sections, the current methodology was especially useful for effectively calculating derivatives with errors in positioning states, which can be inherent to compliant structures. Also, this methodology allowed for measurement of the state of the

inactive sections without intrusive sensors that could restrict the actuation, which was highly necessary for soft structures.

By examining the control derivatives for the flapped wing, trends from the Section 4.1.2.3 became more apparent. By increasing the actuated span of the actuated flap also increased the magnitude of the lift control derivative for the flapped wing at $\alpha=5^o$. This result highlighted the increasing efficiency of a larger flap where the relative effect of in the inboard flap vortex decreased relative to increasing flap size. However, at $\alpha=10^o$ the lift control derivative did not strictly increase with increasing span-actuation of the flapped wing. This non-intuitive result was explained by the much higher drag derivative for this angle of attack as the flapped wing actuation results in flow separation with a higher marginal drag penalty. This result was further reflected by the sharply decreasing roll moment derivative for the flap wing at $\alpha=10^o$.

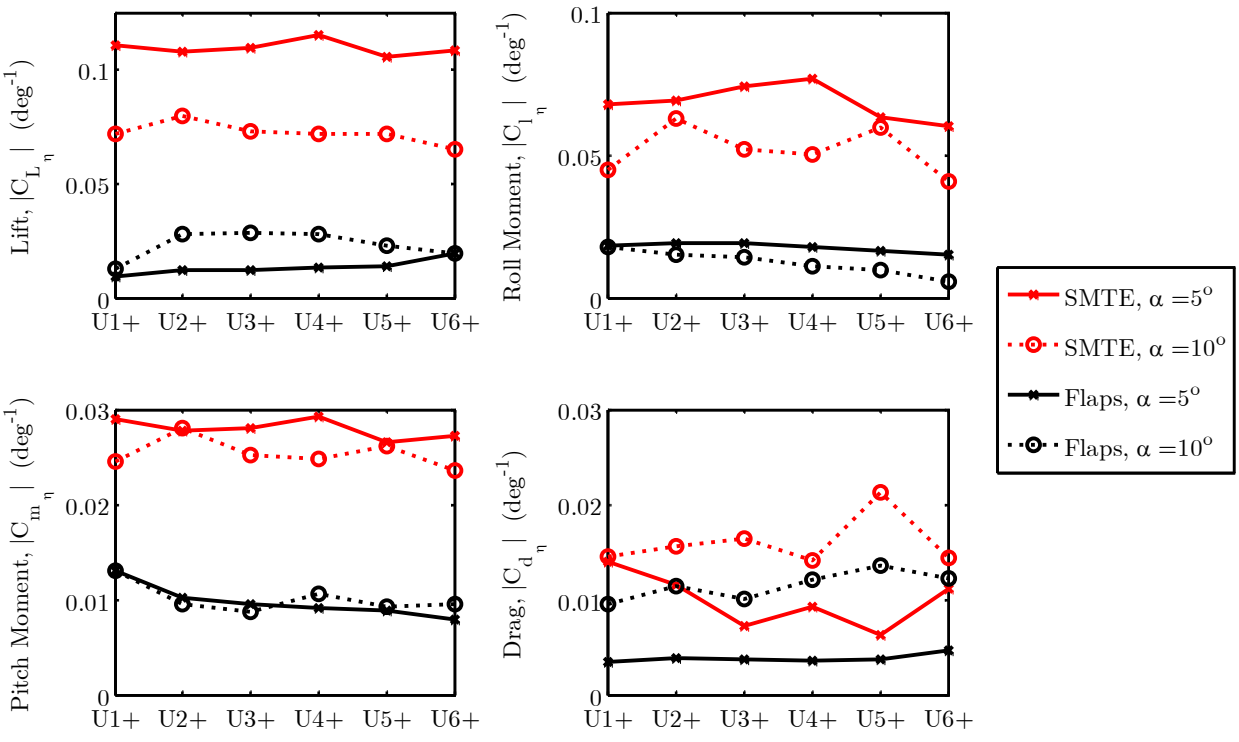

Figure 4.7 Control derivatives for uni-directional configurations

Comparatively, the lift control derivatives for the SMTE did not change as significantly with increasing-span actuation, due to the lack of inboard vortex and the suppression of separation by the smooth shape change. Comparing the magnitude of the control derivatives between the two wings, the SMTE exhibited much greater control over forces for lift and rolling moment (approximately 3 to 4 times) when normalized by tip displacement, but only one to two times as much in drag and pitching moment. These results warranted closer analysis between the wings by matching the tip displacements of the two concepts and comparison with modelled results. Still, the result also motivated morphing designs with larger deflection ranges to further capitalize on this expected improvement due to a smooth surface.

4.1.2.6. Control derivatives for non-uniform actuation

Comparing control derivatives for the spanwise-varying configurations required the mean of the magnitude of the tip displacements to be used in the calculation rather than the mean of the tip displacements. A metric was then defined by dividing the absolute value of the nondimensional forces by the integral of the absolute value of the equivalent flap deflections as measured over the normalized half- span of the wing:

$$C_{L_{\|\eta\|}} = \frac{\partial C_L}{\partial \left|\eta\right|} \quad \approx \quad \frac{\left|\Delta C_L\right|}{mean\left|\eta\right|} = \frac{\left|\Delta C_L\right|}{\int_{\bar{y}=0}^{\bar{y}=1} \left|\eta\right| d\bar{y}} \tag{4.7}$$

where η was the equivalent flap angle defined by Equation (4.3) from the inverse tangent of the tip deflection data.

This metric inherently penalized any actuation from the un-actuated configuration. Intuitively, this comparative metric was useful because it quantified the relative efficiency of the spanwise varying configurations compared to the uni-directional configurations and thus was referred to as “force effectiveness”. Although the prior metric, which utilized signed rather than absolute values, better reduced positioning errors for finer evaluation of the lift and moment derivatives, it could not adequately assess spanwise symmetric configurations, such as *S1* and *S3*, as the integrals in their denominators would result in near zero values.

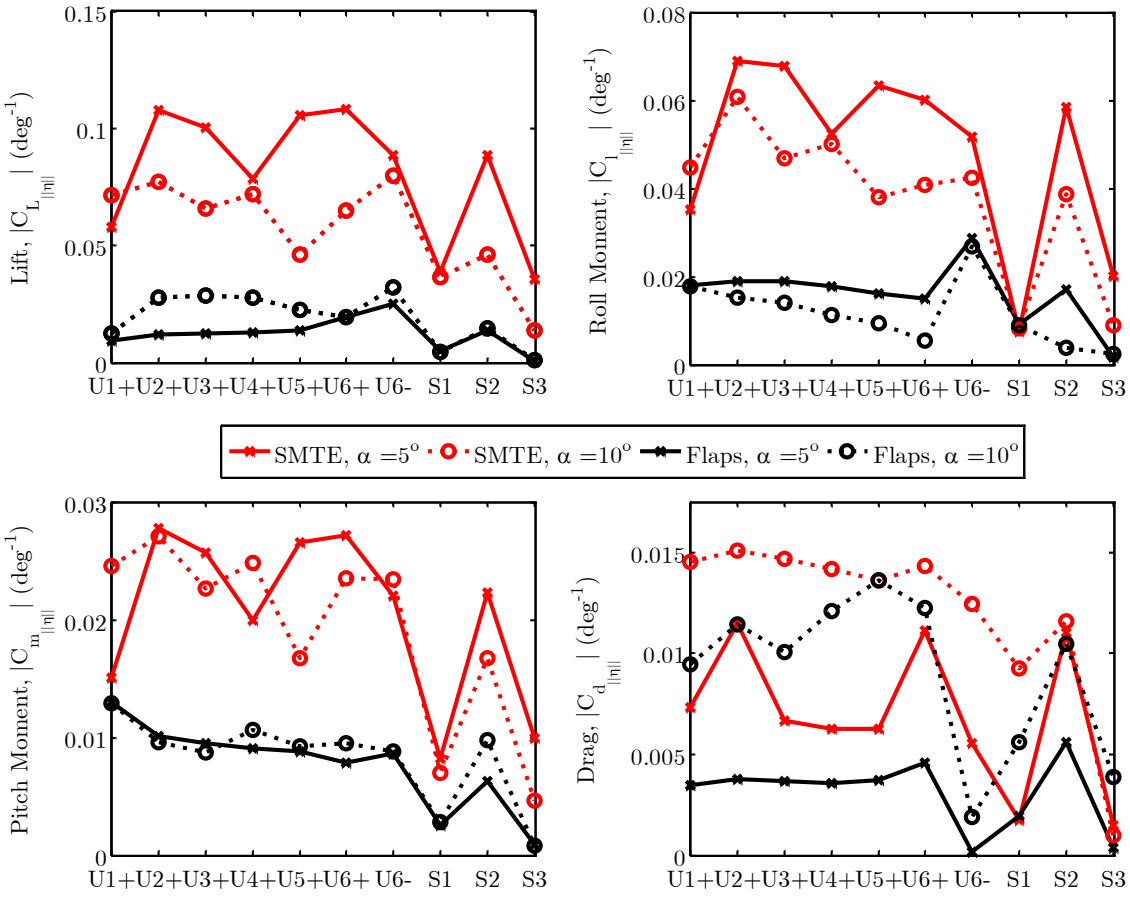

Figure 4.8 Control derivatives for uni-directional and spanwise-varying configurations

Utilizing this magnitude control derivative on all tested configurations, seen in Figure 4.8, the force effectiveness of the various configurations was examined. Examining the uni-directional configurations the positioning errors for the morphing configuration were less accounted for in this metric, but the same overall trends from the previous section remained. The *U6-* configuration showed that only slightly improved effectiveness in lift and rolling moment, achieved by actuating all of the flaps down opposite of the angle of attack, but even this effect was not sufficient to reach the efficiency of the smooth surface wing.

The most immediately apparent result was that none of the spanwise-varying configurations showed an improvement in effectiveness beyond that of uniform actuation. Additionally, the *S1* (linear) and *S3* (sinusoidal) configurations showed decreased efficiency below that of the uni-directional configurations for every metric, except drag. Interestingly, the

S2 (quadratic) configuration showed effectiveness equivalent to that of the uni-directional configurations for both the SMTE and flapped wing. Examining the physical configuration of the flapped wing in Figure 4.2b, the *S2* configuration was found to be nearly gapless spanwise due to the thickness of the airfoil. Thus, due to the particular geometry of this experimental setup, the *S2* configuration largely eliminated the gaps between the flaps as well as the resultant vortices.

This quadratic configuration (*S2*) then represented a control surface that could be fixed both inboard and outboard on the span of a lifting surface and still maintain the effectiveness of a free-free flap or even a fixed-free flap. The implication for this result was that a quadratically-varying (*S2*) configuration could potentially be integrated into a lifting surface where breaks in geometry were not possible or desirable, e.g. a wing ending in a winglet or control surfaces along a blended-wing body aircraft, without a loss in control surface effectiveness.

4.1.3. Summary of initial characterization

The previous section detailed the development and initial performance evaluation of a Spanwise Morphing Trailing Edge (SMTE) control surface for performance improvement of a low speed (M<0.1) UAV. This morphing design sought to reduce the aerodynamic losses associated with adapting to varying flight conditions by creating arbitrary spanwise-varying camber along the trailing edge of a wing, free of discontinuities. The morphing concept was realized via a modular concept for a 0.9 m span finite wing consisting of twelve alternating active and passive sections. The active sections were driven by conformally bending MFCs and the passive sections were made with anisotropic honeycombs bonded to a pre-strained skin. A comparative wing composed of six differentially-actuating, servo-driven flaps was constructed for comparison with the morphing design. Both wings were tested in a wind tunnel at two different angles of attack, 5^o and 10^o for a flow speed of 10 m/s (Re=2x10^5), representing attached and separating flow flight conditions. At these two conditions, the aerodynamic control forces and tip displacements of both wings were measured and compared for eleven different actuation configurations. Non-intrusive measurement of positional actuation was also achieved with a motion capture system, tracking reflective markers spread along the trailing edge.

To account for the difference in ranges of tip displacement, control derivatives for both wings were calculated using the change in nondimensional forces as well as deviations in measured tip displacement from the unactuated configurations. Although control derivatives

have been well established in literature, this represented the first time that these control derivatives were directly measured and examined for a spanwise-varying configurations of a compliant wing.

The results showed that for attached flow, increasing the span of a flapped wing improved the relative performance by decreasing the relative effect of the inboard flap vortex. However, for separating flow, increasing the flap span did not strictly increase lift or roll control, but uniformly increased drag. The morphing wing did not show either of these effects, exhibiting the benefit of a smooth morphing surface to eliminate spanwise losses due to actuation while better controlling separation. Additionally, for attached flow, the morphing wing achieved comparable change in lift for less drag.

Examining the measured control derivatives for the uni-directional configurations, the SMTE showed much greater control over forces for lift and rolling moment (approximately 3 to 4 times) when normalized by tip displacement via flap angle, but only one to two times as much in drag and pitching moment. Comparing control derivatives for the spanwise-varying configurations required the mean of the magnitude of the tip displacements via equivalent flap angle to be used in the calculation rather than the mean of the equivalent flap angle, creating a new metric: force effectiveness. The linear and sinusoidal configurations showed decreased effectiveness compared to uni-directional actuation, but the quadratic (*S2*) configuration showed effectiveness equivalent to that of the uni-directional configurations for both the SMTE and flapped wing. The implications for this result were that a spanwise-varying (*S2*) configuration could potentially be integrated into a lifting surface where breaks in geometry were not possible or desirable while maintaining the efficiency of a uniform actuation. These results warranted closer analysis between the wings by comparison with previous experimental results and modeled results, motivating the following section.

4.2. Comparison with two-dimensional results

To better relate the results from the finite wing with those from two-dimensional results, the control derivatives from the previous sections were then compared with the two-dimensional results from Chapter 3. This comparison provided an assessment of how the method from Section 4.1 related to the unrestricted measurements in two dimensional flow. Because the prior measurements were made at different flow speeds, they also provided understanding regarding

the potential scalability of the concept. To provide additional context, the control derivatives were also compared with the "higher order" conformal surfaces from Chapter 2, via thin airfoil theory, which assumed potential flow ignoring any viscous effects.

4.2.1. Analysis of control derivatives from previous two dimensional results

The change in forces and tip deflections from the large aspect ratio test of the unimorph active section from Chapter 3 were analyzed to provide control derivatives for comparison with the SMTE testbed. For simplicity of analysis, the force and deflection results were not scaled by the previously-derived effective span factor because the lift curve slope estimated that the results would be within 5% error of an infinite wing.

The control derivatives for lift, pitching moment and drag were determined by dividing the difference in nondimensional forces of the maximum and minimum possible actuations by their respective differences in equivalent flap angle. The control derivatives were then plotted against angle of attack over the measured flow speeds to investigate the linearity of the control derivative at various flight conditions, namely angle of attack and flow speed, as seen in Figure 4.9 through 4.11.

The lift control derivative, $C_{L,\eta}$, was relatively uniform for angles of attack near zero degrees, the flight condition where drag was minimized for the symmetric NACA 0012 airfoil. $C_{L,\eta}$ was then found to range from slightly greater than 0.1 (deg^{-1}) to approximately 0.07 (deg^{-1}) at $\alpha=10^o$. However, this metric changed by almost 50% over the tested range of angles of attack. As the magnitude of the angle of attack increased, approaching stall, the control derivative decreased because the maximum achievable lift was limited but not the tip deflections. This was the expected cause for the reduction in lift derivatives for both the SMTE and the articulated flap wing at $\alpha=10^o$. Examining the effect of flow speed in in Figure 4.9b, the lift control derivatives were largely unaffected by increasing flow speed and instead governed largely by how close the airfoil was to the stall condition near $\alpha=10^o$.

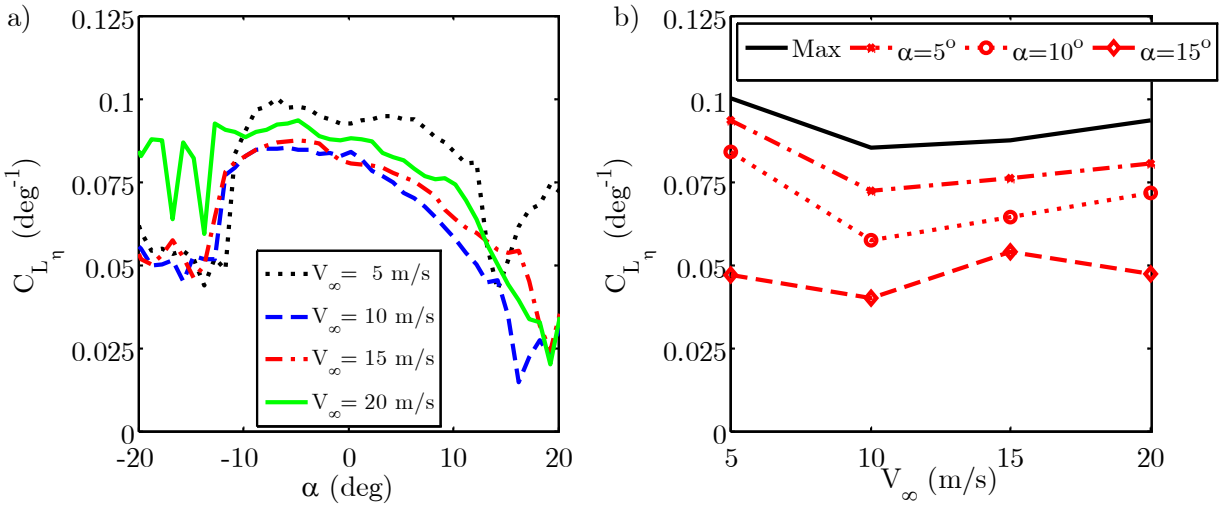

Figure 4.9 Lift control derivative for 2D Unimorph by varying a) angle of attack and b) speed

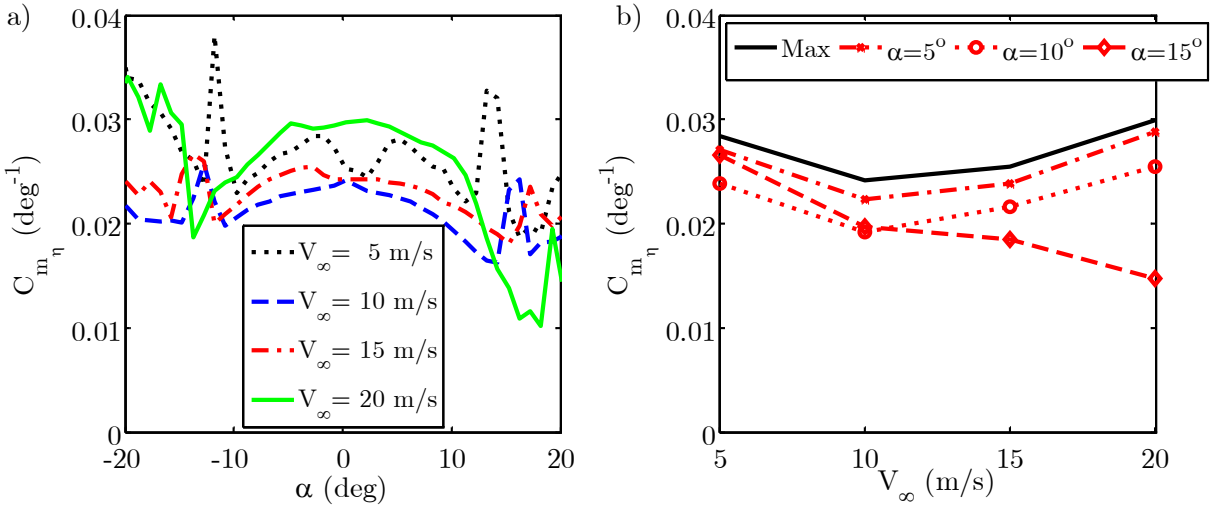

Figure 4.10 Pitching moment control derivative for 2D Unimorph by varying a) angle of attack and b) speed

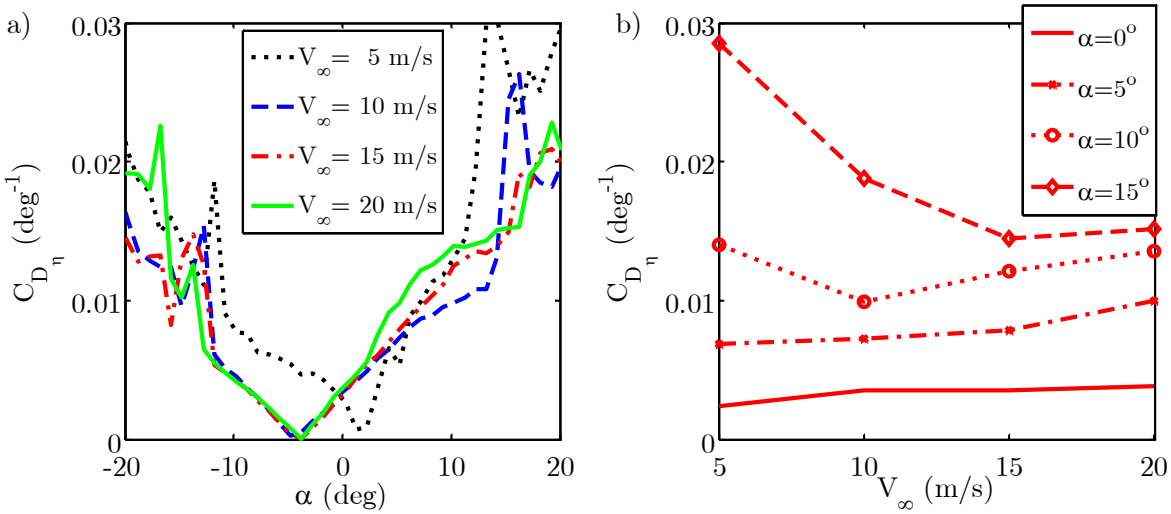

Figure 4.11 Drag control derivative for 2D Unimorph by varying a) angle of attack and b) speed

The pitching moment derivative was more uniform than the lift coefficient across all angles of attack, shown by the close grouping in Figure 4.10b. Also, the pitching moment derivative showed relatively little change in value until after stall. The values ranged from approximately 0.02(deg^{-1}) to 0.03(deg^{-1}) depending on the flow speed. Then there were large variations in magnitudes after stall.

Finally, the drag derivative was shown to vary greatly with both angle of attack and flow speed as seen in Figure 4.11. The linearity of the increasing magnitude of control derivative in Figure 4.11a near zero angle of attack implied a second-order relationship between equivalent flap angle and drag. However, only two configurations were measured at each angle of attack. Accordingly it was desired to measure more variations in equivalent flap angle for comparison in future tests. Also, the centering of the different slopes about shifting non-zero values showed the importance of precise airfoil positioning when evaluating drag. Despite the large change in drag derivatives, they were used to roughly compare with the values from the SMTE test along with the other control derivatives to provide an estimate of the validity of the previous test results. Still, drag derivatives were determined to be an imprecise and flight-condition dependent metric.

Table 4.2 Comparison of Experimental Control Derivatives

	Condition	2D Unimorph	Uniform SMTE	Uniform Flap
Lift $C_{L_\eta}\left(\cdot 10^2\right)$	Max value	9.16	-	-
	α=5°	8.07	9.89	2.20
	α=10°	6.94	7.31	2.50
Pitching Moment $C_{m_\eta}\left(\cdot 10^3\right)$	Max value	27.0	-	-
	α=5°	25.5	24.7	8.20
	α=10°	22.5	23.5	9.20
Drag $C_{D_\eta}\left(\cdot 10^3\right)$	α=0°	3.33	-	-
	α=5°	7.99	8.45	2.66
	α=10°	12.4	13.3	7.62

The control derivatives for the two-dimensional unimorph tests were compiled in Table 4.2 for comparison between the values taken between the *U6+* and *U6-* configurations from the SMTE at various angles of attack. From this analysis, the results were seen to correspond well with the two dimensional results for both angles of attack. When comparing both results to the averaged results from the articulated flap wing, the flapped wing had a much lower lift and pitching moment derivative than the SMTE wing. Encouragingly, the ratio of lift to drag derivatives for the SMTE was 41% higher than that of the flapped wing. This metric indicated that for the same step size in tip deflection, the SMTE could generate approximately 30% less increase in drag for the same lift. Although the drag control derivative was shown to exhibit large sensitivity to angle of attack and flow speed, this comparative improvement in performance warranted further investigations for smaller flap deflections, which were explored in Chapter 5.

4.2.2. Thin airfoil theory

To provide an additional comparison for these values, thin airfoil theory, as originially recommended by Sanders [77] was used to calculate the approximate lift and pitching moment control derivatives. Note that no drag derivatives could be calculated using thin airfoil theory, *i.e.* linearized potential flow, which was inviscid. Kuethe *et al.* page 152 [114], provided explicit of the expected performance of a discrete flap due to thin airfoil theory in a similar manner to that from Chapter 2. By providing a coordinate transfer:

$$\cos(\theta) = 1 - 2\frac{x}{c} \tag{4.8}$$

where x was the chordwise position, and c the airfoil chord, θ the conformal mapping coordinate which reparameterized the airfoil from the cartesian to the polar domain. Thus the start of the trailing edge control surface in the polar domain,θ_h ,could be expressed as:

$$\theta_h = \cos^{-1}(2E - 1) \tag{4.9}$$

where E was the Cartesian start of the control surface normalized by the chord of the airfoil. The mean camber line of the airfoil was then estimated for several flaps of increasing order polynomials. The point of this exercise was to estimate the effect of the aft-shifting of camber of the control surface. In the style of Sanders [77], the slope of the mean camber line, from Equation (2.1), for an N^{th} order polynomial control surface was:

$$\begin{aligned} \frac{dz}{dx} &= 0 && \text{where} \quad x < cE \\ \frac{dz}{dx} &= \frac{\delta_{tip} N}{c \cdot E^N}\left(\frac{x}{c} + E - 1\right)^{N-1} && \text{where} \quad x > cE \end{aligned} \tag{4.10}$$

where x represented the chordwise position, z represented the location of the mean camber line normal to the chord, and δ_{tip} the matching tip deflection for the various "orders" of airfoils. For reference, several airfoils with mean camber lines described by various orders of polynomials were plotted in Figure 4.12 for clarity.

From Kuethe[114], the control derivatives from thin airfoil theory were given by:

$$\begin{aligned} \frac{\partial C_L}{\partial \eta} &\approx \frac{\Delta C_L}{\eta} = \frac{2\pi A_0 + \pi A_1}{\eta} \\ \frac{\partial C_m}{\partial \eta} &\approx \frac{\Delta C_{m_{c/4}}}{\eta} = \frac{\pi / 4\left(A_2 - A_1\right)}{\eta} \end{aligned} \tag{4.11}$$

where the coefficients A_n were derived from the slope of the given mean camber line. The coefficients were defined by the following equations:

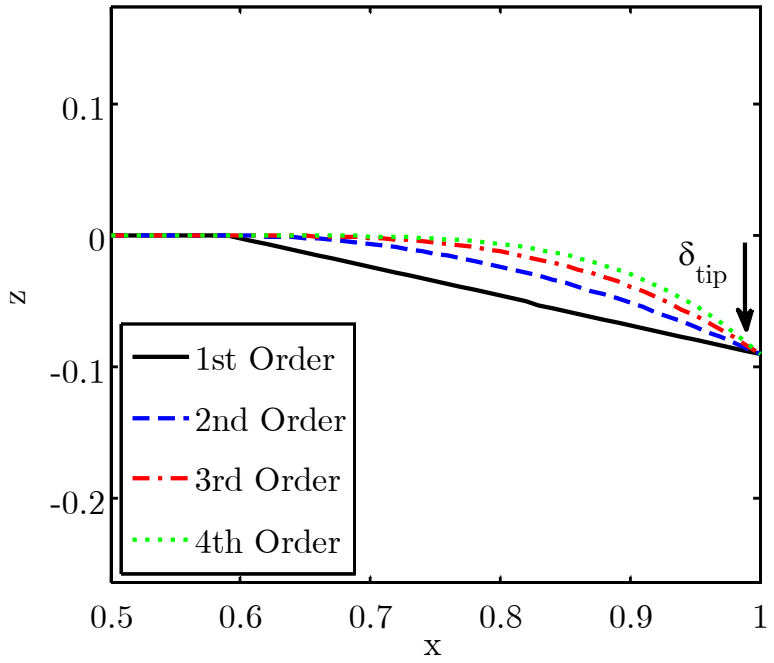

Figure 4.12 Mean camber lines of varying order polynomial conformal flaps

$$A_0 = \frac{1}{\pi}\int_0^{\pi} \frac{dz}{dx} d\theta$$
$$A_N = \frac{2}{\pi}\int_0^{\pi} \frac{dz}{dx}\cos(n\theta)\, d\theta \quad \text{where } n \geq 0 \tag{4.12}$$

which utilized the polar domain for evaluation of the integral, and was defined piecewise about the chordwise starting position of the control surface. The integrations were carried out numerically using Mathematica for several "orders" of control surfaces with the same chordwise sizing as the SMTE test bed. The results were compared to the experimentally measured control derivatives from the previous sections, in Table 4.3.

The SMTE from the initial test seemed to produce lift roughly equivalent to a 1st to 2nd order polynomial control surface, when ignoring viscous effects. Yet, the pitching moment was equivalent to a 4th order surface. This discrepancy was initially explained as the result of viscous forces near the trailing edge of the airfoil. The most dramatic result from this analysis was that the flapped wing was producing much lower lift control derivative than expected by thin airfoil theory, a reduction of almost 74%. As seen in the analysis from the 2D unimorph experiments, the lift control derivative decreased with increasing angle of attack, and fell-off sharply when flow separated. It was concluded that the large deflections of the flap (greater than 15 degrees in both directions), resulted in flow separation near the trailing edge, spoiling the flap effectiveness.

This result was partially questioned by the pitching moment which was close to the expected result for a discrete flap, which would be modelled by *N=1*. To provide an accurate comparison of the control derivatives with an articulated flap wing at the same flow speed, it was then necessary to better match the range of the flapped wing with the SMTE wing. Still, it was expected that even if the inviscid control derivative result for the flapped wing was recovered, the SMTE would show an improvement in lift control derivative of approximately 20%, which could be leveraged for improved control performance.

Table 4.3 Experimentally Measured Control Derivatives compared to Thin Airfoil Theory

	Condition	2D Unimorph	Uniform SMTE	Uniform Flap	Thin Airfoil Theory N=1	N=2	N=3	N=4	N=5
Lift $C_{L_\eta}\left(\cdot 10^2\right)$	Max	9.16	-	-	8.28	10.1	11.2	12.8	13.9
	α=5°	8.07	9.89	2.20					
	α=10°	6.94	7.31	2.50					
Pitching Moment $C_{m_\eta}\left(\cdot 10^3\right)$	Max	27.0	-	-	10.1	15.7	20.0	23.5	26.6
	α=5°	25.5	24.7	8.20					
	α=10°	22.5	23.5	9.20					
Drag $C_{D_\eta}\left(\cdot 10^3\right)$	α=0°	3.33	-	-	-	-	-	-	-
	α=5°	7.99	8.45	2.66					
	α=10°	12.4	13.3	7.62					
Rolling Moment $C_{l_\eta}\left(\cdot 10^2\right)$	α=5°	-	6.85	1.76	-	-	-	-	-
	α=10°	-	5.17	1.22					

4.3. Increased speed testing and skin boundary condition modification

Although the SMTE, with uniform skin provided superior aerodynamic control as compared by linear control derivatives to the articulated flap wing, it was desired to examine the scalability of the concept. Specifically, it was desired to determine how the SMTE performed at higher flow speeds. Although Chapter 2 had shown that skin forward of the rear spar could adversely impact the maximum operational flow speed of the SMTE as well as the overall range of the concept, it had been desired to ensure a smooth surface over the wing due to the low Reynolds numbers at relevant flow speeds.

The following section showed that the SMTE, due to large front section of silicone skin, experienced panel flutter at flow speeds as low as 12 m/s, an unreasonably low maximum speed for LALE and MALE UAVs. To enable testing at higher flow speeds, the wiper with honeycomb configuration from Chapter 2 was tested, enabling flow speeds to at least 20 m/s.

4.3.1. Skin response to higher aerodynamic loads

Upon testing the SMTE from Section 4.1 at higher flow speeds (approximately 12 m/s), the skin and trailing edge of the wing began to oscillate relative to the fixed base of the wing, both with and without use of compensating controllers in the active sections. A video camera monitoring the wing during the ramp-up to the higher flow speed captured the effect which prompted the conclusion that the maximum allowable flow speed of the wing had been reached due to the skin experiencing panel flutter. Scaled data extracted from the video permitted measurements of the oscillation shown in Figure 4.13. From the set of previously-attached reflective markers for positional data measurement, the oscillations at the trailing edge were observed by the two points from Figure 4.13. The two points were the span-center of the trailing edge the two inactive sections that bracketed the third active section as measured from the root of the wing. Note that even due to errors in position measurement from the video, the oscillations were in-phase over the span of the wing, oscillating with a frequency of approximately 4 Hz.

Increasing the flow speed amplified the vibrations, barring higher flow speed testing. Additional characterization of the skin was not performed to prevent destruction of the SMTE testbed. Accordingly a revision in design was desired that permitted higher flow speed testing.

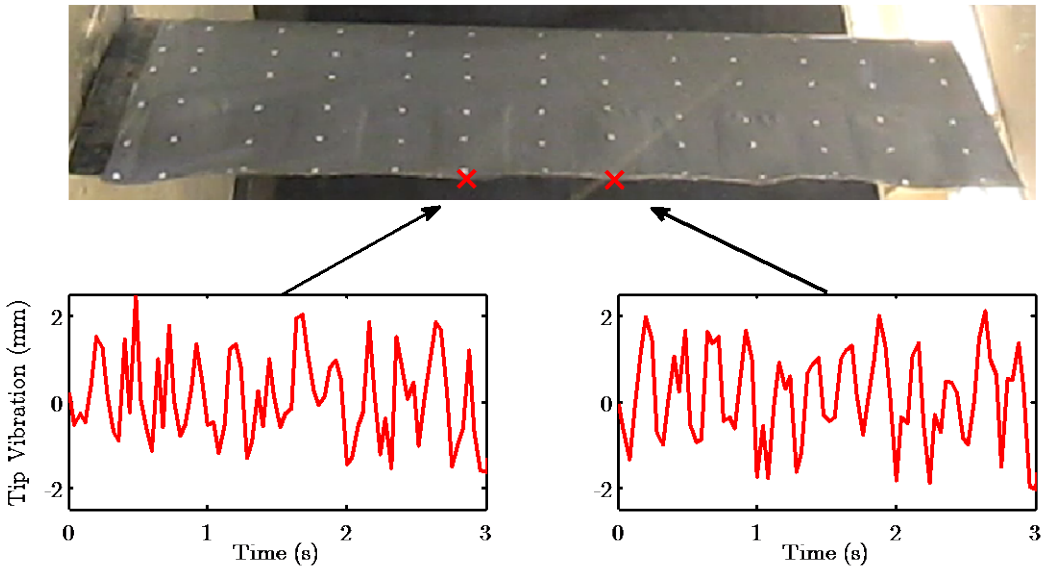

Figure 4.13 Representative tip vibrations relative to base of SMTE with pre-strained silicone skin forward of rear spar at approximately 12 m/s

4.3.2. Description of wing modification

Per the previous testing of the passive sections from Section 2.6, the skin surrounding the SMTE testbed was modified to utilize the "Spanning Honeycomb with Wiper" configuration that had previously been shown in Section 2.6.2 to allow testing up to flow speeds of at least 20 m/s.

Because no honeycombs had been used in the SMTE testbed in front of the rear spar, the modifications simply required trimming the skin to the rear spar, per the description of boundary conditions in Table 2.3. Due to the asymmetric design of the Flexure Box active section, the skin on the underside of the wing was affixed to the rear spar utilizing silicone to cyanoacrylate double-side tape (not pictured). The top side of the wing could not be affixed without severely restricting the range of the Flexure Boxes and eliminating the usefulness of the internal compliant mechanisms. Rather, the skin configuration that had previously been shown to maximize the range of the active sections was used, specifically a sliding interface that was previously referred to as the "Spanning Honeycomb with Wiper".

The "wiper" was implemented as a thin strip of aluminum with the dimensions of 84 cm long by 1.25 cm wide by 0.8 mm thick which ran the length of the moving trailing edge, rigidly affixed to the rear spar. The wiper was installed tangent to the surface of the wing at the rear spar so that it slid over the silicone outer skin of the trailing edge, forming a continuous but unrestrictive surface, as seen in Figure 4.14. Although not an ideal aerodynamic solution, the wiper resolved the complex boundary conditions inherent to the chosen active section concept, namely stiff to out of plane deformation, while compliant in-plane chordwise and compliant in-plane spanwise. Removal of the skin from the front-section of the wing removed approximately 80 grams of mass from the wing, reducing the overall mass contribution of the skin and honeycombs by approximately 38%. Addition of the wiper contributed approximately 22 g of mass to the wing, resulting in a net reduction in overall mass of approximately 58g, which if used in the theoretical "Balsa SMTE" wing from Table 4.1 would represent only a 16% increase in mass over the articulated flap wing.

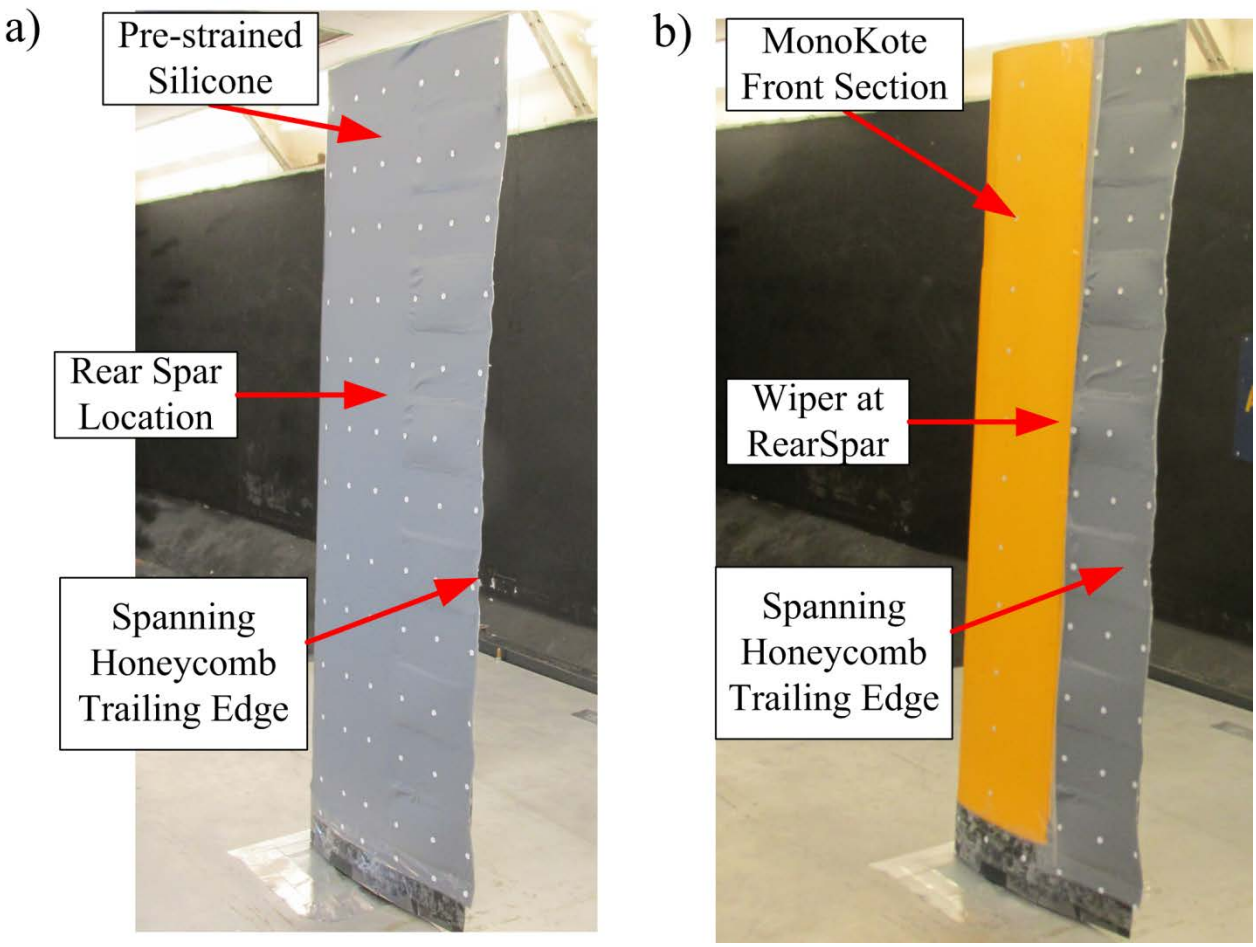

Figure 4.14 Comparison of SMTE with a) pre-strained silicone skin forward of the rear spar and b) an aluminum wiper at the rear spar

4.3.3. Test description

Implementing the wiper into the SMTE testbed eliminated the potentially destructive vibrations from the skin at higher flow speeds while increasing the overall range of the tip deflections of the SMTE under uniform actuation by approximately 20%, consistent with previous results. The resultantly modified SMTE was tested by flow speeds up to approximately 20 m/s utilizing prescribed uniform actuations, i.e the *U6+* and *U6-* configurations, from Section 4.1.2.5 for a constant angle of attack near $\alpha=0^{o}$. This test sought to evaluate the performance of the SMTE under higher aerodynamic loading, which was consistent with a higher cruise speed, and compare the aerodynamic impact of the alteration on the forces and effective control derivatives.

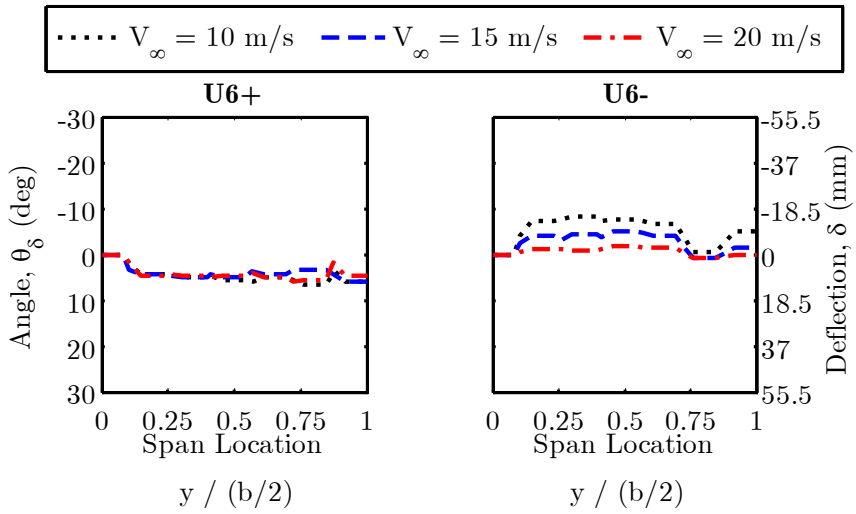

Figure 4.15 Configurations for SMTE with wiper with varying flow speed

4.3.4. Results

4.3.4.1. Deflections and forces

The "uniform" configurations, as measured by the external positional cameras via the reflective markers, were summarized in Figure 4.15. As expected from previous two-dimensional results, the SMTE experienced a significant reduction in overall actuation range by increasing the flow speed from 10 m/s to 20 m/s. Interestingly the reduction in tip deflections appeared to be mostly with the tip actuated down, which was explained by the increased sensitivity of the concept to subtle changes in loading when actuating down, similar to varying the stiffness of the internal compliant mechanism. Also, the majority of positioning errors for the active sections were located toward the wing-tip, indicating the tip vortex could impose additional control effort on the active sections near the tip of the wing. For a closer comparison of the SMTE with wiper to the original SMTE design, examination of the mean effective flap angle and aerodynamic forces were performed.

As seen in Figure 4.16, the SMTE with wiper significantly improved the overall reachable range of the overall actuation of the concept, by approximately 20%. However, the increased tip deflections did not result in increased ability to control aerodynamic loads. The SMTE with wiper actually marginally decreased the ability to affect lift by approximately 4%, roll by approximately 1%, and pitching moment by approximately 5%. Considering experimental

error, these results were summarized as both version of the SMTE generating approximately the same overall ability to affect aerodynamic loads within the linear aerodynamic regime. Note that drag was not compared due to the analysis from Section 4.2 that showed the sensitivity of the measurement due to changes in flow speed or angle of attack.

As expected, the SMTE with wiper permitted investigation of higher aerodynamic loading and suppression of the tip vibrations that had prevented testing with the smooth-skin SMTE configuration. The overall change in lift relative to the two dimensional results ranged from approximately 52%-60%. Considering these two results, approximately 30% of the loss in lift effectiveness of the morphing concept in moving from a two-dimensional test to the finite wing could be ascribed to the loss in sensitivity of lift due to the downwash of the tip vortex, as seen by the reduction in lift-curve slope in Section 4.1.2.1. The other 10-20% was ascribed to the 50% distribution of active and inactive sections over the span of the wing, reducing the effective spanwise density of the active sections and therefore actuation strength. Accordingly, eliminating

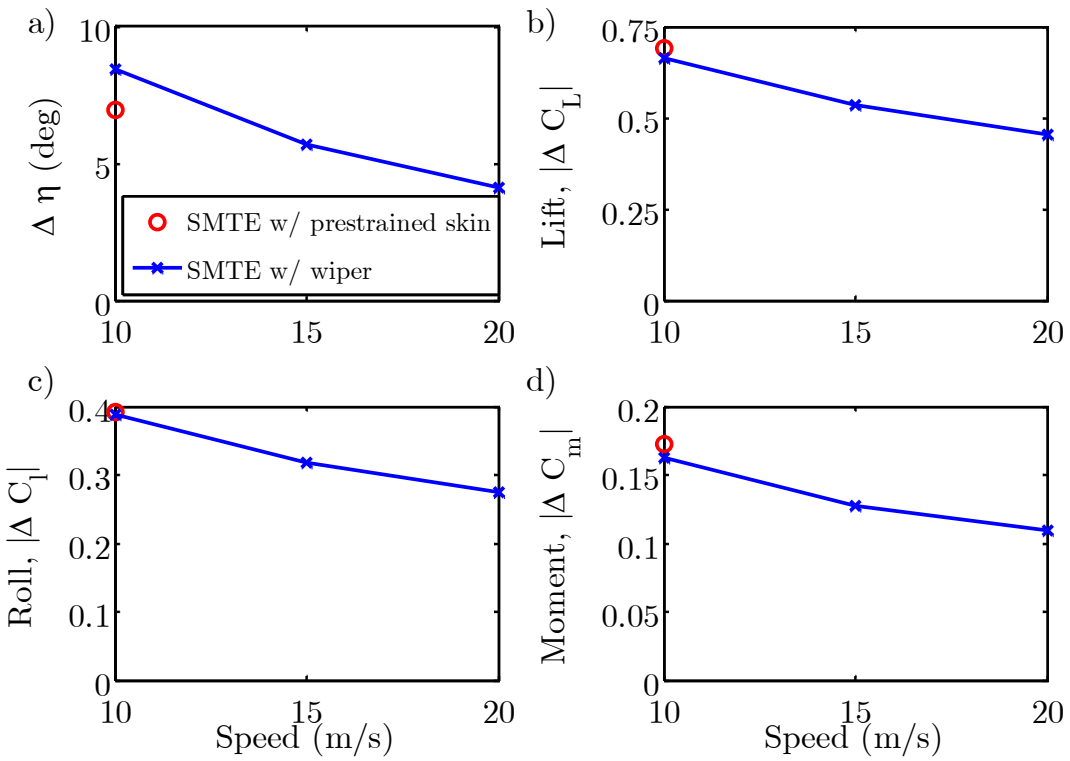

Figure 4.16 Change in a) mean effective flap angle b) lift c) rolling moment and d) pitching moment with varying flow speed

all inactive sections from the wing was expected only to increase the overall ability to affect aerodynamic forces by 10% to 20%.

Examining the overall change in forces, the SMTE experienced a 32% reduction in ability to affect lift, 29% reduction in ability to affect rolling moment, and 32% reduction in ability to affect pitching moment when the flow speed was increased from 10 m/s to 20 m/s, which was a slight improvement from the approximate 40% reduction in lift measured for the two-dimensional unimorph response in Section 3.3.2, possibly due to the reduction in effective loading due to the tip vortex.

4.3.4.2. Control derivatives

For additional clarity of the impact of the test on relevant metrics, the control derivatives were compared between the two versions of the SMTE wing, utilizing the methodology described in Section 4.1.2.5.

The results showed that due to the same overall ability to affect aerodynamic loads, but increased tip deflections, the SMTE with wiper was measured to have a decrease in effective control derivatives as compared to the SMTE with the pre-strained skin, shown in Figure 4.17. Although the SMTE with wiper experienced a reduction in tip deflections and change in aerodynamic effectiveness with increased flow speeds, the two components of calculating the control derivative were not proportional. Accordingly, the control derivatives of the SMTE with wiper increased as the flow speed increased, approximately equaling the value of the unmodified SMTE by 15 m/s and surpassing the values by 20 m/s. These values corresponded with a 2^{nd} or 3^{rd} order control surface as predicted by thin airfoil theory in Table 4.3.These effects could be explained by the increasing Reynold's number with higher flow speed tests, which would also explain the lower experimentally-measured control derivatives as compared to thin airfoil theory for the 10 m/s case. Accordingly, it was concluded that the control derivatives must be evaluated experimentally at the flow speed of interest for this simple metric to be an effective tool. Finally, the small deflections and rapidly-increasing control derivatives showed the importance of fine, internal measurements in the morphing trailing edge for effective positioning and control.

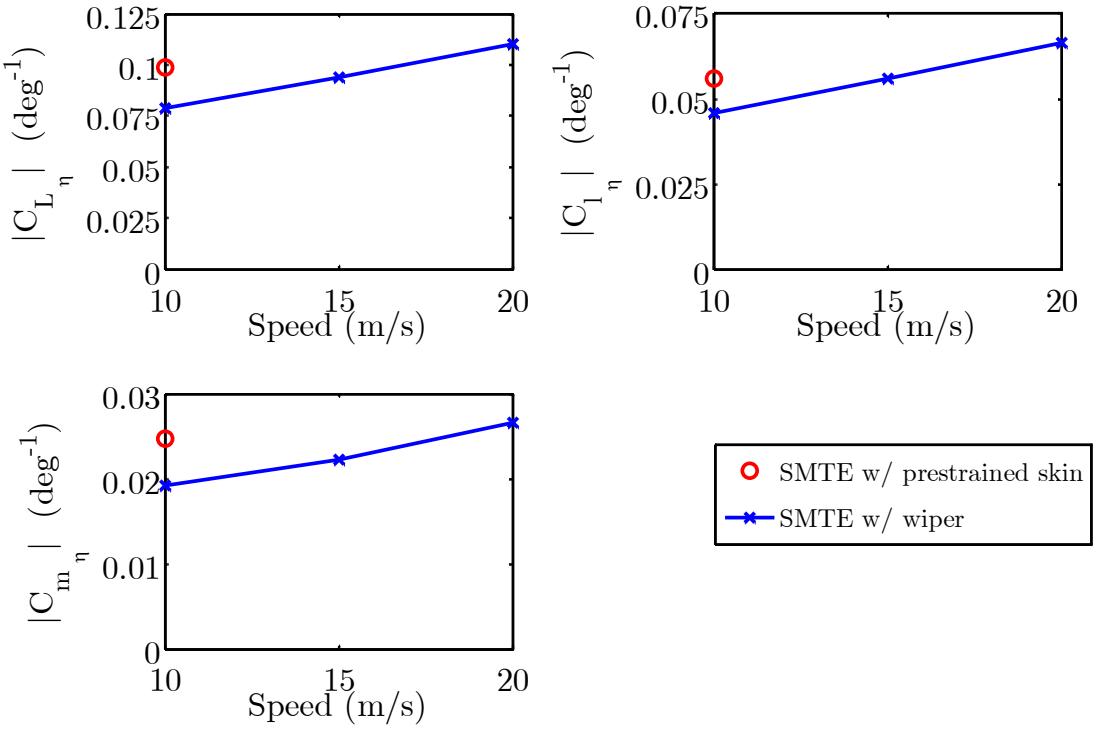

Figure 4.17 Control derivatives for SMTE with wiper with varying flow speed

4.3.5. Summary of SMTE wiper results

These two observations led to the conclusion that the SMTE with wiper represented a design that was more robust to increases in flow speed, with a lower overall mass, and the same ability to affect control forces as the original SMTE design with pre-strained silicone. The SMTE with wiper then represented a more practical and safer configuration to test for finer evaluation of the SMTE concept. Even for testing at lower flow speeds, where the aeroelastic loading effects were minimized the SMTE with wiper would be more desirable due to less overall mass and reduced likelihood of complicating oscillations.

4.4. Summary and Conclusions

This chapter summarized the initial results from comparing the SMTE testbed concept with an equivalent, articulated flap wing. The SMTE was constructed for a finite wing for a small, subsonic UAV. The testbed investigated uniform and spanwise-varying configurations via non-intrusive measurement, which was the first work of its kind on this scale of aircraft

The measured force and positional data permitted the comparison of the articulated flap wing and the SMTE testbed to affect aerodynamic loads at a flow speed of 10 m/s (Re = 2×10^5).

A metric for measuring effective control derivatives for variations in control surface span was established by defining an equivalent flap angle for comparing the two concepts and normalizing by deflections measured over the span of the wing, which was also the first of its kind.

Utilizing this method, the measured control derivatives for the uni-directional configurations, the SMTE showed much greater control over forces for lift. Encouragingly, the ratio of lift to drag derivatives for the SMTE was 41% higher than that of the flapped wing. This metric indicated that for the same step size in tip deflection, the SMTE could generate approximately 30% less increase in drag for the same increase in lift. Also, the pitching moment, which was shown to be largely insensitive to variations in angle of attack and flow speed was approximately three times larger for the SMTE.

Comparing control derivatives for the spanwise-varying configurations required the mean of the magnitude of the tip displacements to be used in the calculation rather than the mean of the tip displacements, creating a force effectiveness metrics. Tested span-varying configurations included linear and sinusoidal configurations which showed decreased effectiveness compared to uni-directional actuation. However the quadratically-varying (*S2*) configuration showed effectiveness equivalent to that of the uni-directional configurations for both the SMTE and flapped wing. The implication for this result was that a quadratically-varying (*S2*) configuration could potentially be integrated into a lifting surface where breaks in geometry were not possible or desirable.

The SMTE control derivative results for the finite wing were compared with previous experimental results in two-dimensional flow, showing agreement within 10% error. However when the lift control derivatives were compared with thin-airfoil theory, the discrete flap did not show good agreement with a first-order control surface, possibly due to viscous effects or the large deflection range of the flap.

Testing the SMTE at higher flow speeds, near 12 m/s, caused trailing edge oscillations when utilizing a pre-strained silicone skin forward of the rear spar. Referring to work from a previous chapter for different skin boundary conditions, a wiper design was utilized at the rear spar, reducing the overall mass of the concept and increasing the maximum achievable tip deflections. The wiper configuration eliminated the vibrations due to the pre-strained skin, and at

least doubled the maximum allowable speed of the SMTE configuration. The modification of the design did not appreciably change the ability of the concept to alter aerodynamic loads. So, the increase in tip deflection range resulted in a calculated loss in control effectiveness. Increasing the flow speed showed that the control derivatives could be effectively restored and were highly subject to Reynolds number effects. Also, the reduction in force effectiveness at increased flow speeds was less for the SMTE concept than measured for two-dimensional flow.

Because the wiper increased the robustness of the SMTE to variations in flow speed, maintained the ability of the concept to alter aerodynamic forces and decreased overall concept mass, it was concluded that the SMTE with wiper would adequately capture the capabilities of the SMTE concept.

4.5. Future work

The results summarized in this chapter represented the first steps at identifying performance improvements of the SMTE concept without an aerodynamic model. Lift, pitching moment and rolling moment were captured well with linear control derivatives, but drag appeared to be better captured as a second-order effect for attached flow.

The results showed that measuring an improvement via the SMTE in drag as compared to conventional, articulated flap would require increased sensitivity to angle of attack, control surface positioning, dynamic pressure and expected results. Specifically, improved equipment and a reduction of the measurement space would be required for the fine comparison of drag between the two concepts.

The measured lift control derivatives showed deviations from the expected results of thin airfoil theory but good agreement with previous experimental results from relevant Reynolds numbers. To adequately model the expected configurations, a combination of experimentally-measured lift control derivatives and a model of the impact of local variations of the control surface on forces of the total wing would be needed. The following chapter addresses these issues.

Chapter 5
Adaptive Drag Assessment of the Spanwise Morphing Trailing Edge Testbed

The following chapter describes the development, implementation and results of a novel test methodology for assessing the drag advantage of a morphing concept with a large number of possible configurations. The methodology is used to compare the ability of a morphing finite wing to a conventional flapped wing while optimally adapting to changing flight conditions. The study specifically focuses on identifying the comparative drag advantage of the Spanwise Morphing Trailing Edge (SMTE) concept in adapting from an off-design fight condition back to a design lift distribution with configurations informed by a simplistic aerodynamic model and experimentally measured forces.

Section 5.1 describes the motivation and development of the test methodology for comparing the drag penalty the SMTE concept with a conventional, flapped wing, resulting in the definition of the "adaptive drag" metric. Motivated by the desire to reduce the design space for the comparative experiment, the need for a simplistic system model is identified. The model is used to predict a "search vector" of possible configurations to restore the wing from its current flight condition to its design lift distribution. By searching along this path of scaled versions of the desired change in lift distributions, the effect of positioning errors and experimental deviations from the modeled conditions are minimized.

Section 5.2, describes the development of the model for predicting these "search vectors". The configurations to be tested in these search vectors are identified by augmenting lifting line theory to include experimentally-measured control derivatives to account for viscous effects. A refined measurement of the necessary control derivatives is performed via a modification to the experimental testing of the two wings for comparison, as informed in the

previous chapter. Then, the search vectors are predicted for a range of flight conditions utilizing an experimentally-informed constrained optimization.

Section 5.3, details the results of the experimental test for identifying the adaptive drag improvements of the SMTE configuration over a conventional articulated flap, utilizing the refined experimental setup and modeled configurations. The results show that even for a simplistic system model, the SMTE can reduce drag penalty associated with adapting from an off-design flight condition by approximately 20% as compared to an articulated flap wing.

5.1. Development of methodology for measuring drag reduction

5.1.1. Motivation for test

Chapter 4 focused on initial characterization of the SMTE as compared to an equivalent articulated flap wing by via control derivatives measured by externally-tracked trailing edge displacements. Utilizing this method, the measured control derivatives for the uni-directional configurations, the SMTE showed much greater control over forces for lift. Encouragingly, the ratio of lift to drag derivatives for the SMTE was 41% higher than that of the flapped wing. This metric indicated that for the same step size in tip deflection, the SMTE could generate approximately 30% less increase in drag for the same increase in lift. Also, the pitching moment, which was shown to be largely insensitive to variations in angle of attack and flow speed, was approximately three times larger for the SMTE.

The SMTE control derivative results for the finite wing were compared with previous experimental results in two-dimensional flow, showing agreement within 10% error. However when the experimentally-measured control derivatives were compared with thin-airfoil theory, the discrete flap did not show good agreement with the lift derivative expected from a first-order control surface. These results were explained by either viscous effects or the large deflection range of the flap. Utilizing the SMTE with a wiper for increased robustness to variations in flow speed, it was sought to exploit this decrease in aerodynamic efficiency by utilizing these improved control derivatives to reduce drag while adapting to various flight conditions.

Similar efforts in recent research on adaptive or “morphing” wings have focused on reduced drag at varying flight conditions for transonic aircraft. Several examples have included: the “Mission Adaptive Wing “(MAW), developed in the 1980s as a test bed for a multirole F-111

tactical aircraft requiring supersonic cruise speed and high maneuverability[12], the DARPA/AFRL/NASA "Smart Wing" program which tested spanwise-varying hinge-less "smart" trailing and leading edge for a transonic military aircraft [17], the Boeing and NASA "Variable Camber Continuous Trailing Edge Flap" (VCCTEF) system for a generic transport-class aircraft [24], and the "Mission Adaptive Compliant Wing" (MACW) concept developed by FlexSys, currently under testing for a Gulfstream business jet [115]. At these speeds, very small reductions in drag at cruise can result in large monetary savings in fuel, such as saving 64,000 gallons a year per aircraft with only a 3.3% improvement in the lift to drag ratio [34]. Still, recent studies have shown relatively little impact on performance of a morphing wing near the on-design condition, i.e. cruise, compared to conventional actuators largely because conventional wings are optimized before construction for high efficiency at cruise conditions [35].

It was expected that the current investigation for an adaptive low-speed UAV wing would show more significant improvement than previous work for two reasons. First, the Reynolds numbers for this scale of UAVs was lower than typically investigated for the transonic aircraft that have been the subject of previous studies, potentially further penalizing discrete flaps via viscous effects. Second, UAVs were expected to undergo large changes in flight condition due to their relatively smaller sizes and flow speeds, warranting larger variations in flight conditions, where the gains of the SMTE were expected to be largest.

Accordingly, it was desired to measure the drag improvement of the SMTE in this viscous regime. As seen in the previous chapters, measuring precise, linear control derivatives while accounting for positioning and other experimental errors was challenging due to the complexity of the experiment involving many independent variables: six independent active sections, the angle of attack, and flow speed. Additionally, drag, the parameter of interest was seen to vary largely due to actuation, angle of attack and flow speed. This situation was not unique to this particular morphing aircraft investigation. As noted by Friswell [116], "there is a lack of a transparent way to define the range of morphing aircraft for optimization that results in a sufficiently low number of design variables for quick sizing, while not constraining the design space a priori." Accordingly, defining the appropriate metrics and methodologies for measuring improvement of a morphing wing as compared to conventional articulated wing without overly complicating the test design space remains a significant problem in morphing research. The

following methodology attempts to address an aspect of this challenge by utilizing low-fidelity modelling to reduce the design space for testing the drag advantage of the SMTE concept.

5.1.2. Metric of interest and test method

The following section details the development of an experimental procedure and the quantities of interest for determining the reduction in drag penalty of the SMTE as compared to an articulated flap wing through a representative scenario.

First, it was required to define an initial or "design" flight condition for the wing that the adaptive concept for a wing was trying to achieve. For simplicity, it was assumed that the goal of the aircraft was to maximize its range or endurance. Per the Breguet range equation, the design flight condition would then minimize drag for a given lift that was specific to system-level requirements for the aircraft. The total drag for a finite wing, $C_{D,Tot}$. was described by three components:

$$C_{D_{Tot}} = C_{D_0} + C_{D_i} + C_{D_{adapt}} \tag{5.1}$$

which consisted of baseline drag $C_{D,0}$, induced drag $C_{D,i}$, and a grouping of the other aerodynamic inefficiencies (including those due to the control surfaces). The baseline drag represented the combined effects of the skin friction and profile drag of the unactuated wing in the flow. The induced drag, $C_{D,i}$, was proportional to the square of the wing lift coefficient:

$$C_{D_i} = \frac{(1+\sigma)}{\pi AR} C_L{}^2 \tag{5.2}$$

where AR was the wing's aspect ratio and σ was the induced drag penalty, which was a parameter representing the efficiency of the wing in minimizing the overall downwash due to the tip, and C_L was the lift coefficient. Ideally, the design lift coefficient, $C_{L,Design}$, represented the maximum possible lift-to-drag ratio and for simplicity it was assumed that parameter was optimized during the design process of the wing and was then fixed once the wing is constructed. A typical design choice for a spanwise lift distribution was the "elliptical" lift distribution, which minimized the induced drag for a finite wing. The elliptical lift distribution was given by:

$$c(\bar{y})C_{L_{2D}}(\bar{y}) = \frac{2\Gamma_0}{V_\infty}\sqrt{1-\bar{y}^2} \tag{5.3}$$

where the product of the chord, *c*, and the local lift coefficient, $C_{L,2D}$, was varied elliptically over the normalized semi-span $\bar{y}$ as described by Γ_0 is the circulation about the center of the span and V_∞.

Without any alteration from the design flight condition, adaptation, or "morphing", was unnecessary. However, for small UAVs, changes in flight condition, such as wind gusts, were larger relative to the overall speed of the aircraft as compared to a transport aircraft, and so changing flight conditions were deemed to be an expected design necessity. Then the increase in drag associated wing adapting the wing back to the design flight condition was expected. This increase in drag was defined as the "adaptive drag penalty, and was the metric of interest, discussed in the following section in an illustrative, representative scenario.

5.1.2.1. Representative airfoil scenario and metric of interest

To identify an instance where adaptation and the adaptive drag penalty were necessary, a demonstrative scenario was assumed. A summary of the geometric conditions and the resultant forces in this scenario were provided in Figure 4.10 and Figure 5.2, respectively.

To begin, it was assumed that a given airfoil (wing cross section) had been designed about a given angle of attack, α_{design}, where it also achieved its design drag, $C_{D,Design}$ at a design lift, $C_{L,design}$ (Point #1). It was then assumed that a disruption in flight condition, e.g. wind gust impacting the wing at a non-zero angle of attack, changed the effective angle of attack to $\alpha_{current}$ and caused the wing to move from Point #1→ Point #2, without any adaptation from the airfoil. For simplicity, it was assumed that the forces on the airfoil and thus the wing largely dictated the forces on the aircraft, e.g. a flying wing aircraft.

Figure 5.1 Physical description of test

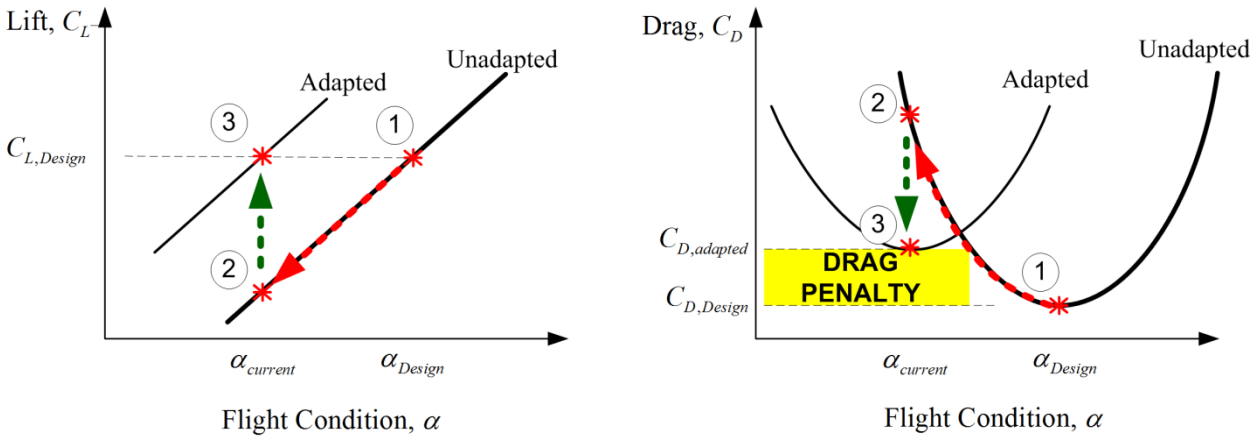

Figure 5.2 Description of test via forces by matching lift and measuring drag penalty

At Point #2, the aircraft was then at a new lift coefficient and drag coefficient, which was unsustainable for maintaining its desired trajectory. The aircraft could have potentially slowed or accelerated to compensate for such a situation, but it was assumed that the penalty for throttling the engine was much greater than that of using a control surface. In such a scenario, the airfoil was assumed to attempt to adapt to achieve the original, design lift coefficient at the new angle of attack moving from Point 2 to Point 3. The difference in drag between Point #3 and Point #1:

$$\Delta C_{D_{adapt}} = C_D\big|_{\text{Point\#3}} - C_D\big|_{\text{Point\#1}} \tag{5.4}$$

was then defined as the “adaptive drag penalty” which was the minimum increase in drag over the baseline drag to achieve the desired lift. This penalty was exclusively due to the capabilities of the morphing concept in adapting to the necessary flight condition, and was the primary metric of interest.

This methodology was used to measure the adaptive drag penalty for finite wings under consideration, with a single caveat, a design lift distribution needed to be specified rather than

simply a design lift coefficient. The following sections describe the reasoning behind this exception, the specification of the design lift distribution, and the metric for ensuring that it was achieved.

5.1.2.2. Generalization to a finite wing

For an airfoil or wing with a single control surface (degree of freedom), such as a single flap, the adaptive drag penalty could not be altered after the construction of the aircraft. However, the wings under investigation consisted of many control surfaces and thus possessed additional degrees of freedom for potentially reducing this drag penalty. Accordingly, an additional constraint was required to define the desired force – state at the design condition, for the morphing wings under investigation. Specifically, the design lift coefficient at each span station needed to be defined by a design spanwise lift distribution, thereby specifying the induced drag at the design condition.

One intuitive choice for limiting the desired test configurations would simply be to minimize the total drag for the wing given the design lift and current flight condition. By minimizing total drag, the lift to drag ratio and thus the range of the aircraft would be maximized. However, modelling both the SMTE and flapped wings with sufficient fidelity to accurately predict and minimize total drag was deemed to require simulations of prohibitive complexity within the scope of the present thesis. Additionally, minimizing the total drag would ignore other system level implications such as aeroelastic effects on the wing box due to alterations in the spanwise load distribution. Finally, both wings utilized control surfaces with only a single degree of freedom per spanwise station. Thus, specifying a spanwise lift distribution represented a sufficient constraint for the drag on the wings under investigation.

In the absence of any system-level requirements, the design lift distribution for the finite wings under investigation was selected as the elliptical lift distribution. As previously discussed, this realistic lift distribution minimized the induced drag on the wing, and was characterized by eliminating a readily available metric, the induced drag penalty, σ, as defined in Equation (5.2) for a given lift coefficient. By minimizing this metric, the closest possible configuration of a wing to the elliptical lift distribution could be found. Then, achieving this lift distribution from any flight condition achieved the same induced drag, so long as the total lift coefficient for the wing was matched and the induced drag penalty sufficiently minimized as to be considered

eliminated. Consequently, the total effect of the induced drag could be predicted for a fully-adaptable wing would be identical to the design value, permitting its grouping and elimination from the measurement of the adaptive drag penalty.

In principle, any achievable design lift distribution could have been chosen so long as a residual for ensuring the matching of the distribution at off-design conditions could be specified and the effects due to induced drag could be properly assessed. For the elliptical lift distribution, these metrics were the conveniently the same. More general lift distributions that minimize induced drag while specifying allowable maneuvering moments include the Klein distribution which minimizes the of induced drag subject to constraints for the root and integrated bending moment, allowing the root bending moment, a convenient surrogate for wing weight, to also be specified [117]. However, without additional specifications about the aircraft weight and mission parameters, aerodynamic maneuver load alleviation was outside the scope of the current study. For additional details regarding the analytically-determined impact of altering the root bending moments at both cruise and maneuver conditions, the reader is referred to Pate [118].

Thus, by specifying the spanwise lift distribution, and utilizing the induced drag penalty as a metric to ensure the matching of this distribution over the span of the finite wing, the previous airfoil scenario could also be utilized to identify the drag penalty of a morphing wing concept in adapting from an off-design flight condition. Accordingly, the following sections will assess the comparative drag penalty between the SMTE and an articulated flap wing in adapting to changes in flight conditions and that are off-design by returning to an optimal lift distribution. The necessary actuations for identifying this drag penalty are determined by lifting line theory utilizing experimentally measured control derivatives.

5.1.2.3. Digression on an alternate test method

To broaden the impacts of the results for this investigation an alternate scenario was considered for the modification of lift coefficient at the current angle of attack. This represented the inverse case of the current methodology, where a change in forces, rather than geometry disrupted the current flight condition.

In this second scenario (not pictured), it was assumed that an aircraft was designed about an initial lift coefficient, $C_{L,design,}$ but after releasing a payload, such as a parcel or munition, the

aircraft then altered its lift coefficient to compensate. In this scenario, the aircraft was assumed be large with respect to the wing and thus the wing maintained the same angle of attack, α_{design}. The second scenario then became simply the modification of lift coefficient at the same angle of attack by scaling the lift distribution, which was already captured by moving from Point #2→ Point #3 in the first scenario. Thus, the first scenario was chosen for investigation, but it was noted that the results between the reported change in flight condition could be scaled by the lift-curve slope of the wing to identify gains relevant to the second scenario.

5.1.3. Test method summary

To summarize, the test method from the previous sections was developed to quickly identify the "adaptive drag" penalty, which was a newly-created metric that sought to summarize the ability of an adaptive concept in restoring a wing from an off-design condition. The adaptive drag was then defined by the minimum increase in drag over the baseline drag required to achieve the design lift at an off-design flight condition. For a finite wing, the adaptive drag definition was generalized to require the attainment of the design spanwise lift *distribution* from the off-design condition. The wings under investigation were constructed with only one control surface per spanwise location, so this represented a sufficient constraint to not require a search for the minimum possible total drag, including viscous forces. Accordingly, a representative "elliptical" spanwise lift distribution was chosen for the design condition. This lift distribution was conveniently identified when the induced drag penalty was minimized, thereby providing a single force residual parameter for identifying when the desired configuration was achieved for a certain flight condition. The following section will address how to predict these configurations.

5.2. Determining optimal test configurations

Per the previous test description to identify the "adaptive drag" penalty, it was desired to determine the configurations that could reproduce the desired spanwise lift distributions for the finite wings under testing. Then, experimentally-derived control derivatives were used in conjunction with lifting line theory to estimate these optimal configurations for several flight conditions, as described in the following section.

5.2.1. Implementation of lifting line theory

To identify the desired test configurations for both the SMTE and flapped wings, a simple lifting line model was used to compute the spanwise lift distribution on a finite wing. The half wing was discretized into spanwise stations, y_0. At each spanwise station, the local angle of attack for the wing was deconstructed as: $\alpha_{current}$ the geometric angle of attack between the zero lifting line of the wing and the freestream flow, α_{act} the contribution of the actuator, $\alpha_{effective}$ the effective angle of attack, and α_i the induced angle of attack from downwash at the tip vortex. Using the Biot-Savart law to represent the tip vortex of a finite wing, the equation enforced at each spanwise station became:

$$\alpha_{current}(y_0) + \alpha_{act}(y_0) = \underbrace{\left(\frac{2\Gamma}{C_{L_{\alpha_{2D}}} V_\infty c}\right)_{y_0}}_{\alpha_{effective}} + \underbrace{\frac{1}{4\pi V_\infty}\int_{-b/2}^{b/2} \frac{\left(d\Gamma/dy\right)}{y_0 - y} dy}_{-\alpha_i} \tag{5.5}$$

where Γ was the location circulation, $C_{L,\alpha,2D}$ the two-dimensional lift-curve slope of the unactuated airfoil, c the chord, b the total wing span and V_∞. Using the method established by Glauert and detailed by Kuethe[114] to represent the spanwise circulation and thus local lift coefficient as:

$$\Gamma(y) = \frac{1}{2} C_{L_{\alpha_{2D}}} c V_\infty \sum_{n=1}^{\infty} \Psi_n \sin(n\theta) \quad \text{where } \cos\theta = 2y / b \tag{5.6}$$

where Ψ_n were the unknown weighting coefficients, y the spanwise location, and θ a discretization of the spanwise location. Note that because only a half-wing was modeled, n, only represented odd-numbers due to the no-lift requirement at the tip of the wing. The contribution by actuating a control surface was modeled simply as:

$$\alpha_{act} = \frac{C_{L_\eta}}{C_{L_\alpha}} \eta \tag{5.7}$$

where $C_{L\eta}$ was the lift control derivative for attached flow, η, the effective flap angle and $C_{L,\alpha,2D}$ the two-dimensional lift-curve slope of the unactuated airfoil. Thus by solving Equation (5.5) at a set of spanwise stations "*y*", the spanwise lift distribution "*Γ(y)*" and thus induced drag of the wing "$C_{D,i}$" could be calculated. In principle, any number of spanwise locations and basis functions could have been used for this method. The only requirement was that an estimate of the control surface change on effective local angle of attack be related to a controllable adaptation parameter.

The difference in induced drag between the wing and the elliptical lift distribution is related by:

$$C_{D_i} = C_{D_{i_{el}}} \left(1 + \sigma\right) \quad \text{where} \quad \sigma = \sum_{n=2}^{\infty} n A_n \; / \; A_1 \tag{5.8}$$

where σ had a minimum possible value of zero when the induced drag of the wing is equal to that of the elliptical lift distribution. For alternate lift distributions or basis functions, an alternative residual, representing the difference in spanwise lift distribution from the desired lift distribution at the current flight condition would need to be formulated. As seen by the simplicity of Equation (5.8), the selected basis functions and lift distribution also resulted in this residual parameter providing an estimate on the effective increase in drag by imperfect adaptations.

The limitations of this theory are: linearized modeling of aileron lift contribution, rough geometric approximation of the wing, and failure to capture any effects of profile drag or gaps between the ailerons on the equivalent wing. Still, the resultant model was determined to provide a simple method for estimating the impact of the various control surfaces on the spanwise lift distribution for a given flight condition.

5.2.2. Refined measurement of control derivatives

As seen in the previous section, the model's predictions of lift due to change in effective flap angle,η, were summarized by a single parameter, $C_{L,\eta}$. The previous chapter showed that there were relatively large deviations in the expected control derivatives of the articulated flap

wing as compared to the values expected from thin airfoil theory. Although this was initially explained by viscous effects over the discrete flap, it was also noted that the deflection ranges of the SMTE and the discrete flap were not matched. Accordingly it was expected that the +/-25^{o} range for the flaps was causing flow separation that led to under-estimation of the effective flap derivative. To precisely predict the desired test configurations at varying flight conditions, a refined measurement of the control derivatives was performed.

5.2.2.1. Refinements to experimental setup

Refinements were made to the previously-described experimental setup from Section 4.1 to provide more accurate measurements while measuring the control derivatives.

Dynamic pressure was recorded actively throughout the test via a differential pressure transducer (Omega PX2650) attached to the pitot tube approximately 2 meters upstream of the wing and 0.3 meters from the top of the wind tunnel as seen in Figure 5.3a.

A high-precision angular displacement sensor to measure the angle of attack of the wing was created utilizing two laser displacement sensors (Keyence LK-G402). The displacement sensors measured the difference in out-of-plane displacement (collinear in the lift direction) of a bar mounted to the force balance along the axis of the quarter-chord, as shown in Figure 5.3b. The differential measurement rejected translational movement of the force balance due to aerodynamic loading and vibration while providing accurate angular position, accruing only 1/3rd a degree of positioning error over a 70 degree range. A closed-loop positional angular control was created with the angular position motor to allow positioning accurate to within 1/25th of a degree.

The angles of the flaps for the articulated flap wing were calibrated using the displacement of the trailing edges, allowing direct command of each flap position to the digital servos. The control program for the SMTE active sections was revised to increase the period for time-averaging and updating locations to permit more precise positioning of the active sections, accurate to within approximately 0.5 degree of equivalent flap angle.

Also of concern to the test was precise measurement of the positions of the control surfaces, regardless of the rotation (angle of attack) of the wing. Then, rather than utilizing external measurement of configurations, the Arduino control code was reconfigured to

continuously record the positions of each active section to a running file on the computer utilizing the GoBetwino interface. The positions measurements were collected when the load cell was being measured and time-averaged to provide accurate positional information, free of errors due to change in angle of attack.

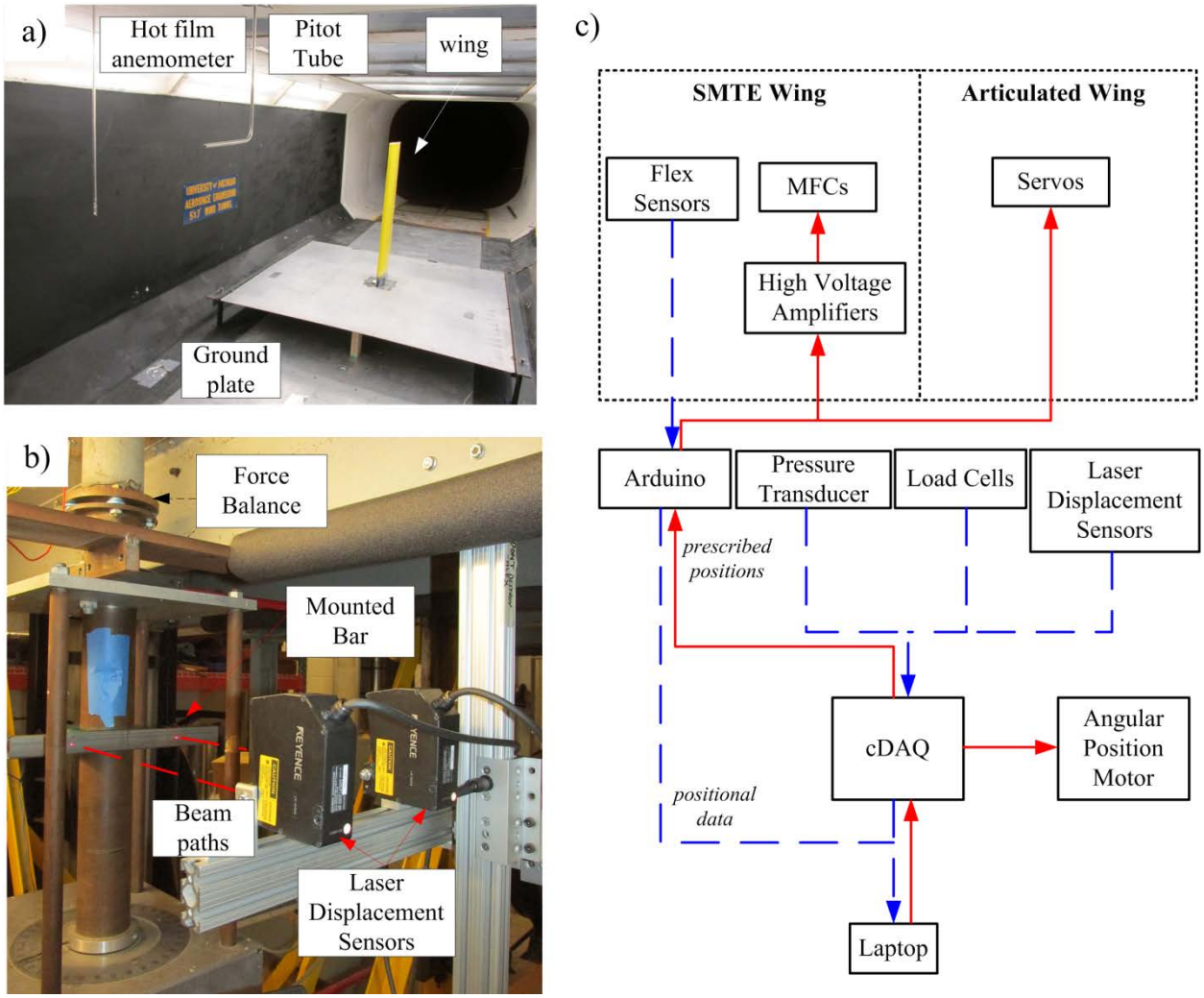

Figure 5.3 a) Pitot tube in front of mounted wing b) angular displacement sensor and c) experimental data flow

The experiment was orchestrated via Matlab [119] running data acquisition on a National Instruments compact DAQ (cDAQ) utilizing the NI 9205 analog input and NI 9264 analog output modules. The positions of the active sections were actively read by Matlab from the running file while the forces and dynamic pressure for the commanded configurations were tested. Each test configuration was time-averaged for approximately 30 seconds to eliminate any transient positioning errors. All instruments except for the aileron positional control were acquired throughout the test. An overview of the data flow was shown in Figure 5.3c.

It should be noted that the tests from Chapter 4 were conducted at approximately 26 ^{o}C (Re=1.95x10^{5}) while the timing of the experiment in this chapter led to a temperature in the test section of, on average, 0 ^{o}C (Re=2.29x10^{5}). Thus, the freezing temperatures dramatically increased the creep associated with the internal compliant mechanisms and elastomeric honeycombs. Although this effect was significant, it was beyond the scope of the current study. To compensate, approximately 30 seconds was given to the SMTE between actuation and measurement of the acquired position. Future studies regarding adaptive actuation of morphing wings should assess the effects of temperature on actuation speed.

5.2.2.2. Measurement of control forces

A single flow speed 10 m/s (Re=2.3x10^{5}) was chosen for investigation, representing a speed where aeroelastic effects for the SMTE would be small and ideally show aerodynamic gains over the articulated flap wing.

The articulated flap wing was actuated uniformly, spanwise in the same manner as the *U6+* and *U6-* configurations from Chapter 4 over its maximum achievable range, $-25^{o}<\eta<25^{o}$, for ranges of angles of attack varying from 0^{o} to 15^{o} degrees to identify the effects of flow separation with increasing flap angle. The mean flap angle was defined in the same manner as before:

$$\eta_{mean} = \int_{\bar{y}=0}^{\bar{y}=1} |\eta| \, d\bar{y} \tag{5.9}$$

which was the spanwise-mean of the equivalent flap angles over the semi-span of the wing. This resulted in a reduction of the tested equivalent flap angles due to the fixed root, but also

realistically summarized the range of the wing. The results were shown in Figure 5.4, with the effective forces plotted against the mean flap angle, including the unactuated root.

For angles of attack less than ten degrees, the lift, rolling moment and pitching moment were seen to have a largely linear region including the unactuated condition when varying the flap angle. As a reminder, positive flap deflection, by convention, increased the effective lift on the wing. Thus, as the angle of attack increased, the positive angle at which the flap experienced separation decreased until at 15^{o} angle of attack, the lift and rolling moment were shown to deviate slightly from the other values.

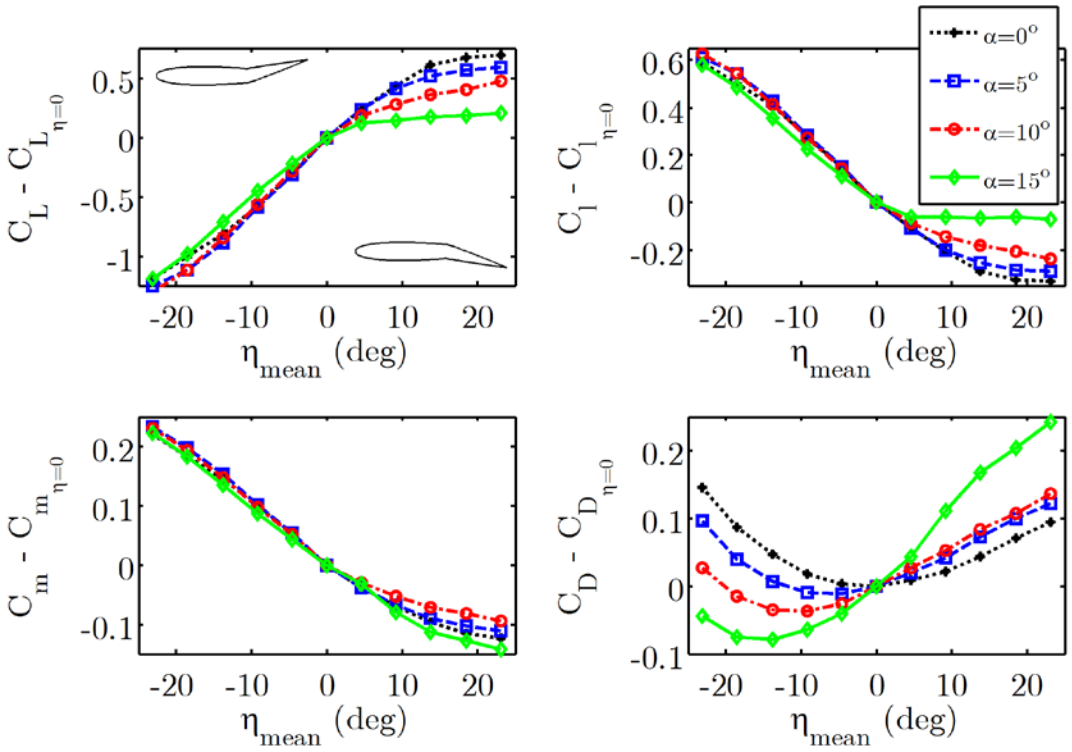

Figure 5.4 Measured control forces for articulated wing with varying angle of attack

5.2.2.3. Secant-measured flap control derivatives

The control derivatives were evaluated in the manner established in Chapter 4 to evaluate the effect of positioning errors and flow separation on the control derivatives under uniform actuation. The flaps were tested for $-25^o<\eta<25^o$ and the results were shown in Figure 5.6 reported by the mean flap angle including the non-actuating root, which reduced the tested range to approximately $-23^o<\eta_{mean}<23^o$. It was seen that the positive actuations for large flap deflections resulted in low control derivatives, which were much lower than expected for a first order control surface as expected from thin airfoil theory analysis in Chapter 4. The pitching moment reached the expected value for tip-up actuations that would induce negative lift (restoring from positive angles of attack), but not for tip-down actuations, which was possibly due to the asymmetry of the control surface hinge, utilized to minimize losses in the gap as shown in Figure 5.5.

As expected, the result was that for downward actuations, the secant-method for evaluating the control derivatives could drastically under-report the control for lift, pitching moment and rolling moment. Even for small tip-up actuations the lift derivative only achieved 80% of the expected first order control derivative result. The drag derivative varied largely with angle of attack and only appeared to be linear for very small selection of actuations that also varied with angle of attack.

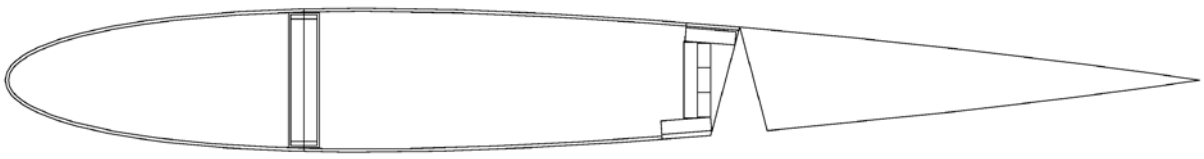

Figure 5.5 Cross section of articulated flap wing utilizing closed hinge for internal linkage control

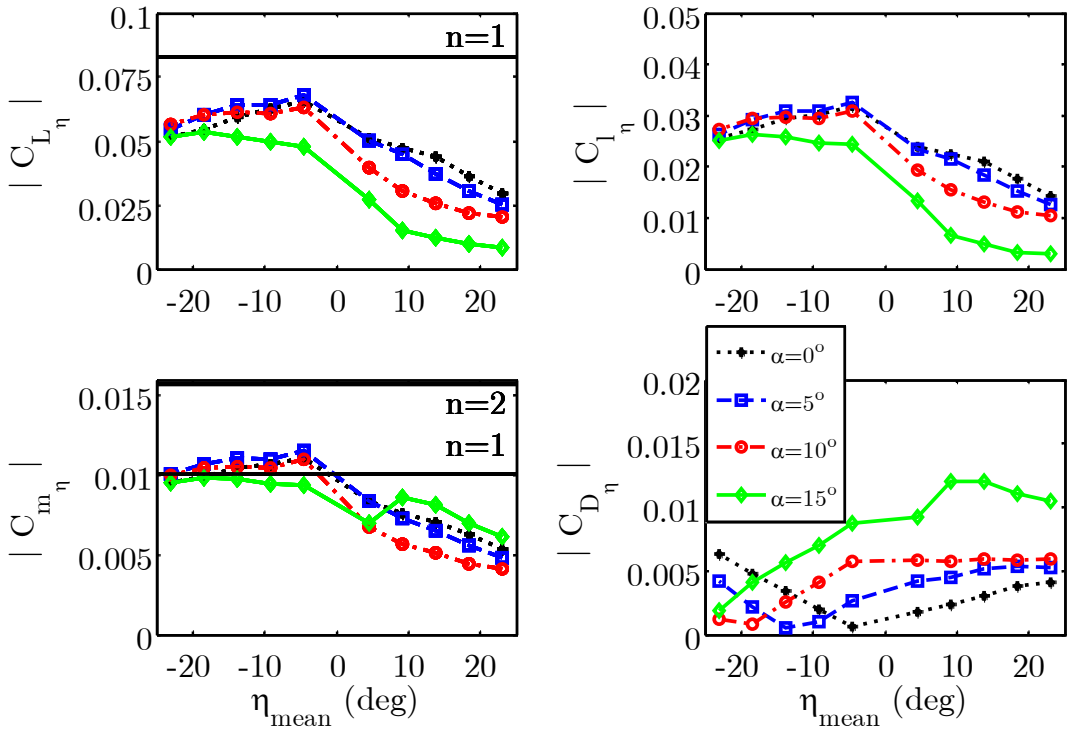

Figure 5.6 Secant-measured control derivatives for articulated flap wing

5.2.2.4. Tangent-fit flap control derivatives

Recognizing the limitation of the secant-measured method for evaluating the control derivatives, it was desired to utilize several measurements at a time to reduce the error in measuring the effective control derivative. The control derivatives for lift, rolling moment and pitching moment were then derived by fitting a tangent curve to the various linear regions of the measured data, as seen in Figure 5.7. As viewed by the slope of the lines, the control derivatives were valid for a large range of upward actuations, but were not valid for downward actuations that would increase lift, for actuations as small as $\eta_{mean}=10^o$ at $\alpha=0^o$. The nonlinear range of lift response increased, symbolizing that the flow was separating over the airfoil slightly for small downward actuations. For the drag coefficient, it was noted that even when a quadratic fit was employed, shifting with the respective center due to angle of attack, positive actuations were inaccurately predicted. As observed profile drag was not included in this initial modeling effort. A summary of the various lift, rolling moment and pitching moment control derivatives as measured by the tangent-fit over the range of tested angles of attack was summarized in Table 5.1.

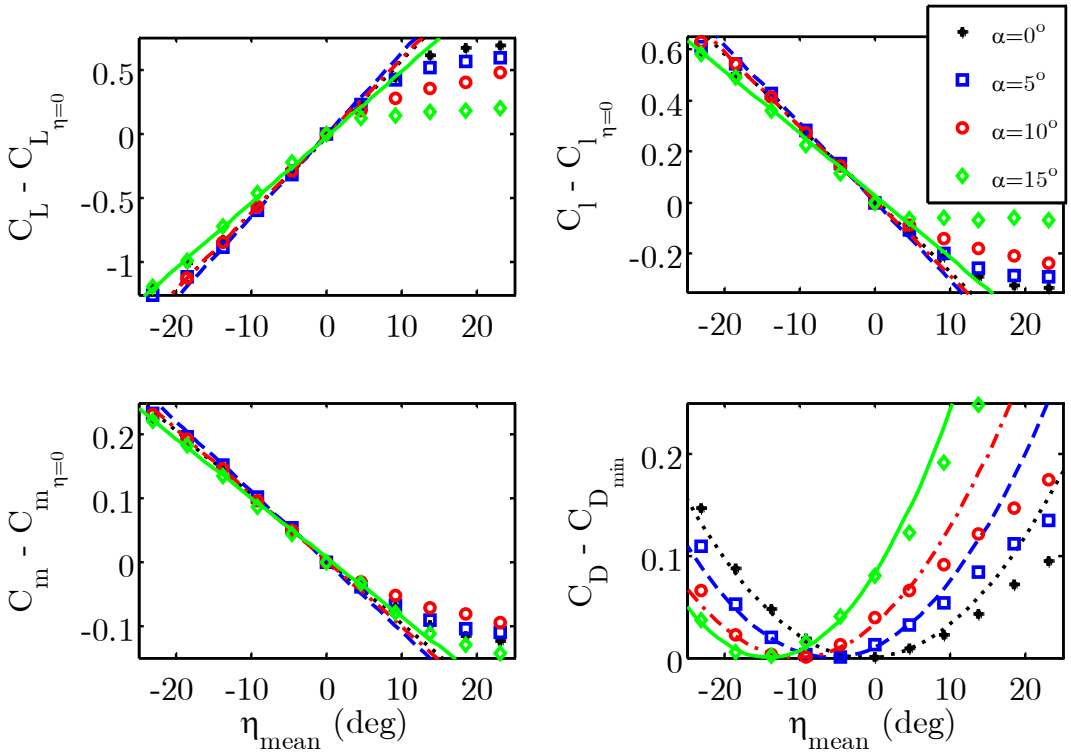

Figure 5.7 Tangent-fit control derivatives for articulated wing

Table 5.1 Tangent-fit control derivatives for articulated wing

Angle of Attack	η=0°	η=5°	η=10°	η=15°	Thin Airfoil for n=1
Lift $C_{L_\eta}\left(\cdot 10^2\right)$	5.94	6.36	5.99	5.10	8.28
Pitching Moment $C_{m_\eta}\left(\cdot 10^3\right)$	10.1	11.0	10.3	9.3	10.1
Rolling Moment $C_{l_\eta}\left(\cdot 10^2\right)$	2.84	3.06	2.90	2.43	-

5.2.2.5. SMTE control derivatives

A similar experiment was conducted for the SMTE, varying the active sections over their achievable ranges which were approximately $-6.5^o<\eta<6.5^o$. Again, the mean flap angle was utilized to characterize the condition. Accordingly, the SMTE as a whole was only capable of

approximately $-5^o<\eta_{mean}<5^o$due to the root section restricting the total actuation. A summary of the forces as measured was shown in Figure 5.8

The force coefficients were roughly fit utilizing the secant method, as shown in Figure 5.9, highlighting the large variation in measured control derivatives, as compared to thin-airfoil theory when utilizing a single data point. Even through this method, it was clearly observed that the SMTE exceeded the performance expected by the first order control surface at almost all actuations for lift. Additionally, the trend of higher than expected pitching moments was confirmed, showing that even when the SMTE exhibited lift performance similar to a first-order control surface, it also exhibited pitching moment roughly equivalent to a third-order control surface.

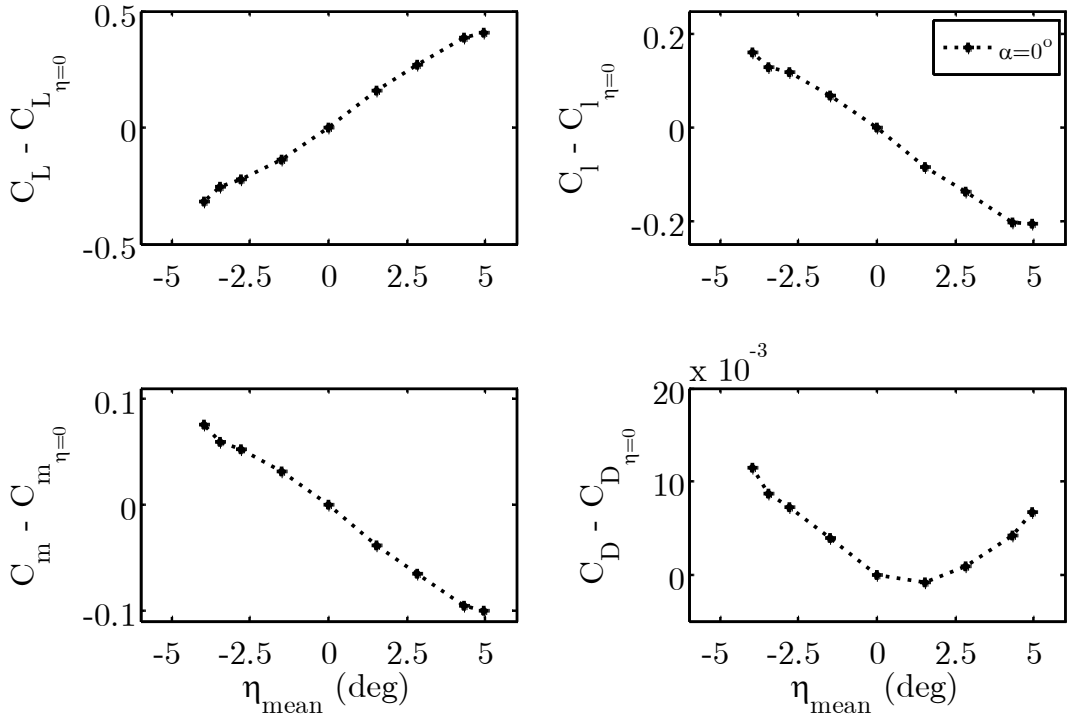

Figure 5.8 Measured control forces for SMTE wing

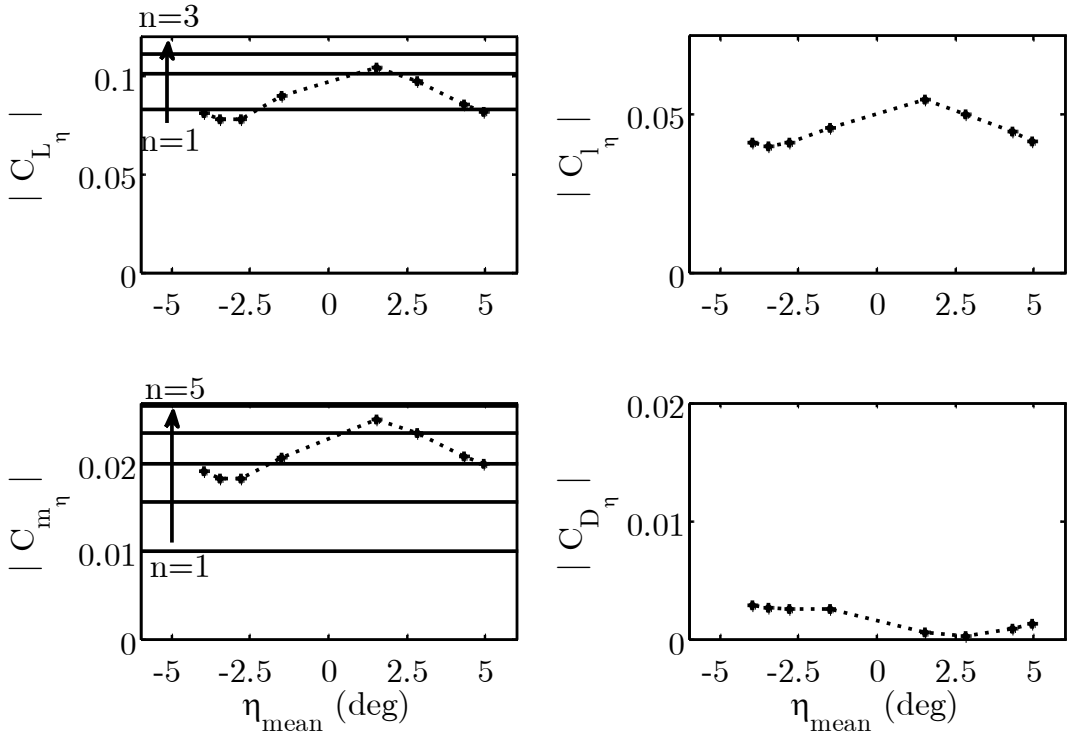

Figure 5.9 Secant-measured control derivatives for SMTE wing

Fitting the SMTE with tangent control derivatives in the same manner as the articulated flap wing decreased the peak measured control derivatives in a similar manner. As seen by the fits in Figure 5.10, the SMTE data for lift, rolling moment and pitching moment fit well for it relatively small equivalent flap angles. A quadratic fit was applied to the drag coefficient, showing positioning error within 1^o or 2 mm of the tip deflection. This allowed the effective flap angle to be re-calibrated by 1 degree, but the linear control derivatives were still valid even with the measured offset.

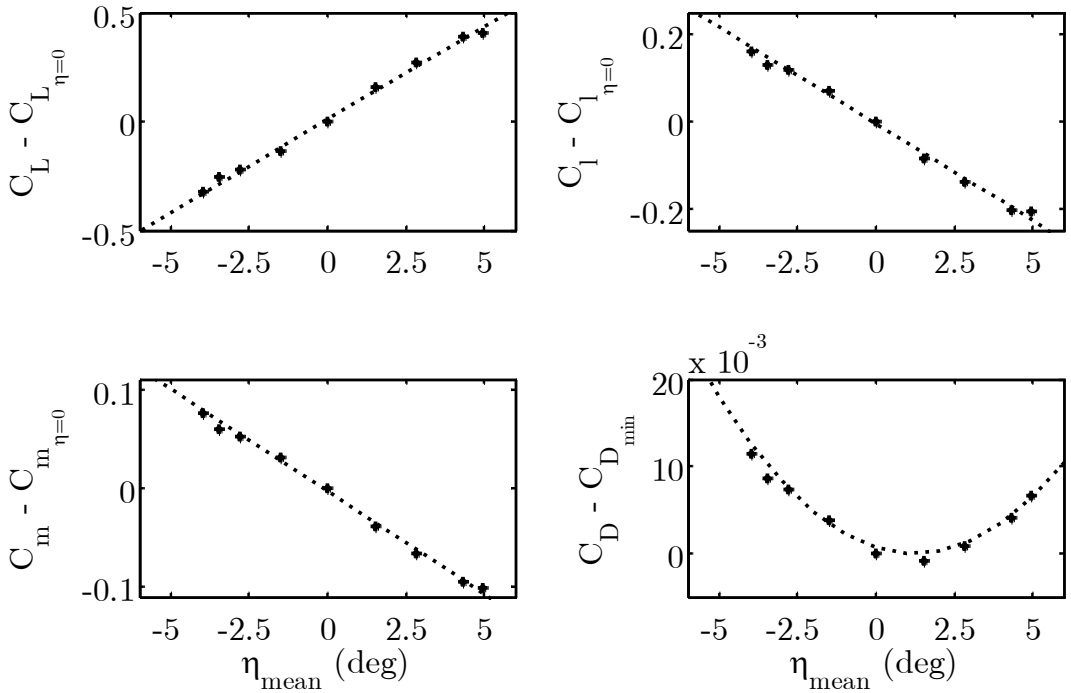

Figure 5.10 Tangent-fit control derivatives for SMTE wing

5.2.2.6. Summary of refined control derivative measurements

The refined tangent-fit control derivative measurements for the articulated flap and SMTE wings were summarized in Table 5.2. The articulated flap values reported were the maximum possible values, i.e. $\eta=5^o$, from Table 5.1.

Table 5.2 Comparison of tangent-fit control derivative magnitudes

	SMTE	**Flaps**	**2D Unimorph**[120]	**Linear Aerodynamics**			
				n=1	**n=2**	**n=3**	**n=4**
Reynolds Number	2.3 x 10^5	2.3 x 10^5	2.1 x10^5	∞	∞	∞	∞
Lift $C_{L_\eta}\left(\cdot 10^2\right)$	8.53	6.36	9.16	8.28	10.1	11.2	12.8
Pitching Moment $C_{m_\eta}\left(\cdot 10^3\right)$	20.6	11.0	22	10.1	15.7	20.0	23.5
Rolling Moment $C_{l_\eta}\left(\cdot 10^2\right)$	4.43	3.06	-	-	-	-	-

The results for the SMTE showed good agreement with the previous results for the two-dimensional unimorph results reported in Chapter 3, with a slight reduction from the two-dimensional value even utilizing the maximum values from Table 5.1. Still, the measured values were utilized due to the relevant difference in measured test temperature, and Reynolds number as mentioned in Section 5.2.2.1.

The articulated flap wing, however, did not achieve the result of the first order control surface, even in its linearized range. However, the articulated flap wing's pitching moment derivative was higher than a first order control surface. Clearly, the linear (viscous free) predictions of control derivatives were not accurate at these Reynold's numbers, resulting in lower lift control derivatives and higher pitching moment control derivatives. This was a significant result, showing the need for experimental control derivative measurements or higher-fidelity modelling at these Reynolds numbers.

The rolling moment control derivatives reflected the increased SMTE control authority measured from the lift control derivative. Assuming the maximum mean equivalent flap angle i.e. $\eta_{mean}=5^o$, from Table 5.1, the SMTE still increased the lift control derivative by 34%, the pitching moment derivative by 87%, and the rolling moment derivative by 45%. As a reminder, these control derivatives, although including several measurement points overestimated the authority of the articulated wing for positive actuations. Still, for small actuations ($|\eta_{mean}|<10^o$ and $\alpha<10^o$), the linear control estimates were determined to be valid approximations.

From these tests it was concluded that the SMTE wing showed dramatic improvement in lift, pitching moment and rolling moment derivatives over the articulated flap wing. The thin-airfoil theory over-estimated the lift control derivatives and under-estimated the pitching moment control derivatives. Still, the trends between first-order and higher-order control surface captured the nature of the control benefits of the conformal flap. However, these control derivatives provided no indication or understanding of projected drag benefit associated with these increased control derivatives. The modeling in the following section sought to address this issue.

Table 5.3 Parameters of simulated, unactuated SMTE test bed

Parameter	Value
Aspect Ratio	6
Lift curve slope	2π (rad^{-1})
Taper Ratio	1
Normalized location of spanwise stations	{0, 0.19 , 0.35, 0.5, 0.6, 0.80, 0.96}

5.2.3. Modeling the test configurations

Having measured the effective control derivatives of the SMTE and articulated flap wings, the experimental results were used to predict the optimal configurations at testable flight conditions using lifting line theory. It was desired to predict the flight conditions to test at which the SMTE could potentially exhibit superior performance over the articulated flap wing.

5.2.3.1. Modelling without actuation

First, the wing was modelled without any control surface actuation to highlight the importance of matching the lift conditions when comparing drag.

A simple, untapered wing, simulating the SMTE test bed was evaluated using lifting line theory with the prescribed parameters in Table 5.3. The location of the spanwise stations for the enforcement of Equation (5.5) represented the root of the wing and the middle of each active section of the morphing aileron locations. Although more spanwise stations could have been used, doubling the number of control points could quickly lead to poor conditioning of the linear solution of the weighting coefficients, Ψ. Thus, for initial assessment, a single control point for each degree of freedom and the root of the wing was deemed sufficient.

This idealized, unactuated wing was modelled with the lifting line theory model from the Section 5.2.1 and the result was compared to the results from the elliptical lift distribution at an equivalent flight condition. Initially, simply comparing the drag of both wings at the same geometric flight condition (angle of attack) was attempted. The lift coefficient for an elliptical lift distribution was given by:

$$C_{L_{elliptical}} = \frac{C_{L_{\alpha,2D}}}{1 + \frac{C_{L_{\alpha,2D}}}{\pi AR}} \alpha_{current} \tag{5.10}$$

,which rearranged Equation (4.1) and multiplied by the current angle of attack, $\alpha_{current}$. Then the reduction in angle of attack due to the induced drag, $\alpha_{i,}$ and the resultant induced drag were given by:

$$\begin{aligned} \alpha_{i_{elliptical}}\left(\bar{y}\right) &= \frac{-C_{L_{elliptical}}}{\pi AR} \\ C_{D_{i_{elliptical}}} &= -C_{L_{elliptical}}\alpha_{i_{elliptical}} \end{aligned} \tag{5.11}$$

where the downwash wash was constant over the wing, by definition of the elliptical lift distribution. The lift distribution was then given by:

$$c_L\left(\bar{y}\right) = \frac{4 \cdot C_{L_{elliptical}}}{\pi}\sqrt{1-\bar{y}^2} \tag{5.12}$$

where $c_L\left(\bar{y}\right)$ represented the local lift coefficients, distributed over the wing.

The equivalent parameters for lift and drag forces over the entire wing were given by:

$$\begin{aligned} C_L &= \pi AR\mu\Psi_1 \\ C_{D_i} &= \pi AR\mu^2\sum_{n=1}^{\infty} n{\Psi_n}^2 \\ \text{where } \mu &= \frac{C_{L_{\alpha,2D}}}{4AR} \end{aligned} \tag{5.13}$$

which were exclusively functions of the aspect ratio, *AR*, the two-dimensional lift curve slope of the wing $C_{L,\alpha,2D}$, and the coefficients Ψ. Similarly, the spanwise lift distribution $c_L\left(\bar{y}\right)$ was:

$$c_L(\bar{y}) = C_{L_{\alpha,2D}}\sum_{n=1}^{\infty}\Psi_n \sin(n\theta) \tag{5.14}$$

where $\bar{y}$ was the non-dimensional span location and θ was the equivalent mapping in polar coordinates given previously in Equation (5.6) according to the basis functions. Then, the downwash due to the tip vortex and the resultant, local induced drag were given by:

$$\begin{aligned} \alpha_i(\bar{y}) &= \mu\sum_{n=1}^{\infty} n\Psi_n\frac{\sin(n\theta)}{\sin\theta} \\ c_{D_i}(\bar{y}) &= -c_L(\bar{y})\alpha_i(\bar{y}) \end{aligned} \tag{5.15}$$

which allowed for an estimation of the impact on induced drag of the local deviation of the airfoil from the elliptical (design) lift distribution.

The modeled wing was compared to the elliptical lift distribution for a representative off-design angle of attack, specifically $\alpha=5^{o}$, as shown in Figure 5.11.

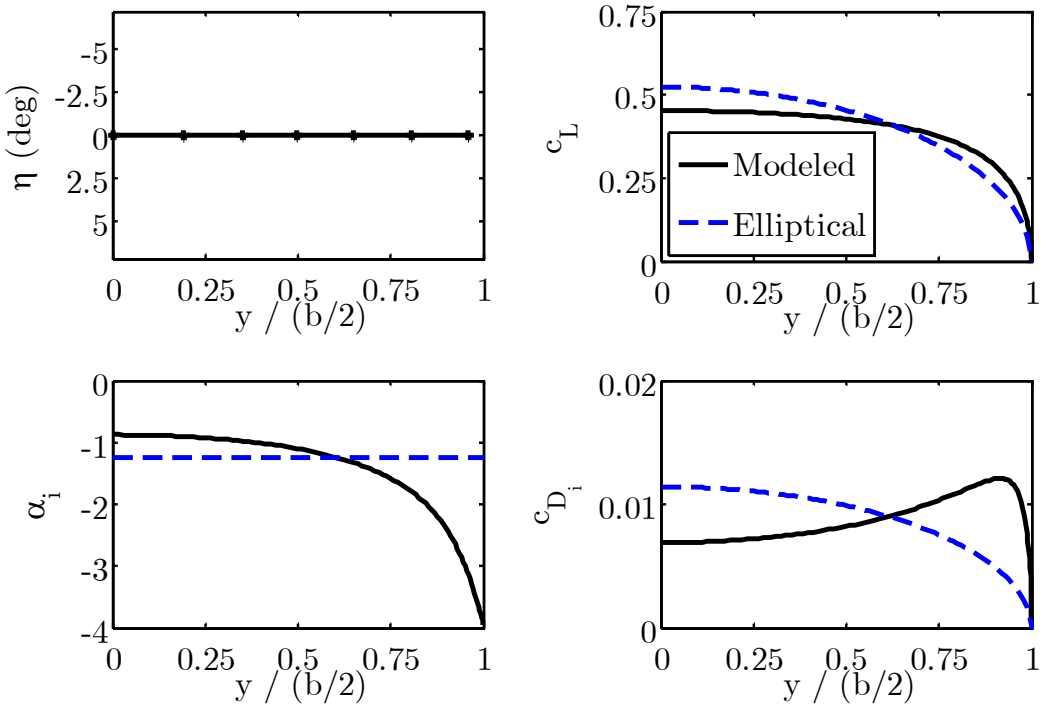

Figure 5.11 Comparing unactuated finite wing with elliptical lift distribution at $\alpha=5^{o}$

Table 5.4 Representative elliptical simulation for $\alpha=5^{o}$

Parameter	Simulated Value	Elliptical Value	Difference
C_L	0.395	0.411	-3.87%
$C_{D,i}$	8.69 x10^{-3}	8.97 x10^{-3}	-3.17%

The simulated straight wing showed less lift at the root of the wing and higher lift at the tip, which was reflected in the downwash. Where the downwash was less than the elliptical lift distribution, the induced drag was left, but at the expense of increasing the downwash outside of the tip. The results of these distributions on the total forces of the wing at the root were summarized in Table 5.4.

Examining the effect on the difference in lift and drag between the two results was very small, within 5%. Additionally, the lift coefficients for the wing were not matched, further confusing the comparison of induced drag.

It was then determined that for the comparison of drags to be valid, the comparative lift distribution needed to be constrained by an equivalent force (lift) condition:

$$C_{L_{elliptical}} = C_{L_{wing}} \tag{5.16}$$

rather than defining the comparative elliptical lift distribution at the same geometric condition (angle of attack), per the incorrect condition in Equation (5.10). The resultant matching of the elliptical lift condition to the current lift of the wing resulted in the modification of the lift and downwash as noted in Figure 5.12.

With the lift constraint appropriately matched, the induced drag of the modeled wing could be appropriately compared to an equivalent elliptical lift distribution at the same angle of attack. As shown in Table 5.5, the difference in drag between the elliptical lift distribution and the modelled lift distribution increased slightly, but was still small (<5%), even though the spanwise lift and downwash distributions showed large variations from the elliptical distributions.

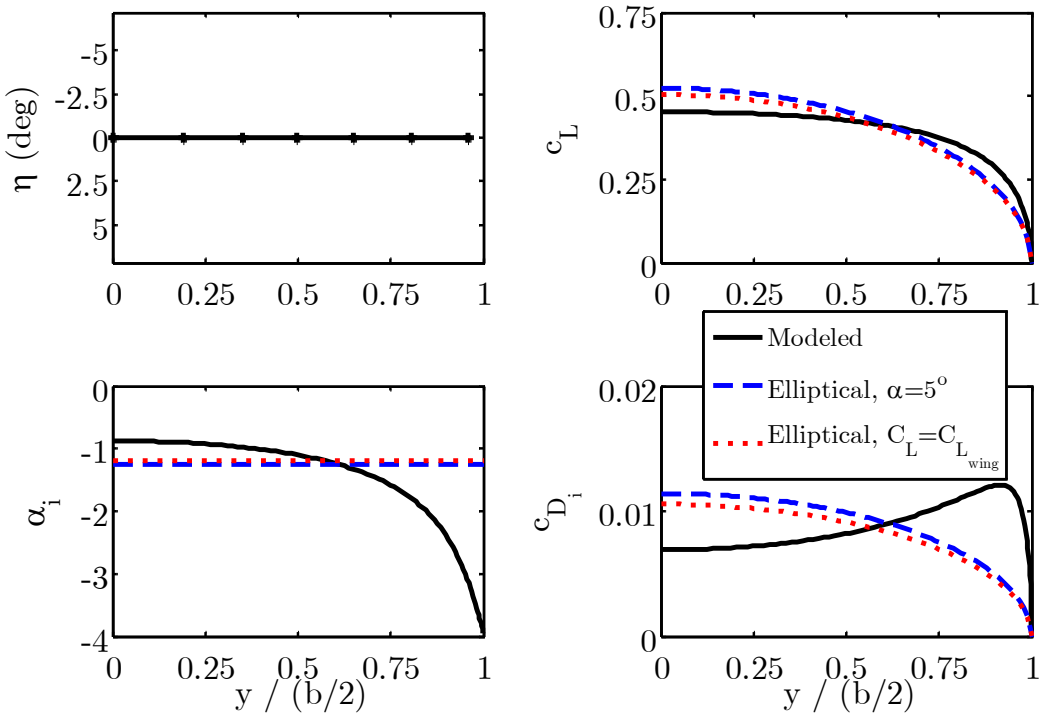

Figure 5.12 Lifting line theory simulation for unactuated finite wing with C_L matched for $\alpha=5^o$

Table 5.5 Representative elliptical simulation for C_L matched at $\alpha=5^o$

Parameter	Simulated Value	Elliptical Value	Difference
C_L	0.395	0.395	0%
$C_{D,i}$	8.69×10^{-3}	8.29×10^{-3}	4.78%

This simulation confirmed that for the small differences in drag being measured, it was important to compare according to the same force condition rather than the geometric condition. It was also noted that adaptation to simply minimize induced drag could easily negate the apparent drag benefit of minimizing induced drag by increasing profile drag, on the order of only a 5% improvement for a straight, untapered wing.

This result motivated that the drag benefit of the SMTE morphing would not be easily found in small adaptations to minute changes in flight conditions but rather in larger changes where the comparative advantage in control derivatives was be expected.

5.2.3.2. Modeling with actuation

The model was then augmented with the experimentally-derived lift control derivatives from Table 5.2, and the maximum achievable local effective flap angles as measured in the test in Section 5.2.2. A constrained optimization, utilizing the *fmincon* algorithm in *MATLAB* [119] was then utilized to find the optimal spanwise actuations of the morphing aileron that achieved the design lift distribution at off-design flight conditions. For simplicity of understanding, the wing was initially modelled without the immovable cowling at its root, resulting in the constrained optimization stated in Table 5.6. Because the design lift distribution was selected as the elliptical lift distribution, the objective function to minimize was simply the induced drag penalty, σ. The results from a representative flight condition, $\alpha=5^o$ were shown in Figure 5.13 and Table 5.7.

Table 5.6 Constrained optimized of induced drag at a single flight condition

Minimize:	Residual parameter, $\sigma(\eta(y))$
Subject to:	$\eta_{min}<\eta<\eta_{max}$ $C_{Lwing}(\alpha_{current}) = C_{L,elliptical}(\alpha_{current})$
Given:	Current flight condition, $\alpha_{current}$ Wing parameters, excluding wing root

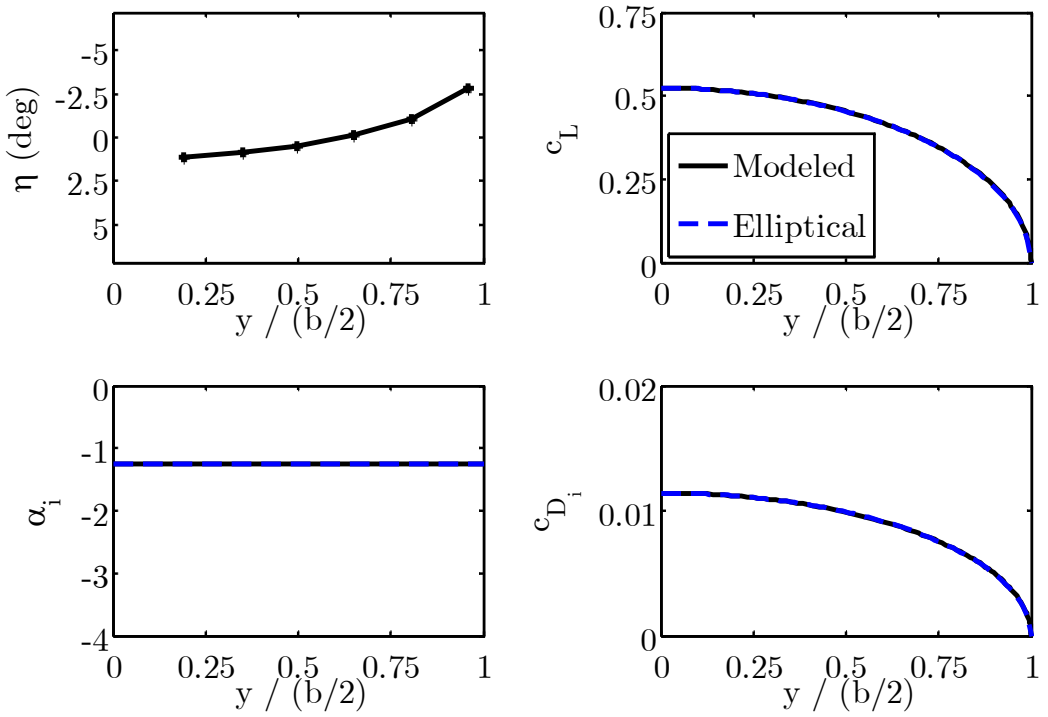

Figure 5.13 Modeled optimal configuration and forces with no fixed root for $\alpha=5^{o}$

Table 5.7 Optimized spanwise actuation to minimize induced drag at $\alpha=5^{o}$

Parameter	Simulated Value	Elliptical Value	Comparison
C_L	0.411	0.411	0%
$C_{D,i}$	8.97×10^{-3}	8.97×10^{-3}	0%

The optimization achieved its desired result of matching the desired elliptical lift distribution and the downwash was constant over the span of the wing. The result was an increase in the effective angle of attack at the root and a decrease in the tip.

Including the fixed root of the wing in the analysis changed the results significantly. To accurately confirm the experiment, an accurate model and comparison was made by fixing the lift coefficient and including the root. The results from the optimization with a fixed root were shown in Figure 5.16 with total forces summarized in Table 5.8.

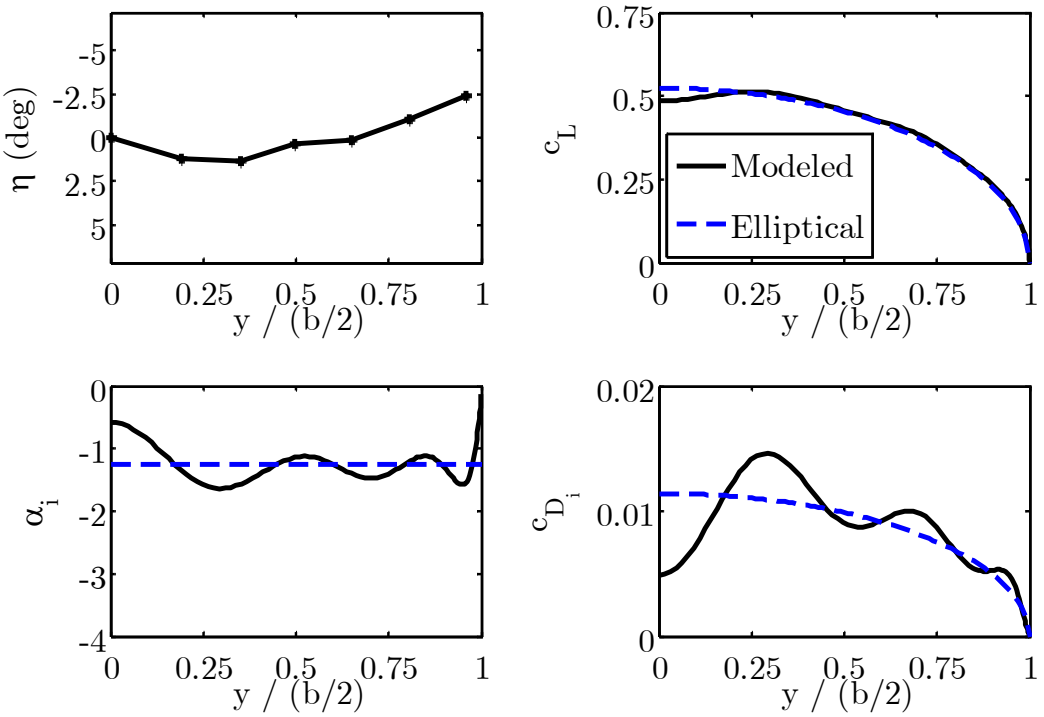

Figure 5.14 Modeled optimal configuration and forces with fixed root for $\alpha=5^{o}$

Table 5.8 Optimized spanwise actuation to minimize induced drag at $\alpha=5^{o}$

Parameter	Simulated Value	Elliptical Value	Comparison
C_L	0.411	0.411	0%
$C_{D,i}$	9.02 $x10^{-3}$	8.97 $x10^{-3}$	0.62%

The resultant optimal actuation did not resemble an intuitive, elliptical compensation, but rather was the result of attempting to compensate for the fixed root of the wing while achieving the desired lift distribution. The fixed root suppressed the ability of the wing to reach the optimal lift coefficient from the elliptical lift distribution, slightly decreasing the root lift coefficient at this representative positive angle of attack. Thus, an exact match of the elliptical lift distribution could not be achieved, but rather an approximation where the locations of the control points were matched. Nevertheless, the induced drag was within 0.6% of the elliptical result, showing that the impact of the fixed root would only slightly impact the drag with proper actuation.

This result showed that for a representative the angle of attack, the wing achieved the desired lift distribution with approximately 0.6% error in induced drag, which was deemed to be

of reasonable fidelity for the current investigation. The result also showed an expected optimal configuration that was not elliptical due to the fixed root of the wing. Ideally, the wings would not include a fixed root, but this was assumed to be a realistic consideration of aircraft design similar to the unmovable fuselage or core of the aircraft.

Although this initial analysis merited higher fidelity simulations including profile drag, such an analysis was not performed. Specifically, the next higher fidelity analysis, i.e. Extended Lifting Line Theory, which utilizes simulated two-dimensional drag polars would not capture the three-dimensional effects of the gaps between the flapped ailerons for comparison, which was part of the focus of the current study.

Finally, these results showed that the maximum benefit of morphing in the SMTE test bed would not be to compete directly with an elliptical planform near a design flight condition, but rather to achieve what a fixed wing could not: adaptation to different flight conditions.

5.2.4. Expected optimal configurations

With the wing configurations sufficiently modeled, the expected performance of both wings was comparatively modeled to better understand the range of flight conditions that could be realistically achieved by the SMTE.

Because geometric parameters (i.e angle of attack) were more easily controlled in the desired experiment than force conditions (i.e. lift), angle of attack was chosen to specify the flight condition. Then, a constrained optimization problem as stated in Table 5.9 was used to find the expected optimal configurations that would achieve the desired lift distribution provided the current flight condition. Note the only difference between this problem and the optimization problem from the previous section was that the desired lift distribution was defined from a previous flight condition, $C_{L,design}$.

Table 5.9 Optimization to achieve design lift distribution from current condition

Minimize:	$\sigma(\eta(y))$
Subject to:	$\eta_{min}<\eta<\eta_{max}$ $C_{Lwing}(\alpha_{current}) = C_{L,design}(\alpha_{design})$
Given:	Design angle of attack, α_{design} Current angle of attack, $\alpha_{current}$ Wing parameters

Because the airfoil selected for the experimentally-tested wing was symmetric and the design lift was taken to be at the minimum drag coefficient per Section 5.1.2., the design angle of attack was found at $\alpha=0^o$. At this "design" condition, the elliptical lift distribution was then a special case where no lift was generated. Although there were many configurations where this condition could have been satisfied, the intuitive and trivial result was a uniform, unactuated lift distribution, i.e $c_L(\overline{y}) = 0$. For brevity, the differences in angle and forces between the "current" flight condition and the "design" condition were defined as:

$$\begin{aligned}
\Delta\alpha &= \alpha_{current} - \alpha_{Design} \\
\Delta C_L &= C_{L_{current}} - C_{L_{Design}} \\
\Delta C_l &= C_{l_{current}} - C_{l_{Design}} \\
\Delta C_m &= C_{m_{current}} - C_{m_{Design}} \\
\Delta C_D &= C_{D_{current}} - C_{D_{Design}}
\end{aligned} \tag{5.17}$$

which for the assumed design condition were:

$$\begin{aligned}
\alpha_{Design} &= 0 \\
C_{L_{Design}} &= 0 \\
C_{l_{Design}} &= 0 \\
C_{m_{Design}} &= 0 \\
C_{D_{Design}} &= C_{D_0}
\end{aligned} \tag{5.18}$$

and so for all case except drag, the change in force coefficients could be thought of as interchangeable with design force coefficients.

5.2.4.1. Ideal optimal configurations

The optimal configurations for adapting the SMTE wing and articulated flap wings from the current angle of attack back to the design condition were modeled for a range of angles of attack utilizing the optimization in Table 5.9. This optimization was carried out for a variation in angles of attack about the design angle of attack. The optimal configurations determined by the optimization were summarized in Figure 5.15, with incremental steps through the perturbation in flight condition of $\Delta\alpha=1^o$. The resultant configurations were symmetric about the unactuated flight condition, which was the selected design configuration.

As noted in the figure, the SMTE reached the limits of its adaptation capabilities by approximately $|\Delta\alpha|=5^o$, where the individual active sections saturated. Although, by $|\Delta\alpha|=4^o$, the limits of the SMTE were beginning to impact its capability to achieve the desired lift distribution. Because the articulated flap wing did not have such stringent restrictions on its actuation ranges, it did not encounter its range limitations over this variation in flight conditions.

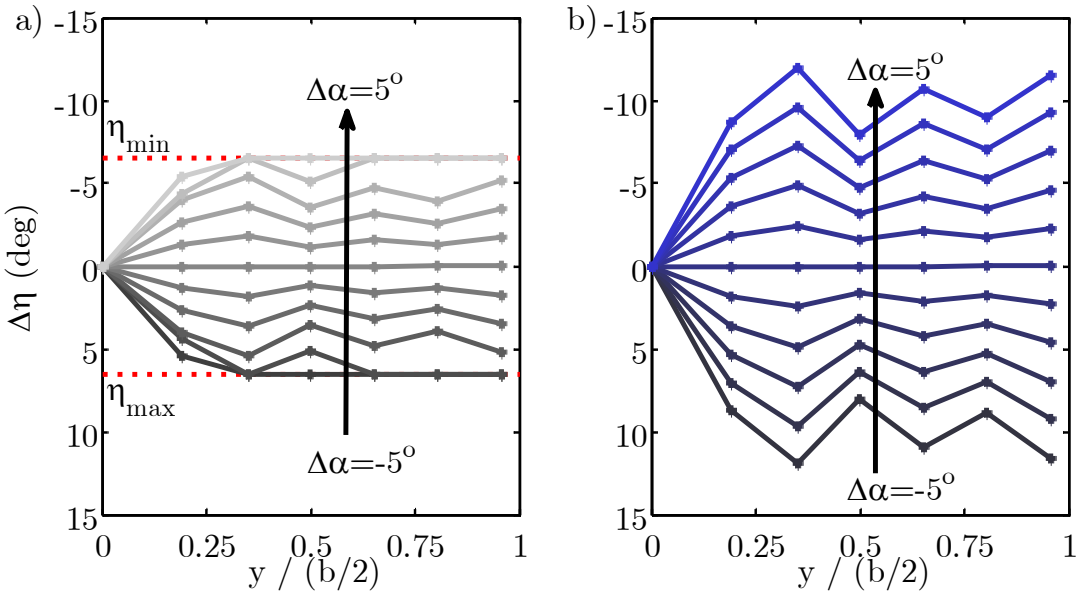

Figure 5.15 Optimal adapted actuation for a) SMTE and b) articulated flap wing while varying current angle of attack with C_L matched for $\alpha=0^o$

Again, it was noted that the equivalent flap angles required to achieve the desired lift distribution were much smaller than that of the articulated flap wing, reflecting the larger lift control derivative of the SMTE. Accordingly, it was expected that these configurations would result in lower profile drag.

The expected forces generated by these optimal configurations at the root of the wing were also analyzed via lifting line theory. Lift and induced drag were modeled provided by Equations (5.13). Rolling moment was then calculated by:

$$C_l = \int_{\bar{y}=0}^{\bar{y}=1} \bar{y} c_L(\bar{y}) d\bar{y} \tag{5.19}$$

which was the spanwise integral of the local lift coefficient, $c_L(\bar{y})$, weighted by the nondimensionalized spanwise location on the wing, $\bar{y}$. The pitching moment was crudely calculated utilizing:

$$C_m = \int_{\bar{y}=0}^{\bar{y}=1} C_{m_\eta} \eta d\bar{y} \tag{5.20}$$

where η was the local equivalent flap angle and $C_{m,\eta}$ was the pitching moment control derivative calculated by uniform actuations for the wing. The results from the calculations were summarized in Figure 5.16.

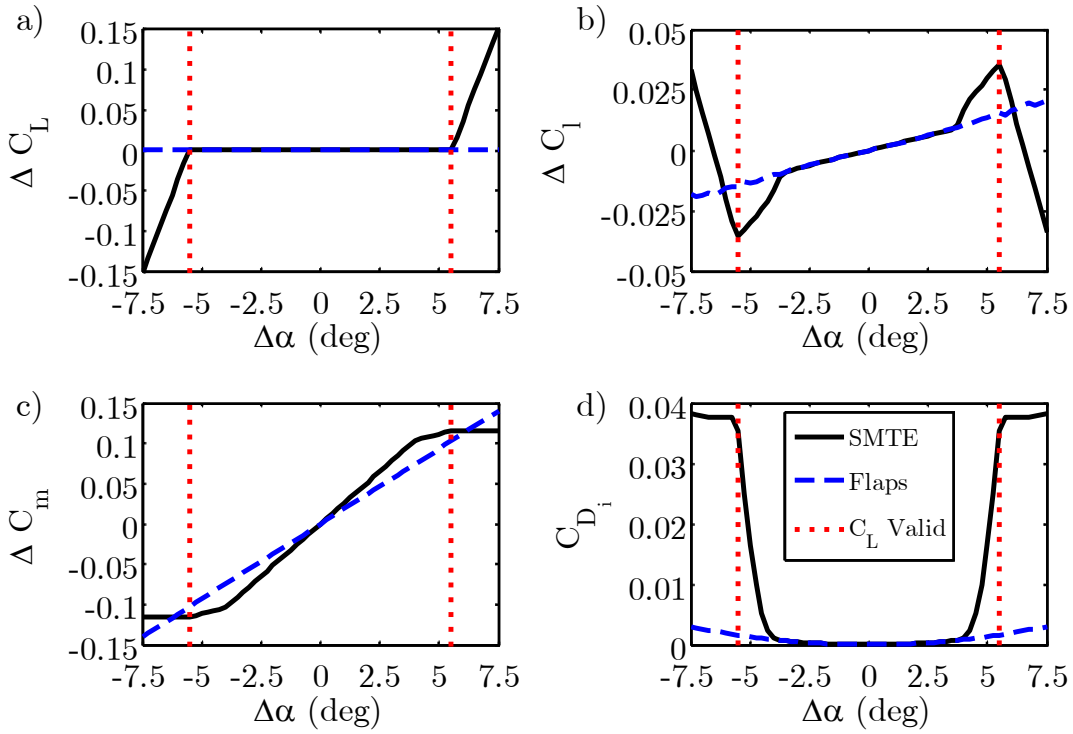

Figure 5.16 Adapted forces a) lift and b) roll c) pitching moment and b) drag while varying current angle of attack with C_L matched for $\alpha=0^o$

As shown in Figure 5.16a, the lift coefficient was sufficiently matched for the SMTE up to $|\Delta\alpha| \approx 5^o$, as predicted by the previous analysis of the optimal configurations. Beyond this flight condition, the SMTE did not maintain the desired lift distribution due to its inability to actuate further. Examining the rolling moment coefficient in Figure 5.16b, which was a measure of the spanwise lift distribution, the SMTE only accurately matched the desired lift distribution until $|\Delta\alpha| \approx 4^o$, which was the approximate condition at which the first active section reached its maximum actuation. Beyond this condition, the magnitude of the rolling moment was first over-achieved then under-achieved as the local lift distributions were altered by the constrained actuations.

The effective penalties of the two concepts when adapting to the desired lift distribution was summarized by the pitching moment and induced drag. As expected by the much larger pitching moment coefficient associated with the SMTE, Figure 5.16c showed that the SMTE achieved much larger magnitudes of pitching moments until the desired lift coefficient could no

longer be matched. Additionally, the induced drag of the SMTE concept was seen in Figure 5.16d to drastically increase once the desired lift coefficient could no longer be matched by the SMTE. This metric confirmed that matching the appropriate lift coefficient and distribution was a strict requirement for comparing the potential drag benefit of the SMTE.

These penalties were assessed as a "percent increase" by normalizing them with a relevant parameter. For pitching moment, the percent increase was simply calculated by:

$$\%C_{m_{increase}} = \frac{\Delta C_{m_{SMTE}} - \Delta C_{m_{flap}}}{\Delta C_{m_{flap}}} \cdot 100\% \tag{5.21}$$

which normalized the difference in pitching moment between the two wings by the pitching moment of the flapped wing. The baseline (minimum) drag value for the wing was experimentally measured to be:

$$C_{D_0} = 0.015 \tag{5.22}$$

by averaging several experiments. Because this study assumed that the wing was designed about this baseline drag, it was assumed that an aircraft designer would measure any performance increase or decrease relative to this value. Thus, the percent increase in drag was calculated as:

$$\%C_{D_{increase}} = \frac{\Delta C_{D_{SMTE}} - \Delta C_{D_{flap}}}{C_{D_0}} \cdot 100\% \tag{5.23}$$

which was the difference in adaptive drag between the two wings normalized by the baseline drag. The projected increases in pitching moment and drag were summarized in Figure 5.18a and Figure 5.18b, respectively.

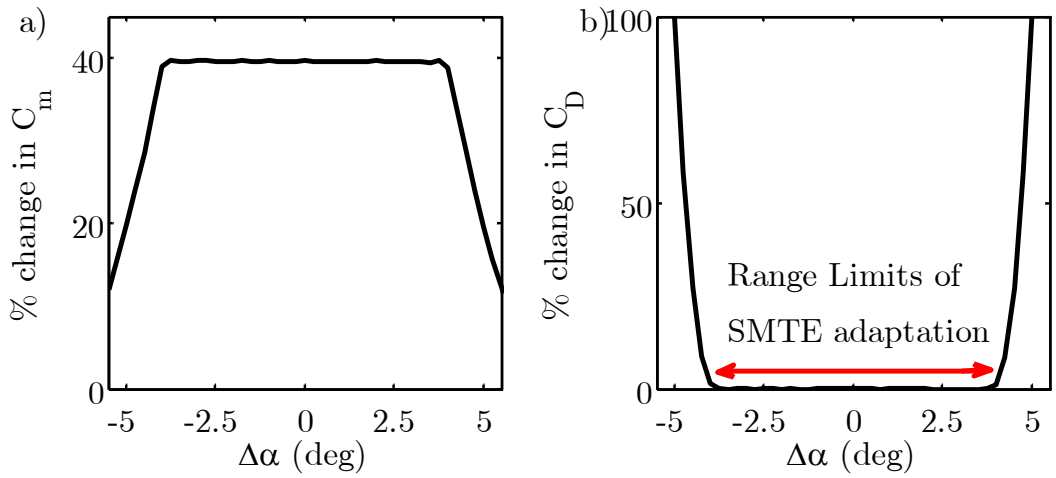

Figure 5.17 a) Modeled pitching moment increase and b) drag bounds for the SMTE adaptation while varying current angle of attack with C_L matched for $\alpha=0^o$

From this plot, it was expected that the SMTE would generate an approximate 40% increase in pitching moment over the achievable range of angles of attack, and that all drag benefit due to the SMTE would be found between $-5^o<\alpha<5^o$ due to the rapidly increasing induced drag. Note that no profile drag benefit was projected within this range by lifting line theory because the model did not include profile drag caused by the saturating active sections.

5.2.4.2. Practical search vector

It was desired to experimentally evaluate the modeled results from Section 5.2.4.1 to realize the expected profile drag benefit of the SMTE that was not modeled by lifting line theory. Ideally, the only points necessary for testing would be the predicted optimal configurations from Figure 5.15 over the range of projected beneficial flight conditions ($-5^o<\alpha<5^o$).As seen in the measurement of the control derivatives in Section 5.2.2, correct estimation of the control derivatives was subject to variation in flow separation due to control surface actuation and angle of attack.

Accordingly, an experimental method was needed to ensure that the design lift coefficient and distribution were reached at the current flight condition despite errors in lift control derivative calculation. Then a “search vector” of predicted optimal configurations along the path from the unactuated, current flight condition (Point #2) in Figure 5.2 to the adapted flight condition (Point #3) in Figure 5.2., was predicted in the neighborhood of Point #3.

Table 5.10 Constrained optimized to generate configurations along "search vector"

Minimize:	$\sigma(\eta(y))$
Subject to:	$\eta_{min}<\eta<\eta_{max}$ $C_L = C_{L,design} + \Delta C_L$
Given:	Current flight conditions Wing parameters

The neighborhood around this condition was defined by a line-search of scaled versions of the desired (i.e. elliptical) lift distribution, described by Table 5.10. The "search vector" was then the set of modeled configurations which represented scaled versions of the desired lift distribution that were parameterized by a deviation in lift coefficient about the design condition

A representative selection of the modeled and measured optimal configurations along the "search vector" for the articulated wing and the SMTE wings were shown in Figure 5.18 and Figure 5.19, respectively. The servo wing did not provide information about its current state and was assumed to achieve the configurations based on its calibration and previous experimental results.

The results from Figure 5.19 verified two important results from the previous modelling. First, the SMTE would need smaller deflections to achieve the same change in lift, which was consistent with the larger SMTE control derivative. Second, the SMTE active sections began to saturate $|\Delta\alpha| = 4.5^o$ due to practical limitations in the active sections, such as pulling against the fixed root of the wing. Thus, around this change in flight condition, the ability of the SMTE to achieve the commanded optimal spanwise lift distribution actuations would follow the trends modelled in Section 5.2.4.1.

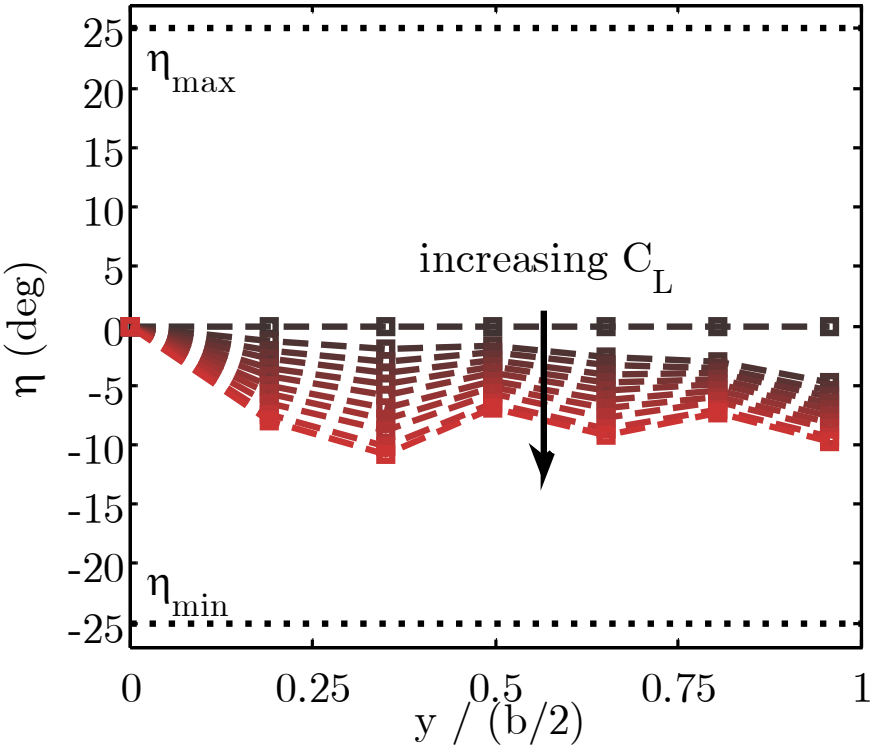

Figure 5.18 Optimal actuations with varying ΔC_L for $\Delta\alpha$=-4.5° for the Articulated wing

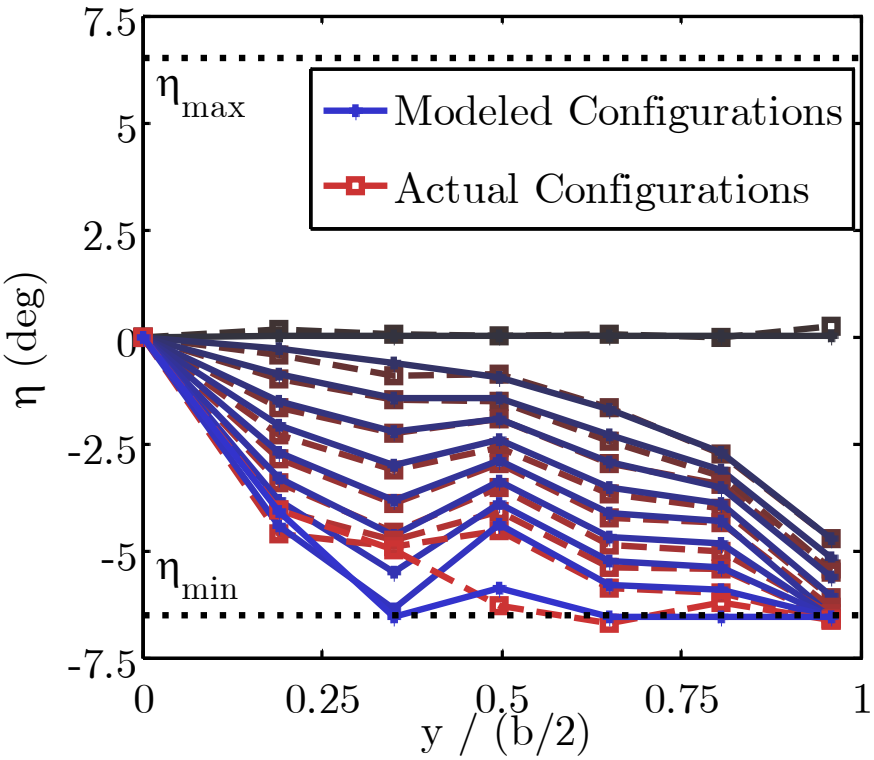

Figure 5.19 Optimal actuations with varying ΔC_L for $\Delta\alpha$=-4.5° for the SMTE wing

5.2.5. Summary of modelling conclusions

The SMTE was expected to match the lift and rolling moment, showing its ability to match the desired lift distribution until approximately $|\Delta\alpha|=4^o$. The pitching moment induced by the SMTE was expected to exceed the flap by approximately 40% over this entire range. At that variation in flight condition, the tip active section reached its maximum achievable deflection and saturated. It was at this point that the SMTE was expected to reach its maximum benefit due to the expected profile drag benefit of the conformal morphing of the SMTE over the articulated wing. Between this condition and $|\Delta\alpha|=5^o$, the remainder of the active sections would reach their maximum deflections and the magnitude of rolling moment would increase, and then sharply decrease as the induced drag rapidly increased.

To experimentally verify these projected conditions, it was desired to sweep along "search vectors" at several angles of attack near the expected maximum benefit. These search vectors, which consisted of scaled version of the change in desired lift distribution, would allow interpolation at the same lift condition and thus determine the expected associated drag benefit, while eliminating the effect of induced drag.

The fidelity of the modelling required these "search vectors" to ensure that the desired lift distribution was not missed by experimental limitations on the estimation of the lift control derivative. Additionally, the modeling could not accurately capture flow separation, profile drag or spanwise losses. These additional losses were grouped together to be experimentally evaluated as the penalty associated with the adaptive concept.

5.3. Experimental results

The following section summarizes the experimentally-measured aerodynamic forces measured by the method described in Section 5.1.2, using the experimental setup described in Section 5.2.2.1 by searching for the optimal adapted flight condition along the "search vectors" at each current flight condition predicted by the aerodynamic model, which was detailed in Section 5.2.4.

5.3.1. Representative search for adaptive drag

An example of the forces measured as part of the methodology used to find the optimal adapted condition along the predicted search vector was shown in Figure 5.20. Then, as a brief reminder, Point #1 represented the unadapted, design condition, Point #2 represented the unadapted condition at the current angle of attack, and Point #3 represented the optimal adapted condition at the current angle of attack to achieve the design lift coefficient with minimum drag.

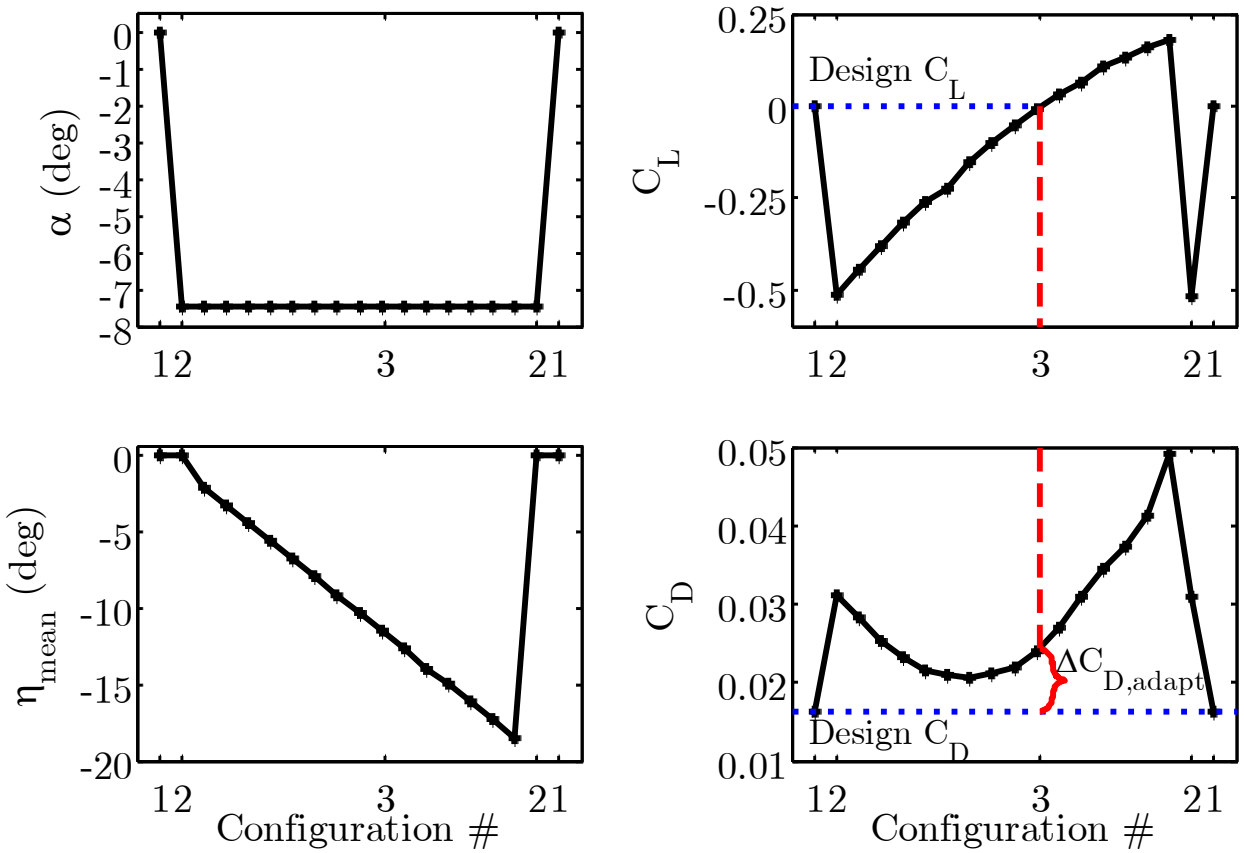

Figure 5.20 Representative search for articulated flap wing at flight condition $\Delta\alpha=7.5^{o}$ along predicted search vector

The test moved from the design condition (Point #1) to the unactuated, current condition (Point #2), then along the "search vector" from (Point #2) to the adapted configuration at the current flight condition (Point#3), overshooting in the process. The test was then completed by repeating Points #2 and #1 to check for repeatability of forces. The design lift coefficient was precisely matched by interpolating the measured data points along the search vector and matching this point to its respective drag. The resultant "adaptive drag penalty", as defined by Equation(5.4), was $\Delta C_{D,adapt}$ was then the difference between the measured drag at Point #3 and Point #1 as seen in Figure 5.20. This measured quantity was assumed to be strictly a result of the ability of the adaptive concept to adapt at the current flight condition, capturing spanwise losses, viscous effects and positioning errors.

5.3.2. Force results

These searches were performed for both the SMTE and the articulated flap wing over a range of angles of attack where the concepts could reasonably achieve the design lift. The aerodynamic forces of the wings, unactuated at the current angle of attack (Point #2) and then optimally adapted to the design lift (Point #3), were shown in Figure 5.21. Arrows identified the result of adaptation, highlighting the range of aerodynamic forces at each flight condition. A close-up of the results about the adapted condition, consistent with previously modelled results was shown in Figure 5.22.

As noted by the modelling in Section 5.2.4.1, the SMTE did not achieve the design lift coefficient by approximately $|\Delta\alpha| = 5^o$. Examining, the rolling moment provided a metric of the ability of the concept to achieve the design lift distribution. By that metric, the rolling moment of the SMTE showed a sharp dive at approximately $|\Delta\alpha| = 4.5^o$ as the concept began to reach the actuation limits of the active section at the tip of the span. The pitching moment and drag represented the effective penalties of the articulated wing and SMTE wing in achieving the design conditions. Consistent with the control derivative results, the SMTE created a much larger pitching moment to achieve the same change in lift. The SMTE however showed a dramatic reduction in drag at off-design conditions, noted as an "area of interest" in Figure 5.22. Considering the relative positioning error in the SMTE as compared to the articulated wing, and the relatively low fidelity of the aerodynamic modelling, this result was dramatic.

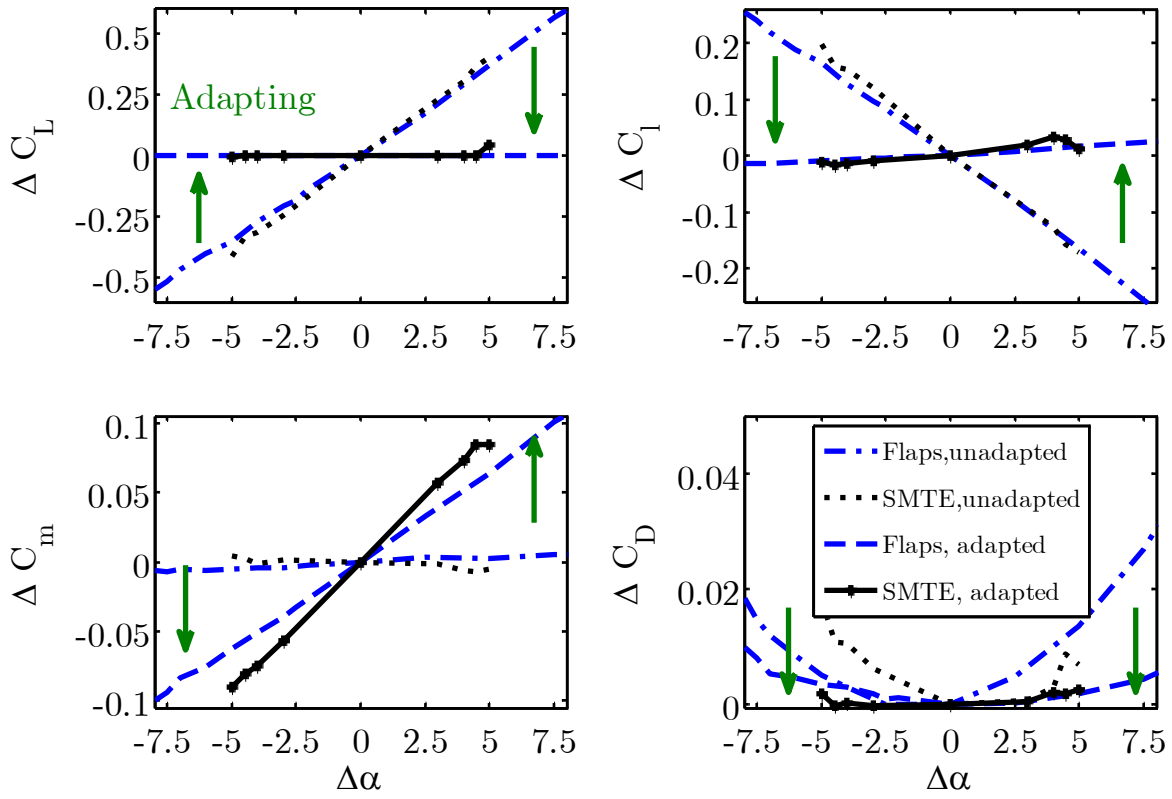

Figure 5.21 Forces for unadapted (Point #2) and adapted (Point #3) configurations at current condition relative to the design condition (Point #1)

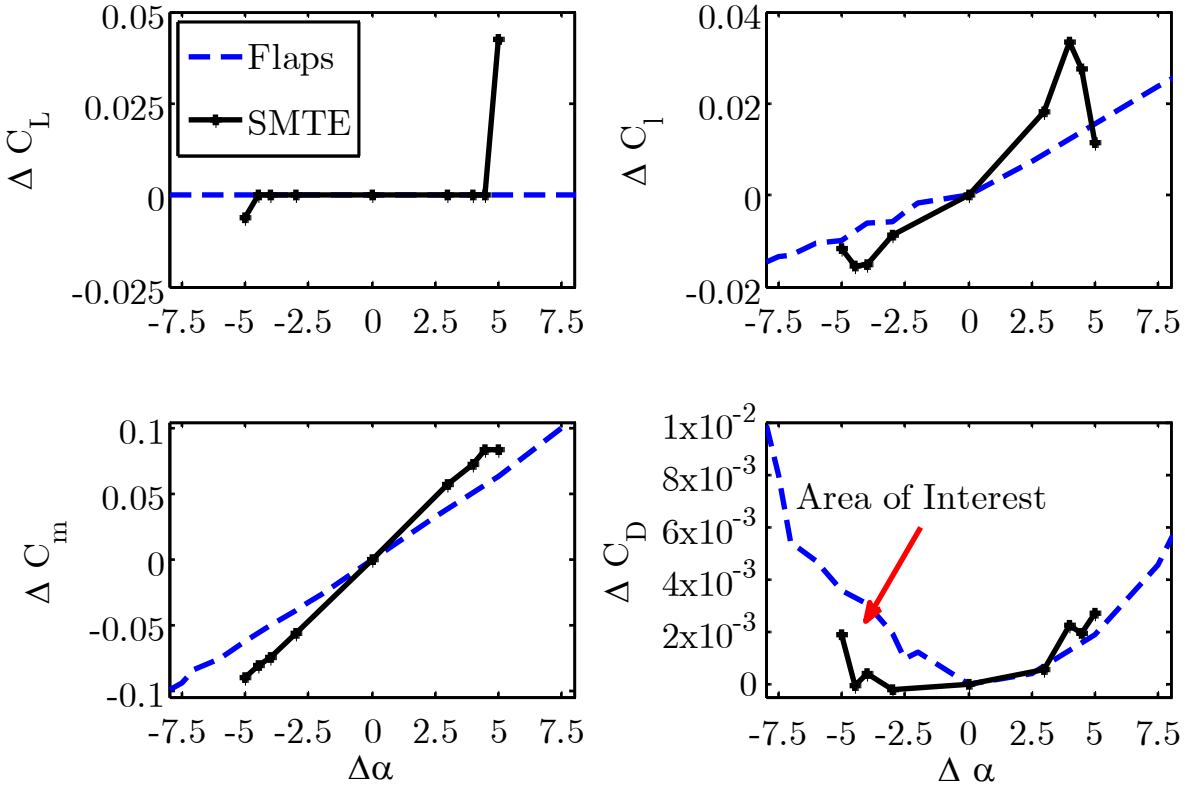

Figure 5.22 Forces for adaptive configurations (Point #3) relative to design condition (Point #1)

The experimental results were combined with the modeled results from Figure 5.17 to understand the limitations of the model and the experiment. As seen in Figure 5.23, the model correctly predicted the divergence of the SMTE from the desired lift distribution but slightly overestimated the maximum change in flight condition |Δα| that the SMTE could still match the lift coefficient. The rolling moment coefficient provided a metric of how accurately the wings matched the desired lift distribution. As seen for the negative angles of attack, the rolling moments for both wings matched well, but at positive angles of attack the SMTE wing showed greater error in matching the desired lift distribution. These effects were accounted for by positioning errors in the SMTE active sections near the maximum deflections of the range. Still, the deviations as compared to the unactuated forces from Figure 5.22 were relatively small.

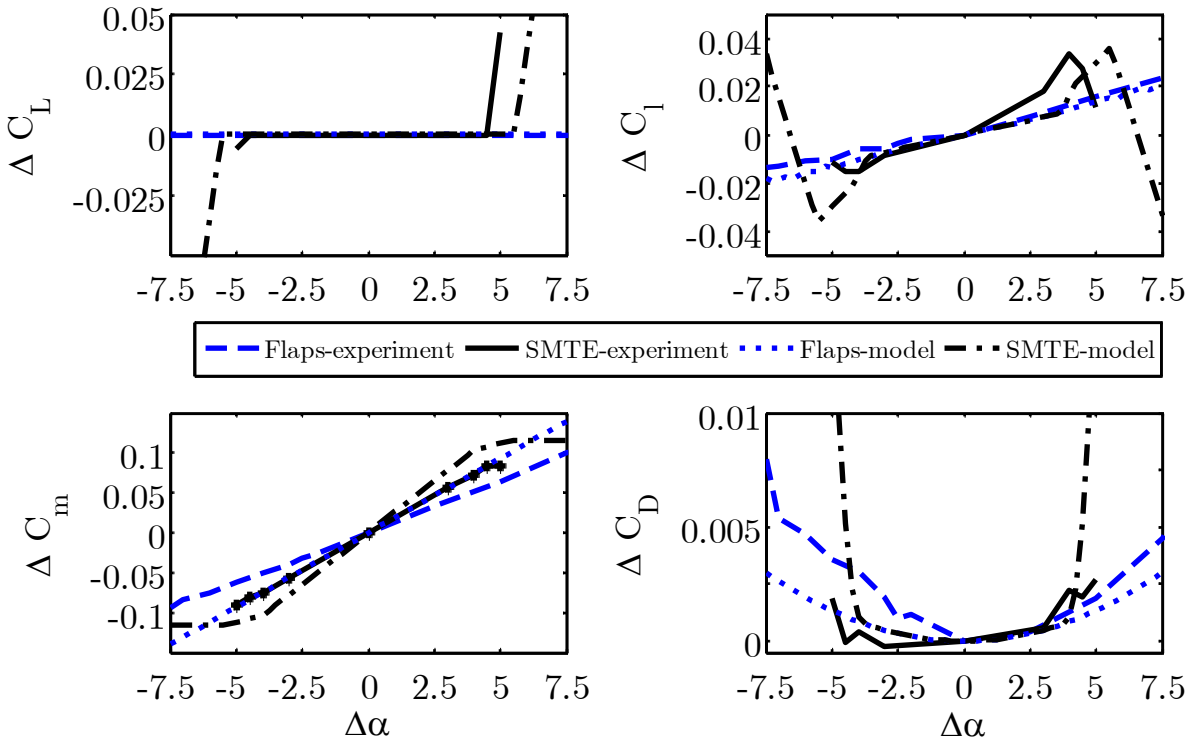

Figure 5.23 Comparison of measured optimal forces to modeled predictions

As expected by not modeling profile drag, the pitching moment and drag coefficients did not match the projected values from lifting line theory. The measured effective pitching moments were reduced compared to the modeled projections utilizing the uniform control derivatives. This could have been caused by a reduced profile drag penalty associated with restoring the airfoil to a lower drag condition. As seen by the change in drag from the baseline, all of the adapted drags were very small. The SMTE approximately equaled the expected calculation of the minimum induced drag for negative angles of attack and to slightly exceed it for positive angles of attack. The real gain as measured by the experiments against the modelling was where the articulated flap wing exceeded the expected induced drag within the SMTEs range of authority, most likely due to the unmodelled profile drag.

To clarify this gain, a summary of the relative penalties of pitching moment and drag as compared to the change from the baseline condition were presented in Figure 5.24 in the manner previously described by Equations (5.21) and (5.23). The change in moment was normalized by the difference between the adapted and unadapted configurations (Point #2 and Point #3) for the articulated wing at the current angle of attack. The change in drag was normalized by the baseline drag.

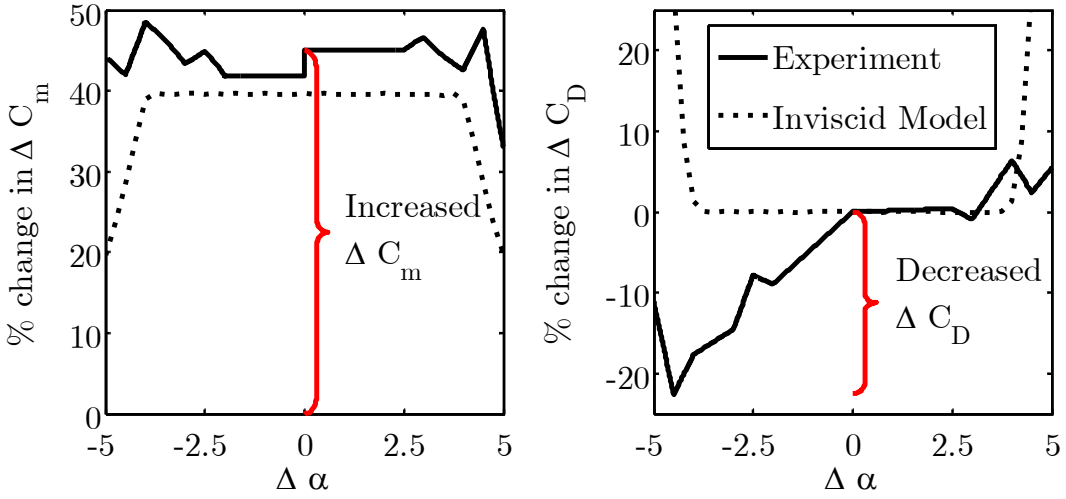

Figure 5.24 Relative moment and drag penalties for SMTE wing

The results showed that the pitching moment increase for the SMTE wing was fairly consistent at all angles of attack, representing a roughly 45% increase. Although this difference was roughly half of the value as predicted by the uniform control derivative results, it was very close to the difference projected by lifting line theory. Although this analysis classified the increased pitching moment as a penalty, the increase relative to the articulated wing was consistent across all angles of attack and then could have been considered as a different design condition when sizing the position and authority of other control surfaces on the aircraft.

Finally, and most significantly, the SMTE showed a 20% drag reduction around $\Delta\alpha$=-4.5^{o}. Although a similar result was not seen at positive angles of attack, the drag of the articulated flap wing was much lower at these conditions and as noted by the change in rolling moment, the SMTE did not completely match the desired lift distribution due to positioning errors. Nevertheless, the SMTE wing showed drag performance roughly equal to the articulated wing at these flight conditions.

5.4. Summary and conclusions

This chapter described the development and implementation of an experimental method for determining the comparative drag advantage of a morphing wing concept at off-design flight conditions. The method was implemented for evaluating the performance of the Spanwise Morphing Trailing Edge (SMTE) concept as compared to conventional articulated ailerons for a half-span finite wing in a wind tunnel. To predict the optimal actuations at each off-design flight condition, a simplistic lifting line model augmented by experimentally-measured lift control derivatives was utilized. The control derivatives implemented in the model were experimentally derived and compared with two-dimensional linear aerodynamic theory and previous experimental results, showing good agreement.

The experimentally measured control derivatives revealed that the SMTE showed significant improvement in lift (34%), rolling moment (45%) and pitching moment (87%). The maximum equivalent flap deflections for both configurations were also identified for the same equivalent flap angle.

The lift control derivatives were implemented in lifting line theory to predict optimal "search vectors" that would minimize induced drag while seeking the design lift coefficient and

lift distribution from an off-design angle of attack. This methodology was utilized to find the "adaptive drag" penalty of the SMTE and articulated flap wings. The results showed drag reduction at off-design aerodynamic conditions up to approximately 22%, with increased pitching moment of approximately 45% near the maximum achievable deformations of the SMTE.

It was noted that the lifting line theory model did not accurately capture the absolute magnitude of the pitching moment, but closely matched the relative advantage. While the profile drag effects were experimentally measured, the model did not capture profile drag effects and could not predict the effect of viscous losses, motivating the use of higher fidelity models.

5.5. Future work

The gains in performance were expected to increase for larger disturbances from the design flight condition, i.e. changes in angle of attack, but were limited by the inherent range of the morphing concept. These results motivate morphing concepts of larger deformation ranges, higher fidelity modelling, and more advanced controls technologies for system-level adaptation to more accurately assess the aerodynamic advantages outside of linear aerodynamic conditions, namely for near stall conditions and unsteady flight.

These results should be viewed as the beginning of possible advantages for similar adaptive wing concepts. The fidelity of the modelling and control of the morphing wing was relatively rudimentary as separated flow, localized viscous effects, and in-the-loop correction for deviation from modeled conditions were not considered in this analysis. The wing's controller would ideally adapt to measured conditions rather than relying upon prescribed deformations from a rough physical model for the system. By improving the deformation range or other camber-line altering capabilities of the morphing concept, these results are only expected to improve.

A hybrid smart-material morphing design that could improve the overall actuation range of the concept, while improving performance for separated flow is developed and discussed in the following chapter as a first step to addressing these issues.

Chapter 6
Hybrid Morphing:
the Synergistic Smart Morphing Aileron

As shown in Chapter 2, the Flexure Box aileron enabled smooth variation of the trailing edge camber of an airfoil by utilizing Macro-Fiber Composite (MFC) patches to function as both skin and bending actuator, with its root boundary condition augmented by an internal compliant structure. In Chapter 3, a design study regarding the number of MFCs utilized per modular active section of the Spanwise Morphing Trailing Edge (SMTE) concept concluded that only two were necessary, captured in the "unimorph" configuration, to sufficiently characterize the concept. This was concluded by showing that increasing the number of MFC patches from two to four reduced the unloaded actuation range and did not improve the Flexure Box aileron's performance under aerodynamic loading. Including more MFCs also detrimentally increased the overall mass. Motivated by the measured aerodynamic gains of the SMTE in Chapters 4 and 5, an improved morphing aileron design was desired to improve the tip deflection range and decrease the degradation in the performance under higher aerodynamic loads.

The following chapter details the development and characterization of a hybrid morphing aileron concept that utilizes multiple smart materials together to overcome the inherent limitations of its constituent smart material actuation concepts. The added complexity of including multiple actuators within the same morphing concept has reduced the number of such designs in the literature. Additional actuators can increase mass as well as the likelihood of failure. Improper inclusion of the smart materials in the design can therefore negate any inherent mass or complexity advantage by combining structure and actuator. Knowledge about implementation, e.g. actuation and force requirements, of different smart materials can also pose an initial barrier to their proper inclusion in the design. Identifying appropriate metrics for

improvement and characterizing both actuators with a common system can also be difficult as the concepts often lack common features. Finally, the actuators must be successfully controlled in the combined concept so as to achieve improvements in these metrics that surpass their individual capabilities. The following chapter describes the development and characterization of a multiple-smart material morphing concept that overcomes these individual challenges

Section 6.1 details the development of the combined hybrid concept, the Synergistic Smart Morphing Aileron (SSMA), and the role of the individual actuation concepts. Section 6.2 describes a novel spectral characterization method for assessing the potential dynamic gains of the hybrid concept. Section 6.2.3 addresses the modeled aeroelastic capabilities of the concept, permitting static characterization without the need for a complex controller and shows the capability of the concept to better alleviate aerodynamic loads and to improve control flow separation near stall. Section 6.3.3 then addresses the development and implementation of a simplistic controller to measure power gains and realize modeled dynamic capabilities for the SSMA

6.1. Development of a hybrid smart material morphing concept

The previous chapter described the aeroelastic characterization of the Macro-Fiber Composite (MFC)-driven flexure box concept in the context of a static morphing application. The MFCs created a compliant structure that could affect the aerodynamic flow about the trailing edge of an airfoil by conformal bending. The relative restrictions of actuation by aerodynamic loads were noted at increased flow speeds. However, it was still desired to utilize a piezo-driven morphing concept, due to the relatively high bandwidth of piezo systems, even compared to conventional electromechanical motors [99]. Thus it was sought to augment the actuation authority of the trailing edge, both maximum tip deflection and resistance to aerodynamic loads, without compromising the high actuation bandwidth of the MFCs, and to potentially improve the functionality of the morphing airfoil. As seen in the study regarding the increased use of MFC patches in parallel, resistance to aerodynamic loads was increased but not overall tip deflection. Adding more MFC patches along the chord of the airfoil (in series) could have increased the tip deflection, but it also would have introduced increased compliance and aeroelastic effects. Additionally it would require significant modification of the spar box of the wing and complex actuation considerations [86]. An additional smart material morphing concept with high work

density (to minimize the impact on mass of an additional actuator), high stroke (to increase actuation range), and high blocking force (to increase authority in series under high aerodynamic loads) was desired.

As previously identified in the introduction, Shape Memory Alloy (SMA) wires are capable of exhibiting high stroke, blocking forces and work density, as illustrated in Figure 1.15, which are capabilities deficient in Macro-Fiber Composites and were subsequently selected to augment the MFC-driven Flexure Box design. To reduce the design complexity of including another smart material in the morphing concept, a pre-existing concept was chosen from the literature. As described by Faria [51] and illustrated in Figure 6.1, the camber line of a sectioned airfoil was shown to be altered by antagonistically heating and cooling the SMA wires located above and below a connecting hinge. By heating one of the wires in an initially deformed state, a reduction in wire length due to transformation strain in the SMA created a relative rotation between structures while straining the opposing wire. After the actuation was complete and the desired angular position reached, reduced energy was required to maintain the temperature of the wires and the deformed shape. The rate of actuation was limited by the rate of heat diffusion from the wires to their surroundings and by the applied power.

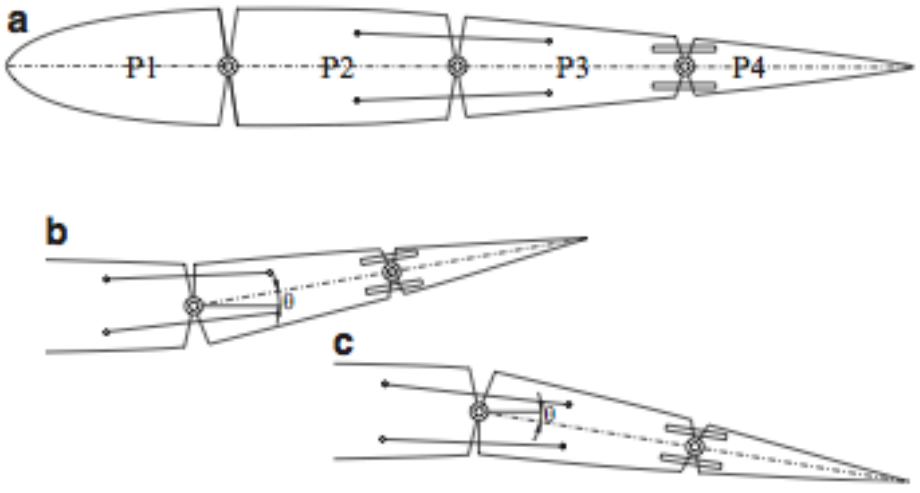

Figure 6.1 SMA-actuated hinge concept in its a) Initial unactuated position b) tip – up position by heating the upper wire and c) tip-down position by heating the lower wire [51]

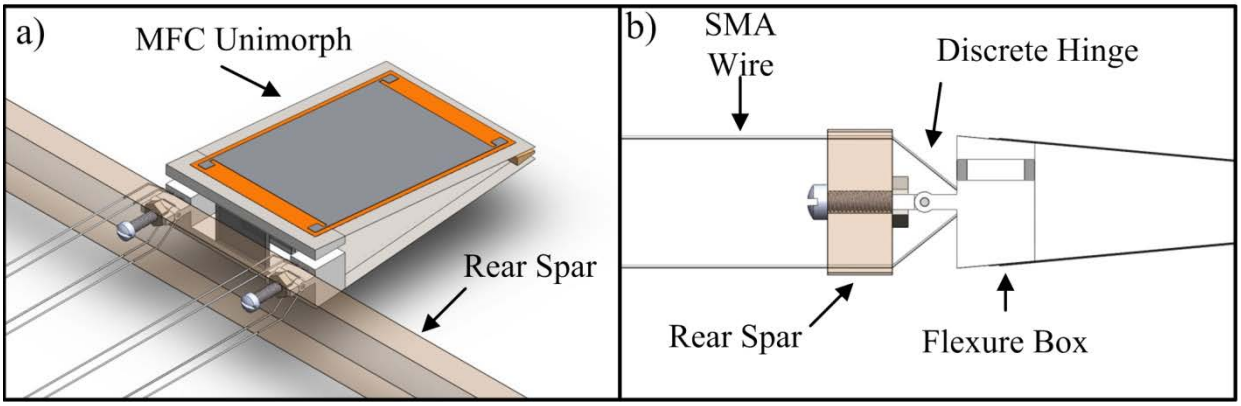

Figure 6.2 SSMA Concept a) Isometric view b) Side view

Thus, a hybrid morphing airfoil design, the "Synergistic Smart Morphing Aileron" or SSMA was introduced. The SSMA used multiple smart materials in a morphing airfoil mechanism to provide increased control capabilities beyond that of its constituent materials, without prohibitively increasing design complexity, as first reported in [121]. Leveraging the differing actuation time scales and ranges of shape memory alloys and piezoelectric fibers, the design uses a combination of antagonistic MFC unimorphs and Shape Memory Alloy wire actuators to control a morphing aileron. The SMA wires controlled a discrete angle deflection at the root of the aileron over a slower timescale while the MFCs controlled precise conformal variations over a faster timescale. This design represented the first hybrid morphing airfoil design utilizing multiple smart material actuators in the literature.

Illustrated in Figure 6.2 in a conceptual drawing, the SMA-driven hinge was located near the front of the Flexure Box aileron. This conceptual design placed the entirety of the control surface after the rear spar, thereby maintaining the continuity of the wing box for ease of implementation. The concepts were placed in series to maximize their effect on camber deformation and thus the resultant flow about the airfoil. The SMA-wire was placed forward of the Flexure Box aileron to effectively leverage the higher blocking stress of the SMA wires while permitting additional length within the airfoil for increased stroke. This device allowed for the combination of both the Flexure Box aileron and SMA-actuated hinge into a single concept without significantly increasing the size or complexity of the actuation aileron or overly complicating the design procedure. Although the Flexure Box was completely solid-state, the hinge for the SMA was constructed using a discrete hinge, due to the chordwise compressive

effect of the SMA wires. The resultant design increased the range of the overall tip deflection while maintaining the ability for quick conformal actuation, and improving aeroelastic response.

6.2. Spectral characterization for hybrid morphing

Although the SMA wires contributed improved work density, blocking force, and stroke requirements, it was not easily understood how the new actuation mechanism would impact the effective bandwidth and performance of the hybrid concept. Although dynamic models for both MFC unimorphs and SMA wires have been developed, it was the comparative improvement of the combined concept that was sought [51,101,122]. Due to the novelty and relative complexity of multiple-smart material morphing concepts, and the large deflections of the combined actuation, a methodology was required to identify possible improvements in the SSMA concept. A spectral characterization method for showing possible bandwidth improvement for a morphing aileron with multiple smart materials was developed here and first reported by [121]. This characterization method represented a novel method for dynamically characterizing a hybrid morphing concept without a complex control system.

To measure the bandwidth improvement of the hybrid morphing concept, a time-dependent parameter of interest was sought that was common to the two smart material actuators and simple to measure. The tip displacement of the morphing airfoil was chosen as a relevant parameter to both actuation mechanisms because it provided a common indicator of the ability of the different actuators to influence the flow about the airfoil as seen in previous chapters. Notably, the equivalent flap deflection parameter was not used as it assumed a monotonically deforming trailing edge control surface. The added degree of freedom in the trailing edge of the SSMA then made the equivalent flap deflection metric no longer valid.

With a relevant parameter identified, a method was needed that could identify the quality of the dynamic response. This concept was complicated by the fact that both the MFCs and SMAs exhibited hysteresis and creep over their actuation range, except at the limits of their ranges. For ailerons and other aircraft control surfaces, a simple metric of the dynamic capabilities was defined by the ability of the control surface to cross its entire displacement range in a given period of time, in the process inputting a square-wave or “doublet”, typical for identifying flight characteristics in aircraft [123]. This type of control was relevant in minimum-time reaching problems and was also relevant for hysteretic actuators. As the maximum actuation

speed of the morphing aileron was of interest and the constituent actuators exhibited significant hysteresis, square wave excitation over the entire actuation range was chosen for its simplicity and reproducibility. Square wave excitation allowed for a simple binary control of input, eliminating the need of a complex control system.

The performance of each active mechanism was evaluated using square wave excitation with the maximum allowable amplitude for each actuator for a range of frequencies, with particular interest in two response metrics: maximum amplitude of motion and the mechanism speed. For the smart materials in use in this application, first-order behavior was expected in response to a square wave input from literature and initial tests. SMA wires undergoing constant-power heating were roughly approximated with first-order strain and displacement responses with respect to time due to Joule heating effects. Also, the MFC-driven Flexure Box was seen to exhibit highly damped dynamic responses to square wave inputs, for which the response to these step-like inputs was also approximated via a first-order response [121].

Based on the assumed mutual response of both actuators as first order systems, the first-order time constant (τ) was chosen as the metric to comparatively evaluate the actuators' speeds. Figure 6.3 below compiled information about the variables used to describe the response of the active mechanism and the excitation signal. The response peak-to-peak amplitude (Δ) was an intuitive concept, while the time constant (τ) was a value derived from the exponential reaching condition for a first order system [124].

Experimentally measuring the first order time constant, $\tau_{\infty,}$ for different square-wave frequencies was impractical as the velocity of the tip displacement exponentially decayed to zero and the asymptotic amplitude could not be realistically reached for any finite time. To simplify measurement, the time constant, τ, was defined as the time at which the first order response reaches 1-1/e ≈ 63.2% of the peak-to-peak amplitude for a square wave input. This metric is derived from the first-order time constant, τ_{∞}, which was only relevant for an infinite-period square wave, i.e. a step input. The relative time constant τ_r, was then defined by:

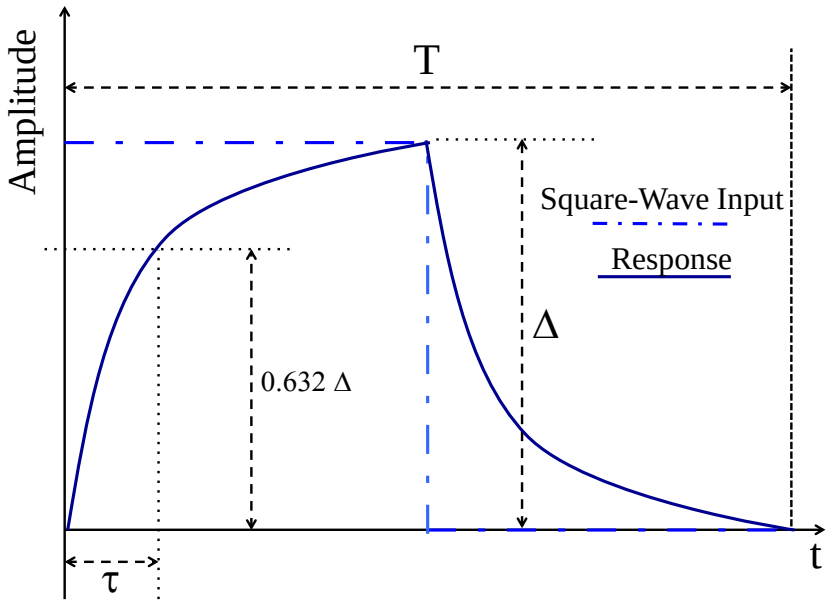

Figure 6.3 Illustration of the square wave time response

$$\tau_r = \frac{\tau}{T} \tag{6.1}$$

where the measured time-constant, τ, was normalized by the excitation period T. This normalization allowed the relative time constant, τ_r, to be directly compared between responses for different input frequencies and thus excitations periods, providing a measure of the bandwidth without the use of a controller.

Equation (6.1) above also intuitively implied that the relative time constant was bounded between 0 and 0.5, simulating a relatively fast and slow response of the actuator as compared to the commanded input frequency. By plotting the finite response amplitude (Δ) and relative time constant (τ_r) against the excitation frequency, a Square Wave Response Function (SWRF) is obtained. To draw meaningful effects and eliminate hysteresis from the plot, it was then important to allow the response to reach a steady-state solution before measuring these values. Then,

$$\tau_r = \frac{\tau_\infty}{T}\left[1 - \ln\left(1 - e^{-T/2\tau_\infty} + e^{-T/2\tau_\infty + 1}\right)\right] \tag{6.2}$$

was used to relate the relative time constant, τ_r , to the first-order time constant, τ_∞, via the excitation period, T.

6.2.1. Spectral characterization of actuation

Selecting a configuration relevant to the SMTE concept from the previous chapters, the SSMA concept was implemented into a NACA 0012 airfoil with 305 mm chord and 76 mm span, as shown in Figure 6.4. This scale was roughly representative of the chord of a wing or control surface of a Low-Altitude Long-Endurance or Medium-Altitude Long-Endurance UAV. The configuration of the actuators was chosen so that the two concepts showed roughly equal tip displacement, simplifying the understanding of the underlying actuation systems.

Two pairs of antagonistic SMA wires were used to actuate about a discrete hinge (52 % chord) that was located between the compliant box, (beginning at 63% chord) and the inactive front of the airfoil. The SMA wires were anchored to a flat plate, on which the flexure box concept was also mounted. This configuration allowed the top and bottom SMA wires to exert equal moments about the hinge, independent of the Flexure Box configuration. The wires passed through thin metal tubes in the rear spar and were anchored to the front spar of the airfoil where appropriate electrical leads were applied, resulting in approximately 110 mm (36% chord) of active, heated length for each of the two SMA wires on each side of the airfoil. The Flexure Box Aileron was manufactured in the unimorph configuration as described by Chapter 3 which consisted of a total of two MFCs on either side of the trailing edge.

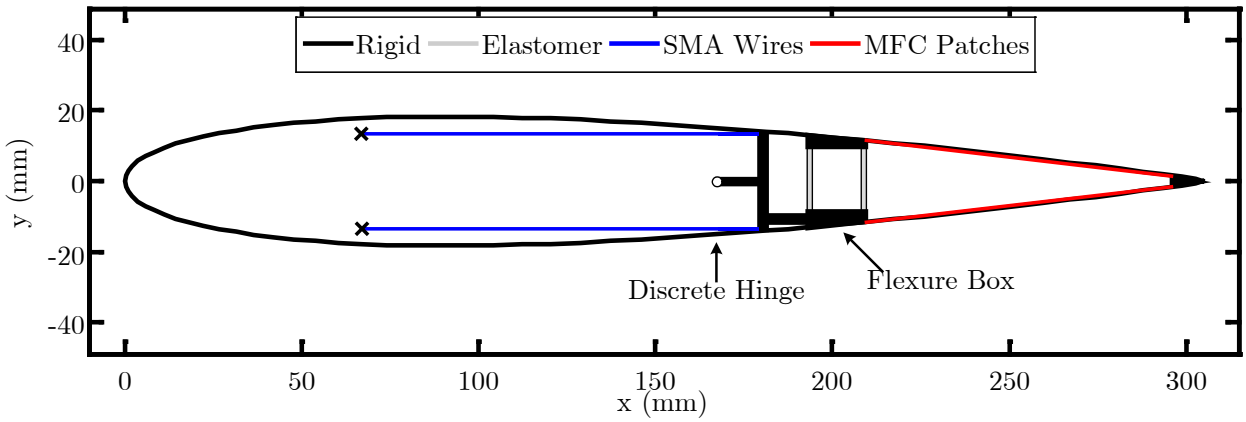

Figure 6.4 Diagram of Synergistic Smart Morphing Aileron concept

Based on the volume of smart materials utilized in this application, the total mass of smart material used was calculated to be approximately 0.1 grams for the SMA-based actuator and 8 grams of PZT in the MFC-based actuator, reflecting the comparatively higher specific work associated with SMAs. For the purposes of evaluation, both the Flexure Box mechanism and the hinge for the SMA were created using the Objet Connex 500 multi-material 3D printer similar to the manner described in Chapter 2.

6.2.1.1. Methodology

The SSMA actuation concept was first constructed in a demonstrative mechanics configuration to experimentally evaluate the ranges and timescales associated with the constituent smart materials, seen in Figure 6.5. A single Keyence LKG-402 laser displacement sensor measured the approximate tip displacement of the SSMA at 142 mm aft of the rear spar.

The two smart material actuators were driven with different (individual) circuits to change camber in the *y* direction as defined in Figure 6.4. The two MFCs unimorphs were operated together in bending, consistent with the "unimorph" configuration from Chapter 2, using an AVID Dual Channel MFC Bimorph High-Voltage Driver. The driver board applied voltage to the unimorphs in a 3:-1 ratio so that the maximum applied voltages were +1500V and -500V for the opposing unimorphs This compact high voltage amplifier was designed to run on 3-cell Lithium Polymer batteries, typical to the scale of aircraft of interest. As shown in Ohanian *et al.* 2012, this circuit was capable of driving MFCs unimorphs of the scale investigated in this paper to approximately 100 Hz, well beyond the frequencies of interest [99].

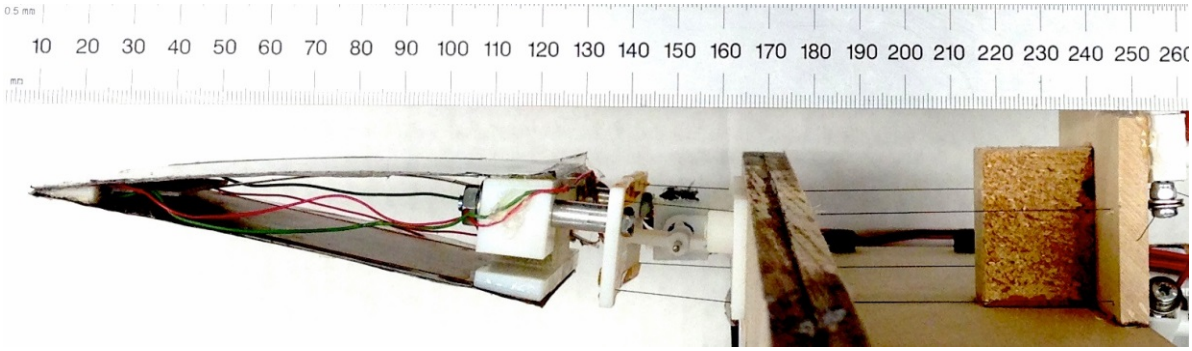

Figure 6.5 Experimental construction of SSMA mechanics demonstrator

Two 200 μm diameter Nitinol wires from Dynalloy, Inc. were anchored at a representative front spar, located at 50 mm chord. Each 238 mm wire ran from the front spar, through the rear spar to the aft mounting location on the flat plate, and then back through the rear spar to the front spar, to close the electrical connection. The wires were driven in an antagonistic configuration (top vs. bottom) by a custom-built relay switching circuit. The relay could alternate a constant current between the two wires when heating was required. The power consumption of the SMA driver circuit was limited to the recommended current draw as provided per the manufacturer. No active cooling system was used. Accordingly, the wires consumed approximately 3 Watts, roughly the same maximum power draw of the MFC driver circuit. Further considerations regarding the sizing of the wires, power consumption, evaluation of the validity of the chosen time constant, and impact of heating power on the cycle lift of the SMA wires was evaluated in Appendix B.

The results from Appendix B indicated that no clear trend in time-constant was available from increase in wire size. However, the time constant reasonably characterized the chosen wire diameter up to approximately 0.4 GPa of applied stress. Additionally, the chosen wire diameter minimized the consumed power while maximizing the resilience to high-stress loading conditions. The recommended applied heating power was also shown to maximize the potential the cycle life of the SMA wires as indicated by the testing at maximum strain conditions.

6.2.1.2. Results

First, the mechanism was used to test only the response of the Shape Memory Alloy-driven mechanism (hereafter denoted as "SMA-only" for brevity). The system was excited with a sweep in square waves from 0.005 Hz to 1 Hz per the spectral characterization method defined in Section 6.2. At each frequency, the system was allowed to reach a steady state and repeat for at least 10 cycles. The resulting Square Wave Response Function (SWRF) including the standard deviations for the measurements was shown in Figure 6.6.

For the lower frequencies the SMA-only mechanism maintained a relative time constant near zero which meant that the device reached the vicinity of the maximum amplitude in a small time as compared to the input period, similar to the representative condition shown in Figure 6.7. As the input frequency increased, the actuation amplitude decreased and the relative time constant increased, indicating that the mechanism performance was degrading. At higher frequencies, the slew rate of the system became insufficient to allow the actuator to reach the commanded bounds within the given time period, as seen in Figure 6.8. Finally, at the highest frequencies, the SMA-only mechanism rate-saturated, which was characterized by a low amplitude and high relative time constant.

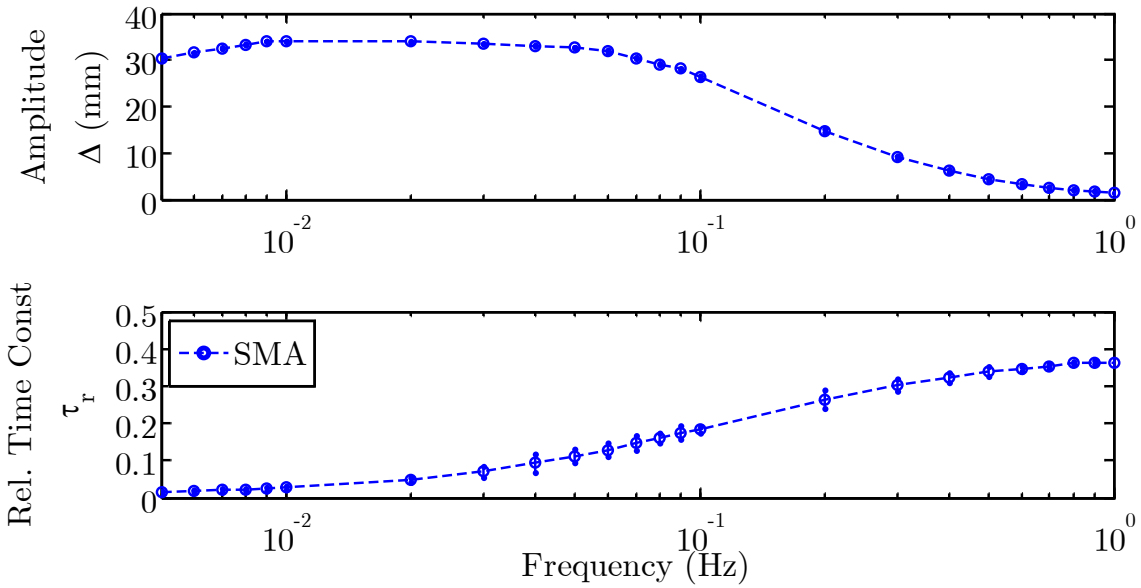

Figure 6.6 Experimental SWRF plots for the SMA-only mechanism

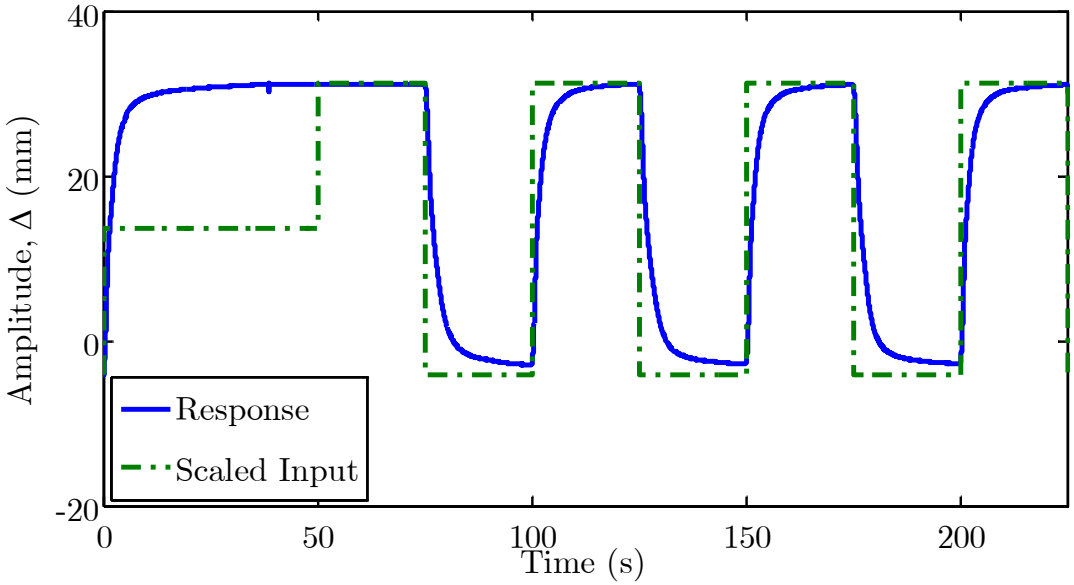

Figure 6.7 SMA-only actuator time response for 0.02 Hz

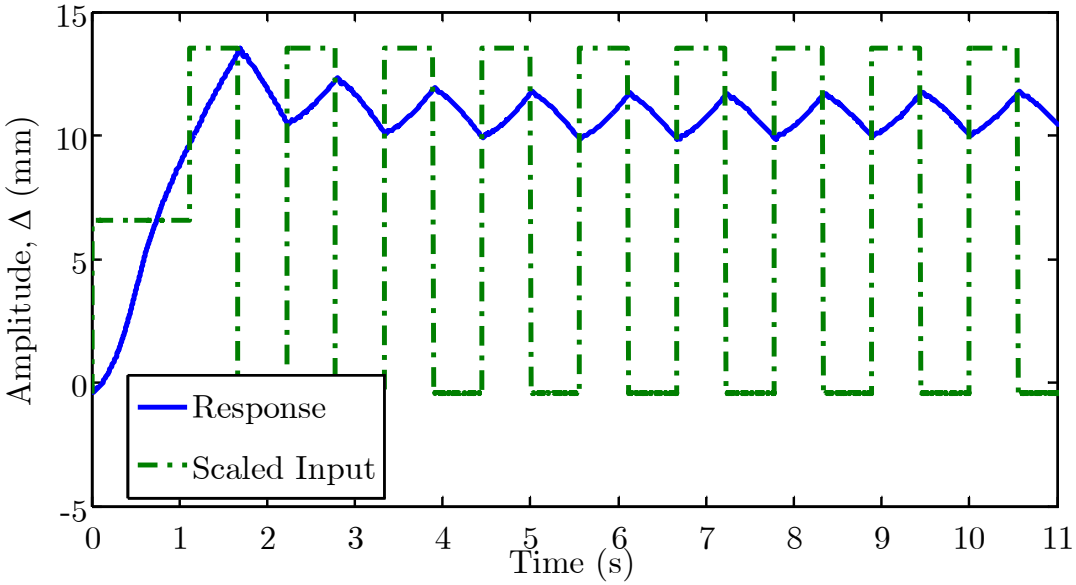

Figure 6.8 SMA-only actuator time response for 0.9 Hz.

For the MFC-based mechanism (hereafter denoted as “MFC), the tests were performed in a similar manner for a different range of square wave frequencies: from 0.1 Hz to 10 Hz. An increased frequency range was elected because it showed a similar trend in the frequency domain for the MFC mechanism. The resulting SWRF was presented in Figure 6.9.

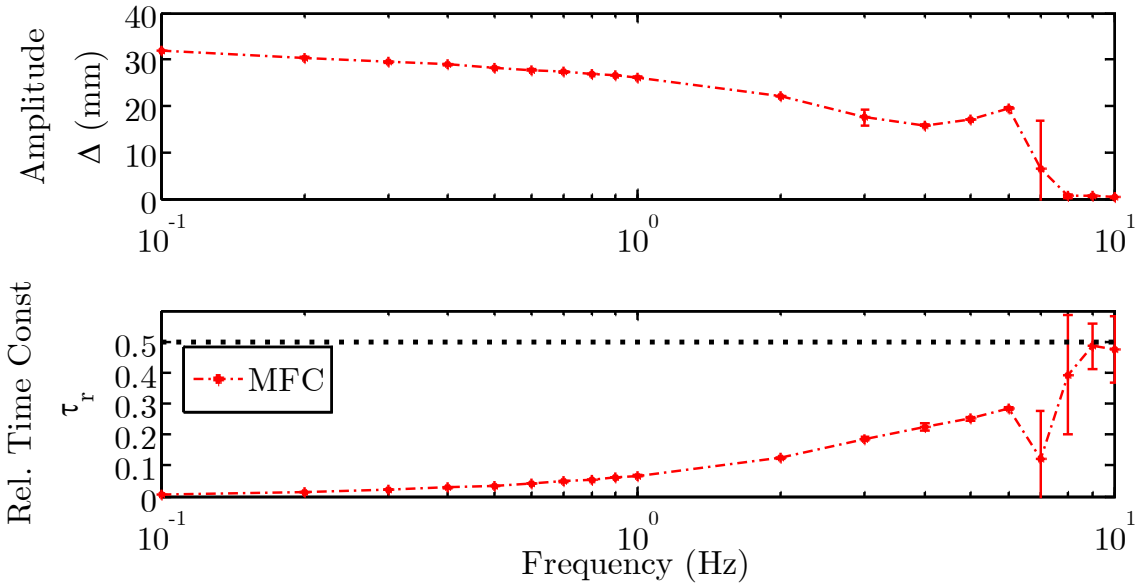

Figure 6.9 Experimental SWRF plots for the MFC-only actuation mechanism

The MFC-only mechanism showed a relatively quick response as compared to the inputs for frequencies up to 1 Hz, as illustrated by Figure 6.10. For slightly higher frequencies, both the amplitude and the relative time constant began degrading in a similar way to the SMA-only mechanism; however for the MFC-only mechanism it occurred for frequencies one order-of-magnitude larger. As input frequency increased even more, the structure reached a resonant mode, as shown Figure 6.11, and then a rate-saturated condition as shown in Figure 6.12. These results were confirmed by the large standard deviations in relative time constant as see in Figure 6.9. These results were also consistent with the experimentally determined resonant mode of the flexure box, as shown in Appendix C.

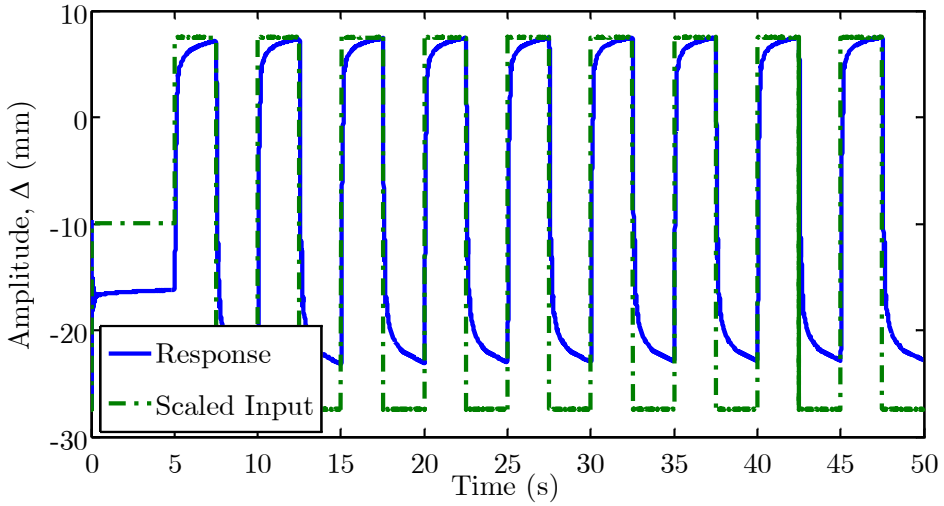

Figure 6.10 MFC-based actuator time response for 0.2 Hz

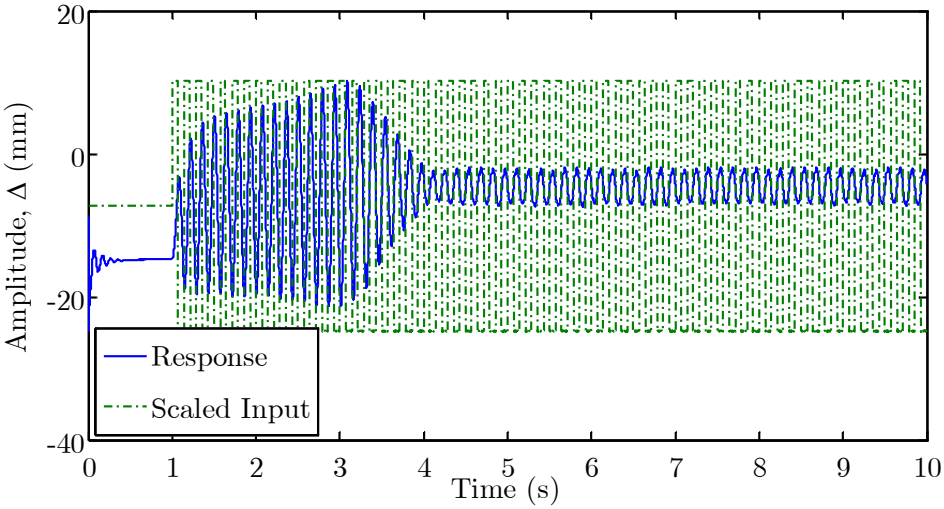

Figure 6.11 MFC-based actuator time response for 7 Hz

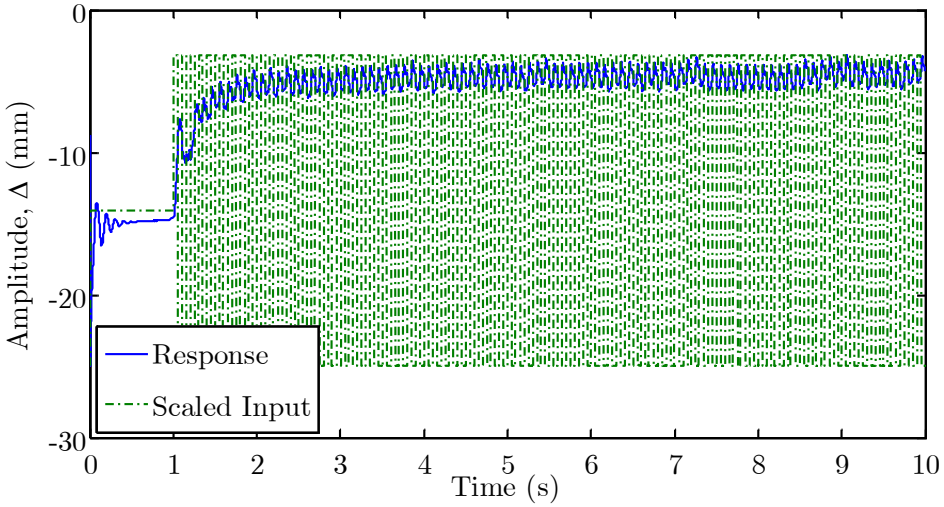

Figure 6.12 MFC-based actuator time response for 10 Hz.

By actuating both the SMA and MFC mechanisms, the performance of the Synergistic Smart Morphing Aileron (SSMA) was characterized. The device was tested in a similar way as its constituent actuators by varying the excitation frequency of the input from 0.05 Hz to 5 Hz, which was a compromise of their individually-tested frequency ranges. Figure 6.13 showed the combined response of the SSMA as compared to its constituent actuators so that a direct comparison could be made across the adaptive concepts.

For low frequency actuation (0.1 Hz) the SSMA system had a good response (high amplitude and low relative time constant). The amplitude of the SSMA device (solid line) was roughly an addition of the amplitude of each individual active component (dashed lines). As expected, when the range performance of the SMA constituent actuator decayed, the SSMA performance followed the same trend until it matched the MFC-based device (around 0.6 Hz). The matching of SWRF plots of the SSMA and MFC proved that only this latter component was effectively responding to the system inputs for frequencies higher than 0.6 Hz. Additionally, the SSMA relative time constant was not affected by the performance decrease of the SMA actuator (from 0.1 Hz to 1 Hz). This result indicated that the MFC-based mechanism was compensating for decrease in performance of the SMA-based actuator at these frequencies. Further discussion about the extension of the relative time constant to predict the response of an ideally-controlled system to other, more general input functions such as a sine wave, as seen in Appendix D.

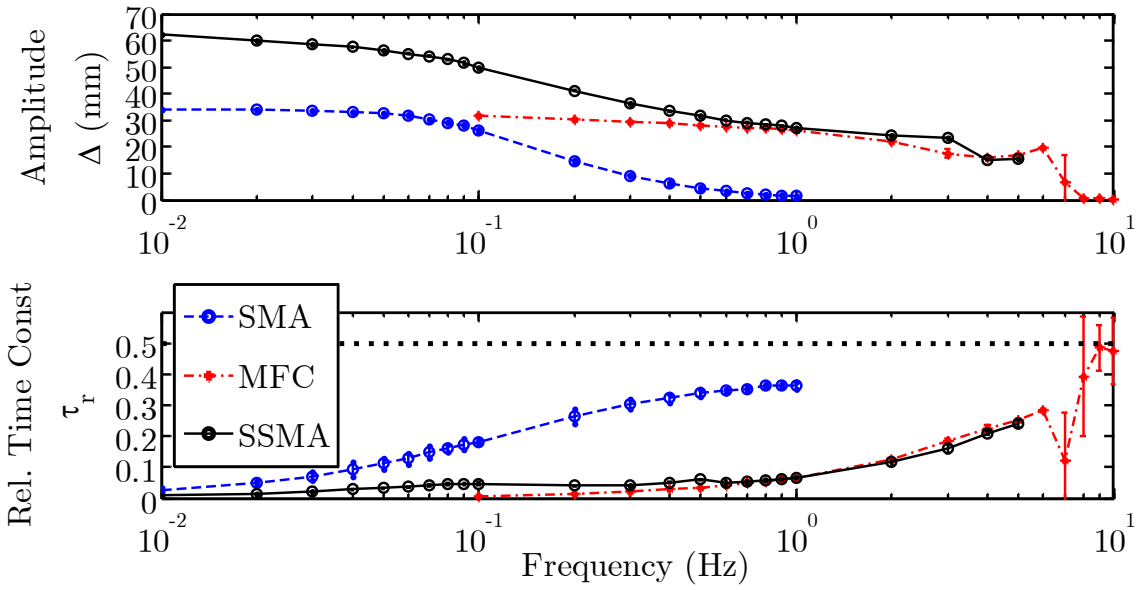

Figure 6.13 Experimental SWRF plots for all measured actuation mechanisms

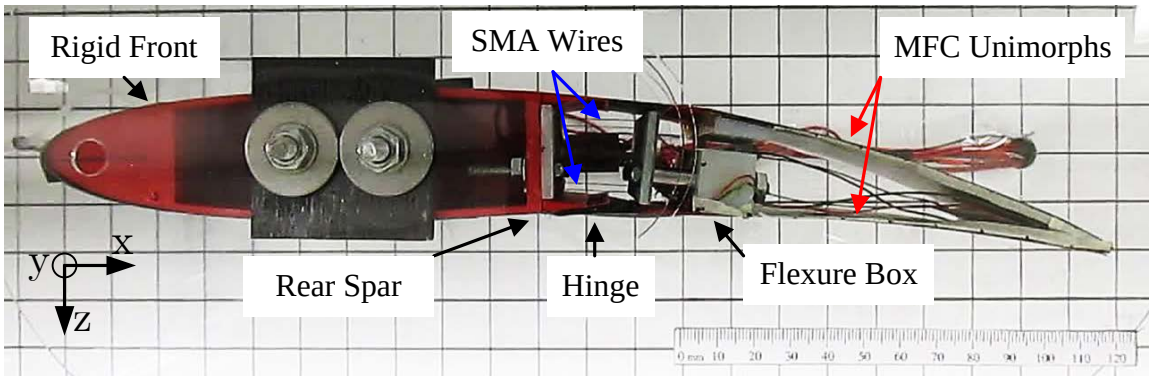

Figure 6.14 SSMA implemented in a representative airfoil

6.2.2. Spectral characterization with aerodynamic loads

With the mechanism and analysis methodology established it was desired to determine whether the characterization method could also capture the changes in performance of the concept under aerodynamic loading. Accordingly, a complete airfoil demonstrator was required, as was shown in Figure 6.14.

6.2.2.1. Experimental setup

The airfoil actuation characteristics were tested in the 1'x1' (304.8 mm x 304.8 mm) wind tunnel located at the University of Michigan. A diagram of the test section was shown in Figure 6.15. Video of the airfoil morphing was recorded using a camera mounted above the wind tunnel. Laser displacement sensors measured the actuation of the airfoil in the z-direction. The finite airfoil (AR=0.25) was bounded on the outside by two 2.5 mm thick acrylic end plates, cut into elliptical shapes, which approximated two dimensional flow over the airfoil without spanning the entire test section, in the reduced aspect ratio configuration described in Chapter 3.

The flow speed in the wind tunnel was measured with a static pitot tube with an uncertainty in flow speed of 0.1 m/s. The pitot tube was mounted upstream of the airfoil to measure the mean flow speed in front of the airfoil. Because the airfoil did not span the entire cross section, the pitot tube was mounted approximately 40 mm below the splitter plates so as to minimize the influence of the measurement on the flow on the actuation of the morphing airfoil. The airfoil displacements and flow speed data were recorded to a PC via Labview using a NI-DAQ 6211 directly connected to the laser displacement sensor using analog output wires.

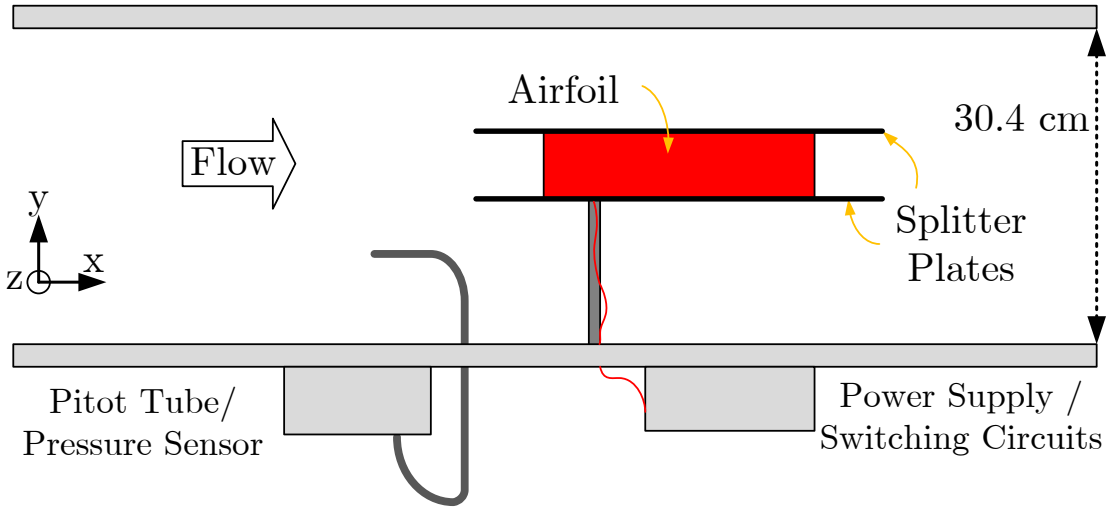

Figure 6.15 Experimental Setup of SSMA in Wind Tunnel

6.2.2.2. Results

Using the characterization setup and method from Section 6.2.1, the dynamic response of the SSMA airfoil and its actuators to square-wave inputs was tested over frequencies ranging from 0.01 to 10 Hz, and flow speeds from 0 to 15 m/s, seeking conditions relevant to small aircraft morphing applications with a Reynolds number ranging from 100,000 to 300,000. To simplify the aerodynamic conditions, a single representative angle of attack was chosen (0^o). This angle of attack was chosen to minimize flow separation on the airfoil during actuation and potentially inform performance for attached flow conditions. Figure 6.16 and Figure 6.17 showed the Square Wave Response Function (SWRF), characterizing the response of the individual actuators by amplitude and relative time constant. These plots helped to understand the role of the individual actuators in the combined concept and give a comparative plot to show improvement of the actuations over their individual limitations.

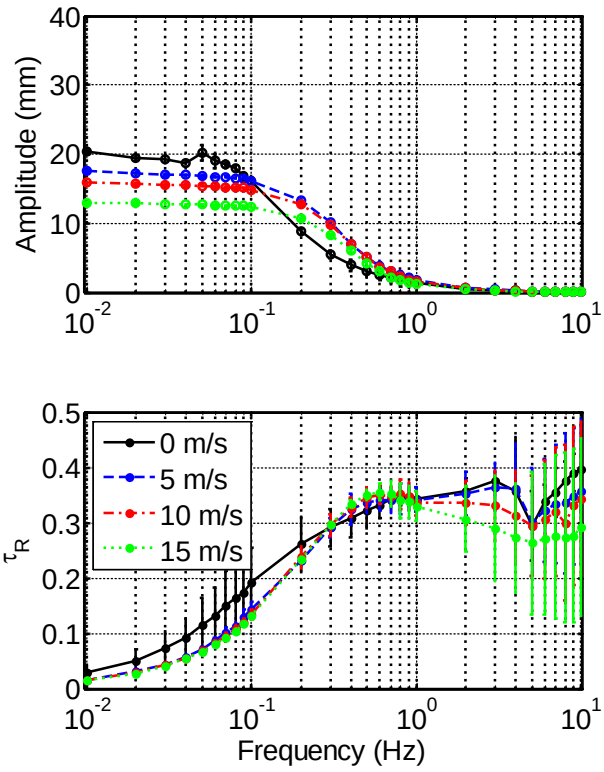

Figure 6.16 Square Wave Response Function for SMA-only actuation

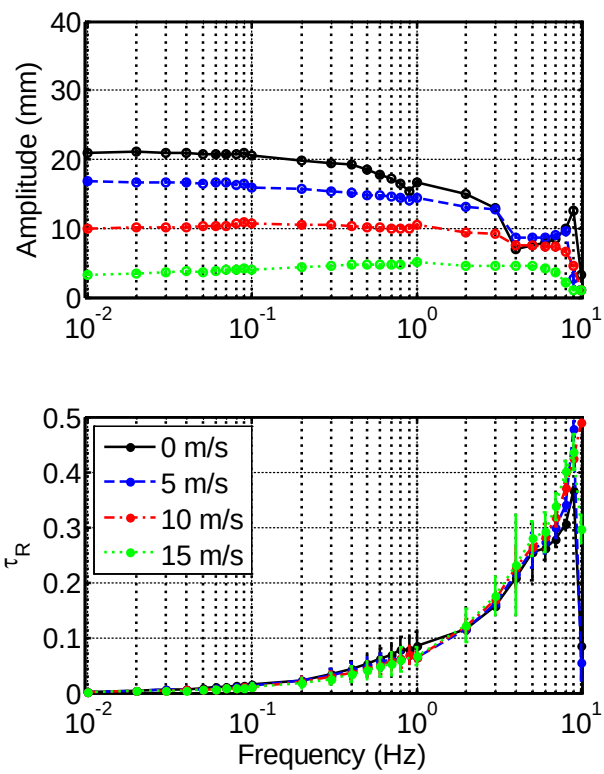

Figure 6.17 Square Wave Response Function for MFC-only actuation

Comparing unloaded cases (0 m/s) of each actuator for long timescales (0.01 Hz), the maximum tip displacement achieved by each actuator was approximately the same. This result exemplified the higher work density of the SMA wires, which are approximately 2 orders of magnitude lighter than the MFCs. As the excitation frequency was increased above 0.1 Hz, the peak-to-peak amplitude dropped dramatically for the SMA as the relative time constant increased, signifying the SMA saturating relative to the MFCs. Above approximately 1 Hz, the relative time constant had little meaning for the SMA wires as the amplitude approaches zero, resulting in larger error bars. By contrast, the MFC amplitude did not reach zero when the relative time constant metric showed larger error bars, showing that the system was beginning to deviate from a first-order response, as expected by the structural mode evidenced from the previous test. Thus it was determined that the large error bars in the relative time constant and erratic amplitude behavior above 5 Hz were due to dynamic effects at these frequencies exciting a structural mode in the Flexure Box system and thus reducing the validity of the quasi-static first-order assumption.

Examining the effect of aerodynamic loads on the SMA-only and MFC-only actuators, the amplitudes decreased with increased flow speed due to aeroelastic effects. This trend held except when comparing the no-flow and flow cases of the SMA wires between 0.1 and 1 Hz. The actuation amplitude of the SMA improved slightly and the relative time constant decreased as the flow speed was increased from 0 m/s to 5 m/s. This was most likely due to very small amounts of air entering the cavity with the SMA wires through gaps in the splitter plate. Such an effect would increase the cooling rate of the un-actuated SMA wire, thereby decreasing the antagonistic force on the actuating wire, improving actuation range and speed slightly in rate-limited higher frequency cases. Thus small amounts of active cooling were determined to potentially augment the actuation rate of the SMA wires, although modification of the active cooling of the wires was outside of the scope of the current work.

Comparing aeroelastic effects on the SMA-driven and MFC-driven mechanisms, the SMA wires showed less peak-to-peak range reduction as a result of aerodynamic loading (30% in the case of the SMA-only actuation as opposed to 80% in the case of MFC-only actuation). In part, this was due to the compliant nature of the MFC mechanism rather than the rigid hinge as detailed in Section 6.2.3. Additional range reduction was also due to the unpowered state of the SMA wires during the MFC-Only test.

Although pre-strained, the unpowered SMA wires were cool and allowed for some stretching, as seen in the time-domain response of a representative case in Figure 6.18. A second laser displacement sensor (SMA Laser in Figure 6.18) was added at 200 mm chord on the bottom, unflexing portion of the Flexure Box to isolate the effect of the hinge rotation on the overall system. This rotation was correlated with the tip laser for the no-flow case of the SMA, shown in Figure 6.16. The estimated effect of the stretching wires on the tip displacement in the MFC actuation case is shown in Figure 6.19. As aerodynamic loads increased, the effect of adverse rotation also increased. To effectively control the position of the SMA hinge at higher flow speeds, wire stretching and heating effects were determined to be important for effective control of the hybrid concept. However, even when compensating for this effect, the MFC experienced more aeroelastic deformation (measured as tip displacement reduction) than the SMA wires, as detailed in Figure 6.19.

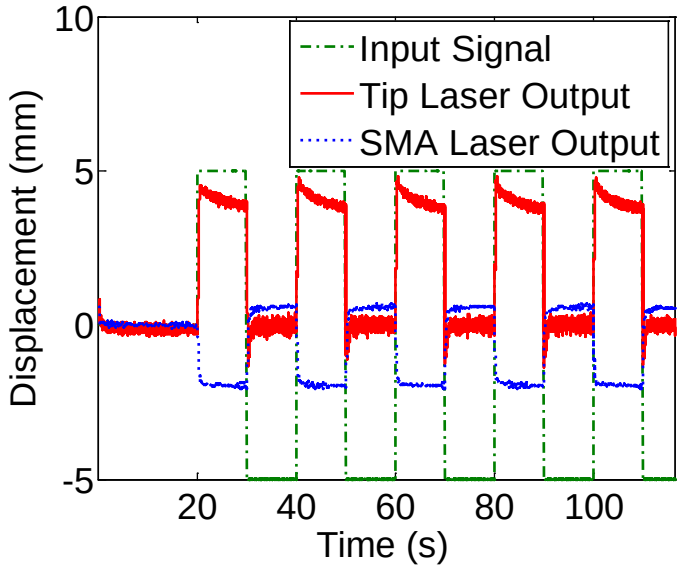

Figure 6.18 Unpowered SMA wire stretching for the MFC actuation case at 0.05 Hz, 15 m/s

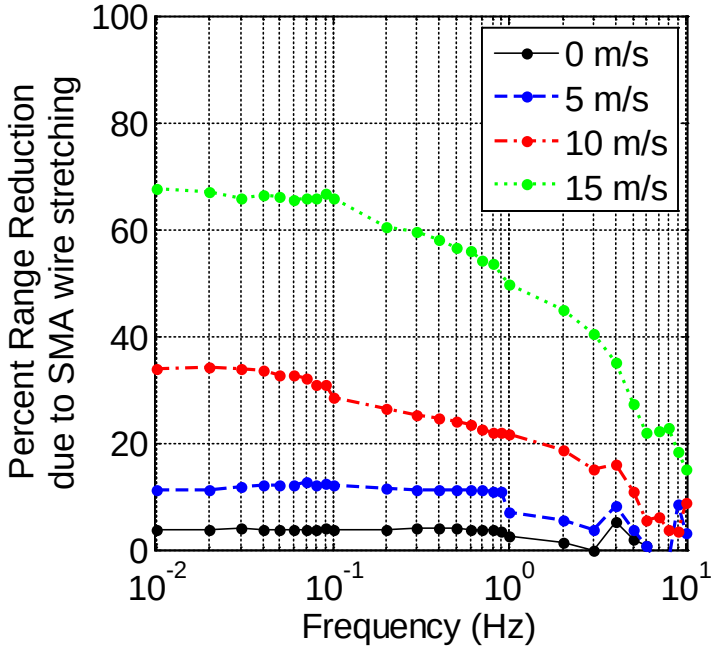

Figure 6.19 Estimated effect of unpowered SMA wire on MFC tip displacement

In the same manner as the individual actuators, the combined response of the SSMA actuation was characterized in a SWRF plot, as shown in Figure 6.20. A comparison of the combined SSMA concept with the individual actuators at each flow speed was also shown in Figure 6.21. For low frequencies, the combined system amplitude roughly tracked the additive effect of the two individual actuators. The difference in deflection amplitude was most likely

due to the increased aerodynamic loading moment at the SMA hinge and additional skin stretching. This result is expected as the series-like configuration of the morphing airfoil should add the displacement of the two actuators when actuated together. The combined system recovering the additive amplitude of its constituent actuators was a useful check to ensure that the combined system has not significantly restricted the capabilities of the individual actuators.

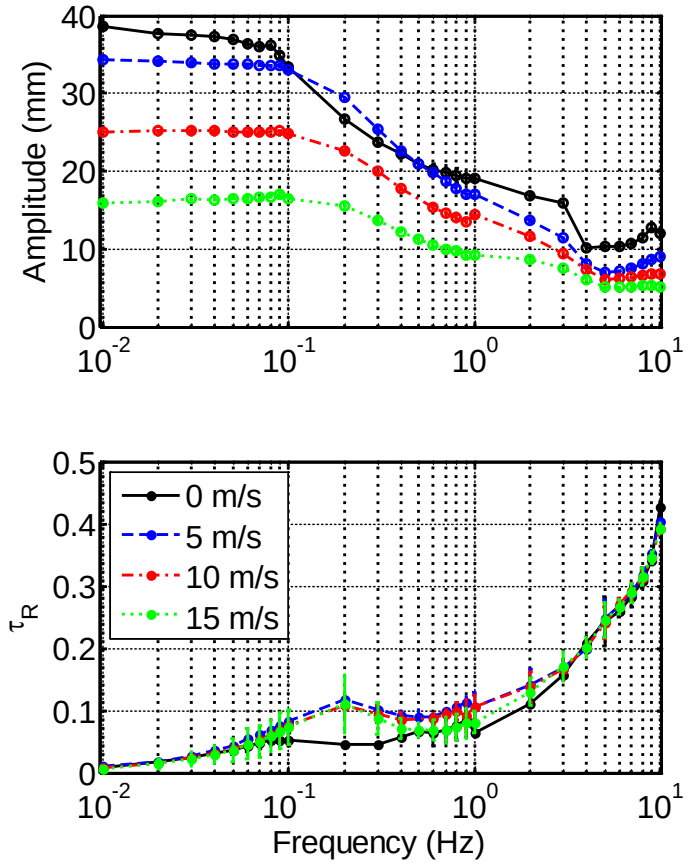

Figure 6.20 Combined SSMA Response

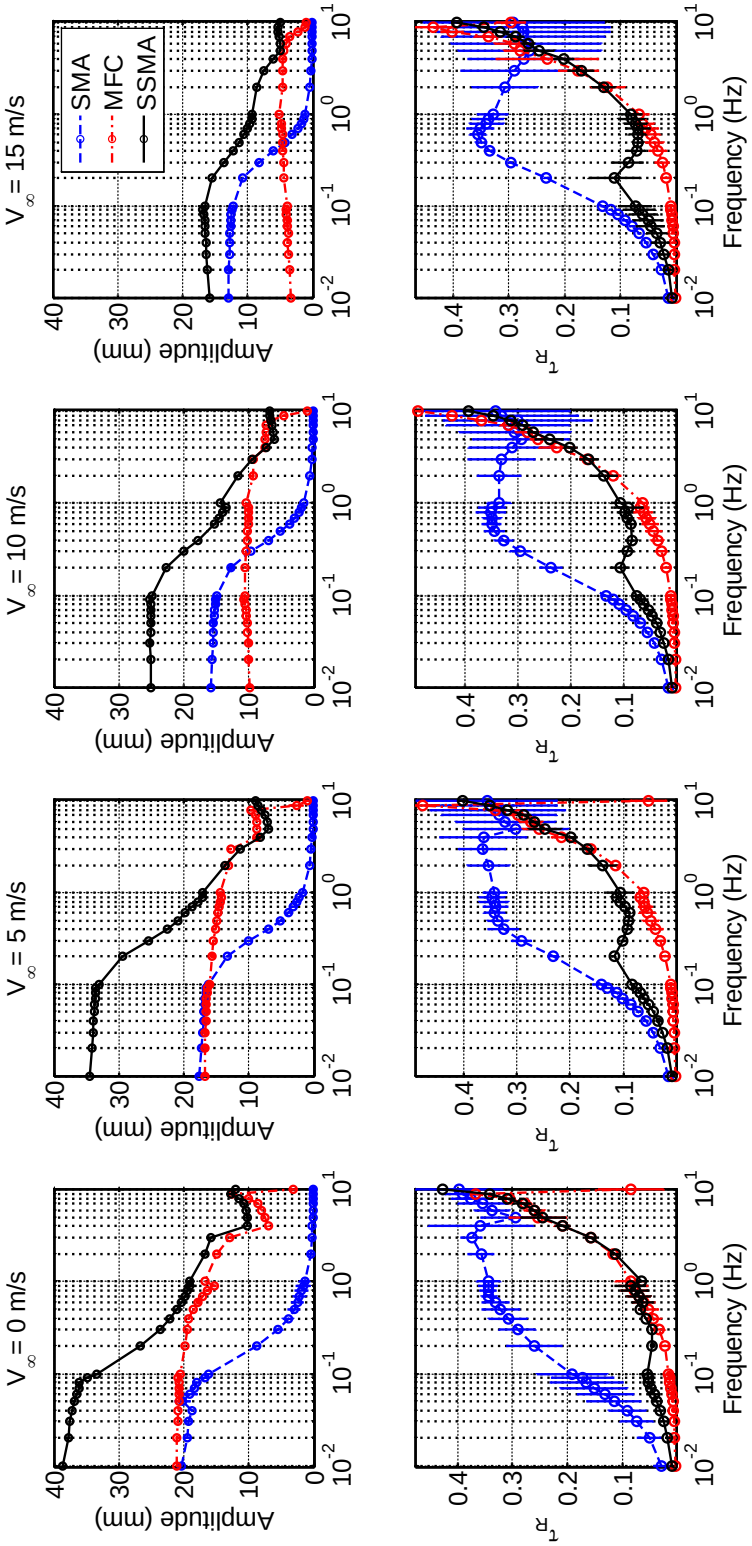

Figure 6.21 Square Wave Response Function for all configurations, changing with frequency

Interestingly, the combined system maintained the additive amplitude of the constituent actuators even for high aerodynamic loading (e.g. 15 m/s). Thus, the combined system leveraged the relative strength of the heated SMA wires to maintain increased hinge moment, especially when considering the larger hinge moment induced by higher aerodynamic loads from both concepts actuating. Thus, the SMA wires still allowed the combined concept to more effectively resist aeroelastic effects compared to the individual concepts. The combined system even realized the previously-mentioned rate benefit of slight cooling of the SMA wires due to airflow

Also, the combined SSMA system maintained the relative time constant of the faster MFC system at higher input frequencies. Examining a sample case in the time domain, Figure 6.22 show the physical significance behind this measurement. Early in the actuation cycle, the combined system actuated quickly due to the effect of the MFC actuator. For this particular configuration, the actuation amplitude of the MFC and SMA subsystems were nearly equal. Accordingly, the amplitude of the combined SSMA system reached the 63% measurement mark for the relative time constant in only slightly more time than the MFC actuator alone. Drawing from this case, the low relative time constant of the SSMA was explained by the hybrid concept tracking the MFC even as the SMA actuation. Thus at higher frequencies, the SMA concept contributed less to the overall actuation. The low time constant of the combined SSMA system then reflected its overall capability to maintain a fast time response across the frequency domain, relative to the input period.

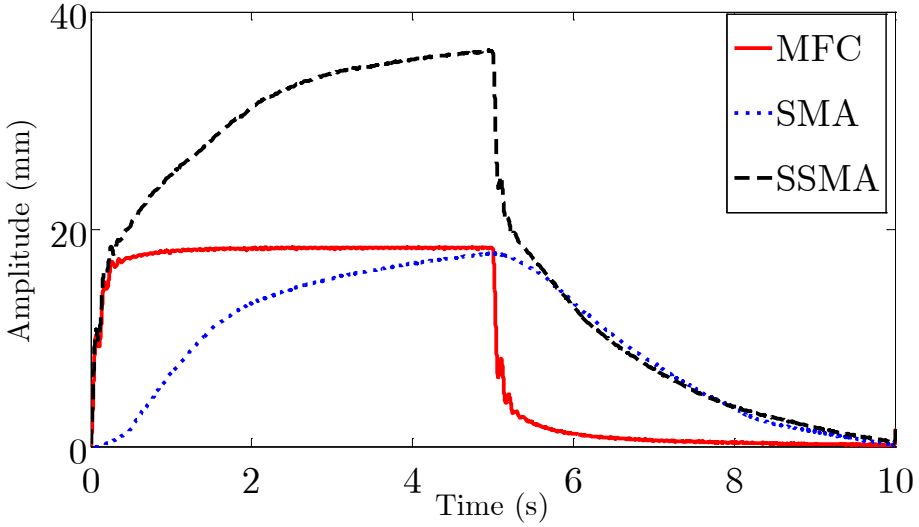

Figure 6.22 Data comparing time-response at 0.1 Hz, 5 m/s for all configurations

6.2.3. Summary of results from spectral characterization

As shown by the presented plots, both actuation systems deflected the tip with roughly the same amplitude. By effectively using the higher work density of the SMAs, a very small amount of SMA wire (0.1g) produced roughly the same tip deflection as 8 g of PZT embedded in two MFC composites with a total mass of 18.4g. Although the unpowered SMA wires slightly reduced the MFCs actuation ability for high loading scenarios, when actively heated, the SMA wires increased aeroelastic capabilities, despite larger loading moments due to relative moment arms of the aerodynamic force. The MFCs exhibited significantly faster response and contributed to the speed of the actuation across all tested frequencies of excitation. The resultant SSMA concept then used the benefits of both constituent actuators to build a concept that improved combined range and maintained actuation speed comparable to the faster actuation system (MFC).

6.3. Modeled static capabilities

The previous section characterized the mechanisms of the Synergistic Smart Morphing Aileron (SSMA) concept, which combined the fast, conformal actuation of Macro-Fiber Composites (MFC) with the high specific work and blocking stress of Shape Memory Alloys wires (SMA).

In this section, the aerodynamic benefits of an ideally-controlled, static SSMA concept are identified theoretical aerodynamic modelling which compares the performance of the combined system with its constituent actuators for the same representative airfoil that was analyzed in Section 6.1.

The optimized uncoupled performance of experimentally measured shapes in a 2D Navier-Stokes simulation is modeled to assess the improvement in ability to affect the flow over a range of flight conditions. A geometrically nonlinear finite element code is coupled with the aerodynamic simulations to further augment the analysis to include aeroelastic effects due to aerodynamic loading. Using this preliminary analysis, the SSMA demonstrates the ability to mitigate aeroelastic effects and flow separation near stall via reflex actuation. These results show a combined system with improved flow control beyond its constituent subsystems without the development of a positional controller.

6.3.1. Static, uncoupled aerodynamic optimization

The aerodynamic benefits of the SSMA concept were first investigated by modeling and optimizing the actuation's effect on the flow and comparing its performance with that of its constituent actuators.

6.3.1.1. Uncoupled morphing simulation method

To identify relevant aerodynamic shapes for modeling the Flexure Box, the achievable shapes were experimentally measured by cycling the box through its entire actuation range, free of aerodynamic loads. This was chosen to represent a bound as the best possible scenario where the structure would not be affected by aerodynamic loads. The maximum and minimum potential differences applied to the MFCs by the high voltage amplifier were +1.5 kV and -0.5kV, respectively. The amplifier was built to scale the voltage ratio 3:1 so that the negative voltage applied to actuate the unimorph in compression is proportional to the positive voltage applied to actuate the other unimorph in tension. Marker points were tracked over 41 steps (21 increasing, decreasing) in the actuation cycle using digital image correlation software. A representative image from one of the steps is shown in Figure 6.23.

The morphing trailing edge was then combined with a NACA 0012 leading edge profile to create a range of morphing airfoils. The y-coordinates for each of the airfoils were then plotted against airfoil arc length and smoothed to eliminate position measurement errors. An example of smoothed data and the resultant airfoil shape is shown in Figure 6.24.

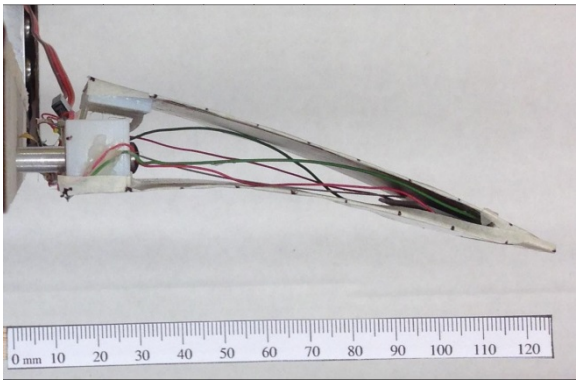

Figure 6.23 Representative Actuation

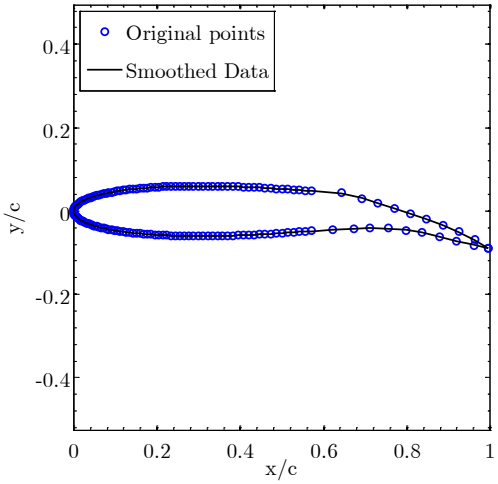

Figure 6.24 Resultant airfoil Shape

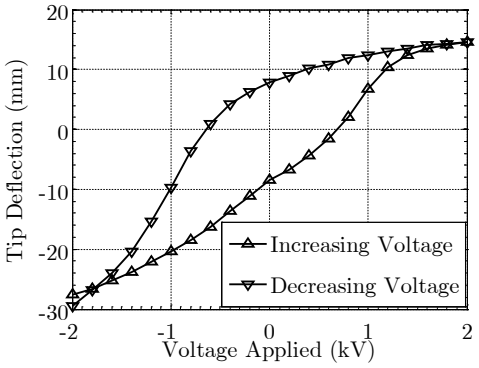

Figure 6.25 Hysteresis of tip deflection

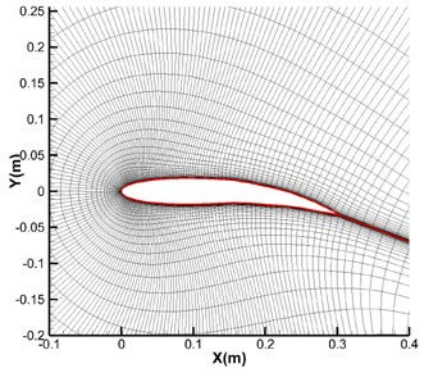

Figure 6.26 Close-up of fluid mesh

The MFCs were voltage controlled and for large actuation amounts experienced hysteresis as seen in Figure 6.25, tracking the y-coordinate of the tip displacement with respect to input voltage. To evaluate the effect of the variation of these shapes on relevant aerodynamic quantities, the aerodynamics were simulated for these shapes using the Unsteady Reynolds Averaged Navier-Stokes (URANS) equations.

The OVERTURNS code, which operates on structured overset meshes, was employed for this purpose. Figure 6.26 showed a sample mesh system for a representative actuation of the MFC [89,125]. The numerical method used a third order accurate upwind scheme to compute the inviscid fluxes, while the viscous terms are discretized using second order accurate central differencing. Low Mach number pre-conditioning [126] was used to accelerate convergence within the context of implicit time integration, as implemented for representative dynamic simulations in Section 6.4.1. For turbulence closure, the Spalart-Allmaras [127] turbulence model was employed. This formulation has been validated extensively over a wide range of flow conditions and geometries [128] including in the transitional and turbulent range of Reynolds numbers [129].

The aerodynamic performance of all 41 experimentally measured shapes were evaluated at 3 different relevant flow speeds (10, 20, 30 m/s) with 3 different angles of attack (-15 ^{o}, 0 ^{o}, 15^{o}). The mean relative error accumulated by ignoring the effects of actuation hysteresis on lift, drag, and lift to drag ratio is linearly interpolated and plotted in Figure 6.27.

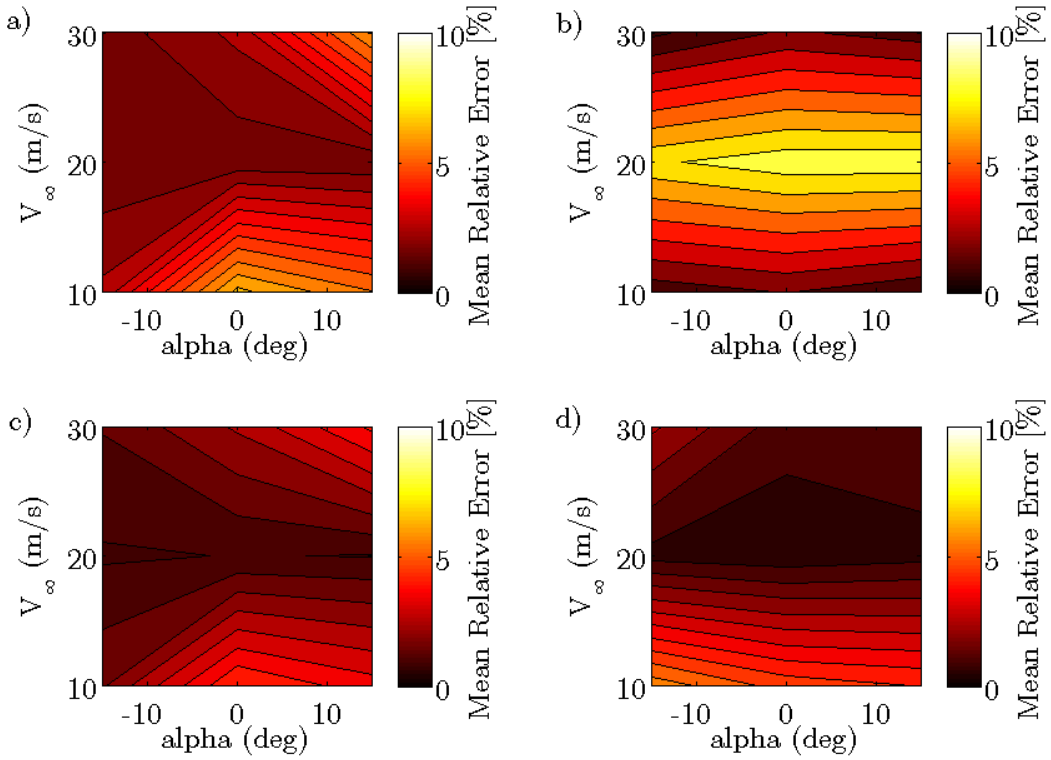

Figure 6.27 Relative error in experimental data due for a) C_L b) C_D c) C_M d) Lift/Drag

Using this data, it was assumed that the tip deflection alone would be an adequate indicator of actuation state of the Flexure Box concept and that the error incurred by this assumption would be small enough to be disregarded for initial performance estimates.

6.3.1.2. Parametric description of the SSMA airfoil

The actuation of the Flexure Box concept, through previous assumptions, is thus described exclusively by the tip deflection, simplifying the actuation space. Accordingly, only half of the flexure box experimental data shapes were necessary to describe all possible morphing shapes. A normalized actuation, MFC_δ, was created which re-scaled the tip deflection to the range [-1,1], which mapped to full actuation tip down and full actuation tip up, respectively for more intuitive understanding.

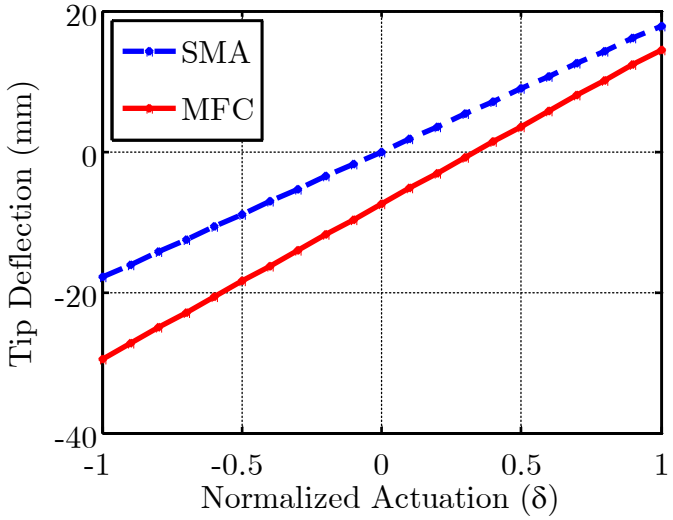

Figure 6.28 Mapping between tip deflection and normalized actuation for constituent actuators

The tip deflection induced by the SMA-driven hinge (measured previously experimentally [121]) was mapped to a normalized actuation, SMA_δ, in a similar manner. Although the SMA wires require pre-stress when built, it was assumed that the range for the SMA-driven hinge was centered on 0 degrees. The mapping of normalized actuation for MFC_δ and SMA_δ is then as follows in Figure 6.28. Again, for brevity, the actuation mechanisms were denoted by their smart material driving mechanism.

Note that the relationships between the tip deflection that were depicted in Figure 6.28 were true for the SSMA concept only for the case where the other actuation mechanism was unactuated. The two different actuation mechanisms were combined so that the SMA and MFC could actuate together or in opposite directions to create an effective reflex camber. The actuators had no effect on the airfoil geometry when the tip deflection for both individual concepts were zero, which was found in the previous plot as $[MFC_\delta, SMA_\delta] = [0.3267,0]$. The MFC had a non-zero center for its normalized actuation due to the linear mapping and the asymmetry of the MFC's achievable range. The range of possible shapes over the total space of the SSMA airfoil was then shown by viewing the bounds of the actuation domain, seen in Figure 6.29.

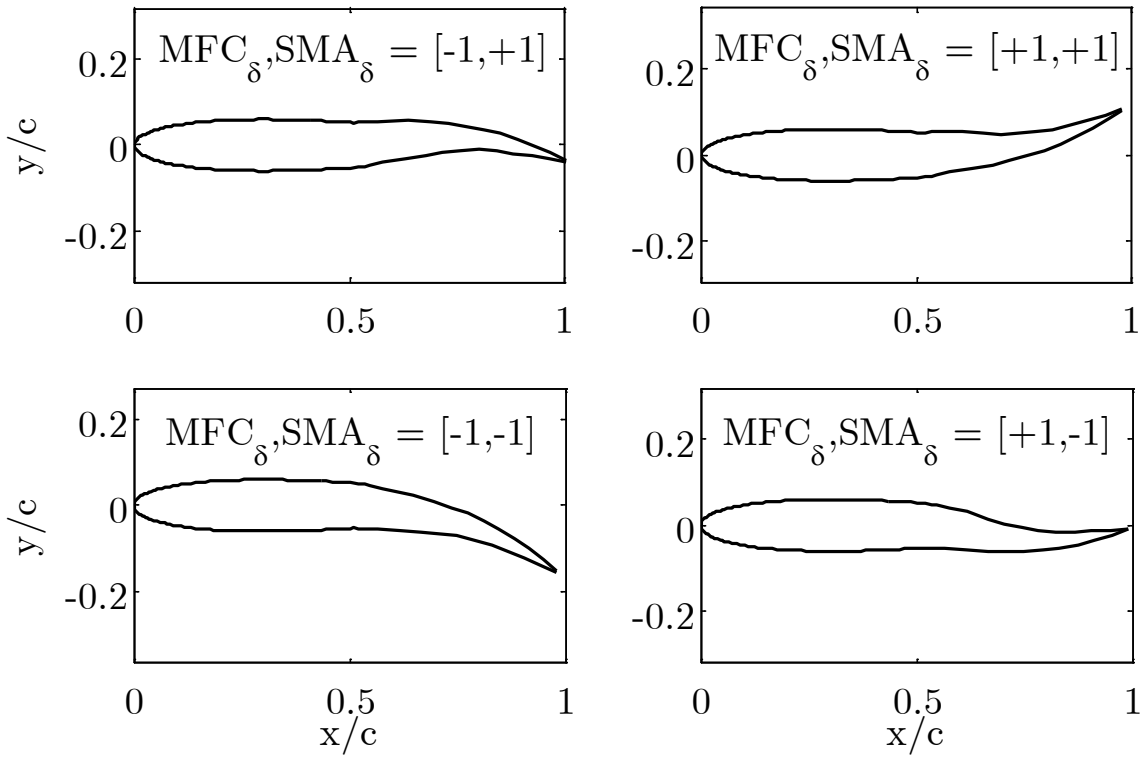

Figure 6.29 Bounds of SSMA actuation domain

6.3.1.3. Effect of SSMA actuation on aerodynamic parameters

The parametric SSMA description was used to create a sampling of 441 different airfoil shapes, spaced evenly as a grid in the normalized actuation domain, as given by [MFC_δ, SMA_δ]. A representative flow speed (V_∞=20 m/s) and angle of attack (α=15^o) were chosen to illustrate the complex effect of the actuation domain on aerodynamic forces especially near stall. The results from the steady Navier-Stokes simulations are summarized in Figure 6.30.

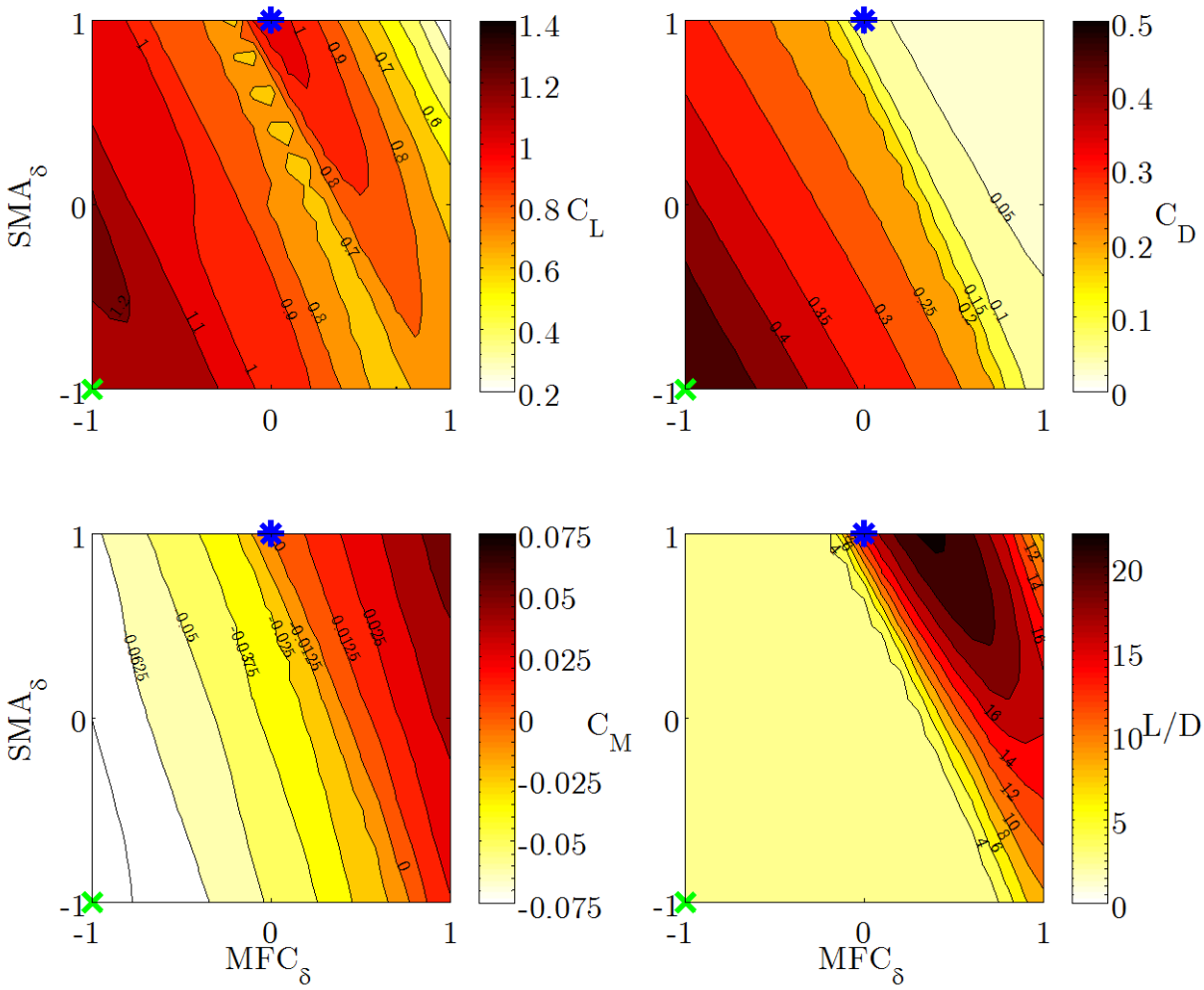

Figure 6.30 Aerodynamic forces over actuation range
for V_∞= 20 m/s, α=15°

As noted in Figure 6.30, near stall, the lift coefficient was shown to have a constrained, local maximum at [MFC_δ, SMA_δ]=[0,1], noted as a blue "*" and an global maximum at [MFC_δ, SMA_δ]=[-1,-1], noted as a green "x" . The constrained maximum at [MFC_δ, SMA_δ]=[0,1] represented a case of reflex actuation, as noted in the previous mapping description where the unactuated configuration was [MFC_δ, SMA_δ] = [0.33,0]. Actuating further downward from the constrained, local maximum caused flow separation seen by a sharp line in all four contours. The flow separation increased lift after an initial decrease, dramatically increasing the drag coefficient, increasing the pitching moment, and decreasing the lift to drag ratio. Interestingly, the constrained local maximum showed a much higher L/D and a near zero pitching moment for almost the same lift.

To visualize this flow separation, the pressure field and streamlines for the global maximum lift condition is shown in Figure 6.31. As a result, it was determined to be important to take into account the effects caused by flow separation when determining the optimal capabilities of the actuators to control aerodynamic forces.

6.3.1.4. Uncoupled aerodynamic optimization results

A range of flight conditions (angles of attack) were then tested to compare the static aerodynamic performance of the SSMA concept to that of its constituent elements. A simple optimizer was used to improve the speed at which the optimal performance was found for each flight condition. A gradient-free Nelder-Mead Simplex optimizer [130] was employed with a merit function that prohibitively penalized actuation points outside of the domain. A gradient free method was chosen due to the discontinuities in aerodynamic parameters seen previously, the black-box nature of the compiled aerodynamic code, and the limited number of design variables. The aerodynamic performance was optimized to find the maximum and minimum lift coefficient over a range of angles of attack (-15^{o} to 15^{o}) and a single representative flow speed (20 m/s). The lift coefficient was chosen as a metric of the actuators to provide continuity with results from previous chapters for flow control. A summary of the optimizations is described in Table 6.1.

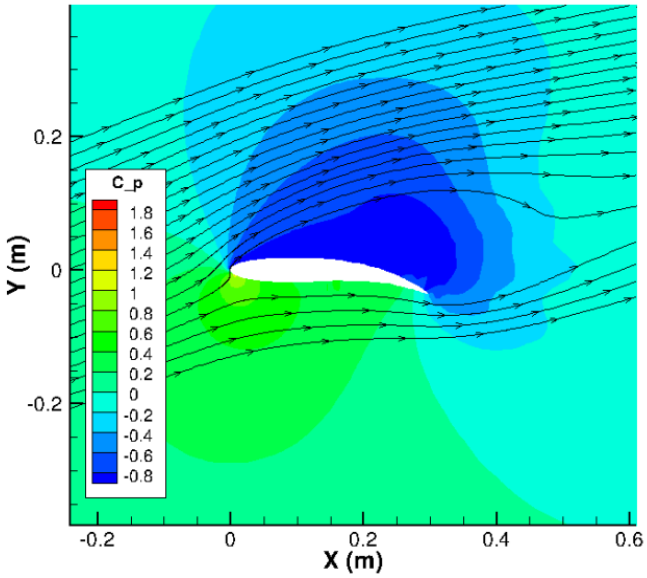

Figure 6.31 Field of pressure coefficient for [MFC_{δ}, SMA_{δ}] = [-1,-1].

Table 6.1 Constrained optimized of actuation

Minimize:	$f(MFC_\delta, SMA_\delta) = C_l$
Subject to:	$-1 \leq MFC_\delta \leq 1$ $-1 \leq SMA_\delta \leq 1$
Given:	Current flight condition: α, V_∞ Airfoil parameter: *c*

Three different cases were chosen to simulate the combined system and its actuators: the SMA-only case, the MFC-only case, and the combined SSMA system, as seen in Figure 6.32. In the case of the MFC-only and SMA-only actuation, a single parameter golden-section optimizer was used with the actuation bounds as the initial search interval and the other actuator remained unactuated with no influence over tip position.

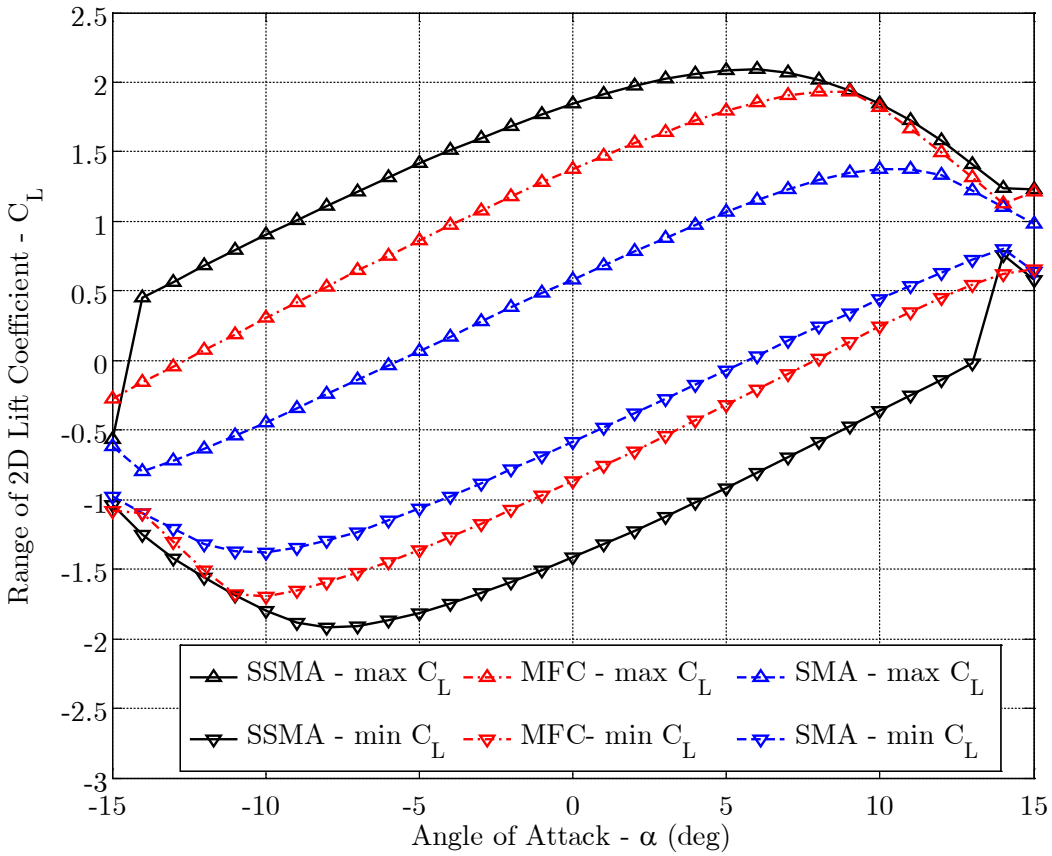

Figure 6.32 Range of achievable lift coefficients for SSMA and constituent subsystems

The difference between the upper and lower bounds for each concept was measured from Figure 6.32 and compiled in Figure 6.33 again measuring the lift effectiveness of the three concepts. The SMA concept yielded the smallest change in lift coefficient for a given angle of attack, which was symmetric about the vertical axis at α=0 degrees, due to the symmetric constraint on deflection angle and the symmetric NACA 0012 airfoil. The conformal morphing of the MFC yielded a larger range than the SMA, albeit asymmetric due to the asymmetry of the flexure box actuation domain. Although the achievable value of change in lift was slightly higher than that shown in Chapter 3, the results were considered reasonable for an initial (uncoupled) estimate of the actuation capability. Finally, the SSMA concept showed a much larger range, nearly equivalent to the addition of the two actuators. The improvement in maximum achievable range of lift coefficient over all flight conditions is show in Table 6.2.

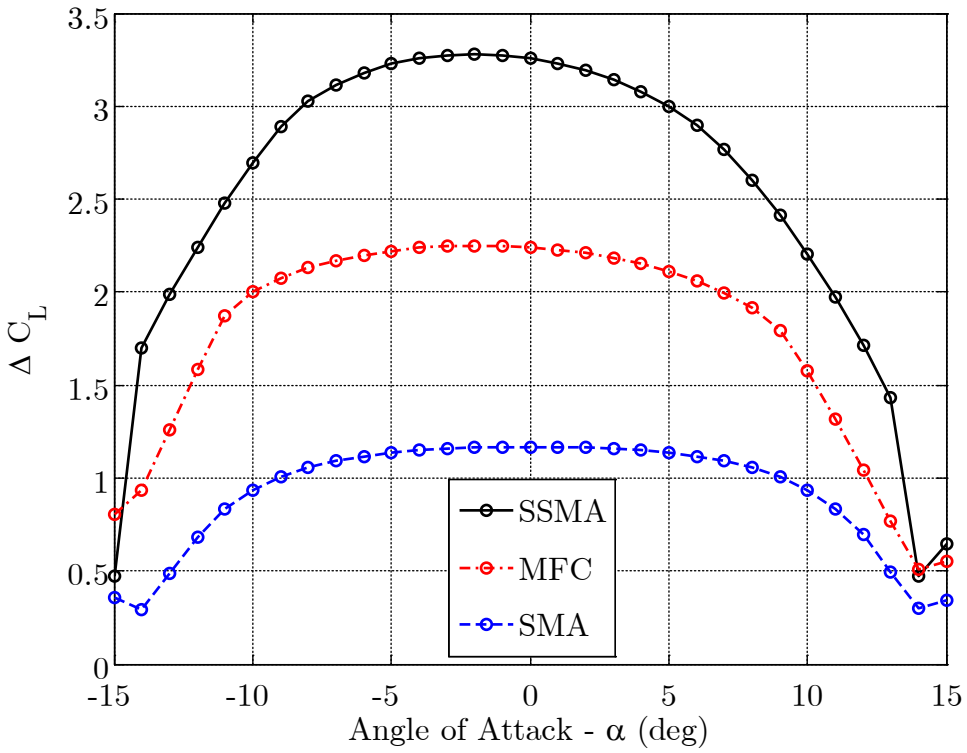

Figure 6.33 Achievable change in lift coefficients for SSMA and constituent subsystems

Table 6.2 Summary of Uncoupled Optimized Results

	Maximum C_L	Percent Improved by SSMA	Minimum C_L	Percent Improved by SSMA	Maximum ΔC_L	Percent Improved by SSMA
SMA	1.378	51.7%	-1.378	39.5%	1.168	180 %
MFC	1.932	8.2 %	-1.696	13.4 %	2.250	45.6 %
SSMA	2.093	-	-1.922	-	3.276	-

The SSMA concept represented a roughly a 50% improvement in maximum or minimum lift coefficient over the SMA-only concept and roughly a 10% improvement over the MFC-only concept. However, these values only represented the absolute maximum and minimum, near stall. The results showed that the SSMA concept roughly added the abilities of the two actuation concepts to change the total lift coefficient, especially at off-maximum performance conditions with some losses (~10%) due to flow separation. The overall ability of the SSMA to affect the flow was improved 180% over the SMA constituent actuator and 50% over the MFC constituent actuator.

6.3.2. Static, coupled aeroelastic simulations

The uncoupled simulations showed that the MFC could affect flow nearly 100% more effectively than the SMA. However, previous experimental results noted that the compliance of the Flexure Box concept and MFC unimorphs experienced significant aeroelastic effects. Namely, the compliant Flexure Box experienced reduction in tip deflection range up to 50% for flow speeds as low as 20 m / s [82].

To incorporate these deformations into the simulations, a structural finite element code was chosen to couple with the aerodynamic simulations. Modeling the aeroelastic effects on the structure was chosen primarily because it enabled the capability to dissect the complex structural and aerodynamic problem without affecting the test itself. Additionally, modeling eliminated the need for closed-loop control, necessary in implementing precise position control for real hysteretic actuators. The goal of the aeroelastic simulations was to capture the same aeroelastic trends noted previously for the Flexure Box concept and then to identify any potential, non-intuitive gains for the combined system, motivating development of a synergistic controller.

6.3.2.1. Implementation of corotational finite element code

As part of the well-known Euler-Lagrangian coupling problem between Computational Fluid Dynamics (CFD) and Finite Element Mechanics (FEM) simulations, the structure was described as in the original configuration, but the aerodynamics loads acted on the structure in the deformed configuration. Because of the relatively large actuator deformations and the relatively high fidelity of the Navier-Stokes simulations it was determined that the structure could not simply be represented as a static shape where the loaded and unloaded configurations were the same. Thus a non-linear structural code was needed to accurately model the aeroelastic effects.

A simple co-rotational finite element code was developed and implemented to provide initial estimates of the expected aerodynamic response of the SSMA under aerodynamic loading at various flight conditions. The co-rotational framework was advantageous in that it separated the geometric nonlinearities associated with large displacements and rotations from the material model, still allowing for the simplified material model of infinitesimal strain [131]. Previous work has shown that such a method can be quickly used to describe both static and dynamic aeroelastic effects on both rigid and flexible airfoils [132]. Using the corotational finite elements described by Crisfield[133] and Battini[131], a two-dimensional cross-section of the SSMA airfoil was constructed using Euler-Bernoulli beam elements. The resultant model is shown in Figure 6.34.

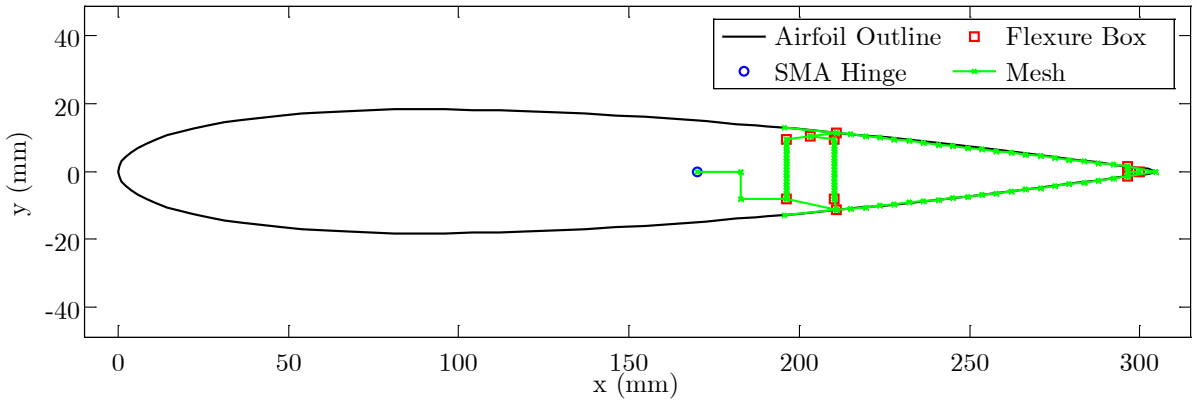

Figure 6.34 Overview of modeled SSMA via finite elements

For simplicity, the skin spanning the gap between the Flexure Box and the rigid leading edge of the airfoil was modeled as a wiper which maintained a C0 continuous surface without bending or adding stiffness to the structure, approximating an ideal skin. This was chosen as an optimal bound for a morphing skin that could maintain the airfoil shape without additional out-of-plane deformations due to aerodynamic loads and without additionally restricting actuation. The optimization of the skin covering this gap was considered outside of the realm of the current study; however it represents a continued challenge in morphing airfoil concepts, as seen in the previous chapters.

The SMA-driven hinge was modeled simply as a prescribed rotation about the discrete hinge because of the relatively high blocking stress of the SMA wires compared to the Flexure Box. The Flexure Box was modeled in three parts. The unimorphs were modeled using a bending stiffness derived by the rule of mixtures, which was experimentally validated. The thick plastic pieces of the Flexure Box were modeled as rigid beams. The actual flexure mechanism, which was modeled as the full-flexure mechanism from Chapter 2, was approximately modeled with a linearly elastic material with an effective modulus determined by fitting experimental data for an applied tip load, shown in Figure 6.35. For this model, each elastomeric section in the flexure box and each unimorph were discretized into 20 evenly-spaced beam elements, resulting in 94 elements in the total model, including rigid components.

To verify the validity of the code to capture non-elastomeric structures, the hinged-box mechanism developed by Bilgen [65] was modeled and experimentally validated in a similar manner. The rigid hinges were modeled by decreasing the stiffness of the top-most and bottom-most elements of the flexure mechanism from Figure 6.34 to near zero and increasing the stiffness in the other beams in the flexure mechanism to that equivalent of the rigid plastic elements.

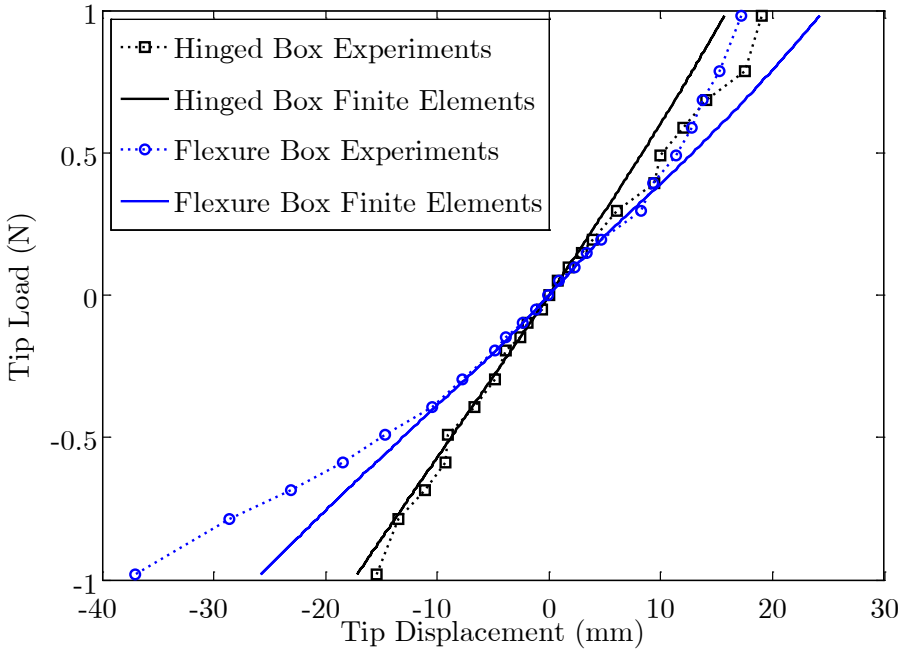

Figure 6.35 Experimental stiffness fitting of the Flexure Box and comparative hinged box

As seen by the difference in smoothness between the flexure box and hinged box experimental data in Figure 6.35, the solid-state nature of the Flexure Box eliminated the frictional position errors observed in the discrete hinges. Additionally, the finite element results correlated well to the hinged box data. The modeled Flexure Box structure was generally slightly stiffer than the experimental results due to the elastomeric nature of its constituent materials. However, it was assumed that the current model would adequately represent the structure when establishing trends about the effects of aerodynamic loading.

Using this model, the normalized actuation amounts [MFC_δ, SMA_δ], were chosen so that the static, unloaded tip deflection range for the two actuators were equivalent to the values previously experimentally measured. For the coupled simulations, MFC_δ prescribed an applied moment over the length of the unimorph element, which was equivalent to the piezoelectric element bending, rather than experimentally measured shape. This simplified modeling of the stiffness of the Flexure Box allowed for the simulation of the aeroelastic effects on it.

6.3.2.2. Coupling the structure and aerodynamics

The corotational finite element code was coupled with the OVERTURNS flow solver by linearly interpolating the pressures on the surface to their respective beam element for a series of iterative steps in pseudo-time. These pressures then followed their respective beam elements throughout the structural convergence step. The geometry for each converged structure was regenerated into a new grid for the CFD solution before each coupling, resulting in a loosely coupled convergence scheme. A flow chart diagraming the overall solution technique is shown in Figure 6.36. The various disciplines were grouped in the following manner: structures in red, aerodynamics in blue, and coupling in green. The method also added the ability of the structural code to adapt the change in forces between aerodynamic load steps to prevent large changes in loading between geometric structural updates achieving a singular tangent stiffness matrix. This adaptive load step was important in ensuring convergence of the structural solution in early aerodynamic load steps at higher flow speeds where large changes in iterative flow between pressure updates initially caused the structural solution to diverge.

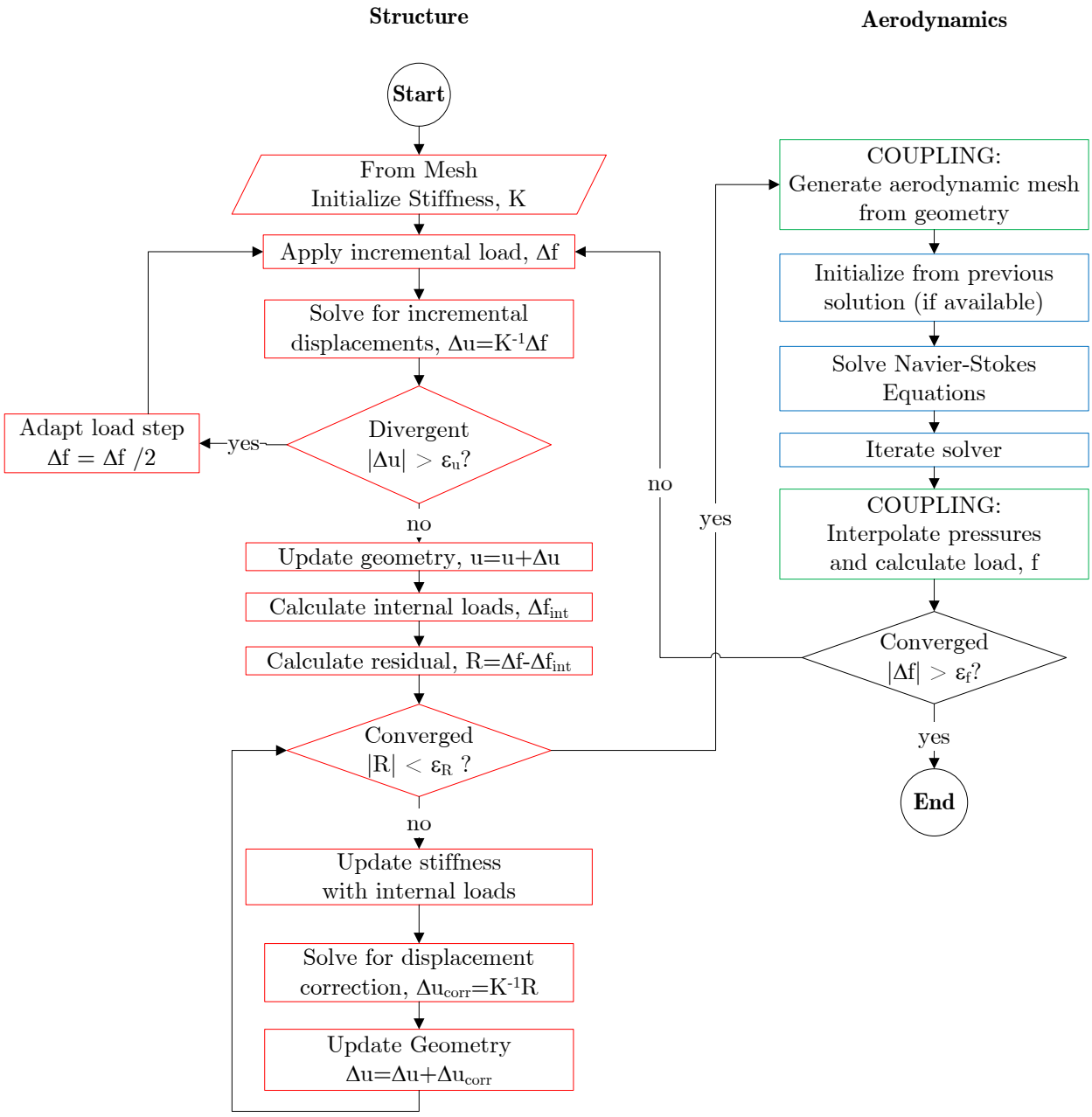

Figure 6.36 Flowchart of structural / aerodynamic solution coupling

6.3.2.3. Coupled aeroelastic results with optimized actuations

Previously, in Section 6.3.1, the uncoupled results assumed that flow speed could only affect the control force results by changing the Reynolds Number due to the assumed, rigid shapes. By coupling the aerodynamic and structural solution, the aerodynamic loads also influenced the achievable configurations at each flow speed. The coupled finite element code detailed in previous sections was used to generate aerodynamic force coefficients over a range of flow speeds (10 m/s to 30 m/s) and angles of attack (-15^o to 15^o). Using the same objective function and constraints as summarized in Table 6.1, the effect of flow speeds on the SMA, MFC and SSMA morphing concepts were evaluated. The Flexure Box structure for the SMA-only case was modeled as rigid to appropriately simulate a rigid trailing edge.

Figure 6.37 summarizes the effects of the optimal actuations on the respective control forces. The sampled points were shown as blue dots and the contours were generated through cubic spline interpolation. Each row represented a different optimization, denoted by the labeled color bar at the right end of the row, and each column represented a different morphing scheme, denoted by the label at the top of the column. This plotting method allowed for direct comparison between the SSMA and its constituent actuators. In each optimization, the ability of each actuator to influence the flow was emphasized by coloring the desirable quantity as dark and the less desirable points with lighter colors. Each row maintained the same color scheme for comparison of optimized quantities and each column represented a single actuator configuration.

Examining the left column, the SMA showed the effect of the discrete hinge with a rigid actuation mechanism on the flow. The maximum and minimum lift coefficient for the flow varied slightly due to Reynold's number effects. Thus the SMA became slightly more effective at higher flow speeds, especially near stall conditions and as seen before, the change in lift coefficient was symmetric about zero angle of attack.

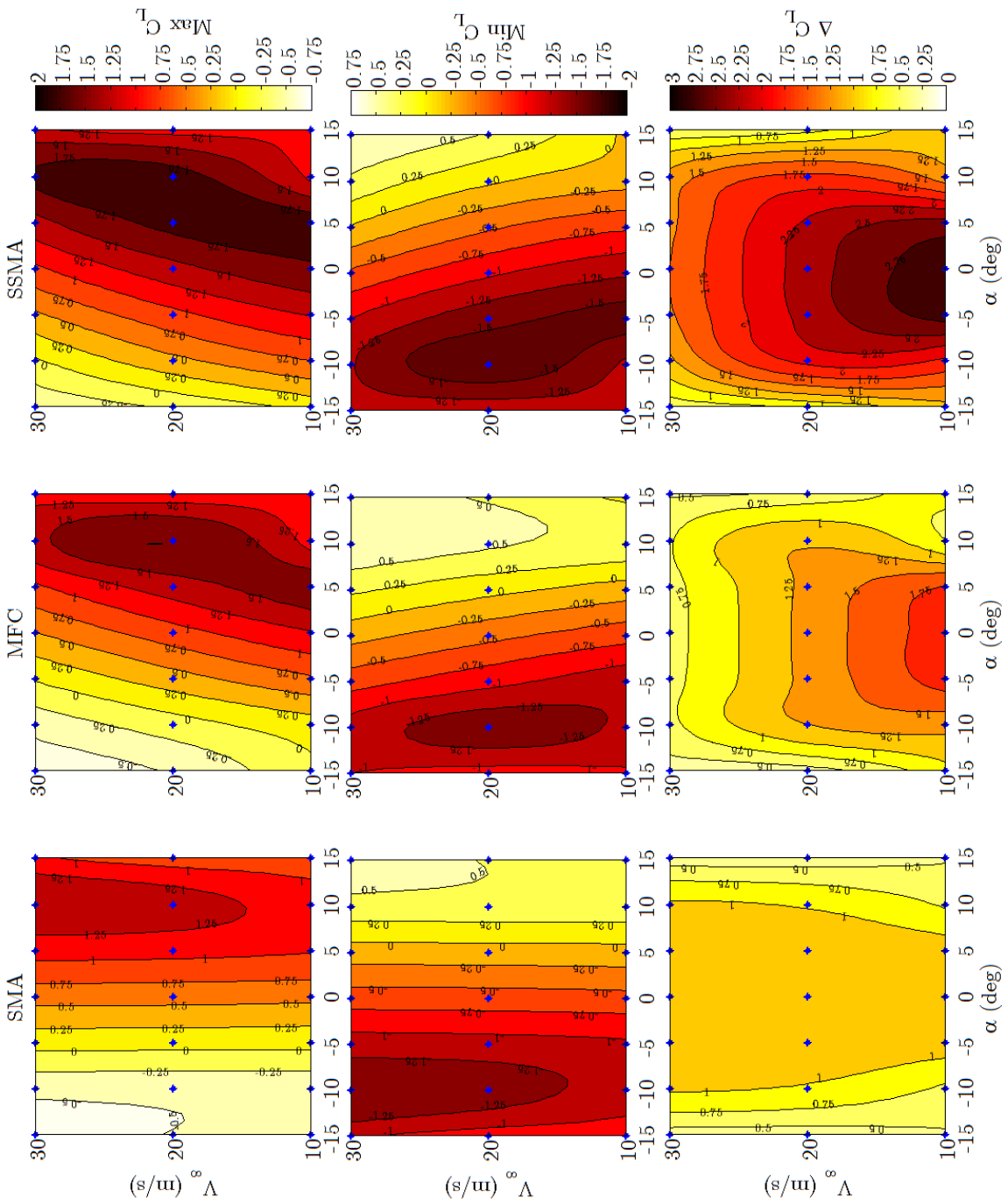

Figure 6.37 Aeroelastic performance of all actuators for max, min, and change in lift coefficient

In the middle column, the MFC showed a slightly more varied effect due to variation in flow speeds, between 10 m/s and 20 m/s the MFC-only actuator increased in effectiveness, achieving larger maximum and minimum lift coefficients, similar to the SMA. However, the ability of the actuator to affect the flow via ΔC_L decreased as flow speed increased due to aeroelastic effects. Until approximately 25 m/s the MFC still exhibited superior actuation over the SMA, due to the curvature of the MFC still affecting the flow despite reduced tip deflection.

In the right column, the SSMA exhibited superior ability over the SMA and MFC at all tested flight conditions. Although the range was slightly asymmetric due to the MFC actuation effects, the two actuators worked together to maximize the effect on the flow at all flight conditions, restoring most of the symmetry in ΔC_L. Additionally, the SSMA experienced only 20% reduction in lift coefficient between 10 m/s to 20 m/s, which was less than expected by experimental results. However, the aeroelastic simulations still reflected that the aerodynamic flow could effectively be influenced by the MFC despite aerodynamic reduction of the tip deflection. This result was confirmed with the experimental results from the scaled testing of the Flexure Box Aileron in Chapter 3.

6.3.2.4. Static reflex camber effect

In addition to analyzing the ability of the concepts to influence the aerodynamic control forces it was desired to identify if the combined actuation concept showed any unexpected gain from the two actuators working together, i.e. synergy. Examining the resultant optimal configurations from Figure 6.37 for the SSMA, the optimization almost always found that the optimal actuation configuration for achieving maximum lift was the intuitive choice, saturated actuation of both the SMA and MFC actuators completely down, i.e. $[MFC_\delta, SMA_\delta] = [-1,-1]$. However, for high angles of attack, the optimizer converged upon a different, unexpected configuration. A sample of the modeled conditions where this non-uniform configuration occurred was marked in Figure 6.38, as indicated by Points #1 through #4.

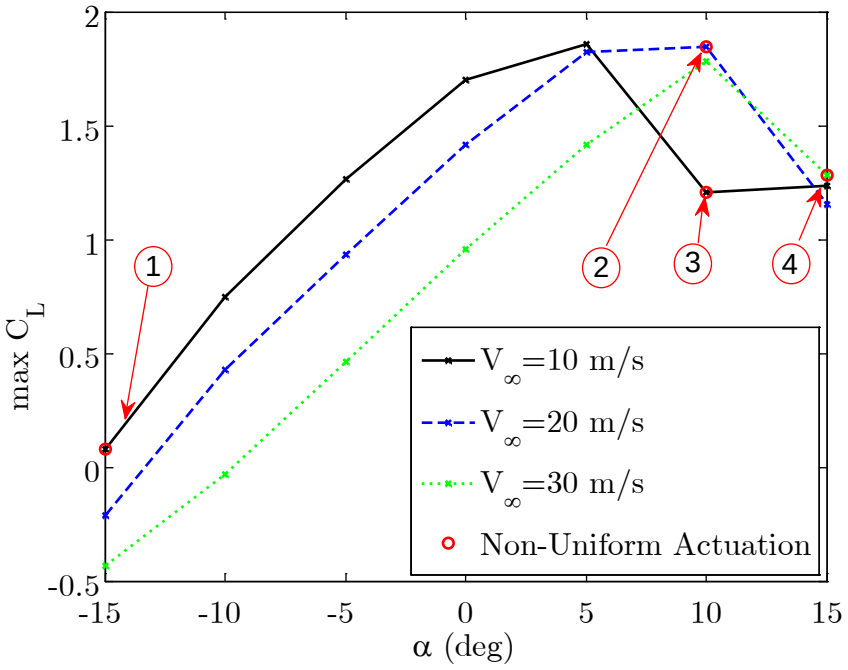

Figure 6.38 Sample of Non-Uniform Actuation Points

Investigating Point #3, which corresponded to V_∞=10 m/s and α=10^o, the flow-field about the converged result for the optimization, shown in Figure 6.39, was compared to the intuitive result, shown in Figure 6.40. This flow condition showed an example of both SMA and MFC working together synergistically to effectively control the flow. For this relatively low flow speed, high angle-of-attack flight condition, the "optimized" reflex actuation showed significantly less flow separation than the intuitive uniform actuation case, reflected by the attached streamlines in Figure 6.39. The optimizer incorrectly finished at the constrained local optimum, which was less than the global optimum. However the lift coefficients for the two cases were nearly identical, as seen in Table 6.3. This result was different from the uncoupled results in Section 6.3.1, where the lift coefficient for the uniform actuation was much higher than the reflex actuation case. Still, similar to the uncoupled results, the drag and pitching moment for the reflex actuation case were still much lower than the uniform actuation case. This was explained by smaller pressure difference between the upper and lower surface near the trailing edge in the reflex configuration, resulting in less-separated flow.

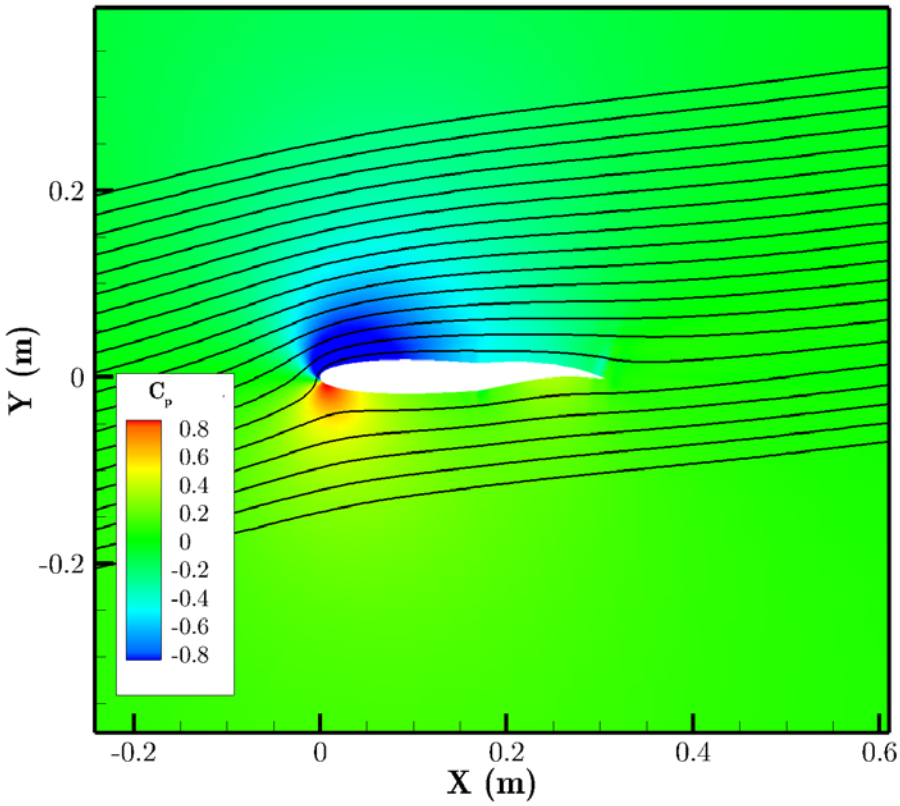

Figure 6.39 Optimized reflex actuation for SSMA at Point #3 (V_∞ = 10 m/s , $\alpha = 10^o$)

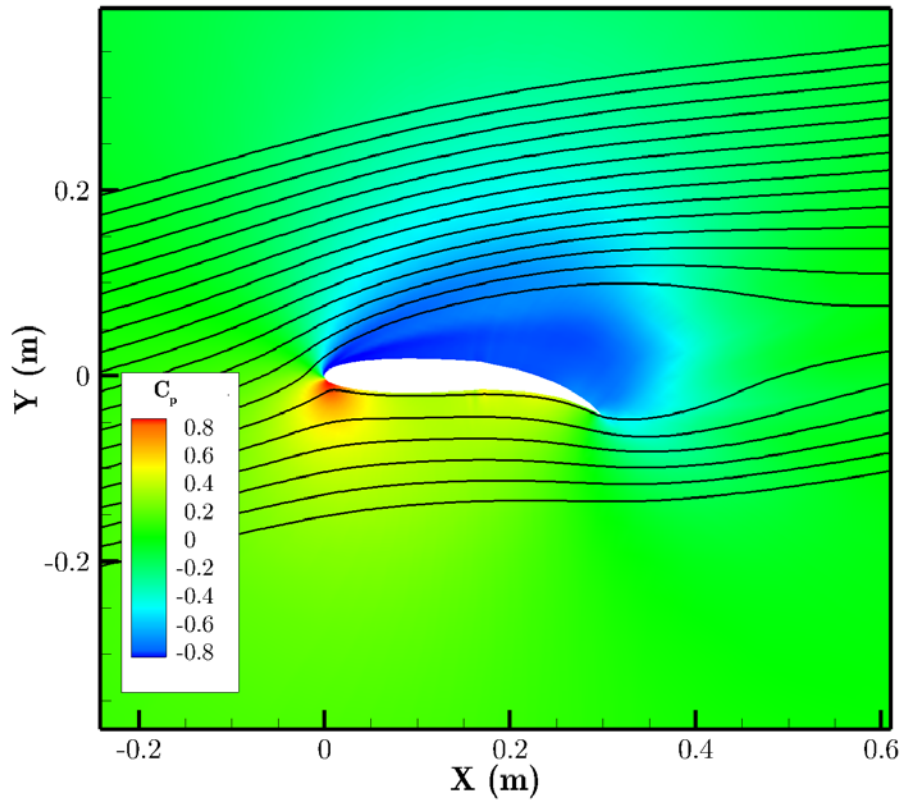

Figure 6.40 Uniform Actuation for SSMA at Point #3 (V_∞ = 10 m/s , $\alpha = 10^o$)

Table 6.3 Sample of Reflex Actuation Effects

	Point #3: (V_∞ = 10 m/s , $\alpha = 10^o$)		**Point #4: (V_∞ = 30 m/s , $\alpha = 15^o$)**	
Configuration	Uniform	Reflex	Uniform	Reflex
[MFC_δ,SMA_δ]	[-1,-1]	[-0.78, 1]	[-1,-1]	[-0.86, 1]
C_l	1.229	1.206	0.988	1.235
C_m	-0.251	- 0.083	-0.179	- 0.053
C_d	0.350	0.059	0.322	0.075

Examining a higher loading case, Point #4, which corresponded to V_∞=30 m/s and α=15^o, reflex actuation was seen to further improve performance at stall for high flow speeds. At this flow speed, as shown inn Figure 6.41, reflex actuation prevented the compliant mechanism from buckling, which was reflected in the decreased curvature of the front flexure box between the uniform and reflex actuation configurations. Additionally, the lift coefficient was dramatically improved in the reflex actuation case versus the uniform actuation case while still lowering the drag and pitching moment, as seen in Table 6.3, and reflected in Figure 6.42 and 6.43. The dramatic improvement between the two flow speeds was largely due to aeroelastic deformations in the structure. Thus, the synergistic effects of reflex actuation became more effective as the aeroelastic effects on the airfoil grew. The SSMA concept compensated for the increased comparative compliance of the Flexure Box by unloading the compliant mechanism for improved flow control.

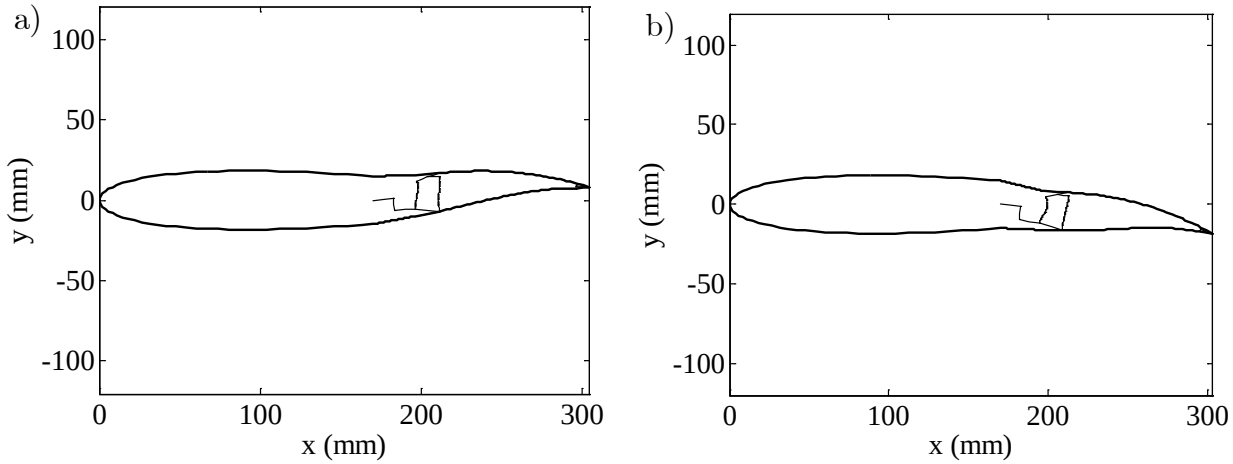

Figure 6.41 a) Optimized reflex and b) uniform configurations for V_∞ = 30 m/s , α = 15^o

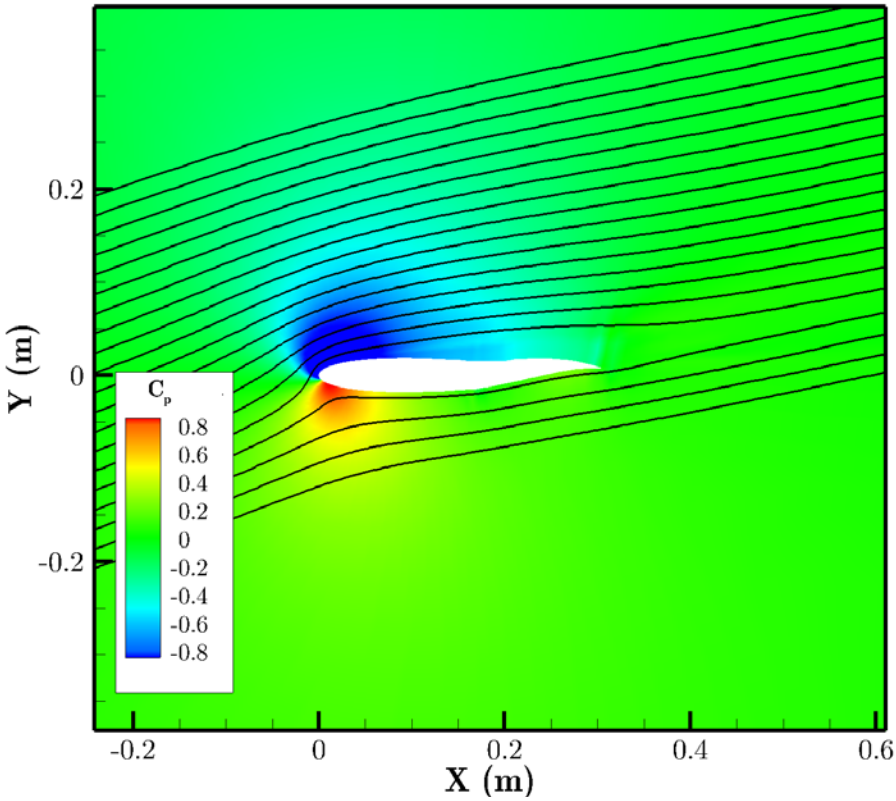

Figure 6.42 Optimized reflex actuation for SSMA at Point #3 (V_∞ = 10 m/s , $\alpha = 10^o$)

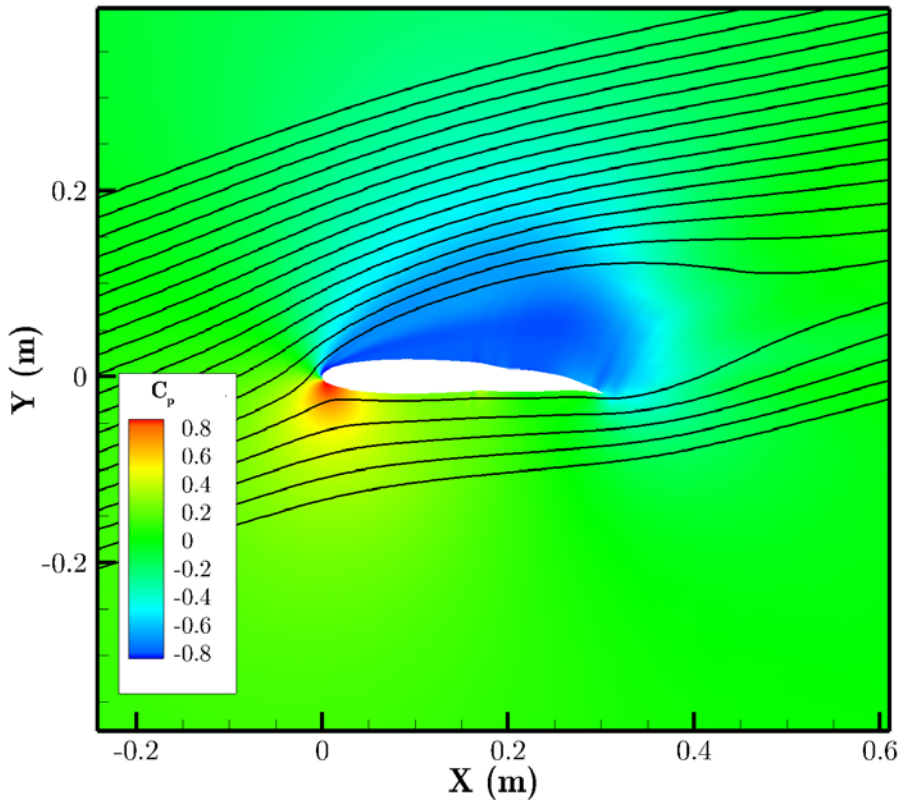

Figure 6.43 Uniform Actuation for SSMA at Point #3 (V_∞ = 10 m/s , $\alpha = 10^o$)

6.3.3. Summary of results from modeled static capabilities

The SSMA concept was shown to create a truly synergistic control surface where the advantages of both the MFC (conformal bending) and SMA (resistance to aerodynamic loads) were effectively utilized. Additionally, the SSMA showed an increased ability to control flow separation, actuating both uniformly and through a novel reflex actuation scheme. This configuration was shown to improve the control of lift, especially at separated flow conditions by unloading the compliant mechanism.

6.4. Dynamic capabilities

The results of the spectral characterization in Section 6.1 showed that the primary quasi-static gains of the SSMA concept occurred between 0.1 – 1 Hz, which corresponded to the gap between the rise in the relative time constant of the tip deflection for the constituent actuators. Although this implied that the aerodynamic gains could also be augmented within this frequency range, the modeled first-order actuation initially resembled a step-response. At low flow speeds, relevant to a UAV, this sudden impulse could result in highly unsteady aerodynamic effects. Accordingly, it was desired to determine if these first-order tip-deflections would result in similar responses of aerodynamic control forces.

The following section shows that by utilizing a simplistic controller defined by the total tip deflection of the hybrid morphing concept, unsteady aerodynamic gains for the combined system can be realized. Additionally, informed use of the state-change of the shape memory alloy wires is shown to potentially realize long-term power savings while utilizing this controller.

6.4.1. Modeled uncoupled aerodynamic gains

A simplified response for the optimal control of both actuators in the SSMA system was assumed to investigate how the combined concept would perform as compared to its constitutive actuators for a representative, attached flow, flight condition. The purpose was to determine whether unsteady gains experimentally measured by the characterization method in Section 6.2 for tip deflections would also extend to aerodynamic forces such as lift, pitching moment, and drag for a representative, attached flow condition.

6.4.1.1. Simplified system response

Previous work focused on experimentally determining a method to characterize the first-order response of the hybrid SSMA concept and its constituent actuators to a step-like input response. It was shown that both smart material systems could be initially characterized by measuring the response to a square wave input of a relevant period. For initial investigation, the effect of both smart material subsystems on the deflection of the trailing edge was assumed to be a first order system with a step input response of infinite period, of the form:

$$\frac{d\delta}{dt} + \frac{1}{\tau_\infty}\delta = f(t) \qquad \text{where} \quad f(t) = \begin{cases} \delta_i & \text{for} \quad t < 0 \\ \delta_f & \text{for} \quad t \geq 0 \end{cases} \tag{6.3}$$

where δ was the displacement of the tip of the morphing aileron, δ_i the initial position of the morphing aileron, δ_f was the final (desired) displacement, and τ_∞ was the first-order time constant as assessed by the lowest frequency input from the experiment in Section 6.2. Assuming that both of the initial and final positions were within the upper, δ_u, and lower, δ_l, bounds of the actuator, the response was of the form:

$$\Delta(t) \sim \left(1 - e^{-t/\tau_\infty}\right) \tag{6.4}$$

where Δ was the difference between the current position and the respective bound of the actuator in the direction of the desired actuation. Then, for a simplistic example, it was assumed that the actuator was already at the lower bound of the actuation, consistent with the characterization method from Section 6.2. Then the initial and lower bounds of actuation were identical and the displacement can be written as:

$$\delta(t) = (\delta_u - \delta_l)\left(1 - e^{-t/\tau_\infty}\right) + \delta_l \qquad \text{for} \quad \delta(t) < \delta_f \tag{6.5}$$

where the system converged towards the opposite saturated condition until the desired condition was reached. Although this model ignored higher-order dynamic effects associated with sudden starting and stopping conditions, it was assumed that it would generally represent the expected path of an optimal control considering the first-order limitations of the system. Then the difference between the upper and lower bound of the respective actuators were defined by:

$$\begin{aligned}\Delta_{SMA} &= \left(\delta_u - \delta_l\right)_{SMA} \\ \Delta_{MFC} &= \left(\delta_u - \delta_l\right)_{MFC}\end{aligned} \tag{6.6}$$

to generalize the modeling for the both the MFC-driven and SMA-driven actuators, respectively. As a result, the combined model system was represented as the summation of two first-order systems, characterized by the individual sub-system's time constants:

$$\delta_{SSMA}(t) = \Delta_{MFC}\left(1 - e^{-t/\tau_{MFC}}\right) + \Delta_{SMA}\left(1 - e^{-t/\tau_{MFC}}\right) + \left(\delta_{l_{MFC}} + \delta_{l_{SMA}}\right) \tag{6.7}$$

where δ_{SSMA} represented the trailing edge deflection of the combined system.

6.4.1.2. Assumed configurations

To identify the impact of this idealized control scenario on unsteady aerodynamic conditions, the shapes from Section 6.3.1 were prescribed to the OVERTURNS simulation utilizing a dynamic time-step. The simulations did not include aeroelastic or dynamic responses, but were rather prescribed motions that were defined by the mapping of actuations from Figure 6.28. Then, Equation (6.7) was simply amended to eliminate the terms for the inactive actuators, where the response for the SMA-only was:

$$\delta_{SMA}(t) = \Delta_{SMA}\left(1 - e^{-t/\tau_{MFC}}\right) + \delta_{l_{SMA}} \quad \text{for} \quad \left|\delta_{SMA}(t) - \delta_{desired}\right| > 0 \tag{6.8}$$

and the response for the MFC-only configuration was:

$$\delta_{MFC}(t) = \Delta_{MFC}\left(1 - e^{-t/\tau_{MFC}}\right) + \delta_{l_{MFC}} \quad \text{for} \quad \left|\delta_{MFC}(t) - \delta_{desired}\right| > 0 \tag{6.9}$$

and after the desired condition had been reached, the actuators remained at the desired position.

The combined system, rather than simply prescribing the actuations by Equation (6.7), sought to achieve the same desired tip position as quickly as possible and maintain it, regardless of local variations in camber. By comparing the time-constants of the constituent actuators, it was apparent that prescribing such an actuation would command the MFC to actuate past its neutral position until the slower SMA-based actuator could compensate. This description

embodied the concept of a synergistic controller. The equations that described this controller were then:

$$\begin{aligned} \delta_{SMA}(t) &= \Delta_{SMA}\left(1 - e^{-t/\tau_{MFC}}\right) + \delta_{l_{SMA}} \quad \text{for} \quad \left|\delta_{SMA}(t) - \delta_{desired}\right| > 0 \\ \delta_{MFC}(t) &= \delta_{desired} - \delta_{SMA}(t) \end{aligned} \tag{6.10}$$

which defined the desired position of the MFC based on the desired total tip deflection of the concept rather, and thus the slower SMA-based actuator.

6.4.1.3. Result from unsteady simulation

By over-compensating past the neutral position of the MFC-based actuator while the SMA-based actuator lagged behind, the SSMA could temporarily enter a state of reflex camber. Beneficially, as seen in Section 6.3, reflex actuation could approach or surpass the capabilities of uniform actuation to generate lift and control flow separation. Accordingly, it was desired to determine how this synergistic control would impact aerodynamic control forces and pressure for a representative flight condition.

Then, to compare the combined system with its constituent actuators, a representative actuation scenario was assumed where the airfoil was desired to adapt from a maximum additional lift condition to a zero additional lift condition in the minimum possible time. For attached flow, the intuitive scenario that prescribed zero additional lift was zero tip deflection and the maximum additional lift condition was the maximum tip deflection downward. The tip deflections summarized by assumed modeling from Section 6.4.1.1 were shown in Figure 6.44.

As seen in Figure 6.44a, the tip deflection of the SSMA achieved the desired tip deflection in approximately 0.33 seconds, which was slightly longer than the MFC actuating alone (0.11 seconds). This slower actuation was a result of the SSMA starting at a maximum downward tip deflection that was 60% larger than that of the MFC-only actuator. As a result MFC traveled further across its achievable range to compensate for the SMA, seen in the comparison of actuations presented in Figure 6.44b. Upon reaching the desired neutral total tip deflection, the MFC slowly varied its tip deflection in proportion to the SMA. The compensation of the MFC actuator within the SSMA ended after approximately 2.1 seconds when the SMA actuator finally reached its neutral to reach the neutral position.

The shapes associated with this action were generated into a set of meshes for use in the previously-mentioned OVERTURNS simulation code via the mapping prescribed by Figure 6.28. A representative flight condition of $\alpha=0^o$ and V_∞ = 20 m/s was chosen for evaluation and a timestep of 1/270 s was used to iteratively evaluate the unsteady forces due to actuation after converging the steady simulation. The resultant shapes and the influences of these shapes on the flow were illustrated via several relevant pressure fields, plotted in Figure 6.46.

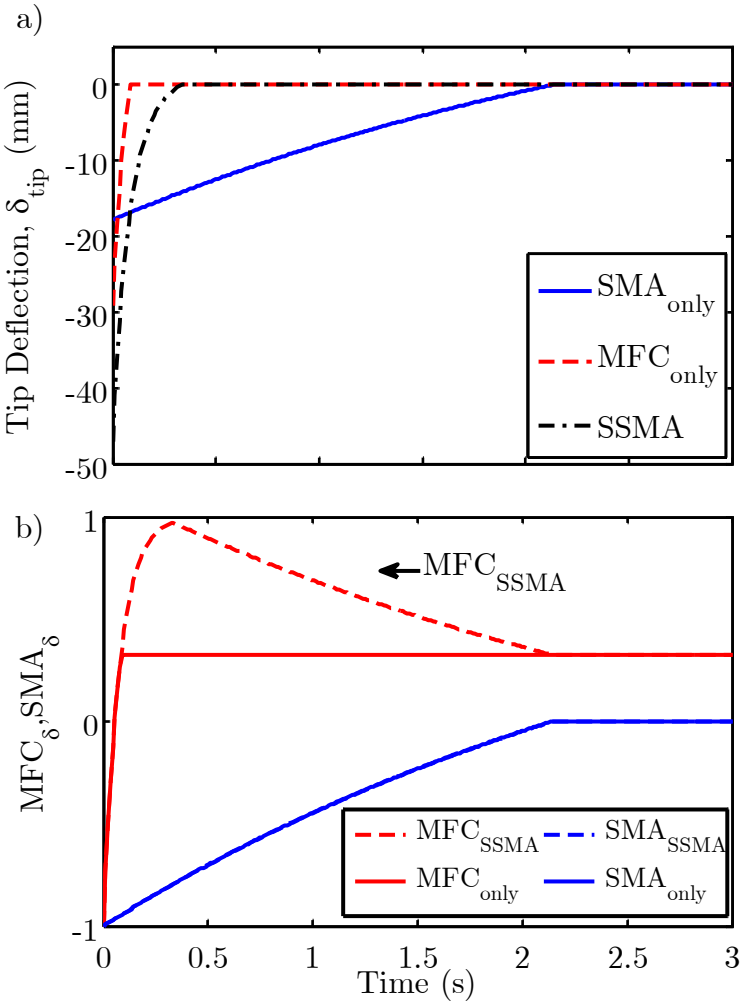

Figure 6.44 a) Prescribed tip deflection for SSMA as compared to constituent actuators and b) resultant actuation amounts for MFC and SMA in both cases

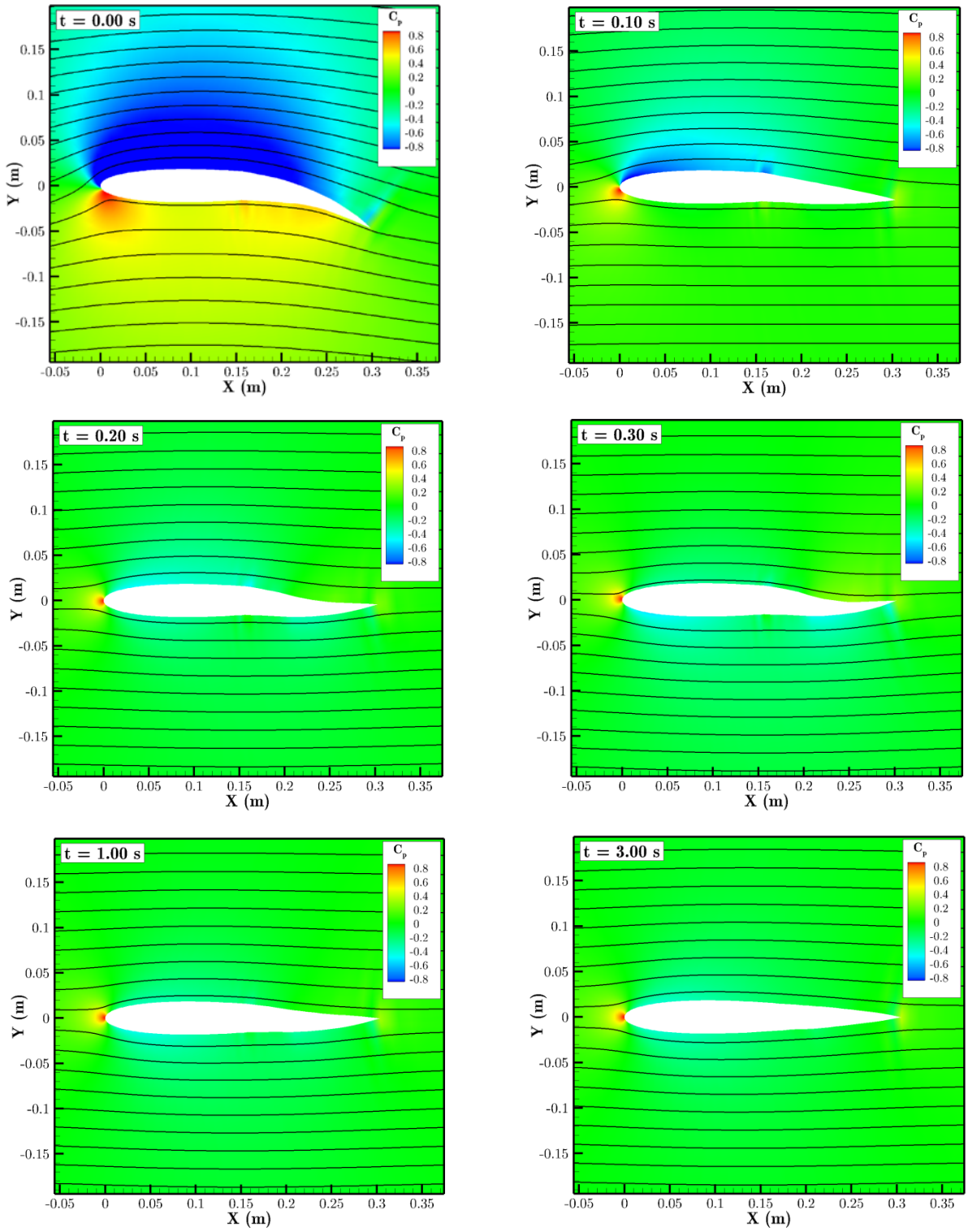

Figure 6.45 Unsteady pressure fields for synergistic SSMA actuation at V_∞ = 20 m/s, $\alpha = 0^o$ for incrementing time

The pressure field for the SSMA actuation in Figure 6.45, at t=0.2 s much more closely resembled the final configuration at t=3.0 s rather than the initial pressure distribution at t=0 s. The pressure distribution at t=0.3 represented one of the maximum reflex camber states, where a negative pressure distribution was found on the bottom of the airfoil, corresponding to a total negative lift, which was reflected by the nondimensional lift force. Between t=0.3 s and t=3.0 s, the reflex camber slowly relaxed until the SMA actuator had reached its neutral position, and the symmetric flow had been restored.

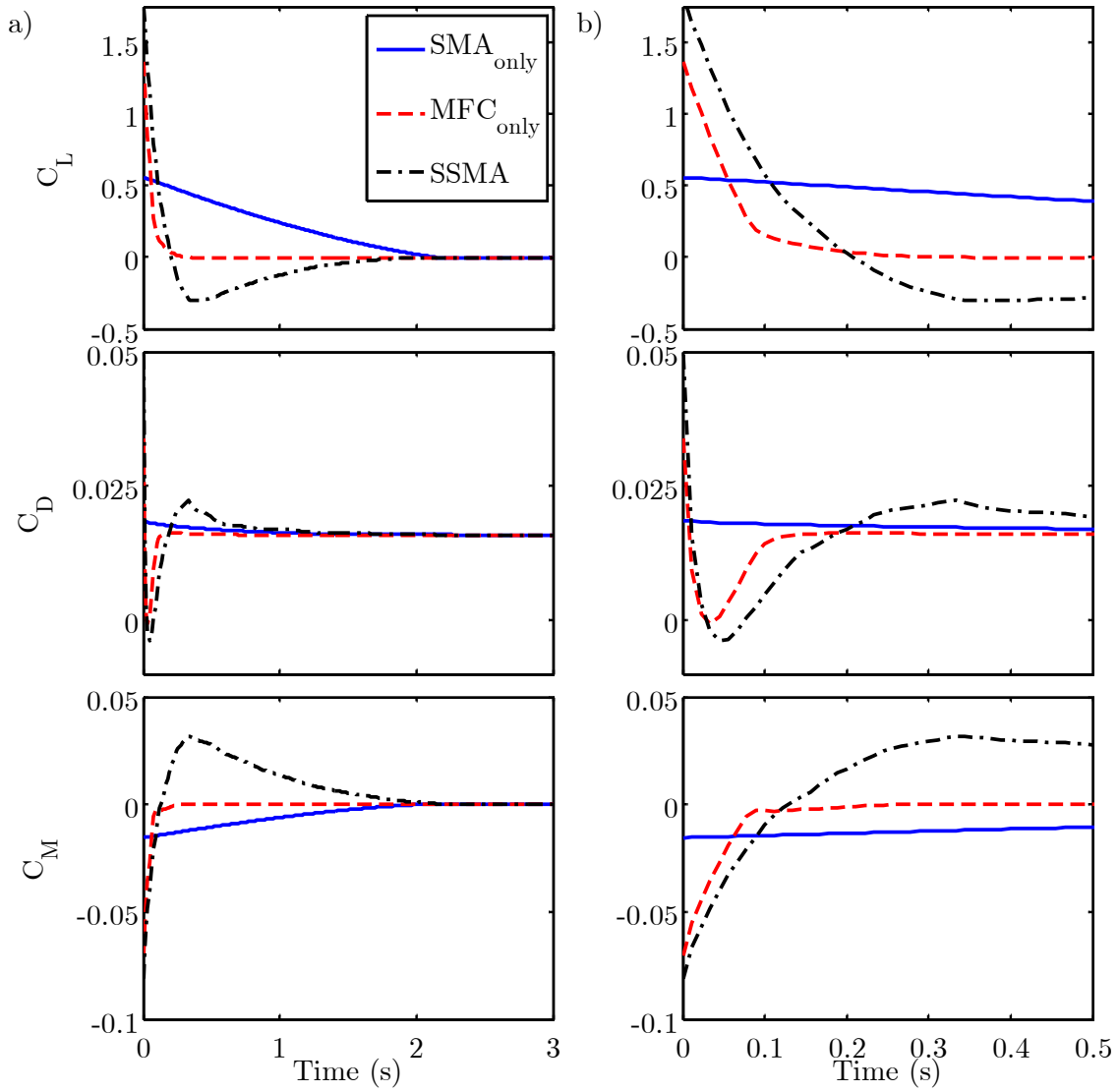

Figure 6.46 a) Unsteady aerodynamic forces for SSMA compared to constituent actuators and b) zoomed-in view of SSMA over a short timescale

The results of the nondimensional aerodynamic forces measured about the quarter chord of the wing were shown in Figure 6.46a and a shorter timescale of the forces prior to 0.5 seconds shown in Figure 6.46b over the maximum compensation by the MFC-based actuator in the SSMA concept. As seen in Figure 6.46b, the reflex actuation resulted in negative lift as the SSMA overshot the zero-lift condition. However, by overshooting the desired lift condition, the SSMA reached zero-lift after approximately 0.2 seconds, which was almost 50% faster than when the tip deflection first reached zero. The reflex configuration also resulted in a pitching moment offset that persisted until the SMA had reached its desired position. Also, the drag of the SSMA reached very low levels during the early phases of reflex actuation.

From these initial results, reflex camber was further motivated as a novel unsteady technique that could not only reproduce tip deflections that approximated a larger, fast actuator, but also alter the aerodynamic control forces on the timescale of the faster actuator

6.4.2. Experimental dynamic results

The results from the spectral characterization of the concept under aerodynamic loads was revealed that even small forced convection of the SMA wires could have significant effects on the actuation speed and positional holding capabilities of the wires. Leaving the wires unpowered while actuating the MFCs stretched the SMA wires, introducing slack and degrading the actuation capabilities. The results from the modeled static capabilities showed that reflex actuation could result in positive aeroelastic benefits leading to greater flow control near separation. Additionally, the unsteady simulations showed that reflex camber could positively impact aerodynamic control forces over short timescales. To realize these potential advantages of the SSMA concept, a closed-loop positional control of the two concepts was desired.

The following section details the implementation of a synergistic controller, following the simplified model from Section 6.4.1.2 and its impact on power consumption as measured for the complete airfoil demonstrator from Section 6.2.2 is described in the following paragraphs.

6.4.2.1. Controller development

As experimentally evaluated in Chapter 3, the capacitive nature of the MFCs combined with the use of high voltage step-up converters caused the power consumption of the MFCs to increase roughly proportional to trailing edge deflection. In addition, once the position had been

reached, the high voltage needed to be maintained to prevent the MFC from relaxing to its unactuated position. The SMA wires exhibited a different actuation method, by changing phase at a specified temperature. Once the position had been reached only minimal power was necessary to maintain the temperature of the wire and hold the position due to the relatively large level of thermal capacitance relative to the thermal dissipation.

The controller was then desired to allow for to quickly adjust for aerodynamic loads using the MFC actuator while the SMA actuator moves into position for long time-scale trim. Additionally, it was desired to power-off the MFC once the position had been reached and maintain the position with the potentially lower-power SMA.

6.4.2.2. Experimental setup

To implement the controller for the SSMA, analog sensors were used to provide calibrated, time-accurate assessments of the contribution of both actuators to the tip deflection. A rotary potentiometer was placed in-line with the axis of the discrete hinge that was rotated by the SMA wires. Then, by using the potentiometer as a half-bridge Wheatstone circuit, the equivalent tip deflection was calibrated against the analog voltage output using a laser displacement sensor. In a similar manner to Chapter 3, the flex sensors were added to the MFC-driven Flexure Box. Both actuators and sensors were calibrated independently to assess their impacts on the total tip deflection.

Then, a synergistic controller was implemented for both actuators in the SSMA demonstrator from Section 6.2.2 via closed loop control of the tip displacement. The calibrated tip displacement was controlled via an Arduino Mega 2560 running at approximately 60 Hz. The MFC was controlled utilizing a simplistic PID controller with representative gains set by the Ziegler-Nichols tuning method. The positioning error utilized in the MFC-only controller was defined by the difference between the desired total tip deflection and the current total tip deflection. When the SMA was included in the controller, the MFC positioning error was then augmented to include a correction for the SMA's current position. In a manner similar to Equation (6.10):

$$\delta_{desired_{MFC}}(t) = \delta_{desired_{total}} - \delta_{current_{SMA}}(t) \tag{6.11}$$

the desired positioning for the MFC $\delta_{desired,MFC}$, was defined by the difference between the total desired position $\delta_{desired,total}$ and the current equivalent tip position contribution by the SMA actuator, $\delta_{current,SMA}$.

To drive the SMA actuator, a simplistic on-off directional controller was implemented. In this method, the controller heated the desired wire at full power until the tip deflection of the SMA had reached the desired position within a prescribed error, ε_{SMA}. Then the controller completely disabled the heating power until the equivalent tip displacement of the SMA actuator began to drift outside of the bounds due to cooling wires or aerodynamic loading effects.

In the event that the MFC was near no applied voltage and the SMA actuator had converged to the desired position, the controller would disable the high-voltage circuitry driving the MFC. Thus, the SSMA had the capability to consume near zero power while maintaining a desired tip deflection, whereas the MFC-only actuation mechanism could not.

In a manner similar to the SMTE from Chapter 5, the desired position of the SSMA was communicated to the Arduino by a single analog output channel from a National Instruments DAQ 6211. This desired position was only changed to start the test and remained constant throughout the remainder of the test. The positions of the constituent actuators were recorded by simultaneously acquiring voltages of the SMA potentiometer and MFC flex sensors via the analog input channels on the DAQ, running at a 1kHz sample rate, which streamed the results to Matlab, which then interpreted the positions utilizing the same calibration that was employed by the Arduino code. Thus, by enabling the MFC control code, the SMA control code or both, the demonstrator could replicate an aileron with either or both control concepts active.

The same representative maximum lift to zero lift test as investigated in Section 6.4.1 was attempted on the test-stand, without an encapsulating skin and free from aerodynamic loads. The three different concepts (MFC-only, SMA-only, and SSMA) were tested for comparison of the concepts a manner similar to Section 6.4.1. The goal of the test was to determine whether the controller could achieve the same synergistic actuation capabilities as the modeled configurations from the previous section and to measure the relevant timescale for potential power gains due to the synergistic controller. The power consumed by each active morphing

concept was recorded utilizing the same custom current-monitoring circuits described in Chapter 4, which constantly streamed the current and voltage draw of the respective circuits.

6.4.2.3. Results from test actuation

The resultant configurations achieved by the SSMA utilizing this synergistic controller for the maximum-lift to zero-lift configuration were summarized in in Figure 6.47 for clarity of the tested configurations. Figure 6.47a showed the initial tip-down configuration for testing the equivalent of a maximum lift configuration. Then Figure 6.47b showed the SSMA in its maximum reflex actuation state, Figure 6.47c showed the relaxing reflex actuation as the MFC compensated for the SMA, and Figure 6.47d showed the final, unactuated state.

The total trailing edge deflection and the contributions to trailing edge deflection of the constituent actuators were summarized in Figure 6.48. Comparing Figure 6.48 with the modeled results from Figure 6.44, the same general trends were reproduced. However, the actuators showed a slightly longer settling time possibly due to the overshoot of the MFC while seeking the initial desired tip deflection. Still, the SSMA augmented the range of the MFC by approximately 100%. Additionally, the MFC was observed to first reach the desired tip deflection within 0.18 seconds, while SSMA reached the desired tip deflection after only 0.23 seconds. Also, similar to the simulations, the SSMA reached the maximum reflex camber at approximately 3.5 seconds. Even with this simplistic controller that did not reach the optimal control that was previously modeled, the potential for synergistic control of the larger deflections over a shorter timescale was realized and the deflections from the simulations were determined to be adequately reproducible.

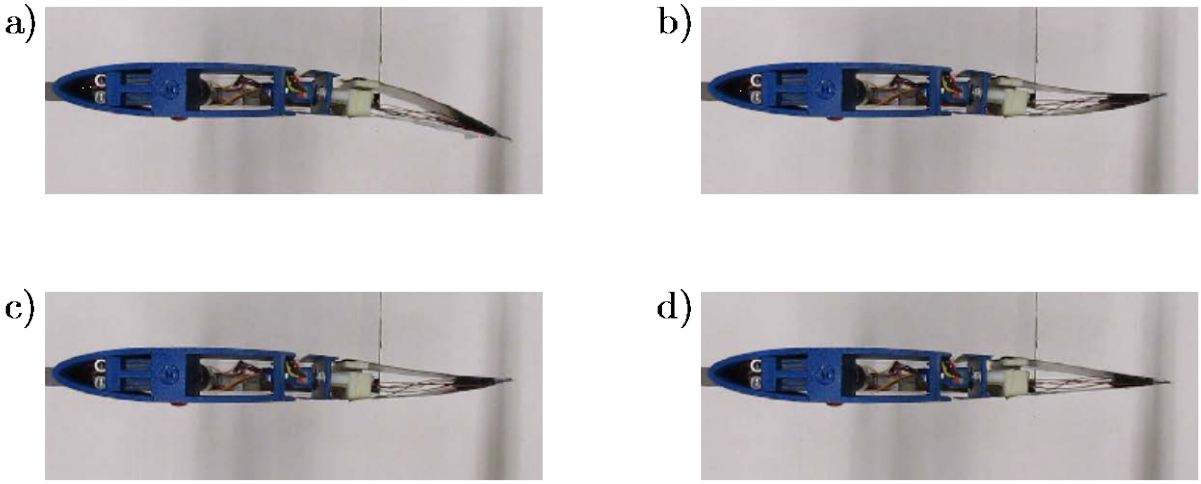

Figure 6.47 Configurations for synergistic actuation including a) initial state b) reflex c) relaxed reflex and d) final state

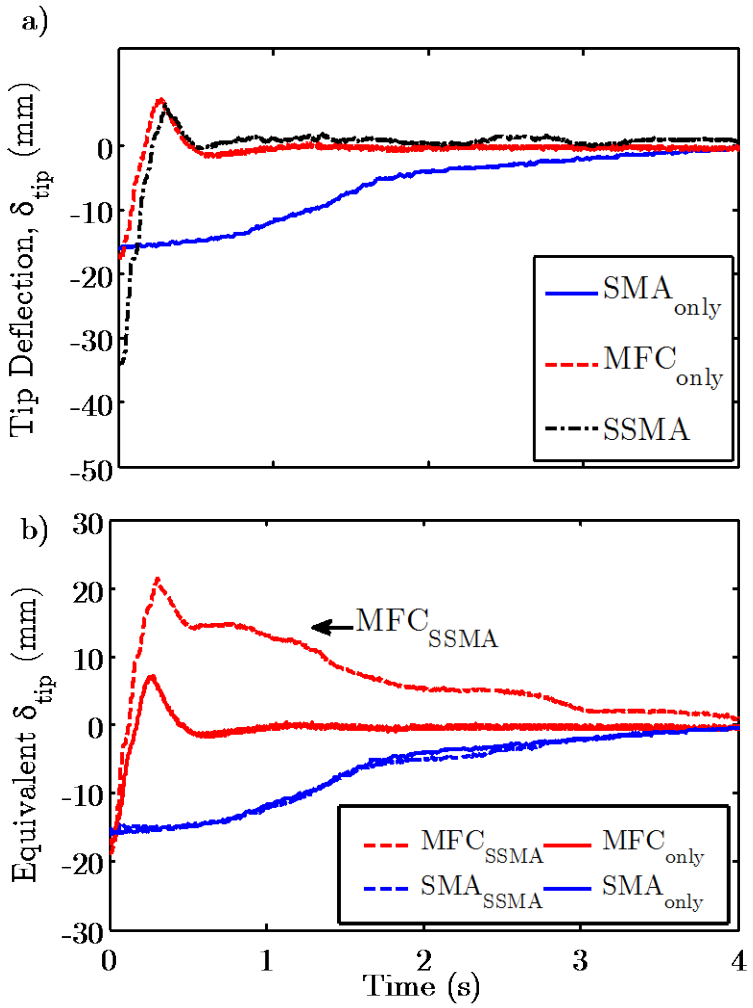

Figure 6.48 a) Measured tip deflection and b) equivalent tip deflection for tests

6.4.2.4. Power

The power consumed by the various actuation concepts during this test was calculated by multiplying the measured values of the voltage and current draw of the high-voltage power supply for the MFC and across the SMA wires for the SMA. The instantaneous power consumption and time-averaged power consumption of both constituent concepts and the SSMA were shown in Figure 6.49 Figure 6.49 with a summary of the relevant periods in Table 6.4.

As shown in Figure 6.49, the SSMA initially utilized the sum of the instantaneous power required by the SMA-only and MFC-only concepts, but within 3 seconds (the approximate reaching time of the SMA for the desired position), the SSMA turned off the power to the SMA actuator, showing a sooner instantaneous power savings. After approximately 3.75 seconds, the positioning error of the tip deflection allowed the SSMA to disable the high voltage circuitry powering the MFCs, resulting in a lower overall instantaneous power consumption. Notably, this power was non-zero because a minimum current draw was required to keep the MFC circuitry active for responding to potential sudden changes in flow conditions. After a timescale of approximately 10 seconds, the SMA had utilized a lower average power than the MFC, and after 17 seconds, the SSMA had utilized less average power than the MFC.

Thus, the synergistic controller was found to also potentially reduce the average power for the combined system and identified the relevant timescale >10 s for potential power gains. Although aerodynamic loading could increase the power required maintaining the position, this result motivated the future experimental testing of the concept under aerodynamic loads and the potential gains of a synergistic controller.

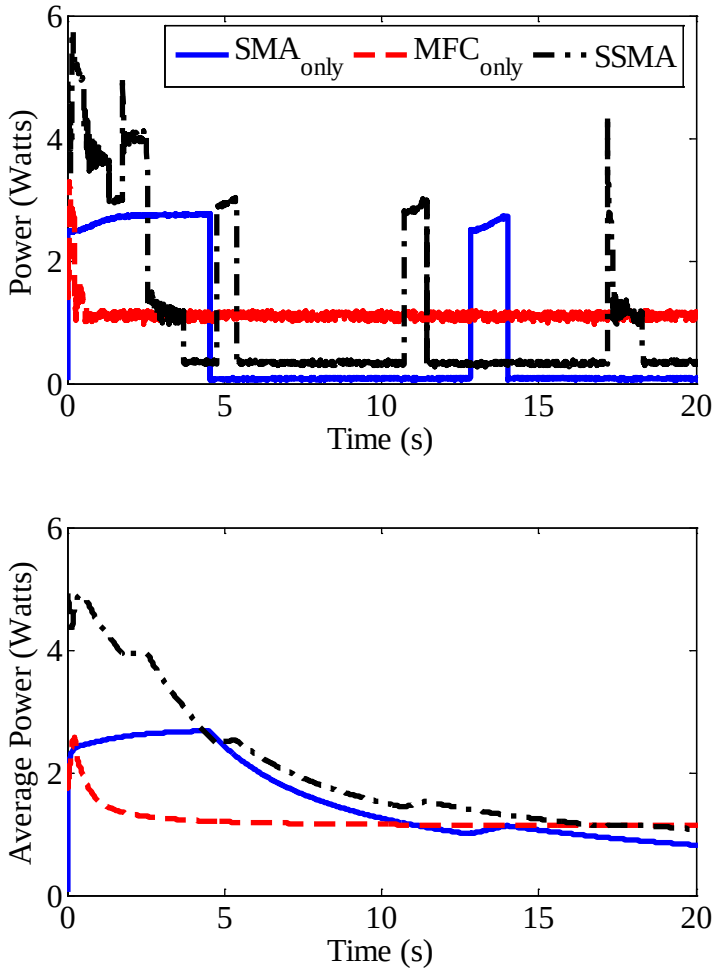

Figure 6.49 Instantaneous and average power consumption of all three morphing concepts for representative test

Table 6.4 Summary of Power Consumption

Configuration	Peak Instantaneous Power	Time for instantaneous power was less than MFC	Time for Mean Power less than MFC
MFC-only	3.29 W	N/A	N/A
SMA-only	2.77 W	4.53 s	11.0 s
SSMA	5.76 W	3.75 s	17.0 s

6.5. Summary and conclusions

Building upon concepts in literature to develop actuation systems using smart materials, a method for developing and characterizing a morphing aileron design with multiple smart materials was detailed. A difference in smart material actuation capabilities and mechanisms was identified between the MFC-driven and SMA-driven subsystems, namely, the higher bandwidth and lower blocking force of the MFC and the lower bandwidth but higher blocking force and work-density of the SMA. To overcome the implicit design complication by using two different smart materials, pre-established actuation mechanisms were used: a SMA wire-driven hinge and the MFC-driven Flexure Box with conformal morphing. A morphing aileron application was chosen, resulting in a fused design, the Synergistic Smart Morphing Aileron (SSMA) concept.

The concept was implemented into a representative airfoil, NACA 0012 with 304.8 mm chord, and tested at several flow speeds and input frequencies in a wind tunnel. A common first-order time response for the two actuators as a result of a square-wave input was identified. The use of a square-wave binary input was used to eliminate the need for complex control while still testing the rate saturation limits of each concept. From this characterization, the amplitude of the tip displacement and a common metric, the relative time constant, were established to compare performance of the individual actuators and the combined design. For the specific configuration chosen, the amplitude of tip displacement for both actuation concepts was relatively equal, approximately 20mm peak-to-peak or 6.5% chord. Testing in the wind tunnel at a single of attack, 0 degrees, over flow speeds ranging from 0-15 m/s showed that the combined design universally improved performance beyond that of its constituent actuators.

To identify potential aerodynamic gains without the use of a complex controller, achievable shapes of the SSMA were modeled using two methods: optimized static aerodynamic performance and optimized static aeroelastic performance. Initially, the aerodynamic performance was modeled using a Navier-Stokes flow simulation with experimentally-measured, unloaded airfoil shapes. Optimizing the performance of the MFC, SMA, and SSMA concepts over a range of flight conditions, the SSMA showed roughly 45% improvement over the MFC and 180% improvement over the SMA in influence over maximum change in airfoil lift coefficient at 20 m/s.

The coupled aerodynamic performance was compared among the actuation concepts by coupling the Navier-Stokes solver with a geometrically nonlinear corotational finite element code. The structure of the actuators was modeled as Euler-Bernoulli beam elements while the actuation of the SMA and MFC were implemented as a discrete rotation and distributed applied moment, respectively. The coupled code simulated the effect of aerodynamic forces on the actuators and allowed for performance analysis under realistic loads. The optimized performance of the SSMA was compared to its constituent actuators and showed improved capability to influence the lift coefficient over flow speeds ranging from 10-30 m/s and angles of attack between -15^{o} and 15^{o}. The SSMA also demonstrated superior flow control at flight conditions with high angles of attack by leveraging its unique reflex actuation capabilities to reduce flow separation and mitigate aeroelastic effects.

Finally, the dynamic performance of the SSMA, without considering aeroelastic loading was evaluated. First, a simplistic controller was defined where the faster MFC-driven concept compensated for the slower SMA-driven concept as measured by the equivalent contribution of each actuator to the tip deflection. The aerodynamic performance for the combined system was assessed for a representative case with attached flow, namely maximum to zero lift. Utilizing an Unsteady Reynolds-Averaged Navier-Stokes simulation, the combined system was also shown to be capable of altering aerodynamic loads on the timescale of the faster constituent actuator. Although the simulation overshot the target lift, the dynamic benefits of reflex actuation were still realized. This control concept was implemented for a experimental demonstrator on a test stand free of aerodynamic loading and the results showed that by utilizing PID control for the MFC and a simple on-off controller for the SMA, results similar to the modeled configurations could be achieved. Additionally, the combined system could attain a lower average holding power for positions than that of the MFC due to the ability to power-off the SMA wires and the high-voltage MFC circuitry. These initial results motivate the use of adaptive controllers that could alleviate usage of power as well as aeroelastic effects over long timescales while achieving larger actuation over short timescales.

Thus the SSMA concept was shown to create a truly synergistic flow actuator where the advantages of both the MFC (conformal bending) and SMA (resistance to aerodynamic loads) were effectively leveraged. Additionally, the SSMA showed an increased ability to influence

flow, actuating both uniformly and through a novel reflex actuation scheme. The improvements of the combined SSMA concept were summarized as:

- Increased overall tip deflection (measure of actuator amplitude of motion) by combining the effects of the constituent actuators and thus increased range in control over all control forces
- Maintained low relative time constant (measure of actuator speed) across a range of relevant frequencies (0.1 to 1 Hz) with respect to the faster actuator
- Added ability of reflex actuation which reduced drag and pitching moment for separating flow while alleviating aerodynamic loading on internal compliant mechanisms
- Added ability of reflex actuation for dynamic control of forces on airfoil over the timescale of the faster MFC actuator
- Potential for reduced power usage through additional control considerations

Rather than choosing an actuator with conformal actuation and higher bandwidth or an actuator with superior aeroelastic performance, the synergistic approach allowed for the combination and analysis of a design that used two different smart materials to achieve both desirable qualities. These smart materials operated over different time scales, with different actuation mechanisms, different blocking forces and work densities. Although the synergistic concept was specific to a morphing aileron application, the approach was general: leveraging the differences in these smart material actuators to achieve improved performance. The result was a device with operational capabilities beyond the capabilities of its constituent subsystems, specifically improved range and capabilities and preserved bandwidth while adding a slower actuator.

Chapter 7
Conclusions

7.1. Summary and contributions

The major contributions of this dissertation were centered on the concept of improving aerodynamic control forces as compared to a conventional trailing edge flap for a typical UAV wing utilizing a smooth, spanwise-varying trailing edge camber. To realize this complex geometric configuration, several novel construction techniques and experimental methods were developed and implemented. A summary of the key contributions are as follows.

Chapter 2 created a modular implementation of a smart-material active section for a morphing wing and was the first utilization of additive manufacturing to produce a stretchable skin while precisely tailoring the response of a morphing skin to resist aerodynamic loads. The design of a modular smart material control surface was a significant contribution towards smart materials' adoption as alternatives to conventional actuators, which can be replaced at the end of their useful work life. The additive manufacturing of elastomeric honeycomb represented a significant first step towards leveraging new construction methodologies for truly anisotropic control of morphing skins undergoing large geometry changes enabling continuous control surfaces.

Chapter 3 found, quite un-intuitively, that for the evaluated configurations, adding more Macro-Fiber Composites to a morphing concept did not universally improve the ability of the concept to control aerodynamic forces on an airfoil. This reduction in performance at low flow speeds was the result of the asymmetric voltage range of MFCs, which was measured via a reduced aspect ratio test article. A significant contribution of this test was the scaling of these results to higher aspect ratios, which could potentially be extended to other morphing

demonstrator concepts where a small aspect ratio test article could reduce experimental complexity.

Chapter 4 showed through implementation of the modular morphing concept into a representative finite wing that control derivatives could be improved beyond those measured for a conventional articulated flap wing. Also, the gapless wing was shown to eliminate the effect of inboard flap vortices with spanwise-increasing control surface actuation.

Chapter 5 showed that these improved control derivatives could be effectively leveraged via a simplistic system model to experimentally measure a reduction in drag. A dramatic reduction up to approximately 20% at off-design conditions was measured as compared to a conventional, discrete-flap wing as measured by a novel experimental methodology for off-design flight conditions.

Chapter 6 developed the first multiple smart material morphing aileron and characterized the relative contributions of its constituent actuators with a novel spectral method. This introduced the field of hybrid actuators to smaller UAVs and presented a realistic method for assessing potential frequency and aeroelastic gains for similar designs. The aeroelastic performance of this hybrid morphing concept was identified by optimizing the simulated actuations with a in-house developed corotational finite elements code coupled with a URANS solver. This simulation method showed that adding the second actuator enabled a new reflex configuration that could alleviate aeroelastic loading and improve performance at stall for high flow speeds. Also, as approximated by uncoupled results, this novel reflex configuration could permit the approximation of a large-displacement, short-timescale actuator due to unsteady aerodynamic conditions for relevant flow speeds. To realize these capabilities a novel controller was developed which commanded the actuation of the faster subsystem on the deviation of the slower actuator from the desired position.

In summary, the primary contributions of this dissertation to the field of morphing were:

- The creation of a modular smart material morphing aileron with embedded positional sensing for closed-loop control and improved adoptability
- The first additively manufactured elastomeric skin for precise tailoring to aerodynamic loads

- A scaling methodology for a smart-material morphing concept that permitted aeroelastic testing with a reduced-span demonstrator
- The first experimentally-measured drag reduction for a smooth, spanwise-varying morphing trailing edge as compared to a discrete-flap wing for a low-speed UAV
- The introduction of a multi smart-material hybrid morphing concept and its resultant characterization over multiple timescales

7.2. Future work

These contributions motivated several directions for potential future work. First, the Spanwise Morphing Trailing Edge (SMTE) concept was designed for a representative wing without the use of any initial optimization. Thus, a system-level optimization for a particular application could be used to improve the design of the elastomeric honeycombs in the passive sections, compliant mechanisms in the active sections, the relative distribution and sizing of the modular sections, as well as the sizing of the wing parameters. The aerodynamic and aeroelastic gains for this pre-optimized configuration could potentially be of even greater interest and applicability to the growing field of commercial UAVs that are concerned with endurance and performance. Additionally, rapidly-advancing additive manufacturing technology should decrease the manufacturing complexity of the construction of these complex designs.

Although system-level optimization may result in highly-integrated designs to maximize the possible gains, it would be desirable to maintain the modularity of the morphing concept. The relatively novel nature of the smart materials would then demand a higher degree of replicability to prevent a single integrated active mechanism from adversely affecting the performance of the wing as a whole. Modular active sections would alleviate this problem, but could reduce the overall performance due to structural redundancy. Thus, failure analysis of the integrated actuators within a morphing concept and how this should inform the optimal design is highly necessary but currently, largely uninvestigated.

Despite utilizing relatively exotic materials, such as additively manufactured elastomeric honeycombs, and integrated Macro-Fiber Composite actuators, the control implementation of the SMTE was conventional, mostly to appeal to the adoptability of the SMTE as an alternative to

conventional ailerons. Specifically, each active section adapted to achieve a “desired” configuration that was specified on the system level. In this work, the system level was modeled with a simplistic lifting line theory that did not account for any flow separation due to the prescribed flight condition or actuating the active section. A simple advancement for further evaluating the advantages of the SMTE would be to experimentally investigate aerodynamic gains at near-separated flight conditions with a higher-fidelity model. As seen by comparing the reduced control derivatives of the conventional with inviscid thin airfoil theory, significant gains from smooth, conformal shape control is expected for these relatively viscous flight regimes.

Another route for potentially expanding the benefits of the SMTE would be to utilize the control system with many distributed actuators and sensors to better sense the current flight condition. In the current design for the SMTE, each active section sought to achieve is own prescribed position regardless of out-of-plane aerodynamic forces or in-plane elastic forces from the other active and passive sections. In this implementation, the specification of the desired configurations could be viewed from the perspective of a server-client relationship, where a database of the best desired configurations was already pre-computed on the server. Then, the individual control surfaces functioned as clients that received the information for the optimal “desired” configuration at the specified flight condition. However, the individual control surfaces did not inform the system level when they had reached their maximum ranges, or if the actuation authority differed from the expected result for the given flight condition. By utilizing the individual control circuits in parallel with the system level, creating a recursive server-client relationship, a single system image of the current flight condition could be created. This augmented image could then be used to inform the capabilities at the current flight condition and better control the aircraft. As the number of actuators and sensors on the wing increases for increasingly exotic morphing configurations, informing the system image via distributed actuation would only increase in its effectiveness.

The Synergistic Smart Morphing Aileron concept also motivated the use of multiple-timescale control techniques for a morphing concept with multiple types of actuators. This concept is still relatively new and unique to UAV morphing because the complexity of including multiple adaptive concepts within the same airfoil has been prohibitive in weight and complexity in the past. Further efforts remain in experimentally investigating the unsteady aerodynamic

morphing capabilities of the SSMA and similar concepts to determine what new dynamic capabilities exist and in what flow regimes. The relatively slow flow velocities of UAVs provide many opportunities for these dynamic actuation capabilities to realize novel gains.

Also, the proper utilization of now-established knowledge of smart materials to reduce the complexity of these multi-smart-material designs could yield novel static and dynamic morphing capabilities beyond the simple reflex camber of the SSMA concept. Even though it would require a clean re-design, morphing the entire wing with an optimized distribution of actuation and compliance could create and maintain complex flow patterns that are not currently possible by morphing the trailing edge alone. This all-morphing wing with multiple smart materials properly fulfilling the appropriate roles of speed, stiffness, stroke and sensing could enable new flight regimes that are currently unobtainable with conventional designs and control methodologies. These capabilities could include: a slow-flying but highly maneuverable state for reconnaissance or package delivery which could be quickly adapted to a fast cruise state without prohibitively penalizing the range, or a self-diagnosing smart skin that automatically adapts integrated, distributed actuation to precisely control the local flow conditions with knowledge of system level constraints and requirements.

Appendix A
Additive Manufacturing Consideration

A.1. Comments on failure modes of additively manufactured parts

The method for characterizing the capabilities of a 3D printer, such as practical resolution for a particular application are, still largely ad-hoc and informed by the particular technician in charge of operating the machine. While it may be initially valid to assume a homogeneous stiffness for a structure when designing a 3D-printed part, this assumption will quickly become challenged in aerospace applications as the desire to reduce mass and stiffness will drive the designer to smaller, lighter, and more flexible parts.

The state-of-the-art in 3D printing is currently fused deposition modelling where a single coil of plastic is heated near melting and precisely deposited in layers that adhere together. This method is used by several common machines such as the Makerbot and the Dimension Elite. The coil, typically a cylinder, is compressed slightly by the print head into the previously deposited layer. The quality of the interface of the two layers is then decided by the properties of the material being deposited, the geometry at the interface, the temperature of the two layers and the temperature of the environment. Errors in the control of these variables can result in deviations in design, such as voids, that drastically weaken the part due to the creation of a crack along the part's weakest direction, shown in Figure A.1. Considering that the voids are introduced between layers where the stiffness of the structure is already weakest, the ability of these errors to deteriorate the toughness of the structure can be significant.

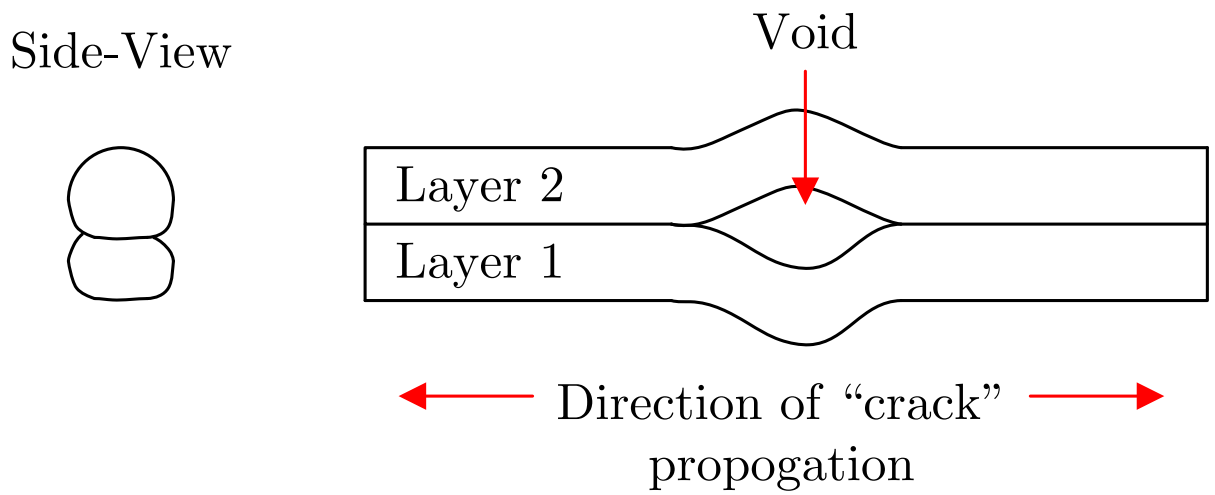

Figure A.1 Depiction of a typical void between layers produced by Fused Deposition Modeling

Errors alone are not the only source of introducing weakness to the structure. Some designs require voids to be introduced within the structure. Representative designs include a hole, or a hemisphere. The slight variations in geometry between the layers can alter their adhesion. The FDM process is then often augmented by also providing the option of a "support material" that can be removed after the construction of the part is complete. Ideally this material would bond together so that it could form a sub-structure that is significantly weaker than the desired part. This is typically accomplished by creating relatively porous designs of the support structure that weaken its toughness to mechanical abrasion. Almost exclusively, the printing machine controls the layout and density of the support material in a "black-box" fashion so that only changes in the position of the part on the printing stage would alter the support material, in ways that are only seen after the construction of the part is complete. The layout of the support material is typically inconsequential as it is typically removed and discarded after construction.

An alternative method for part construction to coils is the use of small droplets of plastic that are then cured post-deposition. These droplets are deposited via a print-head which then mechanically presses them into the previous layer, curing during the process. The Objet Connex multi-material printer utilizes this method because it allows multiple materials to be easily deposited within the same part, switching between them as a printer would switch between colors. Because the change of state from liquid to solid is much more drastic, the method for curing this material is ultra-violet light which diffuses through the layers during the construction

process. The basic unit of this printing process is then a semi-solid droplet which is mechanically pressed into position and cured without heat. The advantages of this method include smaller unit size, increased interface size between units, and separation of material choice from the thermal curing process. Thus the resultant parts can have increased resolution, decreased voids, more material choices, multiple materials within one part, and increased resistance to heat.

The increased design parameter space afforded by the droplet machines also can result in an increased number of failure modes not achievable by FDM. Specifically, the interfaces between all combinations of the part and support materials are highly prone to failure. Mismatches in the stiffnesses and Poisson's ratios of the materials can cause large interface stresses, which has been a well-known problem since the beginning of additive manufacturing [134]. The bond between the different materials can also be weakened depending on the combination of materials selected and their chemistries.

Suitable approaches to this problem include arresting cracks at the interface through geometric structures, generally macroscopically [134,135]. Another suitable approach achievable by a droplet printer could be a gradient-based approach by which the droplets of one material gradually blend into another. Due to the level of detail required by the hinge, only such a gradient-based method would be achievable at the required resolution. However, such a method was not available as the software that decides the material droplet placement was "black-boxed" so that only the sharp, undesirable interfaces could be achieved. Thus, for the current design, the interfaces between changing materials often represented the first point of failure.

Appendix B

SMA Wire Diameter Considerations

B.1. SMA wire diameter investigation

The Synergistic Smart Morphing Aileron (SSMA) was composed of a nickel titanium Shape Memory Alloy (SMA) wire as one of its actuation concepts. To inform design decisions on the selection choice of a SMA wire diameter, it was desired to test:

- How increasing SMA wire diameter affected recovered strain and power consumption
- How selecting an alternate time constant would affect measurements
- How increasing power consumption would affect the work lift of the SMA wires

This appendix addresses these questions by experimental investigation.

B.1.1. Experimental setup

To measure the recovered strain of the SMA wires under varying conditions, an experimental setup was constructed from hanging proof masses, suspended by a single SMA wire anchored to a fixed point, as seen in Figure 5.2 . When enabled, a constant-voltage, current-limited power supply heated the SMA wire to recover its initial strain from an initial extension. A laser displacement measured the displacement, δ , that the SMA wire contracted from its initial position. Upon heating the wire, the laser displacement sensor measured the movement of the proof mass, and transmitted this information to a National Instruments NI-6211 DAQ which recorded the displacements at 100 Hz. The displacement was analyzed as percent strain recovery compared to the initial, undeformed length, L, of the wire.

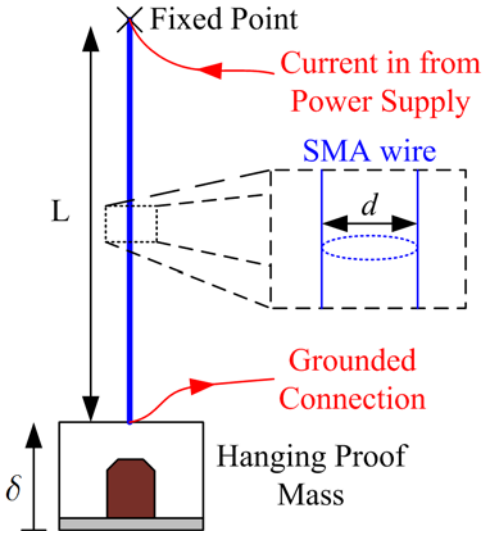

Figure B.1 Description of experimental setup for SMA wire characterization

The SSMA demonstrator informed the scale of the tested wire diameter, length, applied power and proof masses. Three wire diameters (200 μm, 300 μm, and 375 μm) of Flexinol wire supplied by Dynalloy, Inc. were chosen for investigation. The length selected for the wires in this test were 145 mm, similar to the length used in the SSMA demonstrator. Also consistent with the demonstrator, the wires were pre-strained with their respective pre-strain loads to simulate the antagonistic configuration of the SSMA. Applied heating current consistent with the manufacture-supplied specifications were used to heat the wires.

B.1.2. Strain recovery behavior

The first investigation sought to identify any trend in the recovered strain under applied stresses as a function of wire diameter. The resulting data, summarized in Figure 5.2 indicated that there was no clear difference between the selected wire diameters for the constant-strain recovery region. The three tested diameters had constant recovery behavior for approximately $\sigma_{applied}$<0.4 GPa, followed by a rapid decay in performance. A smoothed curve of the measured data points was included for reference. Within this region, the maximum recovery strain was essentially achievable. Relevant points from the applied stress and recovery strain plot were summarized in Table B.1.

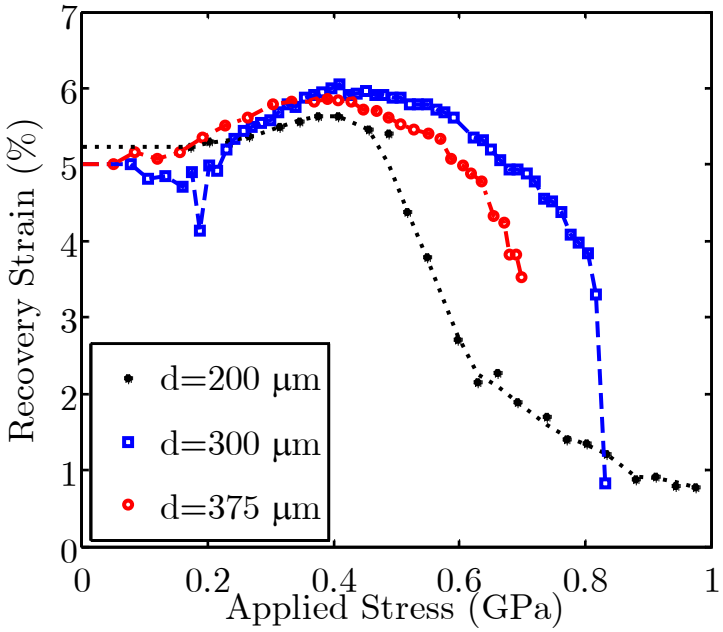

Figure B.2 Characterization of strain recovery degradation

Table B.1 Relevant stress and strain values with increasing wire diameter

Wire Diameter	Applied Stress at Peak Strain(GPa)	Peak Strain (%)	Applied Stress before Failure(GPa)	Recovery Strain near Failure (%)
200 µm	0.407	5.62	0.975	0.77
300 µm	0.410	6.04	0.832	0.83
375 µm	0.389	5.86	0.698	3.53

Expectedly, no distinct trend was found between the peak recovery strain or its applied stress. All wire diameters achieved a peak recovery strain of approximately 6% at an applied stress of approximately 0.4 GPa. After this peak stress, the various diameters of wire showed difference responses with increasing load. The smallest diameter wire experienced the soonest and largest drop in recovery strain the quickest, but could endure the largest applied stress before failure. The 300 µm diameter wire experienced a drop in recovery strain much later but failed at approximately at approximately 17% lower stress. Finally, the 375µm diameter wire failed at the lowest stress at only a 50% reduction in recovery strain. No mechanism was explained for this failure mechanism and all wires were heated with the same power per unit volume of approximately 0.4 W/mm^3. However, it was expected that increased overheating of the wires from increased wire diameters, and thus higher overall power was the root cause. Accordingly, the smallest wire (200 µm) exhibited the smallest power consumption while providing the largest

surface area to volume ratio, which would aid in the response time of antagonistic setup utilized in the SSMA. So, the 200 μm wire was selected for this particular application.

To investigate whether the 200 μm SMA wires could fully actuate under aerodynamic loads, a theoretical estimation of the required recovery strains and applied stresses for the SSMA actuator was performed. Several high hinge- loading scenarios were modeled for the SSMA using the coupled corotational finite element and OVERTURNS code from Chapter 0 to identify whether aerodynamic loading would violate the measured constraint from Figure 5.2. A representative angle of attack ($\alpha=15^{o}$) was chosen to investigate the applied stress and required recovery strain. Then, the flow speed was varied from 5 m/s to 30 m/s to investigate the effect of increased aerodynamic loading.

The calculated moment from the aeroelastic simulation about the discrete hinge was assumed to be distributed evenly between the two wires on each side of the hinge, per the design. The applied force on the wires due to aerodynamic loaded was calculated from the moment arm of the attached wire from the location of the discrete hinge. The secant of the arc length of the rotation from the position of the SMA wire anchor was used to calculate the required stroke between the maximum and minimum actuation positions. Dividing the applied force by the area of the selected wire (200μm), and the stroke by the length of the demonstrator wire length, the applied stress and required recovery strains were calculated.

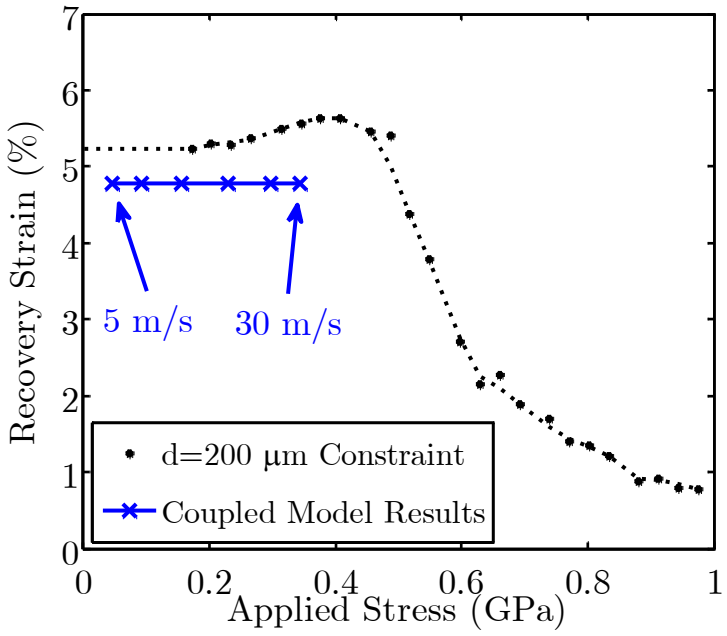

Figure B.3 Evaluation of maximum possible loading on wires due to modeled flow speeds

The resultant applied stress and the amount of strain required to recover the experimentally-measured tip deflections were plotted in in Figure B.3. From this analysis, it was seen that the smallest diameter wire, 200μm, would provide adequate control authority for the flow speeds under investigation even at the maximum stress conditions.

B.1.3. Response time

The variation in actuation response time of the SMA wires due to increased loading was investigated by monitoring the time required for the proof mass to reach its maximum recovered strain under varying applied loads. This data was examined with two metrics: a first-order time constant, τ, which was defined as the time required for the SMA wire to contract 1-1/e or approximately 63% of its final range, and a 10-90% rise time t_r, which was defined as the time required for the SMA wire to contract from 10% to 90% of its final deformation. Again, all wires were heated with the same approximate power rating of 0.4 W/mm^3, per applied current recommendations from the manufacturer. Figure B.4 summarized the impact on the response time metrics of varying the applied stress.

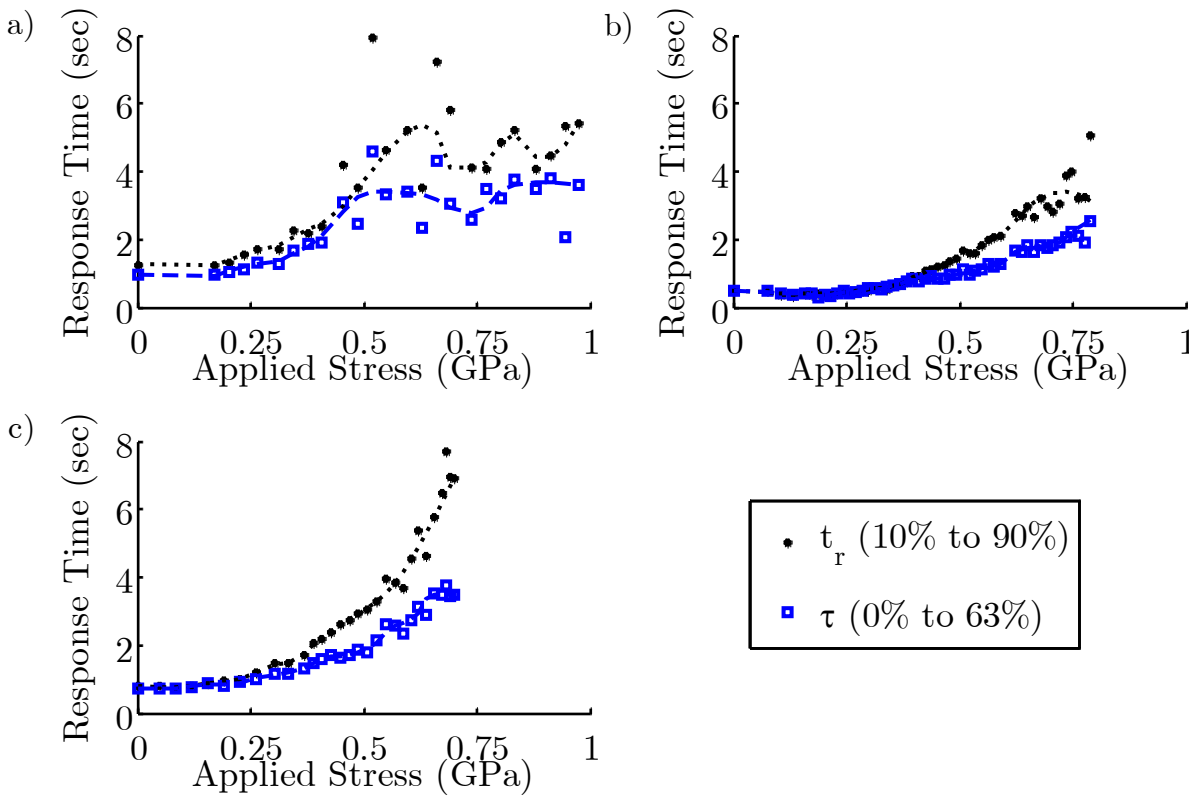

Figure B.4 Response time metrics under increasing loads on a) 200 μm diameter, b) a) 200 μm diameter and c) 375 μm diameter SMA wire

Table B.2 Comparison of mean response time metrics

Wire Diameter	τ	t_r
200 μm	1.27	1.65
300 μm	0.51	0.51
375 μm	0.97	1.16

As seen in Figure B.4, both response time metrics were found to have a fairly constant value from no applied stress until the approximate peak strain condition of 0.4 GPa. After the peak strain, the time constants increased until the recovery strain became limited by the applied stress. This case was seen as $\sigma_{applied}$>0.4 GPa for the 200 μm diameter wire and $\sigma_{applied}$>0.7GPa for the 300μm diameter wire. From these results it was concluded that either response time metric would provide an adequate characterization and was relatively insensitive to applied stress for $\sigma_{applied}$<0.4 GPa. Again, as summarized in Table B.2, by taking the mean of the time metrics

for this applied stress, no clear trend for the response time appeared while varying the diameter of the wire.

B.1.4. Cyclical failure at maximum strain

Because no clear trend regarding the response time of the diameters was selected, it was desired to evaluate the capability of the wire tested by the SSMA concept, namely the 200μm wire, to undergo repeated loading at its maximum strain with increased heating power. The impact of increased power usage on wire failure was investigated by increasing the applied heating power beyond the value recommended by the manufacture and cycling the wire until failure at its maximum strain, as shown in Figure B.5.The points on the left of the plot showed the expected maximum cycles at the applied power utilized for the SSMA concept. Although the test consisted of limited data points, increasing the applied power decreased the cycles to failure. This result was confirmed by the wire audibly creaking at the highest applied power tested. The most likely cause of this mechanism was overheating in the wires post-actuation. Thus, it was noted that for increased applied power, overheating could decrease the work life without the use of a controller to disable the heating. Then, to prevent failure within the SMA wires during initial testing, applied power above the manufacture specifications was not used.

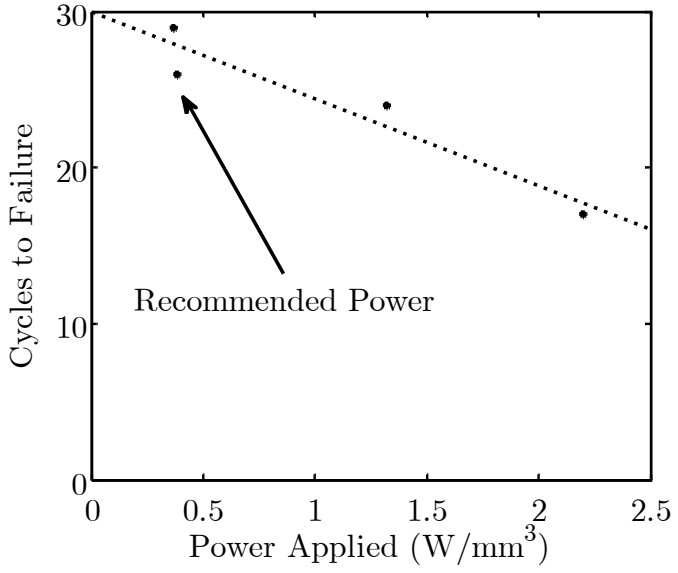

Figure B.5 Cycles to failure of 200μm diameter wire at for increasing applied heating power

B.1.5. Summary

The analysis of SMA wire diameter for implementation in the SSMA demonstrator yielded several key findings for this specific application. First, the recovery strain of the three tested wire diameters, which included 200 μm, 300 μm, 375 μm, remained relatively constant at approximately 6% until the maximum recovery strain at an applied stress of approximately 0.4 GPa. In this range, the response time as measured by a first order time constant and a reaching time remained relatively constant. Past this condition the response time increased rapidly as the recovered strain decreased. No clear trend for this experimental setup was noted for the wire diameter on the expected time constant under constant volumetric heating. So, the smallest diameter wire, 200 μm, was chosen for use in the SSMA demonstrator because it utilized the total power and had the largest surface area to volume ratio, to aid in cooling for the antagonistic setup.

A theoretical analysis of the applied stresses and strains under relevant aerodynamic conditions showed that the selected wire diameter (200 μm) should provide sufficient authority to at least 30 m/s, which was well beyond the experimental range of dynamic pressure under investigation. The selected wire was then determined to be suitably characterized by either a first-order time constant, or a reaching time for the given application. For this particular setup, increasing the power supplied beyond the manufacturer's recommendations decreased the achievable cycles due to overheating without the use of a controller to disable the heating. Then, for initial characterization the manufacturer-recommended heating power was used. Although, for higher heating rates with an appropriate controller, improved speed response would be expected.

Appendix C
Modal Evaluation of Flexure Box

C.1. Modal evaluation of flexure box

Testing of the MFC-driven Flexure Box aileron under quasi-steady square waves in Chapter 6 for a spectral characterization showed large deviations in the amplitude as the forcing frequency approached 10 Hz. Examining the time-history response, dynamic effects were assumed to cause the deviations in steady-state response. To confirm this effect and appropriately integrate the Flexure Box aileron into the Synergistic Smart Morphing Aileron for future dynamic control, it was desired to evaluate its structural modes and whether they could be appropriately modeled.

This appendix experimentally investigates the structural modes of the Flexure Box aileron and attempts to capture the dynamic characteristics with eigenvalue modal analysis of the finite element mesh from the corotational beam code from Chapter 0.

C.2. Experiment

C.2.1. Experimental method

To characterize the modal excitation of the Flexure Box aileron, the displacement response to high voltage excitation was experimentally investigated. The MFCs within the Flexure Box were actuated antagonistically with a 1kV peak-to-peak sine waves via the high voltage divider proposed by Bilgen [80]. A swept sine wave from 1-200 Hz driven by a TREK 2220 high voltage amplifier was used to determine the operational deflection shape over a range of frequencies. The out-of-plane velocity of several points in the z direction over the fixed (bottom) surface of the Flexure Box aileron was measured with a Polytec scanning laser vibrometer system, as seen in Figure 5.2. The mesh of points both chordwise, x, and spanwise, y, aided in determining whether the structure was adequately modeled using a two-dimensional (i.e.

spanwise-stiff) model, and what its natural frequencies were. Two relevant points of interest near the tip of the aileron and towards the middle were specifically identified investigated to provide additional insight as to the dynamic modes of the Flexure Box aileron.

C.2.2. Experimental Results

From the experimental results, the frequency response function of the base displacement with respect to the excitation voltage at Point 1, which represented the tip of the Flexure Box aileron, was plotted in Figure C.2. The first mode was seen to occur at approximately 12 Hz. By approximately 7 Hz, the displacement response had already increased by 3dB, confirming the analysis of the spectral characterization of dynamic effects at this frequency. The next two observed modes occurred at much higher frequencies, approximately 70 Hz and then 180 Hz.

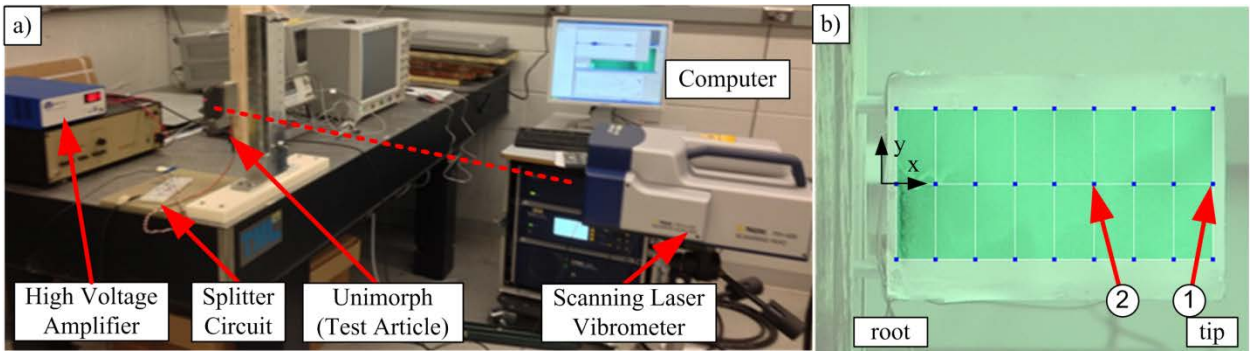

Figure C.1 a) Experimental setup for modal testing
and b) mesh of scanned laser points on unimorph with relevant, marked points

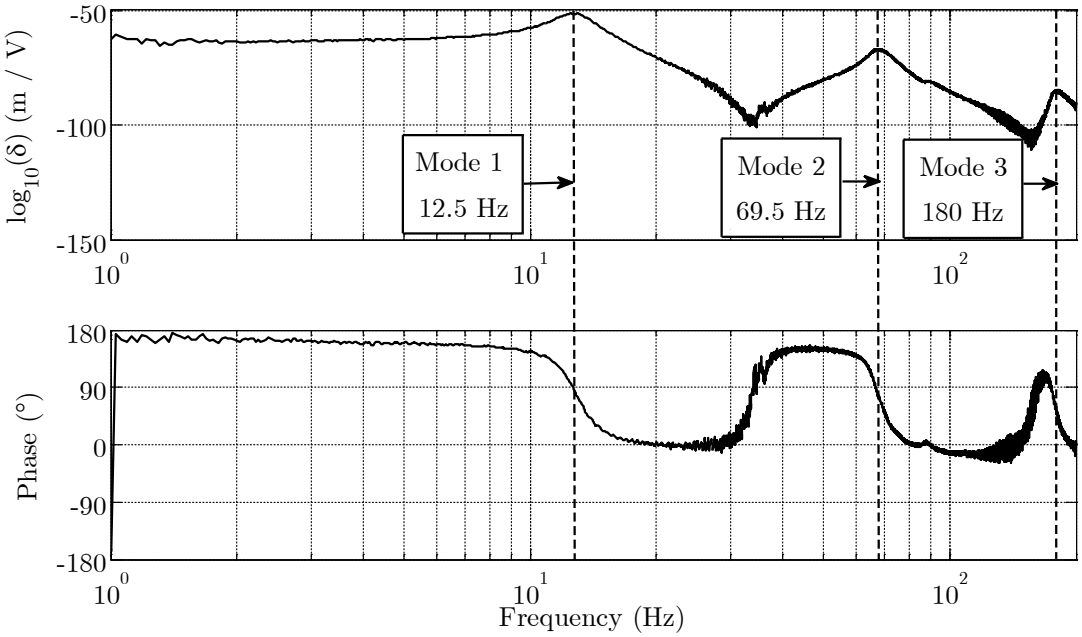

Figure C.2 FRF of output tip displacement compared to input voltage at Point 1 (near tip)

The response of Point 1 near the tip was contrasted with Point 2, which was chosen to be closer to the chordwise middle of the aileron, to reveal any other non-monotonic mode shapes for further characterization of the aileron. As seen in Figure C.3, this second point revealed two other missing mode shapes that were much lower in magnitude. The natural frequencies of these mode shapes were at approximately 100 Hz and 140 Hz. Thus, five modes in the Flexure Box were present at less than 200 Hz due to the relatively large compliance required by the morphing structure.

The operational deflection shapes the frequencies of these five modes were investigated to obtain a clearer picture of the expected mode shapes. Utilizing the full mesh from Figure 5.2b, the operational deflection shapes were independently investigated utilizing the scanning laser vibrometer at these frequencies. The resultant shapes were plotted in Figure C.4.

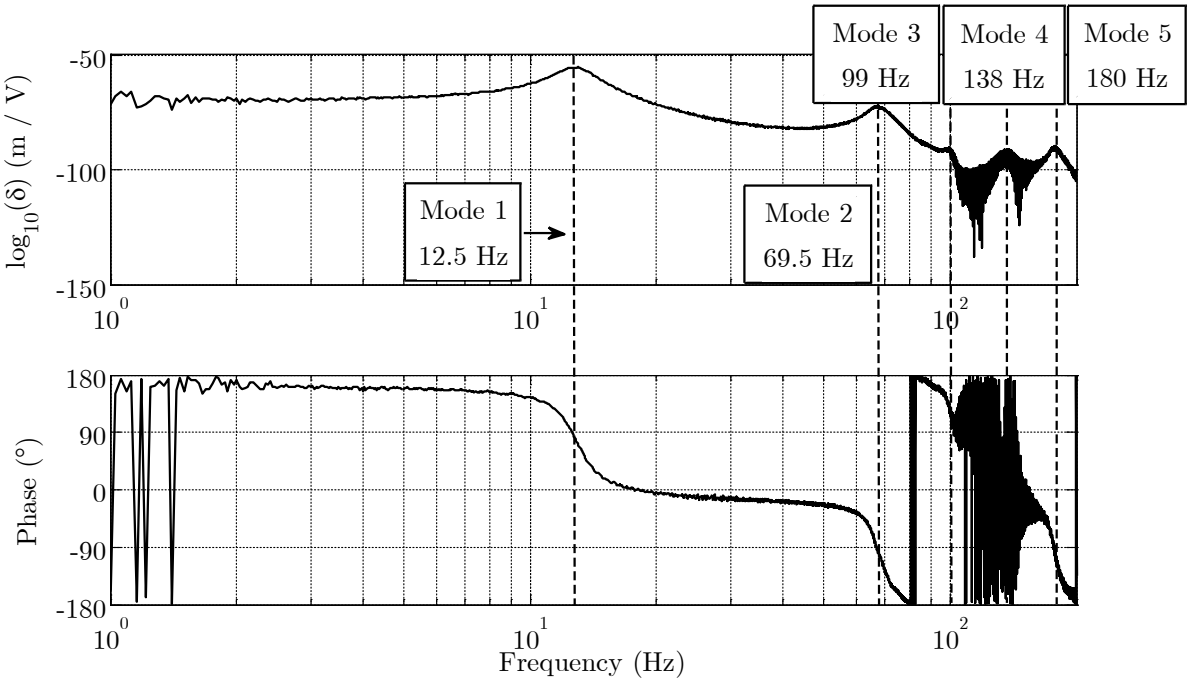

Figure C.3 FRG of output tip displacement compared to input voltage at Point 2 (near middle)

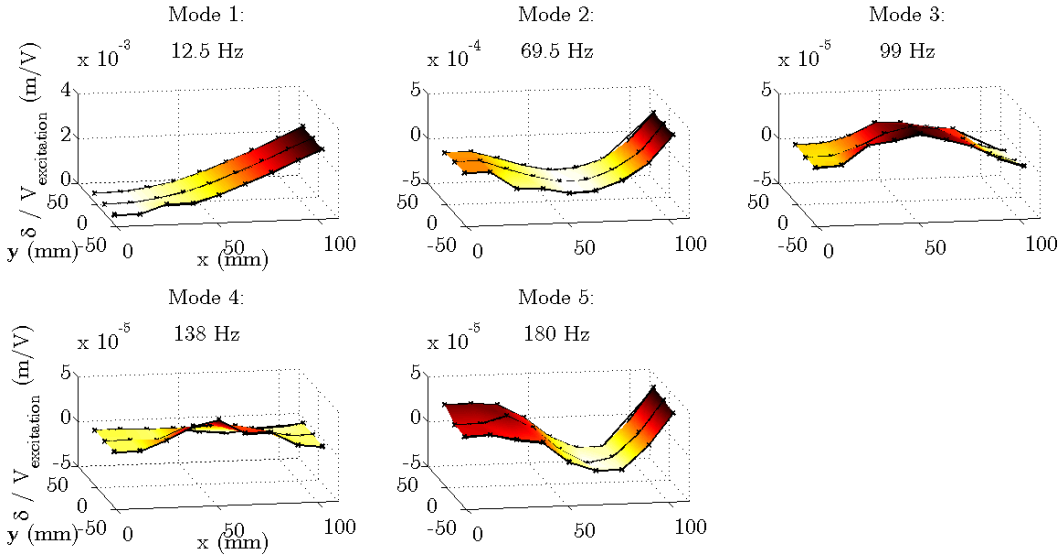

Figure C.4 Operational deflection shapes at measured natural frequencies

Examining the measured deflection shapes, the first mode around 12 Hz clearly captured the expected first monotonic mode for the cantilevered-like unimorph. The second mode at 70

Hz captured the expected second mode for the cantilevered-like configuration, but with much lower amplitude. The third, fourth and fifth modes showed much smaller deflections for the input voltage and began to show slight spanwise variations, possibly due to noise the measurement. Importantly, this test identified:

- The first mode of the Flexure Box occurred around 12 Hz and was characterized by monotonic actuation
- The structure of the Flexure Box was adequately described dynamically as a two-dimensional system disregarding spanwise variations
- The frequencies and operational deflection shapes of the first five modes of the Flexure Box aileron, which occurred below 200 Hz.

C.3. Modeling

C.3.1. Modeling Method

The modal investigation of the Flexure Box aileron in Section C.2 concluded that the Flexure Box aileron could be described by a two-dimensional model. Accordingly, the same corotational beam code utilized to experimentally evaluate the static deformation of the Flexure Box aileron under aerodynamic loads was also tested for its ability to capture its modal response.

The nonlinear geometric capabilities of the corotational beam code were not needed because the modal test from the previous section assumed small deflections. Thus, with the nonlinear geometry and aerodynamics removed, the mesh instead became a series of “space frames” (beams with extension/compression). Appropriate material stiffness and mass properties were assigned to the unimorph elements and flexure mechanisms as summarized in Table C.1. Lump masses were assumed for the thick plastic pieces at the top of the compliant mechanism and at the tip of the aileron. The location of the centroid, mass, and rotational inertia for the lumped masses were calculated from the geometry of the part designs using Solidworks. A summary of the mesh and lump mass locations was shown in Figure C.5 and their assumed values were described in Table C.1. and Table C.2.

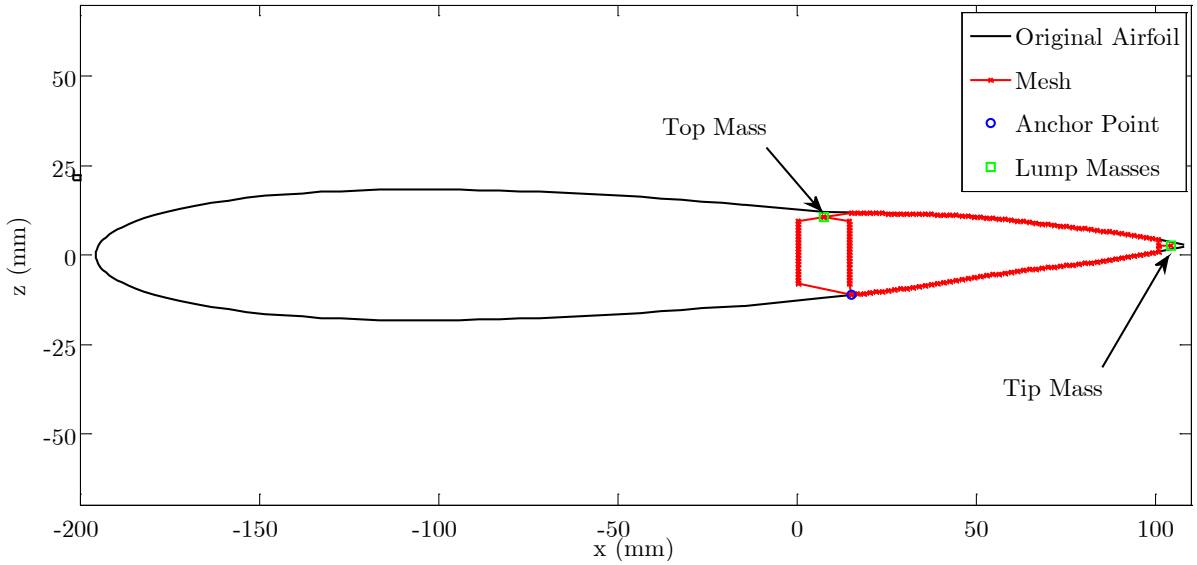

Figure C.5 Mesh overview

Table C.1 Assumed material properties

Material	Stiffness (GPa)	Density (kg/m^3)
Rigid Plastic (ABS)	2	1170
Tango Plus (Elastomer)	$9.2 \cdot 10^{-3}$	1170
Kapton	3	1420
PZT	60	7500
Stainless Steel	200	7800

Table C.2 Assumed lump mass values

Component	Mass (kg)	Inertia (kg m^2)
Top Lump Mass	$5 \cdot 10^{-3}$	$257 \cdot 10^{-9}$
Tip Lump Mass	$2 \cdot 10^{-3}$	$84 \cdot 10^{-9}$

C.3.2. Modeling Results

Utilizing the previously described model, the structural modes were calculated for an undamped, unloaded structure with no applied voltage by solving the eigenvalue problem:

$$M\omega^2 - K = 0 \tag{C.12}$$

where M was the global stiffness matrix, K was the global stiffness matrix, and ω was the vector of natural frequencies. The six smallest natural frequencies were compared with the experimental test from the previous section. The resultant eigenvectors (mode shapes) were normalized by the

mass matrix and plotted in Figure C.6. For comparison, the bottom surface of the plotted shapes was the surface investigated in the previous section.

As expected from the experimental results, the first calculated mode exhibited a monotonic deflection with a frequency at approximately 13 Hz, which was slightly higher than the experimental results. The second mode at 75 Hz exhibited decreased tip deflection, with a non-monotonic shape, similar to the experimental results. Both the third and fourth modes included in phase and out of phase vibration of the upper and lower unimorph surfaces. The natural frequencies for these mode shapes were compared with the experimental results in Table C.3.

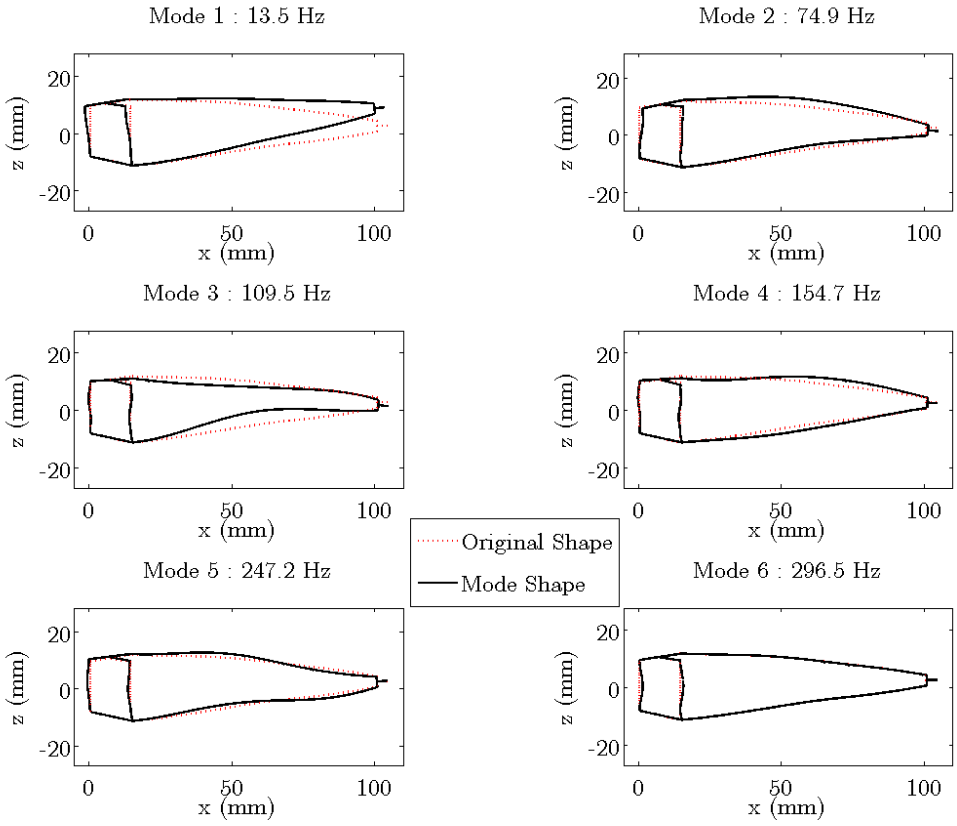

Figure C.6 Modeled mode shapes

Table C.3 Comparison of natural frequencies

Mode #	Experimental Frequency (Hz)	Modeled Frequency (Hz)	Error (%)
1	12.5	13.5	7.7 %
2	69.5	74.9	7.3 %
3	99	109	10 %
4	138	154	12 %
5	180	247	37 %

Notably, the first three calculated natural frequencies were within 10% error of experimentally measured values. Additionally, the third and fourth modes clarified that the vibration of the unimorphs with an effective pinning of the lumped masses diminished the expected tip vibration at higher frequencies. Thus the two-dimensional beam model was determined to be an adequate initial dynamic model of the Flexure Box aileron considering that the finite element mode included no damping, lumped mass modeling, and linear elasticity for the elastomeric elements. Higher fidelity modelling of these features was expected to decrease the stiffness of the overall system, potentially lowering the natural frequencies and narrowing the difference with the experimental values.

C.4. Summary

This initial modal analysis of the Flexure Box Aileron resulted in three conclusions. First, as expected from the spectral characterization, the lowest natural frequency of the Flexure Box aileron occurred near 10 Hz, specifically 12 Hz. Second, the structure could be described dynamically as two-dimensional due to its relatively large spanwise stiffness. Third, the structural mesh from the corotational beam model could approximately capture the modal response of the structure within 10% error of the first three natural modes, providing an initial dynamic model for future investigation and control design.

Appendix D
Extension of Relative Time Constant

D.1. Extension of relative time constant

The spectral characterization of the MFC-based actuator, the SMA-based actuator, and the hybrid SSMA actuator in Chapter 6 measured the relative time constant, which was normalized by the input period. Because the combined system and its constituent actuators had been modeled as first-order systems, the relative time constant was shown to be related to the first-order time constant, τ_∞, with:

$$\tau_r = \frac{\tau_\infty}{T}\left[1 - \ln\left(1 - e^{-T/2\tau_\infty} + e^{-T/2\tau_\infty + 1}\right)\right] \tag{D.1}$$

where the relative time constant, τ_r, was defined as the time that took the actuator to reach 63.2% (1-1/e) of its maximum variation in tip displacement, normalized by the square wave forcing period *T*.

Notably, this model assumed that the system could be described as

$$\frac{dX}{dt} + \frac{1}{\tau_\infty}X = f(t) \tag{D.2}$$

where *X* was the tip deflection, τ_∞ was the first-order time constant, and *f(t)* was an arbitrary forcing function, taken to be a square-wave for the spectral characterization in Chapter 0. Then for this assumed model of the system, the first-order time constant was assumed to remain constant over the entire tested frequency range of the spectral characterization. Then it was desired to investigate how the first order time constant varied with input frequency and how this could inform future experimental investigations and optimal control of these complex actuators.

This appendix then investigates the following questions:

- How do the first-order time constants from the spectral characterization measurements of the three actuation concepts (SMA, MFC, SSMA) vary with increasing frequency?
- How does the variation in time constants inform the expected response of the actuators under ideal sinusoidal tip-deflection tracking?
- How do these results impact the interpretation of the relative time constant?

D.1.1. Method for identifying variation in first order time constant

As noted in Chapter 6, the equivalent first-order time constant could be solved from the experimental measurements utilizing Equation (D.1). Using the mean values of the experimental relative time constants τ_r, the first order time constants τ_∞ were evaluated for the MFC-based actuator, the SMA-based actuator, and the hybrid SSMA actuator using a damped Newton search method.

The first-order time constant for an ideal first-order system was not expected to vary with increasing input frequency. Similarly, it was desired to project how the relative time constant would vary for an unchanging first-order time constant approximating an ideal first-order system. By measuring the first order time constant over an effectively-infinite input period, the expected variation in the relative time constant, τ_r, could then be calculated for a range of input frequencies with a constant τ_∞ utilizing Equation (D.1) directly. This expected "constant τ_∞ theory" provided insight as to how well the actuator was modeled by a first order system and how an ideal first order system with a similar time constant should perform.

Then, for each actuator, the calculated first-order time constant from the longest period sample in the spectral characterization test was used to calculate a baseline first order time constant. It was assumed that the period of the input square waves for this case was much longer than the time constants of the respective systems, symbolized by the near-zero relative time constants, i.e. $\tau_r << 0.5$, in Table D.1. Thus, these time constants were assumed to accurately capture the idealized baseline first-order time constant τ_0.

Table D.1 Baseline measurements

Actuation Method	Period of Input Square Wave	Baseline First-Order Time Constant, τ_0	Baseline Relative Time Constant, τ_r
SMA	200 s	3.08 s	$1.5 \cdot 10^{-2}$
MFC	10 s	0.077 s	$7.7 \cdot 10^{-3}$
SSMA	200 s	0.79 s	$3.9 \cdot 10^{-3}$

A comparison of how the measured relative time constant τ_r and calculated first order time constant τ_∞ varied with increasing input frequency is discussed in the following sections.

D.1.2. SMA Results

The SMA-driven hinge was the first actuation method analyzed for variations in the time constants with increasing input frequency. As seen in Figure D.1, the first-order time constants, τ_∞ , for the measured input frequencies remained small until approximately 0.2 Hz inputs when they began to decrease dramatically. At this frequency, the relative time constant had reached approximately 0.25, symbolizing that 50% of the half-period was spent reaching 63% of the total displacement. This result showed that the SMA actuator had begun to saturate at this input frequency.

The characterization also showed that from 0.002 Hz to 0.1 Hz, the first order time constant decreased by approximately 30% from the baseline value, τ_0. This measurement was not an error, but rather correctly captured the thermally driven nature of the SMA wires. Because the transformation of the SMA wires was driven by temperature, reducing the input period and as a result, the time that the opposing wire was heated, reduced the cooling time of the antagonistic wire. This reduced cooling time reduced the time then reduced the time required for the antagonistic wire to stretch the cooling wire and obtain its full stroke.

From these results, it was seen that the SMA was generally well-modeled by a first order system until the relative time constant reach approximately 0.25. As the actuator saturated, the relative time constant increased much more than expected by an ideal first-order system. Also, the spectral characterization was seen to capture other realistic constraints of the actuator that were not simulated by the first order model.

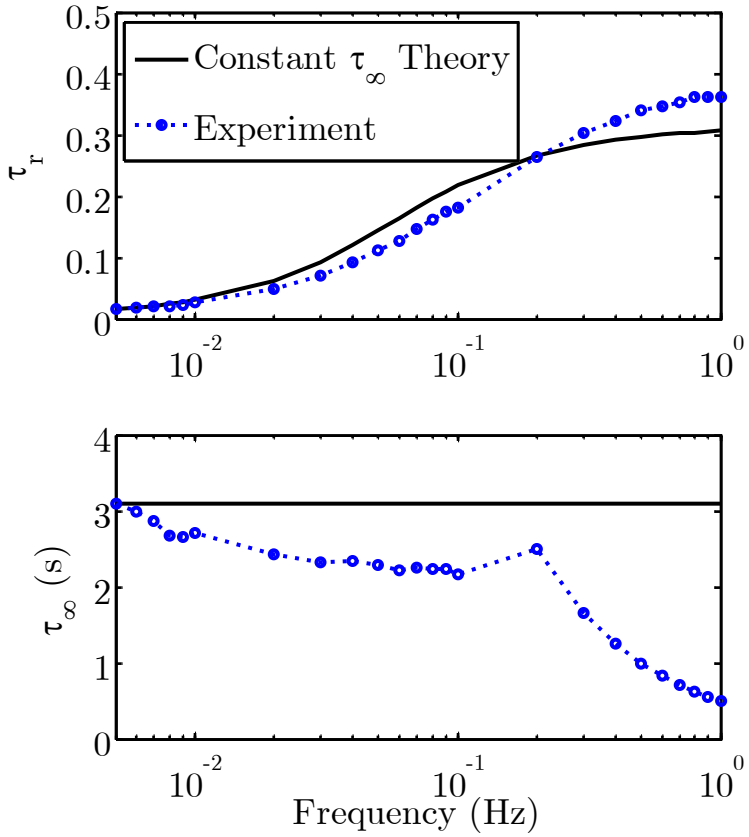

Figure D.1 Comparison of SMA actuator with idealized first-order system

D.1.3. MFC Results

The MFC-driven Flexure Box aileron was analyzed in a similar method, monitoring the variation in time constants with increasing input frequency. As seen in Figure D.2, the MFC followed the first order model much closer than the SMA until approximately 7 Hz when the previously-mentioned dynamic effects caused large variations in the measured relative time constant and the calculate first order time constant.

Again, the first order time constant showed a slight decrease of approximately 18% from its baseline value from approximately 0.1 Hz to 1 Hz. As mentioned previously, the calculated first-order time constant was sensitive to other non-modeled dynamic effects. In the case of the MFC, long-timescale creep from the elastomeric compliant mechanism and the MFCs themselves were observed. Thus, as the input period decreased, the total amplitude decreased as creep contributed less to the total amplitude of the response. Resultantly, the time required to

reach 63% of the maximum amplitude also decreased as the additional range due to creep was eliminated.

Although the dynamic effects above 5 Hz obscured the results, it was seen that the relative time constant showed good agreement with the ideal first-order results until approximately 0.25, similar to the SMA results.

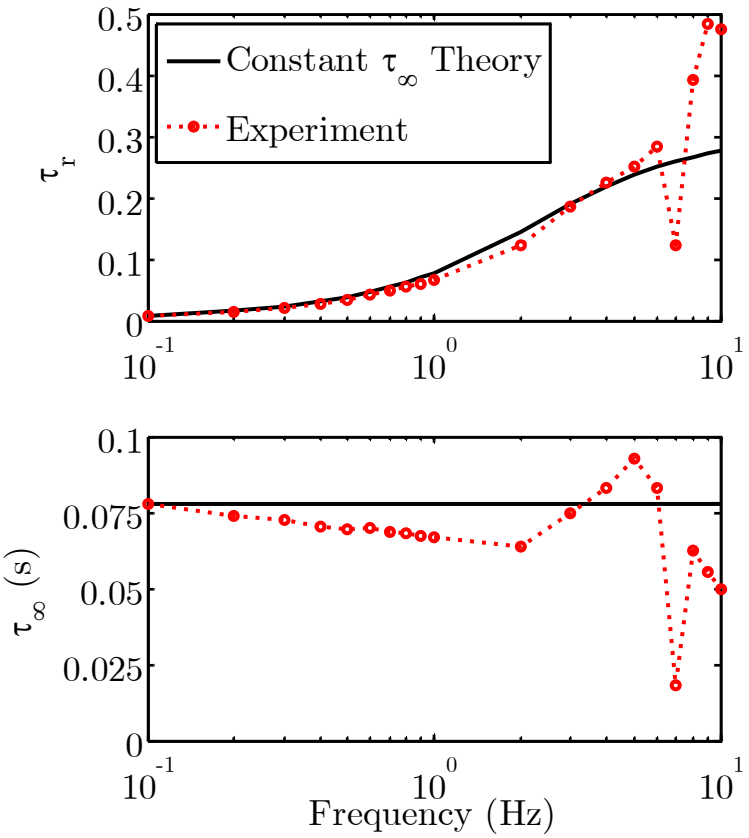

Figure D.2 Comparison of MFC actuator with idealized first-order system

D.1.4. SSMA Results

Finally, the combined hybrid SSMA actuation mechanism was analyzed for variations in from the assumed first order response, as seen in Figure D.3. From 0.005 Hz to 0.02 Hz, the SSMA only showed a 5% deviation in the calculated first-order time constant, showing good agreement with the first order system model. From 0.02 Hz to 0.1 Hz, the first-order time constant decreased by approximately 50% from the baseline value as the SMA actuator began to saturate and the system approached the time response of the MFC. By 0.7 Hz, the first order time constant of the SSMA had crossed the baseline value of the MFC, showing that at that frequency there was no appreciable contribution due to the SMA.

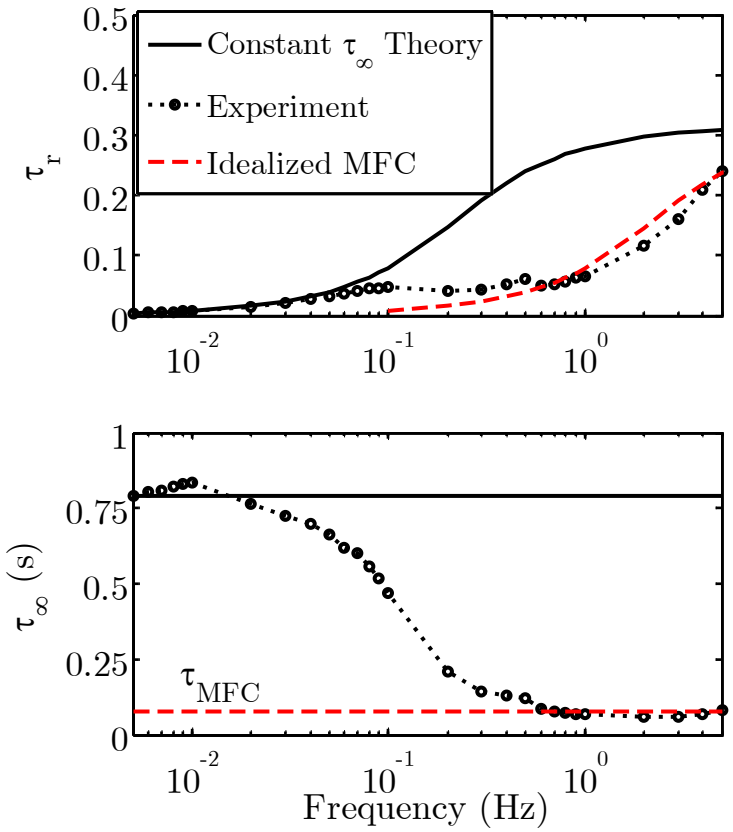

Figure D.3 Comparison of SSMA actuator with idealized first-order system

Examining the first order time constant, the deviation from the idealized first order system was not noticeable until approximately 0.1 Hz. This symbolized that although the first-order time constant was changing, the system was approximating a faster actuator for its given amplitude. Then, the system them maintained approximately the same relative time constant until it reached the response of the MFC at approximately 0.7 Hz and began to follow the response of the MFC.

This result also showed that once the SMA began to saturate, the first-order theory assumption for the combined system was no longer valid. This was explained as the sum of two exponential responses was not in itself an exponential response. Then as the displacement response and time constant of the SMA subsystem saturated, the total system response began to mirror the MFC actuator's response. Still, the region between 0.1 Hz and 0.7 Hz showed improvement due to the inclusion of the SMA actuator, as characterized by the larger amplitudes from Chapter 0. Additionally, the relative time constant was shown to provide a valuable metric for evaluating the response of this hybrid actuation system by including multiple timescales and responses on the same plot.

D.2. Expected response under ideal control

After calculating the first order time constants, the theoretical performance of the actuators under ideal control was evaluated. Specifically, it was of interest to calculate the expected response of the actuators while tracking a sinusoidal tip displacement. The sine wave would provide further information about the degradation of the various actuators and how this related to the relative time constant while better informing future controller design.

Assuming that for very low frequencies the previous square-wave could be approximated as step response of the form:

$$\frac{dX}{dt} + \frac{1}{\tau_0} X = f(t) \qquad \text{where} \quad f(t) = \begin{cases} 0 \ \text{ for } \ t < 0 \\ \dfrac{\Delta_0}{\tau_0} \ \text{ for } t \geq 0 \end{cases} \tag{D.3}$$

where X was the tip displacement, Δ_0 was the baseline amplitude of the tip displacement, and τ_0 was the baseline first-order time constant as measured in the spectral characterization test.

Then a sinusoidal forcing function of a similar magnitude was assumed:

$$f(t) = \frac{\Delta_0}{\tau_0}\sin(\omega t) \qquad \text{where} \qquad \omega = \frac{2\pi}{T} \tag{D.4}$$

that would result in the same maximum tip displacement as the input period, approached infinity. This assumed forcing function then provided the expected system response of an optimal controller on the actuation system while tracking a sine wave. This permitted the system to be analyzed without actually creating this controller that would account for hysteresis and creep.

Then the magnitude of the tip displacement for a sine-wave at a given frequency, ω, relative to the maximum tip displacement over an infinite timescale was given by:

$$\frac{\Delta}{\Delta_0} = \frac{1}{\tau_0}\frac{\tau}{\sqrt{1+(\omega\tau)^2}} \tag{D.5}$$

where Δ was the expected amplitude of the response. Then the frequency, in Hz, that the actuation system would fall to half-power was given by:

$$f_{-3dB} = 1 / (2\pi\tau_0) \tag{D.6}$$

where the magnitude of the response was equal to $1/\sqrt{2}$ or approximately 70% of its original value.

Figure D.4 through Figure D.6 showed the response for the three actuation systems with the first order time constants, experimentally-calculated for varying frequency. Responses were also included for the response of a constant τ_∞ system, and the amplitudes for similar analysis from the square-wave characterization.

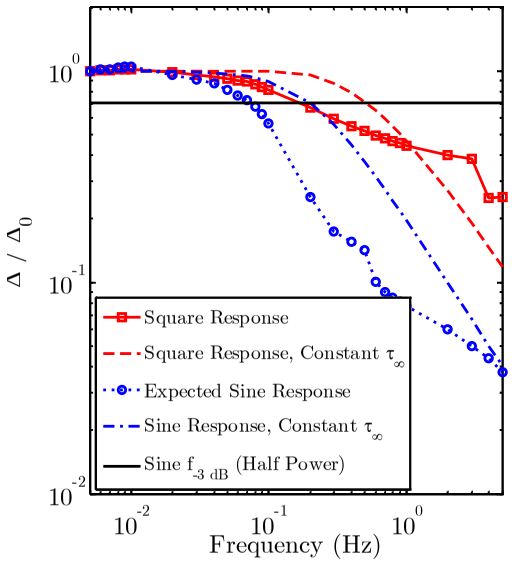

Figure D.6 Predicted response of SSMA to square wave and sine waves from experiments and as expected for an unchanging first-order time constant

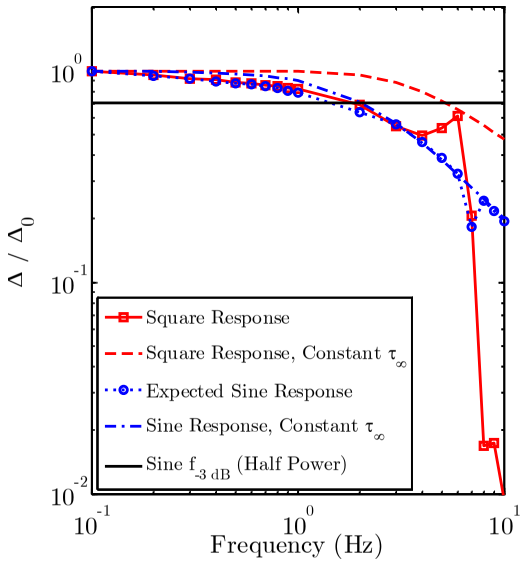

Figure D.5 Predicted response of MFC to square wave and sine waves from experiments and as expected for an unchanging first-order time constant

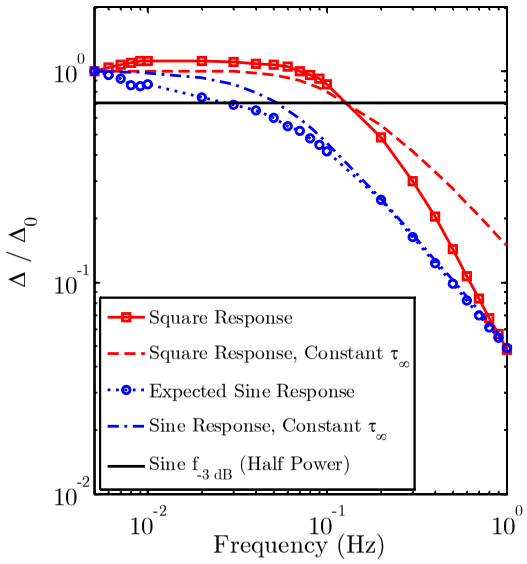

Figure D.4 Predicted response of SMA to square wave and sine waves from experiments and as expected for an unchanging first-order time constant

The frequencies of interest identified in Section D.1 were investigated to identify whether the sinusoidal response could further inform the meaning of the relative time constant with respect to controlled response amplitude. Beginning with the SMA, previous results showed that the system was well-modeled as a first order system for square-wave inputs until approximately 0.2 Hz. Examining the expected sinusoidal response, the half-power response was achieved between approximately 0.03 Hz and 0.05 Hz, which corresponded to relative time constants of 0.07 and 0.144 for the measured τ_∞ and ideal τ_0 responses, respectively. Performing a similar evaluation for the MFC response, the half-power metric also occurred between approximately 1 Hz and 2 Hz, which corresponded to a relative time constant between approximately 0.06 and 0.14.

Finally, the SSMA experienced its half-power metric at 0.08 Hz and 0.2 Hz for the measured and ideal cases. These corresponded to relative time constants of approximately 0.05 and 0.14 respectively. A relationship between the half-power metric and the relative time constant was then assumed from this empirical evidence: for a relative time constant of approximately 0.1, the expected work output of the actuators in tracking a sine wave with idealized control would be reduced by half. Although additional research remains to correlate these parameters, this was considered a general guideline for characterizing the reduction in output power with increasing frequency for a first-order-like actuator.

From these results, the ability of the systems to track a sine-wave at varying frequencies relative to their maximum displacements was characterized. The SSMA did not dramatically increase the frequency of the measured half-power metric. This result was expected as no additional power or dynamic effects were modeled in this system. Thus the characterization showed that the benefits of the SSMA would be limited largely to the MFCs total range as the SMA actuator degraded.

D.3. Summary

In summary, the results found that the SMA and MFC actuators could be well-modeled as a first-order system. For the SMA, the spectral characterization showed good agreement with an ideal first-order actuator until approximately 0.2 Hz. A 30% reduction in the calculated first order time constant was used to characterize the effect of decreased heating time of the SMA wires. The MFC showed good agreement with a first-order actuator until approximately 5 Hz

where dynamic effects became significant. An 18% decrease in calculated first-order time constant also characterized the beneficial effect of creep on the MFC over long timescales. The combined SSMA was also seen to be characterized by a first order system until approximately 0.1 Hz by the relative time constant metric and 0.02 Hz as calculated by deviation from the baseline first-order time constant.

The relative time constant was then seen to be a valuable experimental tool for identifying the performance of the SSMA hybrid actuator system. The expected performance while tracking an idealized sinusoidal tip deflection was characterized for varying frequencies without designing the necessary controller by utilizing the calculated first-order time constants. Although the hybrid system improved the overall time constant, the output power was not significantly changed. Thus, the deflections were determined to be limited to the achievable range of the MFC as the SMA began to degrade. Finally, from these results, an empirical bound for the relative time constant of approximately 0.1 was established for characterizing the half-power idealized sinusoidal response from the spectral characterization method.

Appendix E
Uncertainty in Performance Metrics

E.1. Discussion on Uncertainty

Uncertainty is a valuable metric in assessing the validity of experimental results and the conclusions drawn from them. In this dissertation, the results were primarily reported via changes in nondimensional aerodynamic forces or control derivatives which were simply these nondimensional forces divided by a distance measurement related to the trailing edge displacement. Precise quantification of the error associated with these metrics within the complex design-spaces would require additional testing utilizing design of experiments or models of the responses of the respective systems. Considering that the impact of this dissertation was on the general concepts, structures and methodologies for morphing gains, the reported trends were presented as guidelines of what could be expected for a realistic application. Instead, a general summary of the calibration methodologies and maximum errors for the relevant equipment utilized in these experiments is described in the following sections.

E.2. Calibration of tip displacement

The primary experimental setup for measuring the tip displacement was shown previously in Figure 3.7. By placing the morphing aileron on a known mount with a fixed chordwise distance for a laser displacement sensor to measure out-of-plane displacement, the calibration of the morphing aileron could be assessed automatically by stepping through the range of applied voltages. The scale within the image allowed the laser displacement data to be matched with calibrated vertical tip displacement extracted by Image J. Thus, a linear mapping between the image and the laser displacement sensor provided automated, precise calibration of the tip displacement of the various morphing ailerons to within 0.25 mm, which was within the variation of the surface roughness of the bimorph due to the addition of the MFC on the outer

surface. When a smooth surface was used, the positioning measurement error was within 0.1 mm.

The largest source of error for the tip displacement was the embedded sensor. As seen in Figure 3.9, the embedded sensor, although calibrated, did not result in the complete elimination of hysteresis associated with tip displacement. This could have been due to electrical noise in the system due to high voltage leakage into the sensor circuit. Still, using only the applied voltage to estimate the state of the morphing aileron was seen in Figure 3.9 to result in maximum positioning errors of approximately 1.1 cm out of a total range of approximately 3.4 cm, or 32% relative error. Including aeroelastic effects or elastic effects between the active sections in this calculation would make this error prohibitively large, easily up to 50% of the total range of the morphing aileron. Including the embedded sensor reduced the maximum positioning error to approximately 2.5 mm, or 7.3% error, regardless of aerodynamic or elastic loads. It is these positioning errors combined with asymmetric flap design that was expected to be the main source of the asymmetry reported for the adaptive drag comparison in Section 5.3.2.

E.3. Two-dimensional wind tunnel setup

Although the primary source of error in the experiments was the positioning of the morphing ailerons, other relevant factors that impacted the experiments were quantified.

The endplates for the reduced aspect aileron from Chapter 3 were seen to have a noticeable effect on the ability of the morphing aileron to affect the aerodynamic loading. The physical explanation for this effect was that the boundary layer forming from the endplates was reducing the effective span of the test article exposed to the flow. The investigation in Section 3.2 attempted to assess the effect of the endplates as the aspect ratio was increased. Figure 3.23 provided a comparison of the experimentally-measured lift curve slope with the reported results from [106] to provide an assessment of the effect of the endplates on the baseline drag. Clearly, as the aspect ratio increased, the baseline drag asymptotically approached a value that was much higher than was expected for a clean wing. Still, the metric of interest was the change in forces, which was well characterized in Section 3.3.

The aerodynamic forces were measured via a load balance constructed with three load cells, as shown in Figure E.1.

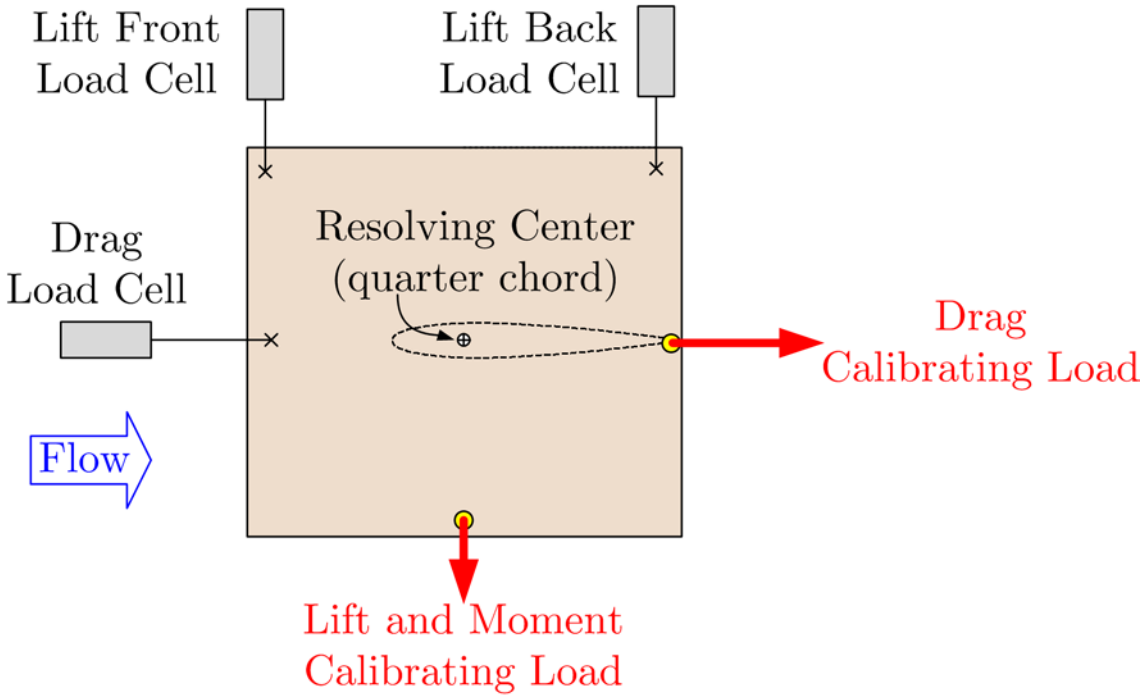

Figure E.1 Two-dimensional force-balance calibration diagram

The load balance had one load cell operating in the drag direction and two load cells operating in the lift direction to measure both lift and pitching moment. The drag load cell was calibrated by hanging calibrated weights in-line with the drag load cell via a pulley system. The lift load cells were calibrated by hanging calibrated weights via a pulley system in line with the resolving center which was in-line with the quarter-chord of the wing and equidistant from both the "front" and "back" lift load cells. A typical result of the calibration is shown in Figure E.2. As can be seen in the residual error of the linear fits, all three load cells exhibited linearity and were only limited by the voltage limits accepted by the data acquisition unit used.

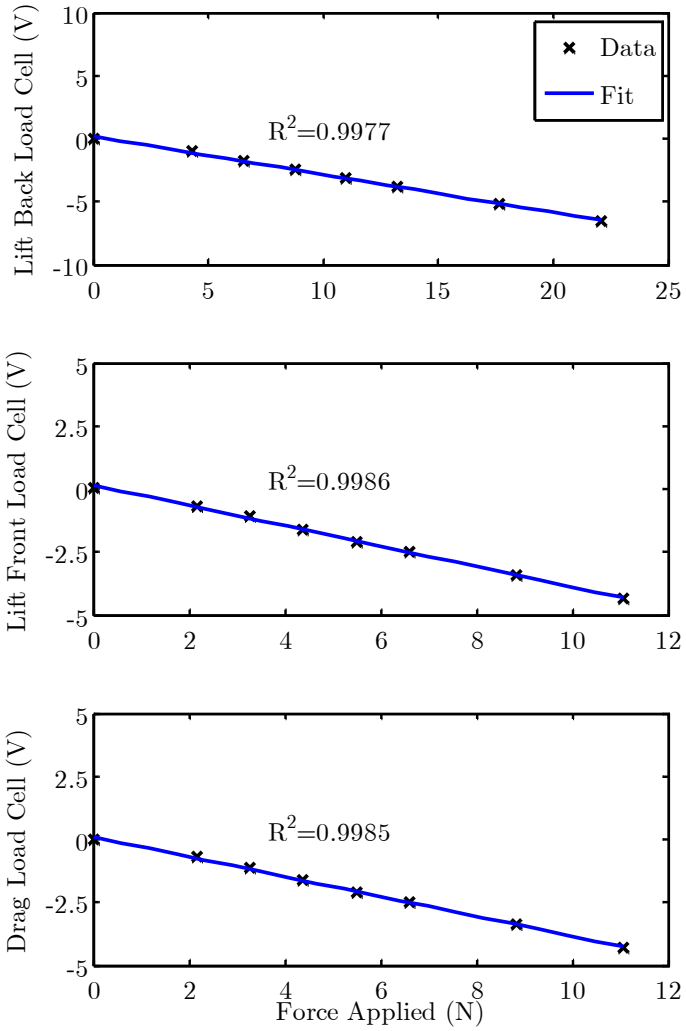

Figure E.2 Typical calibration of two-dimensional force balance

The angle of attack was controlled by a stepper motor that drove a worm-gear connected to the rotary table which set the angle of attack about the quarter chord. The positioning error of this combination of controls was limited by the resolution of the stepper motor which was 1/80th of a degree. The dynamic pressure was measured via a pitot tube connected to a dynamic pressure transducer (Omega PX2650-2D5V) which was reported to have errors in linearity and offset within 1%. The same pressure transducer was used for the three-dimensional wind tunnel setup described in the following section.

E.4. Three-dimensional wind tunnel setup

The load cell for the three dimensional force balance was not calibrated about the measurement center, namely the root quarter-chord of the wing, because the load balance had been built to generally resolve about a point in the center of the wind tunnel, as seen in Figure E.3. The lift and drag load cells were decoupled from moments about this point due to the lengths of the arms used and the locations of the load cell.

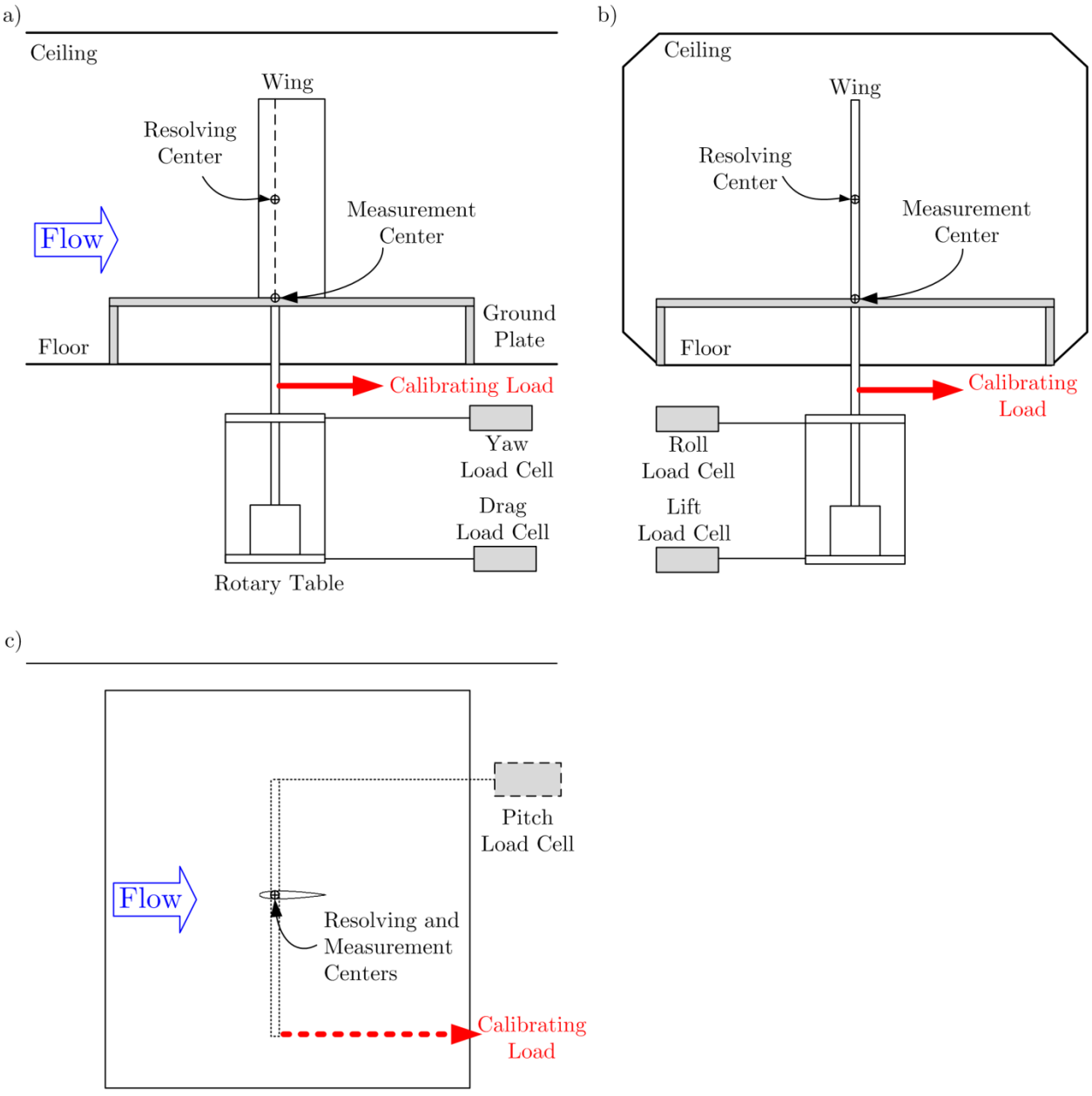

Figure E.3 Description of three-dimensional force balance with a) side b) front and c) top view

Thus, to appropriately calibrate all of the load cells, several loading scenarios were used. First, a set of proof masses outside the wind tunnel were used to apply a known moment to the drag and yawing moment load cells, acquiring fits for the data about the resolving center. Then, a similar procedure was utilized in the lift direction to find fits for the lift and rolling moment about the resolving center. Finally, a loading test was using to fit the pitching moment about the resolving center. A summary of the typical fits from the plot are shown in Figure E.4. As can be seen by the error in the fits, all of the load cells showed good fits about the calibration conditions.

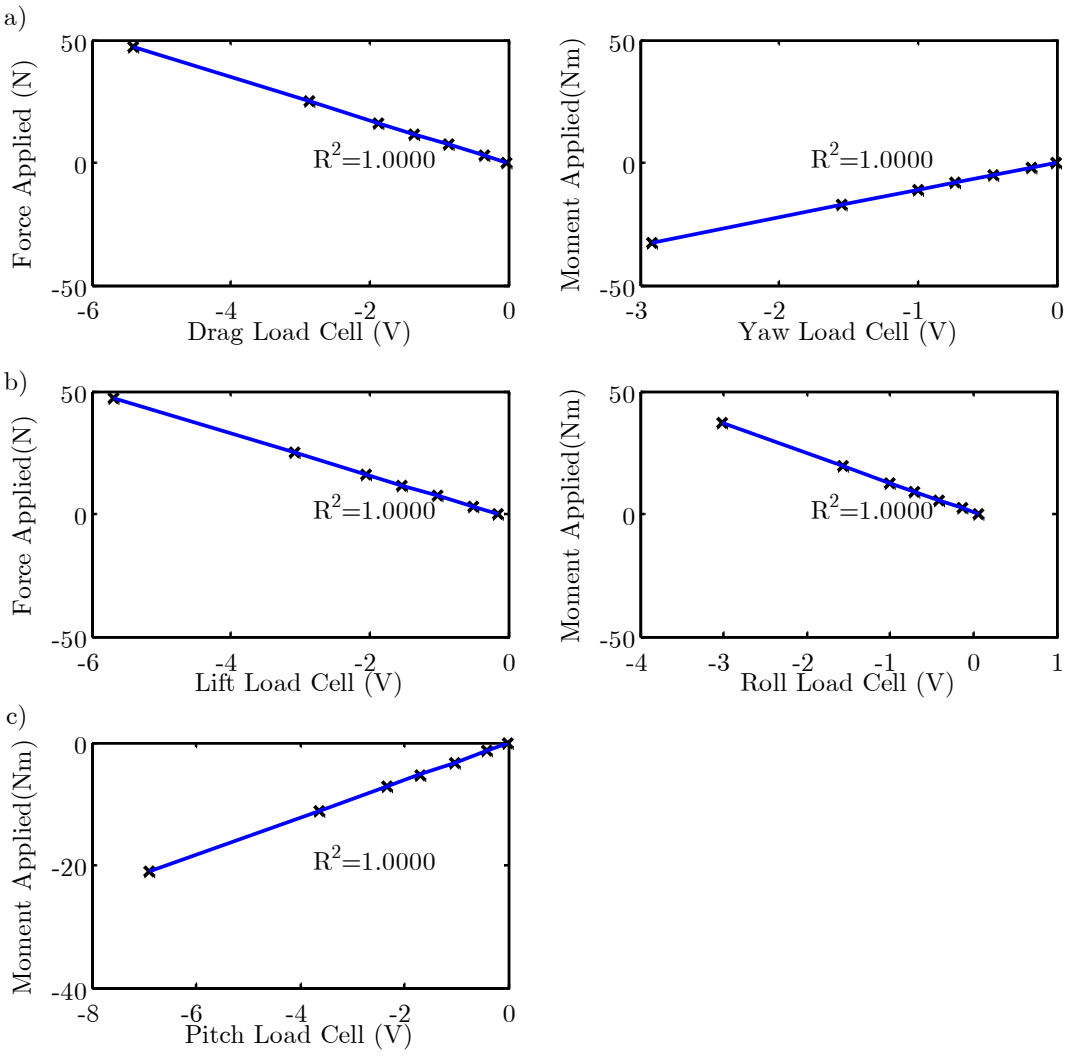

Figure E.4 Representative calibration of three-dimensional force balance for a) drag and yaw b) lift and roll and c) pitch

To measure the forces about the root quarter chord rather than the resolving center, the uncoupled forces and moments about the resolving center (RC) were relocated to the measurement center (MC) such that only roll was coupled with another measurement due to the orthogonal construction of the wind tunnel balance. Due to the highly linear response of the load cells, the error due to this coupling was also determined to be negligible.

The rotary table for the experimental setup was controlled by a custom angular displacement sensor that controlled a worm-gear driven motor. Although previously discussed in Section 5.2.2.1 and shown in Figure 5.3, the fit for the angular displacement sensor follows to aid in uncertainty quantification. The in-plane distance between the laser displacement sensors was measured with a ruler. Then the difference between the out-of-plane displacement values was calculated using the inverse tangent of the difference of the displacement measurements divided by the in-plane distance between them. By utilizing a protractor affixed to the rotary table, the travel of a known point on the load balance could be tracked and calibrated against the protractor to calibrate the offset and measure the error associated with using the laser displacement sensors. The fit from the calibration and resultant positioning error in angle of attack is shown in Figure E.5. The resultant measurement accrues less than 0.2 degrees of error in approximately 60 degrees of travel, with the minimum error occurring at the origin.

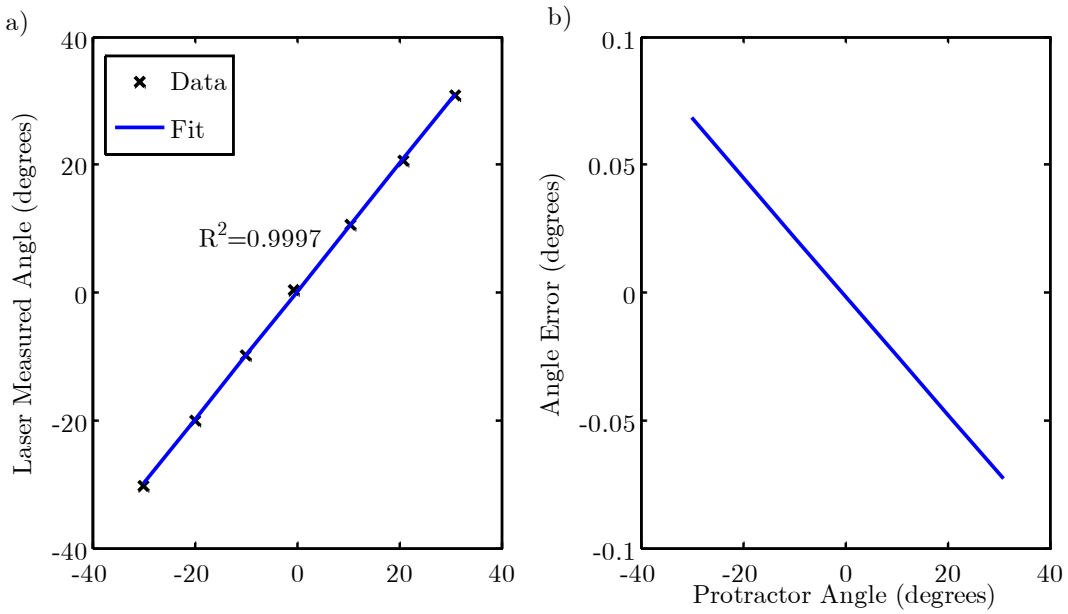

Figure E.5 a) Calibration and b) resultant error of angular displacement sensor comprised of two laser displacement sensors

E.5. Summary

In summary, the largest source of error in the experiments was the positioning of the morphing trailing edges. Although the embedded sensor reduced the maximum positioning error to within 10% of the total range, additional refinements would aid measurements even more. Analysis of the other relevant metrics while measuring control derivatives such as localized pressure distributions would further aid in quantifying the relevant error when matching flight conditions.

Bibliography

[1] "FAA Aerospace Forecast Fiscal Years 2012-2032 ," <https://www.faa.gov/about/office_org/headquarters_offices/apl/aviation_forecasts/aerospace_forecasts/2012-2032/> (8 July 2014).

[2] "Press Release – FAA Approves First Commercial UAS Flights over Land," <http://www.faa.gov/news/press_releases/news_story.cfm?newsId=16354> (7 July 2014).

[3] Smith, C.J., and Taylor, N.W., "Controlling UAS flight operations in a mixed-mode environment today," *Integrated Communications, Navigation and Surveillance Conference, ICNS* (2013) [DOI:10.1109/ICNSurv.2013.6548543].

[4] Gimenes, R.A.V., Vismari, L.F., Avelino, V.F., Camargo Jr., J.B., De Almeida Jr., J.R., and Cugnasca, P.S., "Guidelines for the integration of autonomous UAS into the global ATM," *Journal of Intelligent and Robotic Systems: Theory and Applications* **74**(1-2), 465–478 (2014).

[5] Molinari, G., Quack, M., Dmitriev, V., Morari, M., Jenny, P., and Ermanni, P., "Aero-Structural Optimization of Morphing Airfoils for Adaptive Wings," *Journal of Intelligent Material Systems and Structures* **22**(10), 1075–1089, SAGE Publications (2011) [DOI:10.1177/1045389X11414089].

[6] Barbarino, S., Bilgen, O., Ajaj, R.M., Friswell, M.I., and Inman, D.J., "A Review of Morphing Aircraft," *Journal of Intelligent Material Systems and Structures* **22**(9), 823–877, SAGE Publications (2011) [DOI:10.1177/1045389X11414084].

[7] Rodriguez, A.R., "Morphing aircraft technology survey," *Collection of Technical Papers - 45th AIAA Aerospace Sciences Meeting* **21**, 15064–15079 (2007) [DOI:10.2514/6.2007-1258].

[8] McGowan, A.-M.R., Washburn, A.E., Horta, L.G., Bryant, R.G., Cox, D.E., Siochi, E.J., Padula, S.L., and Holloway, N.M., "Recent results from NASA's morphing project," in *SPIE's 9th Annual International Symposium on Smart Structures and Materials*, pp. 97–111 (2002) [DOI:10.1117/12.475056].

[9] Weisshaar, T.A., “Morphing aircraft systems: Historical perspectives and future challenges,” *Journal of Aircraft* **50**(2), 337–353 (2013) [DOI:10.2514/1.C031456].

[10] De Breuker, R., Abdalla, M.M., and Gürdal, Z., “A Generic Morphing Wing Analysis and Design Framework,” *Journal of Intelligent Material Systems and Structures* **22**(10), 1025–1039, SAGE Publications (2011) [DOI:10.1177/1045389X11414958].

[11] Valasek, J., *Morphing Aerospace Vehicles and Structures*, Wiley (2012) [DOI:10.1002/9781119964032.ch1].

[12] Gilbert, W.W., “Mission adaptive wing system for tactical aircraft,” *Journal of Aircraft* **18**(7), 597–602 (1981) [DOI:10.2514/3.57533].

[13] Parks, S., “Pilot report- AFTI F-111,” *Air Force Magazine* **71**, 82–84 (1988).

[14] Wlezien, R.W., Horner, G.C., McGowan, A.-M.R., Padula, S.L., Scott, M.A., Silcox, R.J., and Harrison, J.S., “Aircraft Morphing program,” *Proc. SPIE* **3326**, 176–187 (1998) [DOI:10.1117/12.310633].

[15] Wlezien, R.W., Horner, G.C., McGowan, A.-M.R., Padula, S.L., Scott, M.A., Silcox, R.J., and Harrison, J.S., “Aircraft morphing program,” in *5th Annual International Symposium on Smart Structures and Materials*, pp. 176–187 (1998) [DOI:10.1117/12.310633].

[16] McGowan, A.-M.R., Horta, L.G., Harrison, J.S., and Raney, D.L., “Research activities within NASA’s morphing program” (2000).

[17] Kudva, J., “Overview of the DARPA smart wing project,” *Journal of Intelligent Material Systems and Structures* **15**(4), 261, SAGE Publications (2004) [DOI:10.1177/1045389X04042796].

[18] Kudva, J.N., Martin, C.A., Scherer, L.B., Jardine, A.P., McGowan, A.-M.R., Lake, R.C., Sendeckyj, G.P., and Sanders, B.P., “Overview of the DARPA/AFRL/NASA Smart Wing program,” *Proc. SPIE* **3674**, 230–236 (1999) [DOI:10.1117/12.351561].

[19] Scherer, L.B., Martin, C.A., Sanders, B.P., West, M.N., Pinkerton-Florance, J.L., Wieseman, C.D., Burner, A.W., and Fleming, G.A., “DARPA/AFRL Smart Wing Phase 2 wind tunnel test results,” *Proc. SPIE* **4698**, 64–75 (2002) [DOI:10.1117/12.475104].

[20] Sanders, B., Cowan, D., and Scherer, L., “Aerodynamic Performance of the Smart Wing Control Effectors,” *Journal of Intelligent Material Systems and Structures* **15**(4), 293, SAGE Publications (2004) [DOI:10.1177/1045389X04042799].

[21] Nguyen, N., and Ting, E., “Flutter analysis of mission-adaptive wing with Variable Camber Continuous Trailing Edge Flap,” *55th AIAA/ASMe/ASCE/AHS/SC Structures,*

Structural Dynamics, and Materials Conference (2014) [DOI:10.2514/6.2014-0839].

[22] Bowman, J., Sanders, B., Cannon, B., Kudva, J., Joshi, S., and Weisshaar, T., "Development of next generation morphing aircraft structures," *Collection of Technical Papers - AIAA/ASME/ASCE/AHS/ASC Structures, Structural Dynamics and Materials Conference* **1**, 349–358 (2007) [DOI:10.2514/6.2007-1730].

[23] Love, M.H., Zink, P.S., Stroud, R.L., Bye, D.R., and Chase, C., "Impact of actuation concepts on morphing aircraft structures," *Collection of Technical Papers - AIAA/ASME/ASCE/AHS/ASC Structures, Structural Dynamics and Materials Conference* **3**, 2355–2366 (2004) [DOI:10.2514/6.2004-1724].

[24] Urnes Sr, J., Nguyen, N.T., and Dykman, J., "Development of Variable Camber Continuous Trailing Edge Flap System" (2012).

[25] Nguyen, N., and Urnes Sr., J., "Aeroelastic modeling of elastically shaped aircraft concept via wing shaping control for drag reduction," *AIAA Atmospheric Flight Mechanics Conference* (2012) [DOI:10.2514/6.2012-4642].

[26] Ippolito, C., Nguyen, N., Totah, J., Trinh, K., and Ting, E., "Initial assessment of a Variable-Camber Continuous Trailing-Edge Flap system on a rigid wing for drag reduction in subsonic cruise," *AIAA Infotech at Aerospace (I at A) Conference* (2013) [DOI:10.2514/6.2013-5143].

[27] Swei, S.S.-M., and Nguyen, N., "Aeroelastic wing shaping control subject to actuation constraints," *55th AIAA/ASME/ASCE/AHS/SC Structures, Structural Dynamics, and Materials Conference* (2014) [DOI:10.2514/6.2014-1041].

[28] Nguyen, N., Ting, E., and Trinh, K., "Flight dynamic modeling and stability analysis of flexible wing generic transport aircraft," *55th AIAA/ASMe/ASCE/AHS/SC Structures, Structural Dynamics, and Materials Conference* (2014) [DOI:10.2514/6.2014-1040].

[29] Urnes, J.M., Morris Sr., C., Sheahan, J., Dykman, J., and Clingman, D., "Control system design for a variable camber continuous trailing edge flap system on an elastic wing," *55th AIAA/ASME/ASCE/AHS/SC Structures, Structural Dynamics, and Materials Conference* (2014) [DOI:10.2514/6.2014-0835].

[30] Hutcheson, F.V., Brooks, T.F., and Humphreys Jr., W.M., "Noise radiation from a continuous mold-line link flap configuration," *International Journal of Aeroacoustics* **10**(5-6), 565–588 (2011) [DOI:10.1260/1475-472X.10.5-6.565].

[31] Hutcheson, F.V., Brooks, T.F., and Humphreys Jr., W.M., "Noise radiation from a continuous mold-line link flap configuration," *International Journal of Aeroacoustics* **11**(5-6), 531–554 (2012) [DOI:10.1260/1475-472X.11.5-6.531].

[32] Hetrick, J.A., Osborn, R.F., Kota, S., Flick, P.M., and Paul, D.B., "Flight testing of Mission Adaptive Compliant Wing," *Collection of Technical Papers - AIAA/ASME/ASCE/AHS/ASC Structures, Structural Dynamics and Materials Conference* **1**, 92–109 (2007) [DOI:10.2514/6.2007-1709].

[33] Lucia, D.J., "The SensorCraft configurations: A non-linear AeroServoElastic challenge for aviation," *Collection of Technical Papers - AIAA/ASME/ASCE/AHS/ASC Structures, Structural Dynamics and Materials Conference* **3**, 1768–1774 (2005) [DOI:10.2514/6.2005-1943].

[34] Kota, S., Osborn, R., Ervin, G., Maric, D., Flick, P., and Paul, D., "Mission adaptive compliant wing-design, fabrication and flight test," *Morphing Vehicles, number RTO-MP-AVT-168-18 in. NATO Research and Technology Organization* (2009).

[35] Lyu, Z., and Martins, J.R.R.A., "Aerodynamic Shape Optimization of an Adaptive Morphing Trailing Edge Wing," *Proceedings of the 15th AIAA/ISSMO Multidisciplinary Analysis and Optimization Conference*, Atlanta, GA (2014) [DOI:10.2514/6.2014-3275].

[36] Kennedy, G.J., and Martins, J.R.R.A., "An Adjoint-based Derivative Evaluation Method for Time-dependent Aeroelastic Optimization of Flexible Aircraft," *Proceedings of the 54th AIAA/ASME/ASCE/AHS/ASC Structures, Structural Dynamics, and Materials Conference*, Boston, MA (2013) [DOI:10.2514/6.2013-1530].

[37] Kenway, G.K.W., Kennedy, G.J., and Martins, J.R.R.A., "Aerostructural optimization of the Common Research Model configuration," *15th AIAA/ISSMO Multidisciplinary Analysis and Optimization Conference*, Atlanta, GA (2014) [DOI:10.2514/6.2014-3274].

[38] Lachenal, X., Daynes, S., and Weaver, P.M., "Review of morphing concepts and materials for wind turbine blade applications," *Wind Energy*, John Wiley & Sons, Ltd (2012) [DOI:10.1002/we.531].

[39] Barlas, T.K., and van Kuik, G.A.M., "Review of state of the art in smart rotor control research for wind turbines ," *Progress in Aerospace Sciences* **46**(1), 1 – 27 (2010) [DOI:10.1016/j.paerosci.2009.08.002].

[40] Van Wingerden, J.W., Hulskamp, A.W., Barlas, T., Marrant, B., Van Kuik, G.A.M., Molenaar, D.-P., and Verhaegen, M., "On the proof of concept of a 'smart' wind turbine rotor blade for load alleviation," *Wind Energy* **11**(3), 265–280 (2008) [DOI:10.1002/we.264].

[41] Daynes, S., and Weaver, P.M., "Design and testing of a deformable wind turbine blade control surface," *Smart Materials and Structures* **21**(10) (2012) [DOI:10.1088/0964-1726/21/10/105019].

[42] Sofla, A.Y.N., Meguid, S.A., Tan, K.T., and Yeo, W.K., "Shape morphing of aircraft wing: Status and challenges ," *Materials & Design* **31**(3), 1284 – 1292 (2010)

[DOI:10.1016/j.matdes.2009.09.011].

[43] Galantai, V., Sofla, A., Meguid, S., Tan, K., and Yeo, W., "Bio-inspired wing morphing for unmanned aerial vehicles using intelligent materials," *International Journal of Mechanics and Materials in Design* **8**(1), 71–79, Springer Netherlands (2012) [DOI:10.1007/s10999-011-9176-0].

[44] Lagoudas, D.C., *Shape Memory Alloys: Modeling and Engineering Applications*, Springer (2008).

[45] Brinson, L.C., "One-dimensional constitutive behavior of shape memory alloys: Thermomechanical derivation with non-constant material functions and redefined martensite internal variable," *Journal of Intelligent Material Systems and Structures* **4**(2), 229–242 (1993) [DOI:10.1177/1045389X9300400213].

[46] Kim, J.T., Kim, C., and Lee, S.R., "Smart composite shell structures with shape memory alloy wires and thin foils," *Proceedings of SPIE - The International Society for Optical Engineering* **5649**(PART 2), 684–691 (2005) [DOI: 10.1117/12.582354].

[47] Roh, J.H.K.K.S.L.I., "Shape adaptive airfoil actuated by a shape memory alloy and its aerodynamic characteristics," *Mechanics of Advanced Materials and Structures* **16**(3), 260–274 (2009) [DOI:10.1080/15376490902746996].

[48] Kang, W.-R., Kim, E.-H., Jeong, M.-S., Lee, I., and Ahn, S.-M., "Morphing wing mechanism using an SMA wire actuator," *International Journal of Aeronautical and Space Sciences* **13**(1), 58 – 63, #635-4, YEOGSAM-DONG, KANGNAM-KU, SEOUL, 135-703, Korea, Republic of (2012) [DOI:10.5139/IJASS.2012.13.1.58].

[49] Barbarino, S., Pecora, R., Lecce, L., Concilio, A., Ameduri, S., and Calvi, E., "A novel SMA-based concept for airfoil structural morphing," *Journal of Materials Engineering and Performance* **18**(5-6), 696–705 (2009) [DOI:10.1007/s11665-009-9356-3].

[50] Elzey, D.M., Sofia, A.Y.N., and Wadley, H.N.G., "A shape memory-based multifunctional structural actuator panel," *International Journal of Solids and Structures* **42**(7), 1943–1955 (2005) [DOI:10.1016/j.ijsolstr.2004.05.034].

[51] Faria, C.T., De Marqui Jr., C., Inman, D.J., and Lopes Jr., V., "Nonlinear dynamic model and simulation of morphing wing profile actuated by shape memory alloys," *Conference Proceedings of the Society for Experimental Mechanics Series* **3**, 21–28 (2012) [DOI:10.1007/978-1-4614-2416-1_2].

[52] Lendlein, A., and Kelch, S., "Shape-memory polymers," *Angewandte Chemie International Edition* **41**(12), 2034–2057, Wiley Online Library (2002).

[53] Ratna, D., and Karger-Kocsis, J., "Recent advances in shape memory polymers and composites: a review," *Journal of Materials Science* **43**(1), 254–269, Springer (2008)

[DOI:10.1007/s10853-007-2176-7].

[54] Thill, C., Etches, J., Bond, I., Potter, K., and Weaver, P., "Morphing skins," *The Aeronautical Journal* **112**(1129), 117–139 (2008).

[55] Austin, F., Siclari, M.J., Van Nostrand, W.C., Weisensel, G.N., Kottamasu, V., and Volpe, G., "Comparison of smart wing concepts for transonic cruise drag reduction," *Proc. SPIE* **3044**, 33–40 (1997) [DOI:10.1117/12.274664].

[56] Sneed, R., Smith, R.R., Cash, M.F., and Anderson, E.H., "Smart-material based hydraulic pump system for actuation of a morphing wing," *Collection of Technical Papers - AIAA/ASME/ASCE/AHS/ASC Structures, Structural Dynamics and Materials Conference* **1**, 14–23 (2007) [DOI:10.2514/6.2007-1702].

[57] Hagood, N.W., and Bent, A.A., "Development of piezoelectric fiber composites for structural actuation," *Collection of Technical Papers - AIAA/ASME Structures, Structural Dynamics and Materials Conference*(pt 6), 3625–3638 (1993).

[58] Wilkie, W.K., Bryant, R.G., High, J.W., Fox, R.L., Hellbaum, R.F., Jalink Jr., A., Little, B.D., and Mirick, P.H., "Low-cost piezocomposite actuator for structural control applications," *Proceedings of SPIE - The International Society for Optical Engineering* **3991**, 323–334 (2000) [DOI:10.1117/12.388175].

[59] Wickramasinghe, V.K., Chen, Y., Martinez, M., Kernaghan, R., and Wong, F., "Design and verification of a smart wing for an extremely-agile micro-air-vehicle," *Collection of Technical Papers - AIAA/ASME/ASCE/AHS/ASC Structures, Structural Dynamics and Materials Conference* (2009) [DOI:10.2514/6.2009-2132].

[60] Ohanian III, O.J., Karni, E.D., Olien, C.C., Gustafson, E.A., Kochersberger, K.B., Gelhausen, P.A., and Brown, B.L., "Piezoelectric composite morphing control surfaces for unmanned aerial vehicles," *Proceedings of SPIE - The International Society for Optical Engineering* **7981** (2011) [DOI:10.1117/12.881770].

[61] Schröck, J., Meurer, T., and Kugi, A., "Control of a flexible beam actuated by macro-fiber composite patches: I. Modeling and feedforward trajectory control," *Smart Materials and Structures* **20**(1) (2011) [DOI: 10.1088/0964-1726/20/1/015015].

[62] Schröck, J., Meurer, T., and Kugi, A., "Control of a flexible beam actuated by macro-fiber composite patches: II. Hysteresis and creep compensation, experimental results," *Smart Materials and Structures* **20**(1), Temple Back, Bristol, BS1 6BE, United Kingdom (2011) [DOI:10.1088/0964-1726/20/1/015016].

[63] Butt, L., Day, S., Weaver, J., Sossi, C., Wolek, A., Bilgen, O., Mason, W., and Inman, D., "Wing Morphing Design Utilizing Macro Fiber Composite Smart Materials," *Society of Allied Weight Engineers* (2010).

[64] “Macro Fiber Composite - MFC,” <http://www.smart-material.com/media/Datasheet/MFC_V2.1-web-2014.pdf> (26 June 2014).

[65] Bilgen, O., Kochersberger, K.B., Inman, D.J., and Ohanian III, O.J., “Novel, bidirectional, variable-camber airfoil via macro-fiber composite actuators,” *Journal of Aircraft* **47**(1), 303–314 (2010) [DOI:10.2514/1.45452].

[66] Bilgen, O., “Aerodynamic and Electromechanical Design, Modeling and Implementation of Piezocomposite Airfoils,” *Virginia Polytechnic Institute and State University, PhD Thesis* (2010).

[67] Jarali, C.S., Raja, S., and Upadhya, A.R., “Constitutive modeling of SMA SMP multifunctional high performance smart adaptive shape memory composite,” *Smart Materials and Structures* **19**(10) (2010) [DOI:10.1088/0964-1726/19/10/105029].

[68] Lee, J.-K., and Taya, M., “Modeling for piezoelectric-shape memory alloy composites,” *Archive of Applied Mechanics* **81**(5), 629–640 (2011) [DOI:10.1007/s00419-010-0440-9].

[69] Hines, L., Arabagi, V., and Sitti, M., “Shape memory polymer-based flexure stiffness control in a miniature flapping-wing robot,” *IEEE Transactions on Robotics* **28**(4), 987–990 (2012) [DOI:10.1109/TRO.2012.2197313].

[70] Chinaud, M., Scheller, J., Rouchon, J., Duhayon, E., and Braza, M., “Hybrid electroactive wings morphing for aeronautic applications,” *Diffusion and Defect Data Pt.B: Solid State Phenomena* **198**, 200–205 (2013) [DOI:10.4028/www.scientific.net/SSP.198.200].

[71] Bar-Cohen, Y., “Comparison of EAPS with Other Actuator Technologies,” <http://ndeaa.jpl.nasa.gov/nasa-nde/lommas/eap/actuators-comp.pdf> (1 October 2013).

[72] Taylor, G.K., Carruthers, A.C., Hubel, T.Y., and Walker, S.M., *Wing Morphing in Insects, Birds and Bats: Mechanism and Function*, in *Morphing Aerospace Vehicles and Structures*, pp. 11–40 (2012) [DOI:10.1002/9781119964032.ch2Document].

[73] Anderson, J.D., *Fundamentals of Aerodynamics*, McGraw-Hill (2010).

[74] Bello, A.L., *Origins of Mathematical Words: A Comprehensive Dictionary of Latin, Greek, and Arabic Roots*, Johns Hopkins University Press (2013).

[75] Ivanov, V.I., and Trubetskov, M.K., *Handbook of Conformal Mapping with Computer-Aided Visualization*, pp. 1–4, Taylor & Francis (1994).

[76] Glauert, H., *The Elements of Aerofoil and Airscrew Theory*, p. 79, Cambridge University Press (1983).

[77] Sanders, B., Eastep, F.E., and Forster, E., "Aerodynamic and aeroelastic characteristics of wings with conformal control surfaces for morphing aircraft," *Journal of Aircraft* **40**(1), 94–99 (2003) [DOI:10.2514/2.3062].

[78] Wood, R.M., "A discussion of aerodynamic control effectors (ACEs) for unmanned air vehicles (UAVs)," *1st UAV Conference* (2002) [DOI:10.2514/6.2002-3494].

[79] Watts, A.C., Ambrosia, V.G., and Hinkley, E.A., "Unmanned aircraft systems in remote sensing and scientific research: Classification and considerations of use," *Remote Sensing* **4**(6), 1671–1692 (2012) [DOI:10.3390/rs4061671].

[80] Bilgen, O., Butt, L.M., Day, S.R., Sossi, C.A., Weaver, J.P., Wolek, A., Mason, W.H., and Inman, D.J., "A novel unmanned aircraft with solid-state control surfaces: Analysis and flight demonstration," *Journal of Intelligent Material Systems and Structures* **24**(2), 147–167 (2013) [DOI:10.1177/1045389X12459592].

[81] "Scan Eagle 2 Product Card," <http://www.insitu.com/images/campaigns/scaneagle2/Scaneagle2_ProductCard_PR102114_sm.pdf> (11 November 2014).

[82] Pankonien, A., and Inman, D.J., "Experimental testing of spanwise morphing trailing edge concept," *Proceedings of SPIE - The International Society for Optical Engineering* **8688** (2013) [DOI:10.1117/12.2009400].

[83] Gopalarathnam, A., and King Norris, R., "Ideal lift distributions and flap angles for adaptive wings," *Journal of aircraft* **46**(2), 562–571, American Institute of Aeronautics and Astronautics (2009) [DOI:10.2514/1.38713].

[84] Bilgen, O., Friswell, M.I., Kochersberger, K.B., and Inman, D.J., "Surface Actuated Variable-Camber and Variable-Twist Morphing Wings Using Piezocomposites," *Proceedings of 52nd AIAA/ASME/ASCE/AHS/ASC Structures, Structural Dynamics, and Materials* **4**(7), 2011–2072 (2011) [DOI:10.2514/6.2011-2072].

[85] Ohanian, O.J., David, B.M., Taylor, S.L., Kochersberger, K.B., Probst, T., Gelhausen, P.A., and Climer, J., "Piezoelectric morphing versus servo-actuated MAV control surfaces, part II: Flight testing," *51st AIAA Aerospace Sciences Meeting including the New Horizons Forum and Aerospace Exposition 2013* (2013) [DOI:10.2514/6.2013-767].

[86] Bilgen, O., Landman, D., and Friswell, M.I., "Low reynolds number behavior of a solid-state piezocomposite variable-camber wing," *54th AIAA/ASME/ASCE/AHS/ASC Structures, Structural Dynamics, and Materials Conference* (2013) [DOI:10.2514/6.2013-1515].

[87] Molina Jr., E., Peel, L.D., and Cohen, A., "Use of 3D multi-material printing to fabricate flexible composite actuators," *International SAMPE Technical Conference* (2012).

[88] Previtali, F., and Ermanni, P., "Performance of a non-tapered 3D morphing wing with integrated compliant ribs," *Smart Materials and Structures* **21**(5) (2012) [DOI:10.1088/0964-1726/21/5/055008].

[89] Duraisamy, K., "Studies in tip vortex formation, evolution and control" (2005).

[90] Liu, L., Yin, W., Dai, F., Liu, Y., and Leng, J., "Static aeroelastic deformation of flexible skin for continuous variable trailing-edge camber wing," in *Proceedings of SPIE* **7977** (2011) [DOI:10.1117/12.880323].

[91] Gandhi, F., and Anusonti-Inthra, P., "Skin design studies for variable camber morphing airfoils," *Smart Materials and Structures* **17**(1) (2008) [DOI:10.1088/0964-1726/17/01/015025].

[92] Murugan, S., Flores, E.I.S., Friswell, M.I., and Adhikari, S., "Optimal Design of Elastomer Composites for Morphing Skins," *ASME Conference Proceedings* **2011**(54716), 551–560, ASME (2011) [DOI:10.1115/SMASIS2011-5021].

[93] Ghabezi, P., and Golzar, M., "Mechanical analysis of trapezoidal corrugated composite skins," *Applied Composite Materials* **20**(4), 341–353 (2013) [DOI:10.1007/s10443-012-9267-6].

[94] Olympio, K.R., and Gandhi, F., "Zero Poisson's Ratio Cellular Honeycombs for Flex Skins Undergoing One-Dimensional Morphing," *Journal of Intelligent Material Systems and Structures* **21**(17), 1737–1753 (2010) [DOI:10.1177/1045389X09355664].

[95] Olympio, K.R., and Gandhi, F., "Flexible skins for morphing aircraft using cellular honeycomb cores," *Journal of Intelligent Material Systems and Structures* **21**(17), 1719–1735 (2010) [DOI:10.1177/1045389X09350331].

[96] Haifeng, P., Erbao, D., Shiwu, Z., and Jie, Y., "Research on flexible honeycomb structure design for morphing aircraft," *Proceedings of 2011 International Conference on Electronic and Mechanical Engineering and Information Technology, EMEIT 2011* **5**, 2271–2274 (2011) [DOI:10.1109/EMEIT.2011.6023564].

[97] Zhang, P., Zhou, L., and Qiu, T., "Design and application of cross-shaped cellular honeycombs for a variable camber wing," *Journal of Aircraft* **49**(5), 1451–1459 (2012) [DOI:10.2514/1.C031733].

[98] "PN2 Aerospace Grade Aramid Fiber Honeycomb," <http://www.plascore.com/pdf/Plascore_PN2.pdf>.

[99] Ohanian, O.J., Hickling, C., Stiltner, B., Karni, E.D., Kochersberger, K.B., Probst, T., Gelhausen, P.A., and Blain, A.P., "Piezoelectric morphing versus servo-actuated MAV control surfaces," *53rd AIAA/ASME/ASCE/AHS/ASC Structures, Structural Dynamics and Materials Conference 2012* (2012) [DOI:10.2514/6.2012-1512].

[100] Edelsbrunner, H., Kirkpatrick, D.G., and Seidel, R., "On the Shape of a Set of Points in the Plane," *IEEE Transactions on Information Theory* **IT-29**(4), 551–559 (1983).

[101] Bilgen, O., Erturk, A., and Inman, D.J., "Analytical and experimental characterization of macro-fiber composite actuated thin clamped-free unimorph benders," *Journal of Vibration and Acoustics, Transactions of the ASME* **132**(5), 0510051–0510056 (2010) [DOI:10.1115/1.4001504].

[102] Wang, Q.-M., and Eric Gross, L., "Constitutive equations of symmetrical triple layer piezoelectric benders," *IEEE Transactions on Ultrasonics, Ferroelectrics, and Frequency Control* **46**(6), 1343–1351 (1999).

[103] Pankonien, A.M., Duraisamy, K., Faria, C.T., and Inman, D.J., "Synergistic smart morphing aileron: Aero-structural performance analysis," *22nd AIAA/ASME/AHS Adaptive Structures Conference* (2014) [DOI:10.2514/6.2014-0924].

[104] "Digital Materials Data Sheet," <http://www.stratasys.com/~/media/Main/Secure/Material%20Specs%20MS/PolyJet-Material-Specs/Digital_Materials_Datasheet.pdf> (4 December 2014).

[105] Martin, C.A., Hallam, B.J., Flanagan, J.S., and Bartley-Cho, J., "Design, fabrication, and testing of a scaled wind tunnel model for the smart wing project," *Journal of Intelligent Material Systems and Structures* **15**(4), 269–278 (2004) [DOI:10.1177/1045389X04042797].

[106] Sheldahl, R.E., and Klimas, P.C., "Aerodynamic characteristics of seven symmetrical airfoil sections through 180-degree angle of attack for use in aerodynamic analysis of vertical axis wind turbines.," *Sandia National Laboratories Energy Report* (1981).

[107] Prazenica, R.J., Kim, D., Moncayo, H., Azizi, B., and Chan, M., "Design, characterization, and testing of macro-fiber composite actuators for integration on a fixed-wing UAV," *Proceedings of SPIE - The International Society for Optical Engineering* **9057** (2014) [DOI:10.1117/12.2045277].

[108] Pankonien, A.M., and Inman, D.J., "Aeroelastic performance evaluation of a flexure box morphing airfoil concept," *Proceedings of SPIE - The International Society for Optical Engineering* **9057** (2014) [DOI:10.1117/12.2046406].

[109] "AMD2012-CE3 High Voltage Amplifier," <http://www.smart-material.com/media/Datasheet/AMD2012-CE3-V12-2013web.pdf> (5 December 2014).

[110] Pankonien, A.M., and Inman, D.J., “Aerodynamic Performance of a Spanwise Morphing Trailing Edge Concept,” *25th International Conference on Adaptive Structures and Technologies* (2014).

[111] Brown, E.L., “Integrated strain actuation in aircraft with highly flexible composite wings” (2003).

[112] Molinari, G., Quack, M., Arrieta, A.F., Morari, M., and Ermanni, P., “Design and realization of a compliant adaptable wing,” *ASME 2014 Conference on Smart Materials, Adaptive Structures and Intelligent Systems, SMASIS 2014* **2** (2014) [DOI:10.1115/SMASIS2014-7531].

[113] Barlow, J.B., Rae, W.H., and Pope, A., *Low-Speed Wind Tunnel Testing*, Wiley (1999).

[114] Kuethe, A.M., and Schetzer, J.D., *Foundations of Aerodynamics*, Wiley (1950).

[115] Kota, S., Hetrick, J.A., Osborn, R., Paul, D., Pendleton, E., Flick, P., and Tilmann, C., “Design and application of compliant mechanisms for morphing aircraft structures,” *Proc. SPIE* **5054**, 24–33 (2003) [DOI:10.1117/12.483869].

[116] Friswell, M.I., “Morphing aircraft: An improbable dream,” *ASME 2014 Conference on Smart Materials, Adaptive Structures and Intelligent Systems, SMASIS 2014* **1** (2014) [DOI:10.1115/SMASIS2014-7754].

[117] Klein, A., and Viswanathan, S.P., “Minimum induced drag of wings with given lift and root-bending moment,” *Zeitschrift für Angewandte Mathematik und Physik (ZAMP)* **24**(6), 886–892, Springer (1973).

[118] Pate, D.J., and German, B.J., “Lift distributions for minimum induced drag with generalized bending moment constraints,” *Journal of Aircraft* **50**(3), 936–946 (2013) [DOI:10.2514/1.C032074].

[119] MATLAB, *8.1.0.604 (R2013a)*, The MathWorks Inc., Natick, Massachusetts (2013).

[120] Pankonien, A.M., and Inman, D.J., “Reduced Aspect Ratio Testing of a Macro-Fiber Composite Morphing Aileron,” *AIAA Journal of Aircraft* (2015).

[121] Pankonien, A.M., Faria, C.T., and Inman, D.J., “Synergistic smart morphing aileron,” *54th AIAA/ASME/ASCE/AHS/ASC Structures, Structural Dynamics, and Materials Conference* (2013) [DOI:10.2514/6.2013-1512].

[122] Shaw, J.A., and Churchill, C.B., “A reduced-order thermomechanical model and analytical solution for uniaxial shape memory alloy wire actuators,” *Smart Materials and Structures* **18**(6) (2009) [DOI:10.1088/0964-1726/18/6/065001].

[123] Abdulrahim, M., Garcia, H., and Lind, R., "Flight characteristics of shaping the membrane wing of a micro air vehicle," *Journal of Aircraft* **42**(1), 131–137 (2005) [DOI:10.2514/1.4782].

[124] Hambley, A.R., Kumar, N., and Kulkarni, A.R., *Electrical engineering: principles and applications*, Pearson Prentice Hall (2008).

[125] Vinod, L., "Computational Investigation of Micro-Scale Coaxial Rotor Aerodynamics in Hover," *Maryland, USA: Uni-versity of Maryland at College Park* (2009).

[126] Turkel, E., "Preconditioning techniques in computational fluid dynamics," *Annual Review of Fluid Mechanics* **31**, 385–416 (1999).

[127] Spalart, P.R., and Allmaras, S.R., "A one-equation turbulence model for aerodynamic flows," *30th AIAA Aerospace Sciences Meeting and Exhibit* (1992).

[128] Baeder, J., Duraisamy, K., and Lakshminarayan, V., "RANS Predictions of Complex Hovering Rotor Configurations: From Micro Scale to Full Scale," *Computational Fluid Dynamics Journal* **18**, 3–4 (2011).

[129] Aranakz, A.C., Lakshminarayan, V.K., and Duraisamy, K., "Assessment of transition model and CFD methodology for wind turbine flows," *42nd AIAA Fluid Dynamics Conference and Exhibit 2012* (2012).

[130] Nelder, J.A., and Mead, R., "A simplex method for function minimization," *The computer journal* **7**(4), 308–313, Br Computer Soc (1965).

[131] Battini, J.-M., "Co-rotational beam elements in instability problems," PhD Dissertation, Dept of Mechanics, Royal Institute of Technology, Sweden (2002).

[132] Relvas, A., and Suleman, A., "Application of the corotational structural kinematics and Euler flow to two-dimensional nonlinear aeroelasticity," *Computers and Structures* **85**(17-18), 1372–1381 (2007) [DOI:10.1016/j.compstruc.2006.08.089].

[133] De Borst, R., Crisfield, M.A., Remmers, J.J., and Verhoosel, C.V., *Nonlinear finite element analysis of solids and structures*, John Wiley \& Sons (2012).

[134] Sachs, E., Cima, M., Cornie, J., Brancazio, D., Bredt, J., Curodeau, A., Fan, T., Khanuja, S., Lauder, A., et al., "Three-Dimensional Printing: The Physics and Implications of Additive Manufacturing," *CIRP Annals - Manufacturing Technology* **42**(1), 257–260 (1993).

[135] Dimas, L.S., Bratzel, G.H., Eylon, I., and Buehler, M.J., "Tough composites inspired by mineralized natural materials: Computation, 3D printing, and testing," *Advanced Functional Materials* **23**(36), 4629–4638 (2013).